Microfluidic Models of Tumor-Stroma Interactions to Study the Interplay of Cancer Cells with their Surrounding Microenvironment

by

Danh Truong

A Dissertation Presented in Partial Fulfillment
of the Requirements for the Degree
Doctor of Philosophy

Approved October 2018 by the
Graduate Supervisory Committee:

Mehdi Nikkhah, Chair
Brent Vernon
Barbara Smith
Ghassan Mouneimne
Joshua LaBaer

ARIZONA STATE UNIVERSITY

December 2018

ABSTRACT

According to the World Health Organization, cancer is one of the leading causes of death around the world. Although early diagnostics using biomarkers and improved treatments with targeted therapy have reduced the rate of cancer related mortalities, there remain many unknowns regarding the contributions of the tumor microenvironment to cancer progression and therapeutic resistance. The tumor microenvironment plays a significant role by manipulating the progression of cancer cells through biochemical and biophysical signals from the surrounding stromal cells along with the extracellular matrix. As such, there is a critical need to understand how the tumor microenvironment influences the molecular mechanisms underlying cancer metastasis to facilitate the discovery of better therapies. This thesis described the development of microfluidic technologies to study the interplay of cancer cells with their surrounding microenvironment. The microfluidic model was used to assess how exposure to chemoattractant, epidermal growth factor (EGF), impacted 3D breast cancer cell invasion and enhanced cell motility speed was noted in the presence of EGF validating physiological cell behavior. Additionally, breast cancer and patient-derived cancer-associated fibroblast (CAF) cells were co-cultured to study cell-cell crosstalk and how it affected cancer invasion. *GPNMB* was identified as a novel gene of interest and it was shown that CAFs enhanced breast cancer invasion by up-regulating the expression of *GPNMB* on breast cancer cells resulting in increased migration speed. Lastly, this thesis described the design, biological validation, and use of this microfluidic platform as a new *in vitro* 3D organotypic model to study mechanisms of glioma stem cell (GSC) invasion in the context of a vascular niche. It was confirmed that CXCL12-CXCR4 signaling is

involved in promoting GSC invasion in a 3D vascular microenvironment, while also demonstrating the effectiveness of the microfluidic as a drug screening assay. Taken together, the broader impacts of the microfluidic model developed in this dissertation include, a possible alternative platform to animal testing that is focused on mimicking human physiology, a potential *ex vivo* platform using patient-derived cells for studying the interplay of cancer cells with its surrounding microenvironment, and development of future therapeutic strategies tailored toward disrupting key molecular pathways involved in regulatory mechanisms of cancer invasion.

DEDICATION

To my amazing girlfriend and life partner, Christine. I thank you for always being there for me and providing me support when I needed it these past years. You are an amazing person and I hope that I can repay your love and kindness.

To my family and friends back in Texas. Thank you for providing me a home whenever I visited. I cannot imagine being able to complete these challenges without knowing that I still had somewhere I could go to be with loved ones.

ACKNOWLEDGMENTS

I would like to acknowledge my doctoral advisor and committee chair, Dr. Mehdi Nikkhah, for his guidance and support in these past couple of years. His mentorship was invaluable for preparing me to become a mature scientist. Being a part of this lab has truly enriched my career as a scientist by providing me with an opportunity to be productive and follow my ideas in research, enabling collaboration with scientists of diverse backgrounds, giving me a chance to mentor and guide students, and providing a venture for proposal writing which I utilized to secure some of my own funding.

I would also like to acknowledge my doctoral committee members, Dr. Barbara Smith, Dr. Brent Vernon, Dr. Ghassan Mouneimne, and Dr. Joshua LaBaer, for spending their time with me to answering my questions and giving me guidance for my research and career. I am truly appreciative.

I would like to thank my lab members, Ali, Harpinder, Nitish, Eric, Jaime, Alex, Supriya, Alison, Thai, Yuka, Zach, and others of the the Nikkhah Lab for their friendship and support over the years.

I would like to thank Dr. Barbara A. Pockaj for giving us the opportunity to isolate patient-derived fibroblasts from tumor biopsies; Dr. Jin G. Park for his invaluable assistance on the processing and analysis of the sequencing data; Crystal Willingham and Kassondra Hickey for their assistance on biological protocols; Dr. Shwetal Mehta, Dr. Roberto Fiorelli, and Ernesto Luna Melendez for their collaboration and expertise on glioma biology and modeling. I would also like to acknowledge the ASU Nanofab facility. Importantly, I want to thank Mr. and Mrs. Daryl Burton for their support of me

and my research. It has really allowed me to reach for opportunities that I would not have been without their support.

Lastly, I would like to acknowledge the funding sources: National Science Foundation Award # CBET 1510700, the 2017-2018 and 2018-2019 Achievement Rewards for College Scientists Scholarship, the 2016-2017 and 2017-2018 International Foundation for Ethical Research Fellowship, and funding from ASU Graduate & Professional Student Association, the ASU Graduate College, and School of Biological and Health Systems Engineering.

TABLE OF CONTENTS

Page

CHAPTER Page

LIST OF FIGURES

Figure Page

Figure Page

PREFACE

This dissertation includes original research and review articles previously published by the primary author. Chapter 1 describes the introduction and background information of this thesis (N. Peela, Truong, et al., 2017). Chapter 2 describes the fabrication of a microfluidic with distinct tumor and stroma regions to study the influence of EGF on cancer invasion into the stroma (D. Truong et al., 2016). Chapter 4 describes the use of a microfluidic model comprised of a tumor, stroma, and vascular region to study the interactions between glioma stem cells and the vasculature (Danh Truong et al., 2018).

CHAPTER 1

INTRODUCTION

1.1 Cancer

Cancer is a world-wide public health issue being the second leading cause of death within the United States with approximately 1.7 million new cancer cases in each year (R. L. Siegel, Miller, & Jemal, 2018). Vast amounts of resources have been poured into stalling or eliminating cancer through discovery of novel drug candidates. However, development of many of these candidates have ended up costing over a billion dollar with an abysmal rate of 10% of these drugs eventually reaching the market (Cox, Reese, Bickford, & Verbridge, 2015). The high rate of failure has been attributed to use of oversimplified *in vitro* tumor models to simple two-dimensional (2D) cell cultures during preclinical screenings (Cox et al., 2015; N. Peela, Truong, et al., 2017). These models often did not reflect the complexities of the tumor microenvironment and therefore did not fully represent the intricacies of cancer. In fact, numerous investigations have pointed out that components of the tumor microenvironment, such as tissue dimensionality, and tumor-stroma interactions, comprising of spatial organization of cells, cell-cell and cell-ECM crosstalk, are prominent factors influencing tumor growth, progression, and resistance to therapy (Friedl & Alexander, 2011). Despite that, 2D testing remains as the standard for drug screening and testing during the early stages of drug development. Furthermore, even the simplest 3D models consisting of only cancer cells in a 3D matrix resemble the gene expression profiles of human cancers more closely than 2D models (Ridky, Chow, Wong, & Khavari, 2010). Therefore, it is necessary to design more complex and validated 3D *in vitro* models that appreciates the complexities of the tumor

microenvironment to improve understanding of cancer biology as well as predicting the efficacy of drug screening.

1.2 The Tumor Microenvironment

The importance of the tumor microenvironment (TME) has been increasingly accepted as the growing body of literature over the past decade have demonstrated that cancer cells do not act alone during tumor progression (Joyce & Pollard, 2009). However, the roles of the individual components within the TME during cancer invasion are still being elucidated (Dvorak, 2015; Kalluri, 2016). The TME could be divided into two major components, the malignant cells and the stroma. Although some aspects of the stroma have been appreciated, such as importance of the extracellular matrix (ECM) on cancer invasion, the contributions of the stromal cells residing near or within the tumor have not as nearly been focused on. Indeed, cancer cells do require assistance from the stromal cells as the tumor progresses toward metastasis (Mao, Keller, Garfield, Shen, & Wang, 2013). Interactions with stromal cells have also been implicated in promoting resistance to conventional cancer therapies (Castells, Thibault, Delord, & Couderc, 2012). Unfortunately, dissecting the consequences of the interactions between tumor and stromal cells are further complicated by the evolution of stromal cell phenotypes during tumorigenesis, such as activation of fibroblasts or polarization of macrophages (Sugimoto, Mundel, Kieran, & Kalluri, 2006). This brings forth context dependent influence of stromal cells which can alter the TME by promoting or inhibiting cancer invasion (Mueller & Fusenig, 2004). Therefore, understanding the dynamic interactions between the tumor and the stromal cells will lead to significantly better cancer therapies.

Harold Dvorak in 1986 proposed that tumors were wounds that did not heal and that they required the presence of the surrounding stroma for the tumor to grow beyond 1 to 2 mm (H. F. Dvorak, 1986). This hypothesis eventually laid the foundation for understanding how the tumor co-opted the surrounding stroma for nourishment and growth (Dvorak, 2015). As noted by many even before Dvorak, wound healing has many parallels to tumor growth and progression (Balkwill & Mantovani, 2001). Histology and gene expression profiling of both wounds and tumors have provided evidence in demonstrating similar biological processes occurring in both and that cancer cells did not create a new biological program but instead exploit an existing biological program – wound healing (Chang et al., 2004; H. F. Dvorak, 1986). Wound healing generally begins with a local tissue injury resulting in leakage of plasma proteins, platelets, and blood cells. Platelets aggregate and release growth factors, such as platelet-derived growth factor, transforming growth factor-β, and fibroblast growth factors, which act as chemoattractants and mitogens for stromal fibroblasts to infiltrate and proliferate. Fibroblasts are cells that reside in connective tissue whose roles includes synthesizing and depositing components of the ECM as well as promoting wound re-epithelialization and contraction (Florin, Maas-Szabowski, Werner, Szabowski, & Angel, 2005). Keratinocytes, the predominant cell in the epidermis, rearrange their actin cytoskeleton and reduce cell-cell contact to promote efficient migration and wound contraction during wound healing. Vascular factors from platelets induce vascular leakage promoting infiltration of inflammatory cells and plasma proteins. The inflammatory cells scavenge and remove tissue debris and foreign matter while also releasing vascular endothelial growth factor to promote angiogenesis or the process of new capillary formation. Overall,

this results in granulation tissue comprising of cells, edema, vessels, and connective tissue (Dvorak, 2015). Once the wound is healed, the granulation tissue is resorbed resulting in a scar. Likewise, tumor formation and progression follow a very similar biological process. However, instead of a tissue injury, tumor cells promote vascular leakage through secretion of VEGF which is triggered due to hypoxic conditions in the tumor. In addition, tumor cells replace the role of platelets in recruiting fibroblasts and promoting ECM remodeling. Further, tumor cells also behave similarly to keratinocytes by adopting a mesenchymal phenotype to migrate and proliferate. In fact, similar gene profiles have been observed between keratinocytes during wound healing and cancer cells (Chang et al., 2004). Likewise, both wound re-epithelialization and migrating/growing tumor cells are affected by similar stromal-derived mitogens and chemoattractants, including stromal-derived factor 1 (SDF1), epidermal growth factor (EGF), and hepatocyte growth factor (HGF). Inflammatory cells, like macrophages, are also recruited into the tumor during cancer progression. Although, this may seem counterproductive to tumor development, there is much evidence pointing out that inflammatory cells promote cancer through stimulating angiogenesis, proliferation of cancer cells, and suppressing tumoricidal actions.

Indeed, tumors are much more complex than wounds. For instance, unlike wounds, tumor cells exhibit genetic instability leading to loss of tumor suppression genes and promotion of oncogenes that drive tumor progression (Hanahan & Coussens, 2012; Hanahan & Weinberg, 2011). Further, enhanced expression of oncogenes could indeed engage the wound healing program further to generate a tumor-promoting microenvironment. This of course necessitates the need to understand the interaction

between tumors and their microenvironment, specifically stromal cells, to abrogate the dynamic communication involved in promoting cancer growth and progression. Herein, we review some of the pro-tumorigenic stromal cells and how they contribute to cancer invasion.

1.2.1 Contribution of Stromal Cells to Cancer Invasion

Cancer invasion and metastasis is considered as one of the defining hallmarks of cancer (Hanahan & Weinberg, 2011). Indeed, stromal cells have been implicated as major contributors to promoting invasion and metastasis (Figure 1.1). A variety of stromal cells that are currently being studied could be classified generally as fibroblast, endothelial, and immune cells.

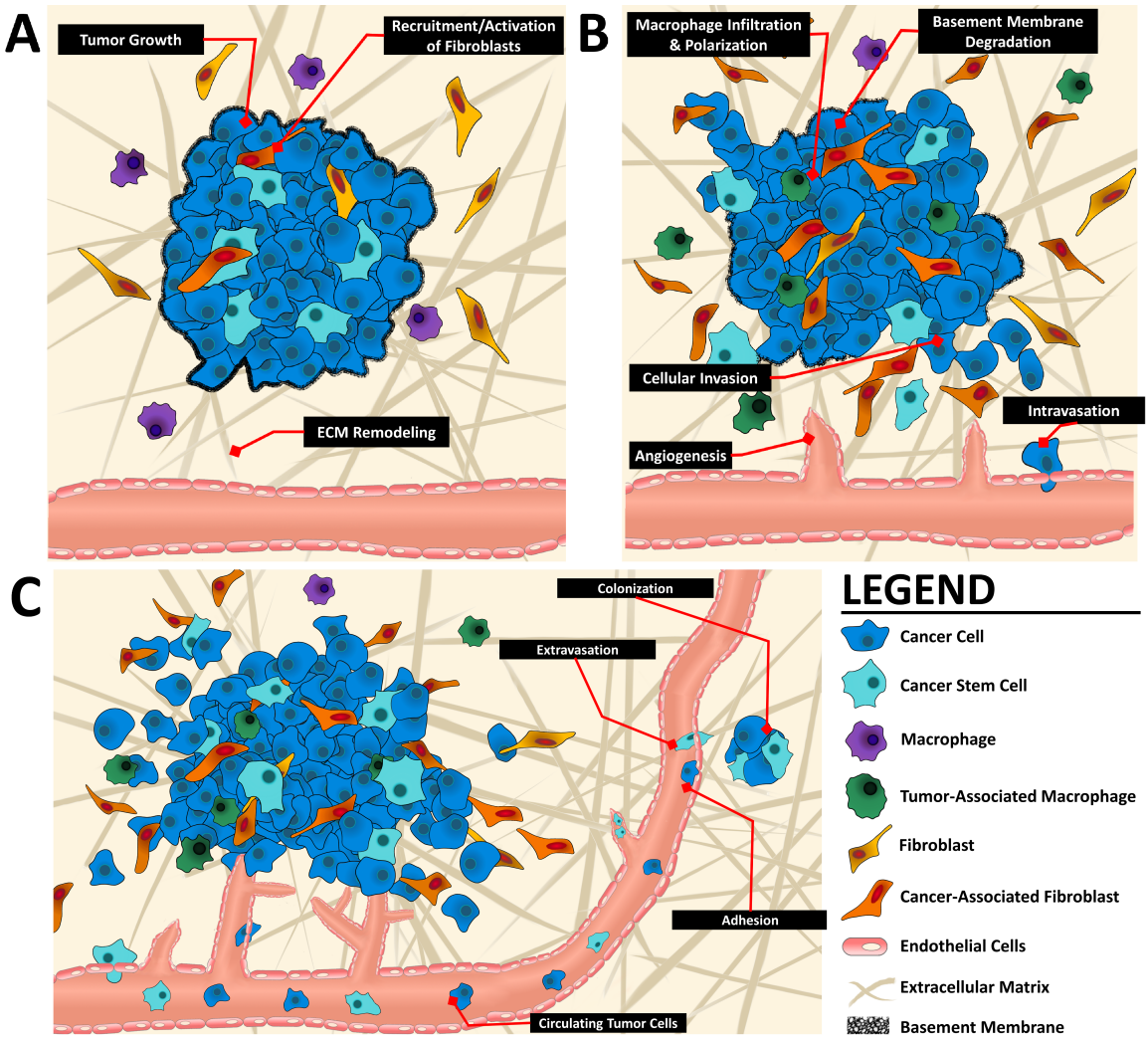

Figure 1.1 Schematic of the metastatic cascade.

Tumor growth and development results in ECM remodeling (A) as well as differentiation of cancer stem cells and fibroblasts. Subsequently, angiogenesis, cancer cell invasion, and intravasation (B) occur. Finally, surviving cancer cells and cancer stem cells circulate through the body, attach to blood vessels, and extravasate (C) to form secondary metastases.

1.2.2 Fibroblast Cells

Cancer-associated fibroblasts (CAFs) among other non-cancer cells within the stroma stand out as the most prominent cell type within the TME (Kalluri, 2016; Ohlund, Elyada, & Tuveson, 2014). There ubiquitous nature within the TME allows them a unique position to significantly influence cancer invasion (Figure 1.1A). Ongoing studies have highlighted and demonstrated that the presence of CAFs promoted significant growth of different cancers, such as breast (Orimo et al., 2005), prostate (Olumi et al., 1999), ovarian (Zhang et al., 2011), colon (Nakagawa et al., 2004), and non-small cell lung cancer (Bremnes et al., 2011). They have specifically implicated them as key components in cancer initiation, promotion, and therapeutic responses (Luo, Tu, Liu, & Liu, 2015; Ohlund et al., 2014; Paraiso & Smalley, 2013). Studies showed that the crosstalks between cancer and CAFs involve mediating factors such as growth factors, cytokines, and proteases that supports tumor growth and development (Allinen et al., 2004; Jia et al., 2013; Olsen, Moreira, Lukanidin, & Ambartsumian, 2010; Orimo et al., 2005; Soon et al., 2013; Sung et al., 2013). For instance, Orimo et al. demonstrated that CAFs present in the tumor promoted cancer growth through SDF1-α signaling as well as angiogenesis in part by the same cytokine (Orimo et al., 2005). Furthermore, CAFs have also been implicated in mediating tumor-enhancing inflammation. Erez et al. demonstrated that CAFs enhanced tumor growth by recruitment of macrophages into the TME. This process is highly dependent on NF-κB signaling (Erez, Truitt, Olson, Arron, & Hanahan, 2010). Furthermore, CAFs are a major source of proteases, including matrix metalloproteases (MMPs), during matrix remodeling. Giannoni et al. identified a reciprocal crosstalk between prostate cancer cells (PCCs) and fibroblasts that promoted MMP secretion and invasiveness. They showed that PCCs produced interleukin-6 (IL-6)

that activated fibroblasts which in turn led to increased secretion of MMP-2 and MMP-9. They suggested that this crosstalk was the basis for promoting cancer migration (Giannoni et al., 2010). Notably, other studies demonstrated that removal of CAFs from the *in vivo* TME within mice led to enhanced efficacy of chemotherapeutics as well as reduction in tumor volume and blood vessel density (Rakesh K. Jain, Duda, Clark, & Loeffler, 2006; Santos, Jung, Aziz, Kissil, & Pure, 2009). As such, understanding and targeting the crosstalks between cancer and CAFs within the TME is an appealing strategy for reducing cancer progression.

1.2.3 Endothelial Cells

The microvascular environment plays important physiological roles within the human body aside from supplying oxygen and nutrients to the surrounding tissues. For instance, the vascular endothelium wall functions as a selective barrier to control distribution of certain biomolecules. On the other hand, angiogenic signals from injured tissue cause the nearby endothelial cells (ECs) to migrate to the damaged area to form new capillary systems (Carmeliet & Jain, 2000). Inflammatory cells, such as macrophages and neutrophils, use the endothelium wall as an adhesion site for transendothelial migration to nearby tissues. However, in a TME, the tumor-associated vessels are often abnormally grown (Kerbel, 2008). Often these vessels are irregular, lack a basement membrane, and more leaky than normal endothelium (Carmeliet & Jain, 2000).

Tumor-associated angiogenesis and vascular growth is largely dependent on pro- and anti-angiogenic factors and the abundance of these factors depend on the

microenvironment (Figure 1.1B). Well-orchestrated gradients of angiogenic factors are required to properly produce new vessels, but unregulated release of angiogenic factors, like vascular endothelial growth factor (VEGF), from cancer cells can lead to misguided vessel formation (Hanahan & Weinberg, 2011). The resulting structure of tumor vasculature is heterogeneous, highly disorganized, and tortious with uneven diameters and gaps within the endothelium. Major consequences are regions of hypoxia that could select for more malignant cancer cells and lack of pericytes and smooth muscle cells that reduce the function of vessels (Kerbel, 2008). In addition, these defects lead to enhanced leakiness and permeability altering the TME and reducing the effectiveness of pharmacological drugs. Non-uniform surface markers are a result of tumor-associated angiogenesis as well. Lack or heterogeneic expression of these surface markers may explain why leukocyte–endothelial interaction is relatively low in tumors (R. K. Jain et al., 1996). This further creates challenges in targeting tumor vasculature due to differences or lack of targetable surface markers.

The lymphatic system was historically thought to only play a passive role in cancer metastasis by providing tracks for cancer metastases (Christiansen & Detmar, 2011). However, recent studies have indicated that there are dynamic interactions between the lymphatic system and cancer cells. For instance, secretion of VEGF-C and VEGF-D from cancer cells to lymphatic ECs (LECs) have been demonstrated to create highly permeable peritumoral lymphatics while also enlarging the existing collecting lymphatic to facilitate metastatic spread (Hirakawa et al., 2007). In fact, VEGF-C expression is well correlated with lymphatic metastasis while enhanced expression is raises the risk of distant metastasis and death (Akagi et al., 2000; Kurebayashi et al.,

1999). In addition, the lymphatic vessels serve as a trafficking system for immune cells to travel from peripheral tissues to lymph nodes. This process is highly regulated by chemokines to coordinate the homing of immune cells. However, cancer cells have been demonstrated to exploit this process by expressing chemokine receptors therefore mediating their invasion toward distant tissues (Muller et al., 2001). For instance, LECs were shown to traffic dendritic cells (DCs) by secreting CC-chemokine ligand (CCL21) which is the ligand for receptor CCR7 located on the DCs (Vaahtomeri et al., 2017). Likewise, cancer cells have been shown to express CCR7 and experiments have demonstrated that this enabled migration toward CCL21 (Shields, Emmett, et al., 2007). Expression of CXCR4, a chemokine receptor for SDF-1 or CXCL12 mentioned earlier, has also been clinically associated with spread to lymphoid sites (M. Kim et al., 2010). Normally functioning lymphatics typically promote immune cell infiltration through regulated chemotactic gradients of CXCL12, but tumor-induced lymphatic vessels secrete CXCL12 in a de-regulated manner promoting cancer cell invasion (Hirakawa et al., 2009). Surprisingly, CCR7, an overexpressed receptor on cancer cells mentioned earlier, has also been identified as a receptor for CXCL12 (Cabioglu et al., 2005). Taken together, the complex interactions between the lymphatic system and cancer cells highlight the dynamic contribution of the lymphatics to cancer invasion.

1.2.4 Immune Cells

Immune cells represent a class of cells that infiltrate the stroma and play an active role in tumorigenesis by promoting tumor growth, survival, and migration. For instance, tumor-associated macrophages (TAMs), which have a similar phenotype to activated M2

macrophages, facilitate cancer cell migration through secretion of chemokines and mitogenic factors, by suppressing destructive immune functions and degradation of the surrounding matrix. One such chemokine and mitogen, epidermal growth factor (EGF) had been implicated in a positive feedback loop enabling cancer invasion (J. Wyckoff et al., 2004; J. B. Wyckoff et al., 2007). Cancer cells release colony stimulating factor 1 (CSF1) attracting TAMs which lead to further secretion of EGF from TAMs developing into a migration relay between the two cell types. Other well-known chemoattractants and mitogenic factors have included, chemokines like CXCL12, TGF-β, and interleukins. Infiltrating immune cells also suppress immune destruction and enable tumor cells to evade the immune surveillance (Quatromoni & Eruslanov, 2012). For instance, signaling through CCL22 have been shown to attract regulatory T (T_{reg}) cells which suppresses autoreactive T cells, which normally target and destroy tumor cells (Curiel et al., 2004). In fact, recent studies showed high populations of T_{reg} cells residing in tumors and lymph nodes (Beyer & Schultze, 2006; Curiel, 2007). In addition, like T_{reg} cells, myeloid-derived suppressor cells (MDSCs) serve as another avenue for evasion and suppression of the immune system (Bayne et al., 2012). These cells are immature myeloid cells known to regulate tissue homeostasis during times of injury. However, within a TME, this could lead to disruption of immune responses such as inhibition of dendritic or natural killer cells. Still, the role of other immune cells has not been well characterized in cancer.

1.3 Tumor Microenvironment Research Models

1.3.1 Conventional in vivo and in vitro models of the tumor microenvironment

To characterize the cellular and molecular basis of cancer invasion in response to stromal factors, a significant effort has been devoted to developing tumor models recapitulating tumor-stroma interactions. *In vivo* models play a crucially important role in studying the cellular and molecular basis of disease progression (Figure 1.2). For example, mouse models have utilized to study the role of signaling factors and chemokines, such as EGF (Provenzano et al., 2006; Provenzano et al., 2008; J. Wyckoff et al., 2004). Additionally, the role of stromal cells in cancer cell invasion such as CAFs and TAMs have also been studied using *in vivo* systems (Orimo et al., 2005). However, these models suffer from lack of high resolution observation and analysis of cell-cell interactions as well as precise control over critical parameters, like manipulating stromal cells, in the TME (Britta Weigelt, Ghajar, & Bissell, 2014). Importantly, this lack of precise control has created challenges to determining the cause and effect relationships within the heterotypic dialogues between cancer and stromal cells like CAFs (B. Weigelt, 2014). Then there are crucial molecular and cellular differences between humans and mice limiting the scope for animal models to fully recapitulate human diseases (Mak, Evaniew, & Ghert, 2014).

To overcome some of these problems, conventional *in vitro* platforms, including transwell assays and 3D spheroid-based models, have been used to study the role of microenvironmental factors on cancer invasion (Figure 1.2) (N. Peela, Truong, et al., 2017; B. Weigelt, 2014). 2D assays have been extensively used to assess the role of chemoattractants on cancer cell migration (Saadi, Wang, Lin, & Jeon, 2006; S. J. Wang, Saadi, Lin, Minh-Canh Nguyen, & Li Jeon, 2004). Further, co-culture set-ups using fibroblasts or endothelial cells have teased out influences of ECM and soluble factors on

cancer cell invasion (Alexeyenko et al., 2015; Alkasalias et al., 2017; Alkasalias et al., 2014; Kramer & Nicolson, 1979). Still, these models are often oversimplified and do not recapitulate proper organotypic arrangement of the tumor-stroma architecture due to random mixing of cells. This limits the available analyses to proliferation, morphology, and protein expression as opposed to precise spatial organization of cells which could enable assessment of migration metrics (i.e. distance, speed, persistence) (Orimo et al., 2005; N. Peela, Truong, et al., 2017). Importantly, these models are often end-point assays that do not allow real-time observations of dynamic tumor-stroma interactions at cellular and molecular levels (Figure 1.2).

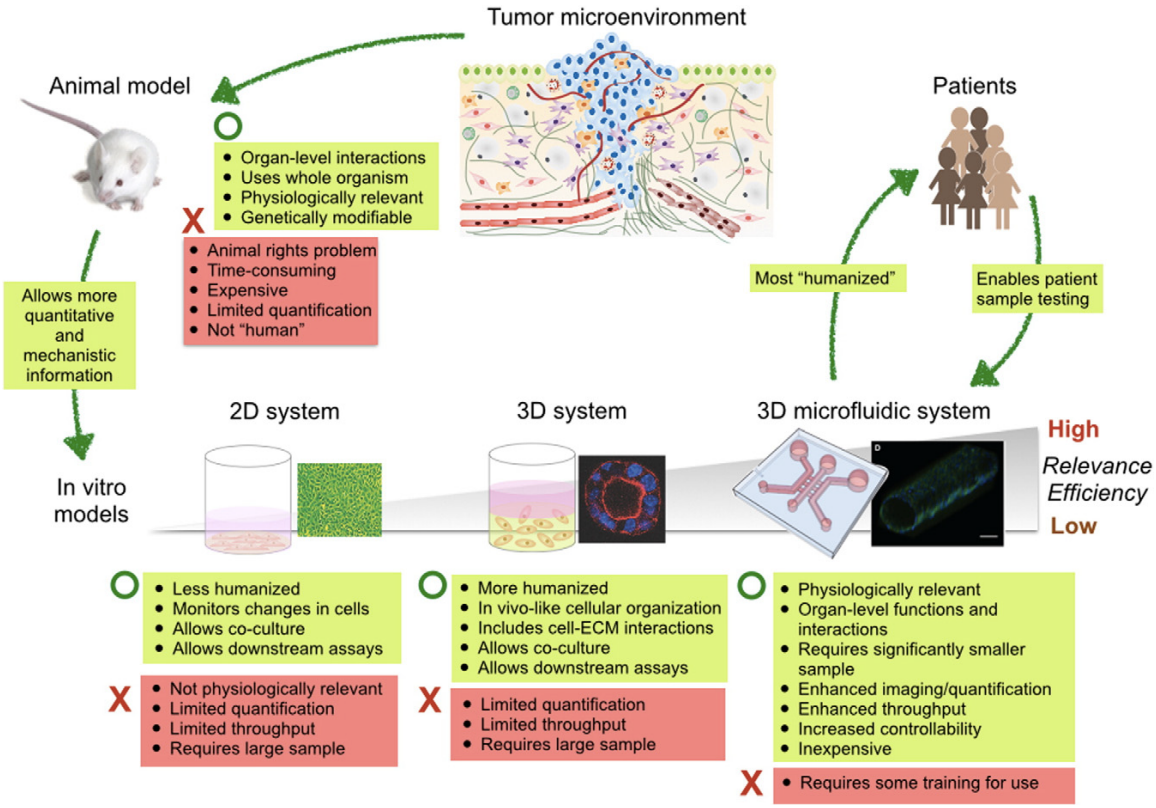

Figure 1.2 Comparison of cancer research models.

Reprinted from Microfluidic 3D models of cancer, 79-80, Sung, KE., Beebe, DJ., 68-78, Copyright (2014), with permission from Elsevier (Appendix F).

1.3.2 Microengineered models of the tumor microenvironment

With the difficulties and challenges of conventional *in vitro* models of the TME (Figure 1.2), microengineering technologies has emerged to model different aspects of cancer unveil the cellular and molecular basis of cancer invasion in response to tumor-stroma interactions (B. Weigelt, 2014). These technologies consist of 3D assays that enable tunable microenvironments to understand the complex interactions between tumor cells, stromal cells, biochemical and biophysical cues. As a result, large bodies of works have been devoted to developing these advanced 3D *in vitro* models of cancer to individually dissect important factors involved in cancer progression to reveal new biological insights (Figure 1.2).

Recent work by Boghaert *et al.,* developed elastomeric stamps of PDMS to mold collagen microwells for 3D co-culture of mammary epithelial and tumor cells (Boghaert et al., 2012). The microwells were topped with a layer of polymerized collagen to create hollow ducts (Figure 1.3A) Following this, they studied the spatial positioning of tumor cells to observe their growth and invasive capacity and found that non-invasive tumor cells proliferated at a significantly higher rate at the edge of the ducts. Downstream computational (i.e. finite element) analysis revealed higher mechanical stresses at the edges, suggesting that biophysical parameters, such as tensional stress, contributed to cancer cell motility. This microengineering technique offered the ability to modulate the tissue geometry and mechanical stress, to assess their role on tumor growth and migration.

In addition to micromolding techniques, UV-based photopatterning has been widely used to develop *in vitro* 3D models for studying tumor growth and progression. For instance, Kaemmerer *et al.* utilized photocrosslinkable gelatin methacrylamide (GelMA) hydrogel to study the growth of ovarian cancer cell (Kaemmerer et al., 2014). GelMA hydrogel has previously been demonstrated to be advantageous for 3D culture of numerous cell types due to the high concentration of matrix metalloproteinase- (MMP) sensitive degradation sites (Navaei et al., 2016; Nichol et al., 2010; Nikkhah et al., 2012; Saini, Navaei, Van Putten, & Nikkhah, 2015). Additionally, the photocrosslinkable properties of GelMA provide distinct advantages over purely natural hydrogels by enabling the development of tissue constructs with well-defined microarchitectures (N. Peela et al., 2016). By modulating the concentration of GelMA hydrogel, the authors were able to regulate numerous biophysical attributes (i.e. stiffness, pore size, MMP-cleavable sites) and subsequently assess the role of these factors on the morphology of the tumor. Encapsulated ovarian cancer cells uniformly assembled as loose aggregates at lower (2.5%) concentration of GelMA, while at higher hydrogel concentration (7%). spheroids were mostly non-uniform and displayed decreased metabolic activity. Additionally, within 5% GelMA, the spheroids exhibited tight intercellular junctions along with the highest metabolic activity and spheroid size. Furthermore, inhibition of MMP production decreased the spheroid size, confirming that the presence of MMP-cleavable sites provide sufficient cues amenable for tumor formation (Kaemmerer et al., 2014).

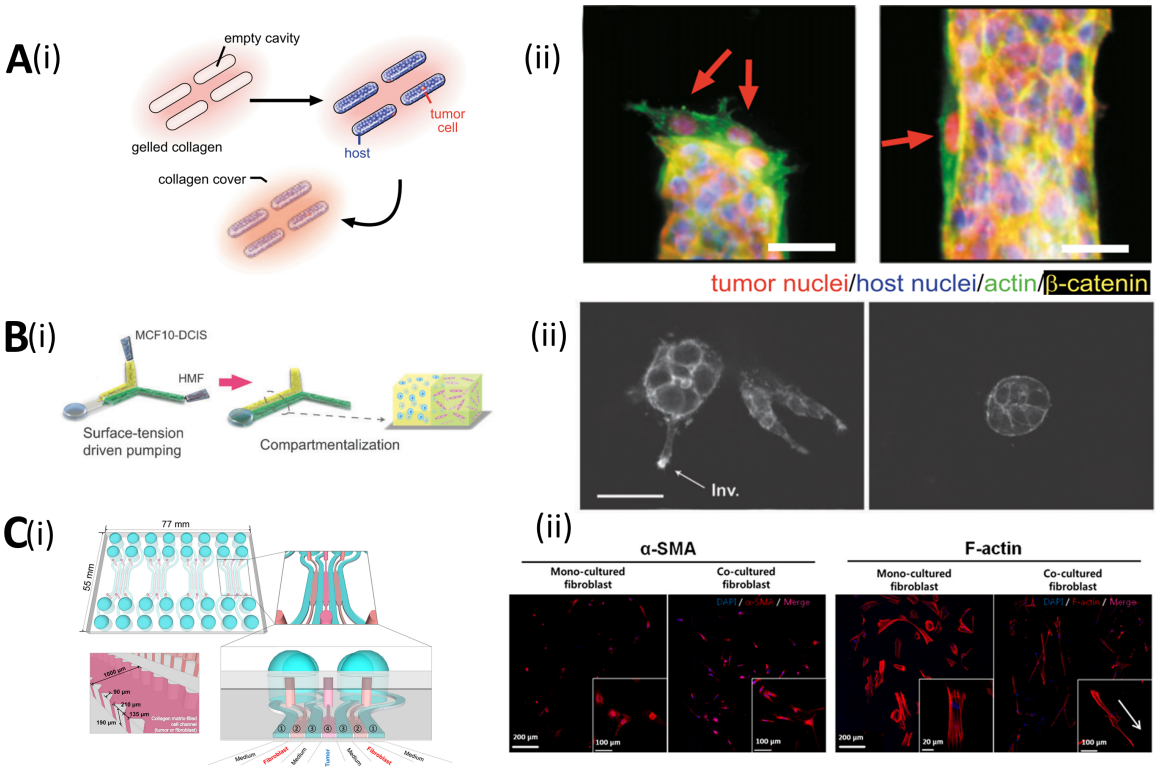

Figure 1.3 Example Microengineered Models of Cancer

(A) Schematic (i) of fabrication of microengineered tissue surrogates, and representative immunofluorescent images (ii) of demonstrating invasion of tumor cells from the end of the cavities. Adapted with permission from the National Academy of Sciences: [PNAS], copyright (2012). (B) Schematic of microfluidic model (i) to study transition of MCF10A. DCIS to Invasive Ductal carcinoma in presence of Human mammary fibroblasts, and F-actin structure (ii) of co-cultured group MCF10A.DCIS cells as compared to mono-cultured MCF10A.DCIS cells. Adapted with permission from the Royal Society of Chemistry (RSC): [Integr. Biol.], copyright (2011). (C) Schematic (i) of seven channel microfluidic device, and immunostained images (ii) of Alpha SMA and F-actin in mono-culture and co-culture conditions. Adapted with permission from PLOS: [PLOS ONE], open-access (2016).

Various groups have also utilized tumor spheroids embedded within ECM matrices to study mechanisms of cancer cell invasion (Carey, Starchenko, McGregor, & Reinhart-King, 2013; Jimenez Valencia et al., 2015; Kopanska, Alcheikh, Staneva, Vignjevic, & Betz, 2016). The Reinhart-King group developed tumor spheroids using cancer cell lines that were embedded in collagen to study the role of tumor heterogeneity in collective cell migration (Carey et al., 2013). They showed that collagen fiber alignment and proteolysis of the matrix modulated the invasion of different population of cancer cells. When spheroids were created using MCF10A cells, the collagen fibers were oriented parallel to spheroid boundary, but use of MDA-MB-231 cells led to perpendicular alignment of collagen fibers. Time lapse imaging of the multicellular tumor spheroids revealed that MDA-MB-231 cells degraded the surrounding matrix, and MCF10A cells followed the microtracks left by the MDA-MB-231 cells (Carey et al., 2013). This study was crucial in elucidating the interactions between leader and follower cells within a 3D microenvironment indicating that this model could be used as a suitable invasion assay to study novel mechanisms of cancer cell migration.

In a recent study, Kraning-Rush et al. created a tumor spheroid model encapsulated in collagen gel using PDMS stamps and micromolding (Kraning-Rush, Carey, Lampi, & Reinhart-King, 2013); a technique pioneered by Nelson et al. (Celeste M. Nelson, Inman, & Bissell, 2008; C. M. Nelson, VanDuijn, Inman, Fletcher, & Bissell, 2006). Using photolithography techniques, silicon wafers were first fabricated with unique microarchitectures. Elastomeric stamps were next used to imprint collagen resulting in engineered microtracks. This technique allowed for rapid fabrication of a

high-density array of tumor constructs with desired geometry and spatial arrangement. The authors analyzed cellular microtracks created by invasive MDA-MB-231 cells in bulk collagen gel by using confocal reflectance microscopy. The authors further utilized micromolding techniques to recreate microtracks prior to cell seeding to evaluate migration within these patterned tracks. Their results demonstrated an increased single cell migration rate and distance in both non-invasive MCF10A and invasive MDA-MB-231 cells in pre-formed microtracks compared to when encapsulated within nonpatterned collagen. To further investigate the effects of matrix architecture (i.e. microtracks) on cell migration, MT-MMP1 was knocked down preventing ECM degradation, which decreased the speed of invasive cancer cells on unpatterned collagen. However, cells within patterned collagen microtracks still maintained their initial speed despite MT-MMP1 knockdown. These results suggest an alternate motility pathway that compensates for lack of MMPs by using microtracks within the ECM. Additionally, this result provided a basis for the potential cause of failure MMP inhibitors (Kraning-Rush et al., 2013).

1.4 Microfluidic Systems for Modeling the Tumor Microenvironment

The prior mentioned microengineered models are some of the great and promising works that have been used to investigate cancer progression and provide biological insights. In particular, microfluidics are another type of microengineered technologies that have emerged allowing great control over cellular, biophysical and biochemical cues from the TME (Figure 1.2). As such, microfluidic models could also be used to bridge the gap between complex *in vivo* and simpler *in vitro* models to better recapitulate the tumor-

stroma interactions (Sung & Beebe, 2014). One key advantage of microfluidics is the micro-scale nature which requires lower volumes of sample input providing an advantage in cases such as rare or difficult to obtain cells and materials (i.e. patient-derived cells, ECM, soluble cues) (I. K. Zervantonakis et al., 2012). In addition, their ease of design allows these devices to encompass multiple TME architectures to enable micro-compartmentalization of different cells (i.e. fibroblast, immune and endothelial) and ECM (i.e. collagen, fibrin, laminin). This enables control over physiological scaling and architecture of complex cell-cell arrangement to better mimic the diseased tissue. Importantly, experiments using microfluidics could be designed using cells and ECM exclusively of human origin providing an advantage over animal models. Due to their flexible nature in design and low cost, microfluidic technologies have been pushing the boundary to replicate organ-level function (Huh, Hamilton, & Ingber, 2011). As such, microfluidics are a capable platform for modeling tumors of several kinds, like breast, brain, lung, etc., and at different steps of metastasis, such as growth, invasion, intra/extravasation (Jeon et al., 2014; H. Lee, Kim, Chung, Kim, & Jeon, 2014; Nagaraju, Truong, Mouneimne, & Nikkhah, 2018; N. Peela, Truong, et al., 2017; Ryu et al., 2015; D. Truong et al., 2016; I. K. Zervantonakis et al., 2012). Importantly, the transparent nature of the microfluidic enables observation of dynamic cell processes with high-resolution without requirement of complex microscopy used in animal models. Additionally, with the type of control that microfluidics provide in modulating the TME, it can also visualize rare events such as cell-cell interactions during cancer invasion which is difficult to image *in vivo*. This of course enables microfluidics with relative ease to model the different steps of the metastatic cascade like tumor-stroma interactions

(Sung et al., 2011), invasion (Haessler, Kalinin, Swartz, & Wu, 2009; B. J. Kim et al., 2013), angiogenesis (C. Kim, Kasuya, Jeon, Chung, & Kamm, 2015; J. Kim et al., 2015; H. Lee, Kim, et al., 2014), intravasation (I. K. Zervantonakis et al., 2012), and extravasation (Bersini et al., 2014; Jeon et al., 2015).

Tumor-stroma interactions is comprised of the interplay between the cancer cells and the stromal cells residing in the surrounding TME. To model the interaction, different microfluidics have been fabricated. For instance, work by Sung et al. developed a 3D microfluidic model to spatially compartmentalize invasive MCF10DCIS.com breast cancer cells with mammary fibroblasts to mimick the tumor stroma interface (Sung et al., 2011). They utilized a Y-shaped microfluidic platform so that two adjacent channels were loaded with cancer and stromal cells respectively to (Figure 1.3B). The aim of this study was to assess the transition of breast cancer from ductal carcinoma in situ (DCIS) to invasive ductal carcinoma (IDC) in the presence of mammary fibroblast cells. Their results demonstrated that MCF10A.DCIS cells transitioned from normal mammary or DCIS morphology (i.e. circular morphology) at the ECM interface between cancer and fibroblast cells to a more invasive phenotype when compared to the mono-culture condition (Figure 1.3B). Further downstream analysis correlated the changes in cellular morphology with remodeling of ECM, demonstrating downregulation of E-cadherin and degradation of ECM. Their work demonstrated that their microfluidic set up enabled crosstalk between the two cell types to observe the resulting transition of cancer cells toward an invasive phenotype while also demonstrating ECM remodeling due to fibroblasts in a single model. In separate study by Jeong et al., a seven-channel

microfluidic device was used to co-culture colorectal carcinoma tumor spheroids embedded in collagen hydrogel with normal colon fibroblasts (Figure 1.3C) (Jeong, Lee, Shin, Chung, & Kuh, 2016). The authors observed that co-culture with fibroblasts promoted significant increase tumor spheroid diameter compared to the mono-culture condition without fibroblasts. Further analysis revealed that the increase in diameter of the spheroids was not due to cancer cell proliferation, but instead due to the deposition of fibronectin within the spheroids. Consequently, during a drug study, paclitaxel diffused more slowly through the hydrogel in the co-culture condition due to the presence of fibronectin. They also demonstrated that the co-culture condition induced the transition of colon fibroblasts to a CAF phenotype, confirmed by increased expression of α-SMA and higher cell motility (Figure 1.3C). On the other hand, Kim et al. developed a microfluidic system to study the invasion of MDA-MB-231 cells through a 3D microenvironment in response to dual gradients of CXCL12 and EGF (B. J. Kim et al., 2013). This model highlighted the capability of controlling gradients of biochemical cues using the small channels in microfluidics. Notably, Zervantonakis et al. created an advanced microfluidic model consisting of a vascular endothelium, resident macrophages, and migrating tumor cells in a 3D microenvironment. Their work provided insight on the role of TNFα in tumor-macrophage-endothelial interactions. (I. Zervantonakis et al., 2010; I. K. Zervantonakis et al., 2012). They observed that macrophages released TNFα which resulted in enhanced endothelium permeability leading to higher rates of intravasation (I. K. Zervantonakis et al., 2012). Gioiella et al. fabricated a microfluidic model and incorporated MCF7 cells in a tumor region and normal fibroblasts (NFs) in a stroma region to study the reciprocal effect of the two cell types on one another (Gioiella,

Urciuolo, Imparato, Brancato, & Netti, 2016). Upon 48 hours, fibroblast cells within the stroma when in presence of MCF7 cells exhibited marked expression of αSMA as well as PDGF, suggesting activation of NFs to a CAF-like phenotype. Extracellular matrix proteins including collagen, hyaluronic acid and fibronectin were expressed higher in presence of the tumor cells. Using second harmonic imaging, ECM remodeling was observed in co-culture condition confirming the activation of NF when co-cultured with tumor micro-tissues. This study illustrated the ease of microfluidic platforms to study various aspects of cancer invasion including stroma activation, ECM remodeling, and cell migration.

To that end, microfluidic platforms have shown significant promise to study different aspects of cancer through better recapitulation and direct control over distinct components (i.e. cells, ECM, soluble factors) within the TME (Sung & Beebe, 2014). These recent innovations have enabled the capture of different facets of metastasis such as biochemical signaling (I. Zervantonakis et al., 2010), tumor-stroma interactions (Sung et al., 2011), invasion (Haessler et al., 2009; B. J. Kim et al., 2013), intravasation (I. K. Zervantonakis et al., 2012), and extravasation (Bersini et al., 2014; Jeon et al., 2015). Despite significant progress, most of the previous findings have relied on models with simplified 3D models containing distinct tumor and stroma regions to precisely control spatial cell-cell and cell-ECM interaction. Notably, there have also been a lack of integrated molecular analyses, like proteomic or transcriptomic profiling, to probe for possible molecular mechanisms in tumor-stroma interactions during invasion. Further, current 3D microfluidic models of invasion have utilized established cell lines. While

these cells have provided a detailed understanding of the underlying biology mechanisms during invasion, cell lines often lose their *in vivo*-like phenotype. Incorporation of patient-derived cells within microengineered models will enable development of relevant understanding of invasion that also accounts for tumor heterogeneity, better design of therapeutic compounds, and fine-tuning of the models for applications geared toward personalized medicine.

1.5 Thesis Aims and Overview

The failures of current clinical studies have been attributed to lack of understanding cancer and stromal cell interactions from the TME. These interactions have been found to significantly affect many biological processes in cancer progression, such as tumor growth, cell survival and invasion. Therefore, the crosstalk between stromal and tumor cells still require further elucidation to effectively target as an anti-cancer therapy.

This thesis aims to develop a microfluidic model to study the interplay between tumor and stromal cells during cancer invasion. In this work, we have developed a 3D microengineered platform with configurable tumor-stroma architecture coupled with cellular and molecular assessments. This model contains distinct cell culture compartments to create 3D tumor and stroma regions. The proposed microfluidic is applicable across many types of cancer, due to flexibility in cell and ECM compositions. For proof of concept, we will first use breast cancer as our model system while also branching to glioblastoma. Following a bottom-up approach by additive addition of

stromal components and cells, we studied the influence of stromal factors on cancer invasion. We developed a breast tumor-stroma model by incorporating patient-derived fibroblasts of mammary origin in co-culture with breast cancer cells to study the influence of the fibroblasts on invasion. Then we utilized transcriptomic profiling to provide insight on the molecular mechanisms of enhanced invasion due to fibroblasts and we screened for a clinically relevant gene, *GPNMB*, and studied its role in cancer invasion using our model. Finally, building upon our prior works, we developed a glioma stem cell – vascular interaction model to study the influence of the vascular niche on glioma stem cell invasive behavior.

We propose to complete this study through the following specific aims:

1.5.1 Specific Aim 1

Investigate the effect of biochemical stimuli (i.e. EGF) on invasion of cancer cells into a 3D stroma using microfluidics. Using our microfluidic tumor model and SUM-159 as our model invasive cancer cell line, we will investigate our hypothesis that EGF promotes further invasion of breast cancer cells into the stroma of our biomimetic TME.

1.5.2 Specific Aim 2

Study the influence of patient-derived CAFs on cancer cell invasion and gene expression profile and determine a possible mediator of invasion due to tumor-stroma interactions. We will refine our microfluidic model developed in Aim 1 by

introducing patient-derived cancer-associated fibroblasts to reflect the native TME. Using this system, we will investigate the hypothesis that cancer-associated fibroblasts promote further migration of invasive cancer cells. We will also investigate a sub-aim of identifying possible mediator of invasion due to co-culture with cancer-associated fibroblasts.

1.5.3 Specific Aim 3

Use a microfluidic platform of the GSC vascular niche to study the influence of endothelial cells (ECs) on patient-derived GSC behavior and identify signaling cues that mediate their invasion and phenotype. We introduce a third region in the microfluidic model used in Aims 1 and 2 to incorporate tumor-associated vasculature. We will investigate the role of the TME on the phenotype and invasiveness of a sub-population of glioblastoma cells, glioma stem cells. These studies will investigate our hypothesis that the vascular niche promotes migration of glioma stem cells while maintaining stem phenotype.

CHAPTER 2

AIM 1: Investigate the effect of biochemical stimuli (i.e. EGF) on invasion of cancer cells into a 3D stroma using microfluidics.

2.1 Abstract

In this study, to model 3D chemotactic tumor-stroma invasion *in vitro*, we developed an innovative microfluidic chip allowing side-by-side positioning of 3D hydrogel-based matrices. We were able to (1) create a dual matrix architecture that extended in a continuous manner, thus allowing invasion from one 3D matrix to another, and (2) establish distinct regions of tumor and stroma cell/ECM compositions, with a clearly demarcated tumor invasion front, thus allowing us to quantitatively analyze progression of cancer cells into the stroma at a tissue or single-cell level. We showed significantly enhanced cancer cell invasion in response to a transient gradient of epidermal growth factor (EGF). 3D tracking at the single-cell level displayed increased migration speed and persistence. Subsequently, we analyzed changes in expression of EGF receptors, cell aspect ratio, and protrusive activity. These findings show the unique ability of our model to quantitatively analyze 3D chemotactic invasion, both globally by tracking the progression of the invasion front, and at the single-cell level by examining changes in cellular behavior and morphology using high-resolution imaging. Taken together, we have shown a novel platform recapitulating 3D tumor-stroma interactions for studies of real-time cell invasion and morphological changes within a single platform.

2.2 Introduction

Breast cancer is the one of leading causes of cancer-related death among women in the United States (R. Siegel, Ma, Zou, & Jemal, 2014). This disease progresses in many steps ranging from tumor growth, stroma invasion, and spreading throughout the body (Gupta & Massague, 2006; Hanahan & Weinberg, 2011). Invasion into the surrounding stroma begins a process of interactions between tumor cells and the stroma by cellular crosstalk and paracrine signaling (i.e. fibroblasts, pericytes, immune cells, endothelial cells, etc.) and is influenced by biochemical/biophysical cues (i.e. drug and nutrient transport, ECM composition and stiffness, etc.) within the stroma (Conklin & Keely, 2012; Hanahan & Weinberg, 2011; Khamis, Sahab, & Sang, 2012; Mao et al., 2013). Despite significant advances in therapeutic regimens, anti-cancer drugs often fail due to lack of comprehensive preclinical studies utilizing models incorporating the complexities of the native tumor-stroma microenvironment (dit Faute et al., 2002; J. M. Lee et al., 2013; McMillin, Negri, & Mitsiades, 2013; Paraiso & Smalley, 2013; Thoma, Zimmermann, Agarkova, Kelm, & Krek, 2014). In this regard, the interactions that specifically arise from a variety of biochemical and biophysical gradients, and cellular components should not be overlooked when developing *in vitro* tumor microenvironment models (Knowlton, Onal, Yu, Zhao, & Tasoglu, 2015; B. Weigelt, 2014).

Chemoattractants, such as epidermal growth factor (EGF), are aggressive drivers of cancer invasion by activating cell membrane receptors and intracellular pathways that provide guidance and motility cues to the cells(Gupta & Massague, 2006). For example, cancer cells have been shown to secrete colony stimulating factor-1 (CSF-1), which then causes macrophages to produce gradients of EGF (Goswami et al., 2005; Hagemann et al., 2004). This would often lead to enhanced proliferation, survival, and motility of

cancer cells (Dudu, Able, Rotari, Kong, & Vazquez, 2012; Meng, Xia, Fang, Rojanasakul, & Jiang, 2006; Price, Tiganis, Agarwal, Djakiew, & Thompson, 1999; J. Wyckoff et al., 2004). For example, micro-needles filled with Matrigel® and EGF inserted into the mouse fat pads attracted breast cancer cells to the site of injection. However, this model required expensive imaging, such as multiphoton laser-scanning and second harmonic generation (Provenzano et al., 2006; Provenzano et al., 2008), to observe the effect of EGF on cancer invasion in real-time (J. Wyckoff et al., 2004). Furthermore, animal models do not allow decoupled control of cell-cell and cell-ECM interactions creating significant difficulties in elucidating the role of each separate stromal component. For instance, migrating cells *in vivo* have been shown to migrate toward one specific areas of vascularization. However, it was unclear whether the cancer cell's response was due to the sole role of biochemical (i.e. chemoattractants) or biophysical (i.e. interstitial flow or collagen stiffness) gradients (Shields, Fleury, et al., 2007). Moreover, stromal cells, such as macrophages or fibroblasts, localized to specific regions within the tumor microenvironment can generate interfering signaling cues and chemoattractant gradients, which make it especially challenging, to elucidate the sources that trigger cancer cell invasion (Patsialou et al., 2009; Pinner & Sahai, 2008; J. B. Wyckoff et al., 2007).

Conventional *in vitro* 2D assays have been extensively used to assess the role of chemoattractants on cancer cell migration (Saadi et al., 2006; S. J. Wang et al., 2004). Wang et al. utilized a 2D platform simplifying the tumor microenvironment to only a monolayer of cells. They demonstrated that breast adenocarcinoma cell line (MDA-MB-231) migrated on 2D surfaces towards higher concentrations of EGF with varying speeds

(S. J. Wang et al., 2004). Although the findings were significant, the 2D model utilized in this study did not recapitulate the organization of tumor-stroma and ECM heterogeneity, normally found within the native tumor microenvironment. Most importantly, the lack of encapsulated cells within 3D ECM-based matrices, which are representative of cancer invasion within the stroma, could influence the biological findings (Yamada & Cukierman, 2007).

Traditional 3D systems currently used in invasion studies, such as Boyden chambers and Transwell migration assays, lack the ability to precisely control the spatial organization of cells in 3D matrices, cell-cell interactions, and cell-ECM interactions. To that end, microfluidic platforms have shown significant promise to study different aspects of cancer through better recapitulation and direct control over distinct components (i.e. cells, ECM, soluble factors) within the tumor microenvironment (Sung & Beebe, 2014). These recent innovations have enabled the capture of different facets of metastasis such as biochemical signaling (I. Zervantonakis et al., 2010), tumor-stroma interactions (Sung et al., 2011), invasion (Haessler et al., 2009; B. J. Kim et al., 2013), intravasation (I. K. Zervantonakis et al., 2012), and extravasation (Bersini et al., 2014; Jeon et al., 2015). Despite significant progress, most of the previous findings have relied on models with simplified or no compartmentalization of 3D interconnected tumor and stroma regions to precisely control spatial cell-cell and cell-ECM interactions. For example, some models that seeded cancer cells on 2D channels lacked the physiologically relevant influence of the 3D matrices (Chung et al., 2009; Jeon et al., 2015; I. K. Zervantonakis et al., 2012). There are also microfluidic devices that have demonstrated cell migration within 3D hydrogels (Haessler et al., 2009; B. J. Kim et al., 2013), but they were missing

incorporation of tumor-stroma entities, thus having only a single compartment for cancer cell encapsulation. These limitations reduced their ability to study cancer invasion through side-by-side heterogeneous ECM, organized co- or tri-culture of cells as well as transport of growth factors and nutrients through diffusive barriers (i.e. solid tumors). Apart from technological development, these models often have been limited by the lack of 3D real-time single cell migration analysis from the tumor toward the stroma region during active invasion. Alternatively, models that compartmentalized cells into separated 3D stroma and tumor regions were not specifically intended to demonstrate real-time 3D invasion studies and enable modulation of microenvironmental cues (e.g. biophysical and biochemical signaling). Moreover, these platforms did not contain perfusable channels surrounding the tumor-stroma regions to assess the influence of chemotactic gradients on cancer cell invasion (Sung et al., 2013; Sung et al., 2011).

In this study, we have developed a new microfluidic cancer invasion platform capable of spatially organizing 3D cell-embedded hydrogel matrices while enabling real-time capture of 3D cancer invasion within heterogeneous ECMs. The microengineered platform was designed to introduce 3D interconnected tumor and stroma regions with different ECM and cell compositions. This approach primarily provides an advantage over 2D platforms by enabling the study of 3D cellular migration within a native-like tumor microenvironment using hydrogel-based matrices. Moreover, our design allows the capture of an ECM-embedded high-density cell population (~ 15 million cells/mL) within a single compartment to mimic mechanical cues and diffusion of soluble factors within a 3D solid tumor not possible in 2D platforms (B. Weigelt, 2014). On the other hand, when compared to previously established 3D platforms (B. J. Kim et al., 2013; Sung et al.,

2011; I. K. Zervantonakis et al., 2012), our model contains a specific tumor region surrounded by a separate ECM-filled entity (stromal region) permitting a juxtaposition of different ECM or cell mixtures (e.g. cancer-associated fibroblasts (CAFs)) to recapitulate continuous cancer invasion throughout a heterogeneous tumor-stroma microenvironment. We utilized the proposed model to specifically assess how exposure to EGF impacts 3D cancer cell invasion through the stroma. In addition, the proposed design enabled generation of competing microenvironments, due to the presence of two separated channels, to specifically assess the effect of differential gradients of EGF on cancer cells invasion. We took advantage of our device to visualize and quantify 3D cell migration metrics and morphology, utilizing advanced microscopy technique, at both a global and single-cell level, within different time frames. As a result, we noted enhanced cell speed and persistence in the presence of EGF along with increased levels of cell proliferation and clustering of EGF receptors (EGFRs) indicative of cells responding to EGF. Furthermore, we correlated the enhanced invasiveness to cell morphology changes such as increased aspect ratio and number of protrusions. Overall, this work underscores a technical advance that was designed to recapitulate invasion of cancer cells in adjacent tumor and stroma regions of different ECM and cell compositions within a microengineered platform. This will allow future studies to assess the influence of various combinations of cell-cell and cell-ECM interactions on cancer invasion in a well-controlled experimental condition.

2.3 Methods

2.3.1 Microfluidic design and fabrication

The microfluidic platform was fabricated using photo- and soft-lithography techniques. First, the design was created utilizing cad software, and subsequently, a transparent mask was fabricated from this design to undergo SU-8 photolithography. SU8-2075 (MicroChem) was spun onto a silicon wafer with a height of 200 μm. Next, the wafer was placed underneath the transparent mask and exposed to UV to generate the mold for the microfluidic device. Polydimethylsiloxane (PDMS, Sylgard 184 Silicon Elastomer Kit, Dow Corning) was casted over the SU-8 wafer and baked for 1 h at 80 °C. Afterwards, the PDMS was peeled off and the devices were cut out with blades, and afterwards, the inlets and outlets were cored using biopsy punches. Next, these devices were treated with oxygen plasma (PDC-32G, Harrick Plasma) and were then bonded to glass with channel side facing down to create a sealed environment. The fabricated microfluidic chips were sterilized by wet autoclave followed by a dry autoclave. The chips were surface treated by injecting 1 mg/mL poly-d-lysine (PDL, Sigma-Aldrich) into the channels and chambers. The devices were incubated at 37 °C for 1 h and then washed with deionized (DI) water. Next, 0.1% (v/v) glutaraldehyde (GA, Sigma-Aldrich) solution was added into the channels and chambers and incubated at room temperature for 1.5 h. Finally, the devices were washed 4 times with DI water and placed in an 80 °C oven overnight to render the surfaces hydrophobic.

2.3.2 Diffusion across the tumor-stroma

COMSOL simulation of EGF diffusion was used to characterize and predict the time-dependent gradient within the platform. When performing the simulation, diffusion in x and y axis were the most important to investigate the diffusion of EGF due to the fact

there were no major influences on the diffusion in the z-axis as the EGF was uniformly distributed in the media. In addition, the diffusion coefficient of collagen remained relatively constant in all dimensions within the hydrogel so there would be no major change in diffusion influenced in the z direction of the hydrogel. Therefore, we utilized a two-dimensional model to simulate diffusion of EGF in the horizontal cross section or top-down view of the 3D device. In that regard, the geometry was created within AutoCAD and imported into the COMSOL software as a 2D-plane. Based on Stokes-Einstein $D_c = kT/6\pi\eta R$ relationship (Kothapalli & Honarmandi, 2014), where k is the Boltzmann constant (1.38×10^{-23} J•K^{-1}), T = 298.15 K, R is the Stokes radius (23 angstroms), and η is the dynamic viscosity of the media (0.78×10^{-3} N•s/m^2) (C. Wang, Lu, & Schwartz, 2012), the diffusion coefficient for a 10 kDa molecule within media at 37 °C was calculated to be 9.25 x 10^{-11} m^2/s. The coefficient for the 3D collagen I gel (2.0 mg/mL) was determined to be 8.7 x 10^{-11} m^2/s by multiplying the media coefficient by the diffusion hindrance coefficient 0.94 (i.e. diffusion through the gel compared to the solution). This value is predicted based on the area fraction of collagen related to the fiber diameter of isotropic fiber networks. The pores (> 0.75 μm for collagen area fraction of less than 1%) (Stylianopoulos, Diop-Frimpong, Munn, & Jain, 2010) within the collagen hydrogel being larger than the hydrodynamic radius of the dextrans (Stylianopoulos et al., 2010; I. K. Zervantonakis et al., 2012) resulted in approximate diffusion hindrance to be 0.94 based on work done by Stylianopoulos et al. Inlet was set to zero flow, the outlet was set to zero pressure, the concentration of the molecule within the channels was set equal to 10 μg/mL, and the inlet concentrations were set constant at 10 μg/mL.

Fluorescent dextran (10 kDa FITC-Dextran (10 μg/mL)) was injected into the media inlets and the resulting fluorescent intensity across the platform was recorded over time for 2 h every 5 min. Relative intensity of the concentration gradient was quantified in ImageJ by using the profile tool.

2.3.3 Cell Culture

SUM-159 breast cancer cells was chosen as a suitable cell type to invade through a 3D hydrogel(Sabeh, Shimizu-Hirota, & Weiss, 2009). The MCF-7, SUM-159 and mCherry-labeled SUM-159 breast cancer cells, provided by Mouneimne lab, were cultured in MCF-7 specific media (Dulbecco's Modified Eagle Medium supplemented with 5% heat inactivated fetal bovine serum (FBS), 1x penicillin-streptomyocin) and SUM specific media (Ham's F-12 with L-glutamine and supplemented with 5% heat inactivated fetal bovine serum (FBS), 1x penicillin-streptomyocin, 1 μg/ml hydrocortisone, and 5 μg/ml insulin) respectively. CAFs (passage > 55) were acquired from ATCC (ATCC® HTB 125™) and cultured in MCF-7 specific media. The cells were maintained within a humidified cell culture incubator at 37 °C and 5% CO_2.

2.3.4 Invasion assay

To load the cancer cells into the device for invasion experiments, cells were trypsinized and pelleted into 0.5 mL microcentrifuge tubes. Matrigel® (Corning), collagen I (2.0mg/mL, Corning® Collagen I, Rat Tail, 100mg, Product #354236, Corning) and a 1:1 mixture of Matrigel® to collagen type I (2.0 mg/mL) was added to the cells to create a mixed hydrogel cell solution (final concentration of collagen I at 1

mg/mL) with a density of 15 million cells/mL. The mixed hydrogel cell solution was injected into the tumor region of the microfluidic chip and polymerized by placing the devices into the humidified cell culture incubator at 37 °C. These chips were flipped every 1 min to create a homogenous distribution of cells within the mixed gel. After 8 min within the incubator, the devices were taken out and subsequently a 2.0 mg/mL collagen type I solution was injected into the stromal region. For co-culture with CAFs, 100,000 cells/mL were encapsulated in the collagen type I solution. The collagen was polymerized within the humidified incubator at 37 °C for 8 min. Next, SUM media was added into the channels of each device and the microfluidic chips were placed into the cell culture incubator overnight. On the next day, the media within EGF-stimulated devices ((+) EGF) was exchanged with SUM media supplemented with EGF (50 ng/mL). Unstimulated devices ((-) EGF) were based on the use of normal SUM media. Media was changed daily for the whole culture period.

Phase-contrast images of the cells were acquired once every day using 4 x 3 tiles with a 10x objective. Distribution of invading cells was quantified from these images by measuring the distance from the cells to the nearest micropost. If there was a cell in a cluster, only the furthest point on the furthest cell from that cluster was measured unless clear cell borders were distinguishable. Each measurement was taken from the most distal protrusion of the cell (not the cell body). To quantify the invading edge of the tumor (i.e. the invading tumor front), only the cells on the periphery were measured by considering the most distal points of the most distal cells. In this case, only the cells at the edge of the tumor (i.e. cells that have traveled the highest distance from the tumor region from each degree) were included in the quantification.

To perform time-lapse imaging, mCherry-labeled SUM-159 cells were mixed together with normal SUM-159 at a ratio of 1:9 prior to the invasion assay. The devices were placed inside a custom miniature incubator (TC-MWP, Bioscience Tools) with a 4-well insert, which enabled imaging of 4 devices at a time at 37 °C and 5% CO_2. Fluorescent time-lapse imaging was performed using a fluorescent microscope (Zeiss Axio Observer Z1, Zeiss) equipped with the Apotome.2 and a 10x objective. The z-resolution and the time interval were set to 3.45 μm and 45 min, respectively. 3D time-lapse images were taken within 24 h of adding EGF and between days 3 and 4 of the invasion assay. Speed (defined as distance over time) and persistence (defined as euclidean distance over accumulated distance) were utilized to quantify cell migration metrics. To filter out the cells to obtain those that migrate toward the gradient, the average angles of each cell trajectory were compiled and reduced to those cells within ± 30 ° of the y-axis (i.e. the direction of the gradient).

2.3.5 Fluorescent staining

For immunofluorescent staining, the cells were fixed by adding warmed 4% paraformaldehyde into the channels of the microfluidic chip for 30 min. The devices were then washed twice with PBS-glycine (100 mM glycine in PBS) for 10 min at room temperature. This was followed by a single wash using PBS-Tween (0.05% (v/v) Tween-20 in PBS). Next, immunofluorescent (IF) buffer (0.2% (v/v) Triton X-100 + 0.1% (v/v) BSA (radioimmunoassay grade) + 0.05% Tween 20, 7.7 mM NaN_3 in PBS) + 10% (v/v) goat serum was added into the channels and the devices were incubated at room temperature for 1.5 h. Later, primary antibodies, monoclonal Anti-α-Tubulin (1:500,

T9026, Sigma-Aldrich), Ki-67 (1:100, (DSHB Hybridoma Product AFFN-KI67-3E6)), EGFR (1:1000, MA5-13319, Thermo Scientific), or pEGFR (1:100, 3777S, Cell Signaling Technology®) were diluted at in IF buffer and devices were parafilmed and kept at 4 °C overnight. Afterwards, the microfluidic channels were washed 3 times utilizing IF buffer for 20 min each. Then, the secondary antibody (Alexa Fluor® 488, 555, or 647, Thermo Fisher Scientific) was diluted in IF buffer for 45 min at room temperature in the dark. The devices were washed once with IF buffer for 20 min and twice with PBS-Tween for 10 min each at room temperature. Afterwards, the nuclei and F-actin fibers were stained by using 4',6-diamidino-2-phenylindole (DAPI, Invitrogen) (1:1000) and Alexa Fluor® 488 Phalloidin (Invitrogen) (1:40) overnight at 4 °C. The dilutions were done using PBS-Tween. Finally, the devices were washed 5 times in PBS-tween for 10 min each before imaging.

2.3.6 Imaging and analysis

All imaging was performed using a Zeiss Axio Observer Z1 with the Zen Pro software suite. Phase-contrast images of the invasion assay were captured using a 10x objective lens. Immunofluorescent images were taken with 10x and 40x objective lenses together with the Apotome.2 (Zeiss). The Apotome.2 created optical sections of our devices, reducing scattered light, to generate clear fluorescent z-stacked images for 3D images.

To quantify cell proliferation, cells expressing mCherry were counted on days 1 and 3 and compared. Moreover, Ki-67 proliferative marker was also quantified by comparing the cells expressing Ki-67 to total cell population. The index was developed

by dividing Ki-67 positive cells by all nuclei within a field of view (40x magnification, 223 x 167 μm^2).

To analyze EGFRs and pEGFRs on days 2 and 4, we thresholded images (40x magnification) of the receptors in ImageJ with actin for their respective coverage areas. EGFR and pEGFR areas were divided by the area of the cell body resulting in a normalized ratio. We also divided the pEGFR area by the EGFR area to analyze the phosphorylated receptors among the non-phosphorylated ones. Heat maps were created using the 3D surface plot plugin in ImageJ.

To investigate the cytoskeletal organization of the cells, we looked at the actin area, cell shape, and protrusiveness. The actin fibers were thresholded in ImageJ producing an area value based on the number of pixels representing the F-actin fiber coverage area. Subsequently, this area was divided by the cell total count (nuclei) in the field of view (20x magnification, 0.45 x 0.34 mm^2) on days 1 and 4 of culture. We used the particle analyzer plugin within the ImageJ suite to further quantify cell shape (i.e. aspect ratio, circularity, and roundness) based on the actin masks. Finally, the protrusions of the cells were manually counted in the actin cytoskeleton by quantifying the number of extensions (> 3 μm in length and 1 μm in width) from the cell body.

2.3.7 Statistical Analysis

All measurements were compiled from three or more independent devices for each experimental condition. The data were compared using unpaired student's t-test, multiple comparisons test, and correlation analysis within the GraphPad Prism software (GraphPad Software).

2.4 Results

2.4.1 Development of the 3D Spatially Organized Cancer Invasion Platform

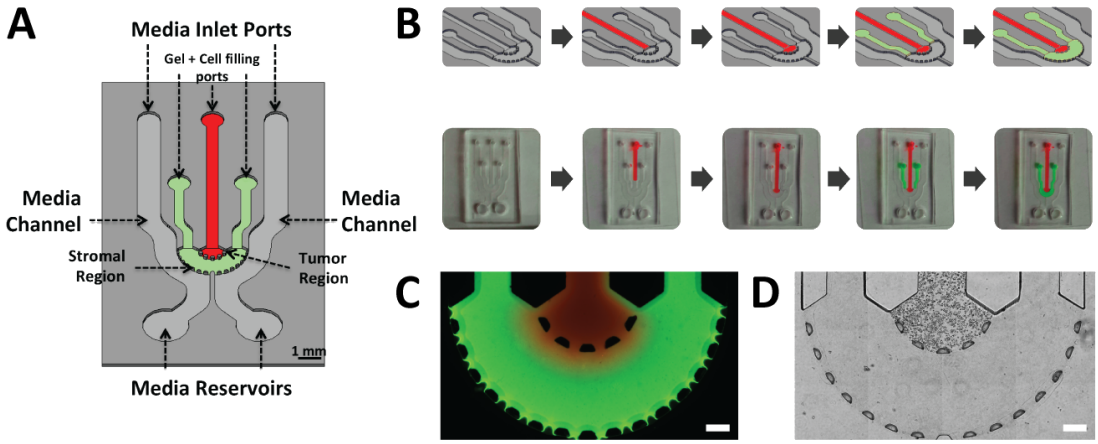

Figure 2.4 Spatial-organization of ECM and cells.

(A) The tumor region is represented by the red color and the stroma is represented by the green. The depth of the channels is 200 µm. (B) Spatial-organization of cells and/or ECM is performed in a two-step process. Cancer cells were encapsulated in a tumor matrix and injected into the tumor filling port. The matrix was polymerized and then the stroma matrix was injected into the stromal filling port. This matrix was then polymerized and the final result is a tumor surrounded by a stroma. (C) Fluorescent image demonstrating ECM compartmentalization. A red hydrogel was injected into the tumor region while a green gel was injected into the stroma (scale bar: 200 µm). (D) Phase-contrast image of cells isolated within the tumor region while a cell-free stroma hydrogel surrounds it (scale bar: 200 µm).

Motivated by the need to simulate the invasion of cancer cells from the primary 'tumor' into the enclosing stroma, a microfluidic platform was designed to organize the

cancer cells into a central tumor region surrounded by a stroma entity (Bissell, Radisky, Rizki, Weaver, & Petersen, 2002; C. M. Nelson & Bissell, 2005). The microfluidic device specifically consisted of an inner chamber (tumor region) bordered by an outer chamber (stromal region) (Figure 2.1A) to produce a side-by-side arrangement of 3D matrices. The diameter and height of these concentric chambers were 3 mm and 200 μm, respectively. The distance between the edge of the inner chamber and outer chamber was 1 mm. Both of these chambers were bounded by trapezoidal micro-posts spaced evenly at 100 μm to create a concentric spatial organization with clear interfaces while allowing interaction between the different regions. The trapezoid shape was chosen to permit uniform gel formation between the posts due to the angle of the trapezoid being supplementary to the contact angle of the gel solution and PDMS (Farahat et al., 2012; C. P. Huang et al., 2009). Tumor cells were encapsulated within a hydrogel solution and loaded first into the device through the central cell filling port (Figure 2.1B and Appendix Figure A.1). The stromal region was then loaded with cell-free hydrogel to produce an interconnected platform. The platform had two inputs that can be filled with cell media containing a variety of molecules (e.g., EGF) to enhance or suppress cancer invasion. Additionally, the design of the platform enabled creating symmetric and asymmetric gradients of biomolecules. Compared to 2D models (Saadi et al., 2006; S. J. Wang et al., 2004) and other conventional 3D models(B. J. Kim et al., 2013; B. Weigelt, 2014; I. K. Zervantonakis et al., 2012), this assay particularly allowed for control over 3D spatial compartmentalization of cells, ECM heterogeneity, and biomolecular gradients.

To demonstrate the formation of a clear-cut spatial arrangement of ECM, we first utilized fluorescent-labeled hydrogels. Rhodamine-6G hydrogel solution was loaded into

the tumor region followed by a fluorescein hydrogel solution loaded into the stromal region. After gelation, the formation of the hydrogels within specific regions of the platform was visualized under a fluorescent microscope (Figure 2.1C). There were no gaps between the posts that could disrupt the interconnectivity of the two side-by-side regions, and the trapezoidal posts held the gels in place while also separating the inner and outer chambers. In that regard, the interconnectivity of the regions within the platform enabled signaling from the channels to the stroma to the tumor. Next, to demonstrate cell-ECM spatial organization, SUM-159 breast cancer cells were encapsulated within a collagen I matrix and loaded into the tumor region while cell-free collagen I was loaded into the stromal region. Following successful gelation of the hydrogels, carcinoma cells were present only within the tumor region while leaving the stroma pristine (Figure 2.1D). Additionally, no gaps or bubbles were present between the tumor and stroma and the cells were distributed in 3D (Appendix Figure A.2). The spatially organized tumor-stroma potentially allows for further studies utilizing different cell types and/or different ECM compositions, which will provide insight and understanding into how other cell types and environments influence cancer invasion (McMillin et al., 2013).

2.4.2 Characterization of Diffusion Across the Platform

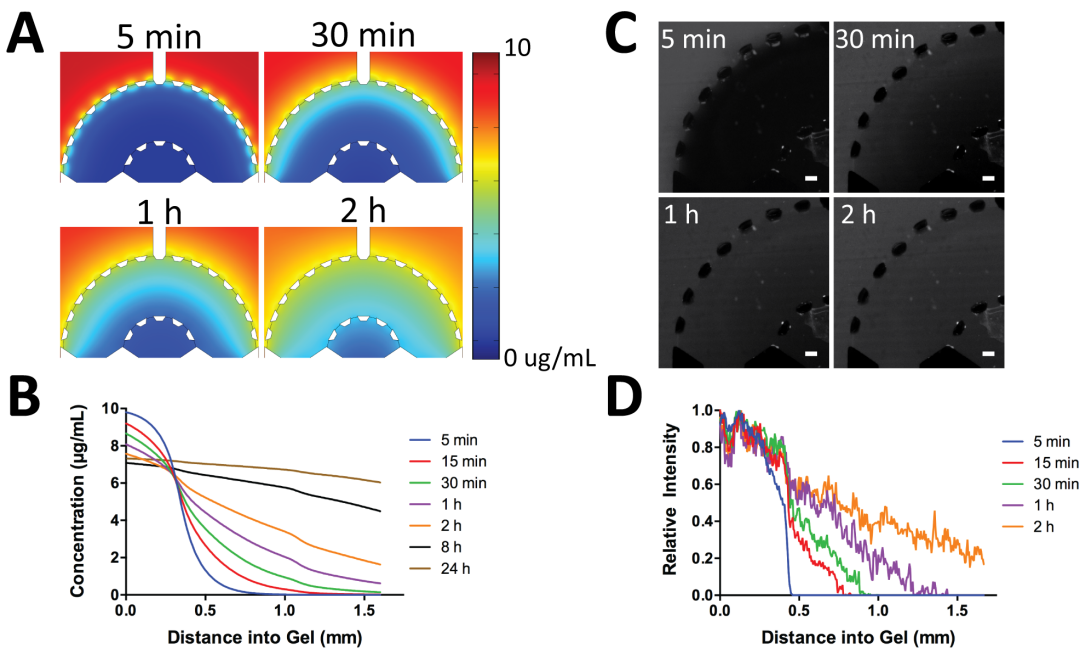

Figure 2.5 Diffusion of molecules through the two regions.

(A, B) COMSOL simulation of 10 kDa molecule (10 µg/mL) through the device demonstrates the concentration gradient profile over time. (C) FITC-Dextran (10 kDa, 10 µg/mL) was diffused from the stroma to the tumor region to demonstrate successful interconnectivity and concentration gradient between the two regions (scale bar: 100 µm). (D) Quantified experimental results of diffusion of FITC-Dextran (10 kDa, 10 µg/mL).

COMSOL simulation of EGF diffusion was used to characterize the time-dependent gradient during chemoinvasion within the platform. Diffusion of 10 kDa molecules was simulated within a 3D collagen I gel (2.0 mg/mL) at 37 °C. Figure 2.2A demonstrates the computed time-lapse of the concentration gradient across the tumor-stroma microenvironment. In addition, Figure 2.2B shows the simulated concentration profile within the device. To experimentally demonstrate diffusion across the platform

and show that the regions within the device were well interconnected, 10 kDa FITC-Dextran (10 μg/mL) was injected into the media inlets and the resulting fluorescent intensity across the platform was recorded over time. By 30 min (Figure 2.2C), the fluorescent dextran had continuously diffused across the stroma and into the tumor region, demonstrating that the interface between the two regions enabled diffusion of biomolecules from one region to the other while showing an established concentration gradient. Figure 2.2D provides the quantified experimental results for the concentration gradient profile showing similarities to the simulated gradient profile up to 2 h (Figure 2.2B). Differences between the experiments and simulation likely arise from small convective flows generated during media changes. A gradient was established for up to 2 h and leveled out afterwards. This suggests that there is an optimum window to replenish the media at this time but other factors that can perturb the gradient profile are also in play such as cell-ECM interactions and cell-biochemical cue (i.e. the diffused cues) interactions.

2.4.3 Cell Behavior within a Physiologically Relevant 3D Microenvironment

To represent the invasive tumor microenvironment, SUM-159 breast carcinoma cells were initially encapsulated at a high density (15×10^6 cells/mL) within three distinct matrices namely, Matrigel®, (2 mg/mL) collagen I, and 1:1 mixture of Matrigel® and collagen I (final concentration of collagen I at 1 mg/mL) and were subsequently loaded into the tumor region. The stroma region was kept constant for all conditions by only loading the outer chamber with collagen I (2 mg/mL), which is the most abundant ECM protein outside the primary breast tumor area (Provenzano et al., 2006; Provenzano et al., 2008). Initial studies revealed that the SUM-159 cells that were encapsulated within the

Matrigel® matrix demonstrated a mixture of round and elongated morphology after one day of culture (Figure 2.3A**)**. As the cells migrated out from the tumor region and into the collagen matrix of the stroma, they began to adopt more elongated morphology representative of an invasive phenotype (Sung et al., 2011). On the other hand, breast carcinoma cells that were still within the tumor region (Matrigel®) maintained their roundness. SUM-159 that were encapsulated within collagen I (2mg/mL) matrix also exhibited a mixture of round cells and elongated cells after one day of culture (Figure 2.3B). However, by the third day within the collagen-only tumor region, there were little to no round cells (Figure 2.3B), whereas the Matrigel®-only matrix still had round cells by day 3 (Figure 2.3A). Although the cells encapsulated in either collagen I or Matrigel® were able to successfully migrate out of the tumor region, there were significant matrix disruptions. The disruptions near the microposts created gaps within the matrix that would have prevented cells from traversing through the 3D microenvironment. To prevent the gap formation so that the cells may continuously invade from the tumor into the stroma while maintaining a physiologically relevant platform, Matrigel® and collagen I (2 mg/mL) were mixed at a ratio of 1:1 prior to cell encapsulation. As seen in Figure 2.3C, cells demonstrated a mixture of round and elongated morphology within the mixed gel that was similar to the previous two matrices (Figure 2.3A and B) demonstrating the continuous invasion. By the third day, the cells invaded into the stroma without disruption of the matrix in contrast to the previous two conditions (Figure 2.3A and B). Additionally, unlike the collagen-only hydrogel, there were still round and elongated cells within the tumor region on day 3, which demonstrated similar morphology to the Matrigel®-only matrix. Thus the mixed gel was chosen for all subsequent experiments to

represent a more physiologically relevant primary tumor region (B. Weigelt, 2014), while still allowing cells to continuously invade throughout the platform with little matrix disruption. This potential to decouple and modulate the tumor and stroma characteristics could allow further studies to develop stiffness and ligand-density gradients to elucidate the effects of haptotactic and biophysical cues on invasion dynamics.

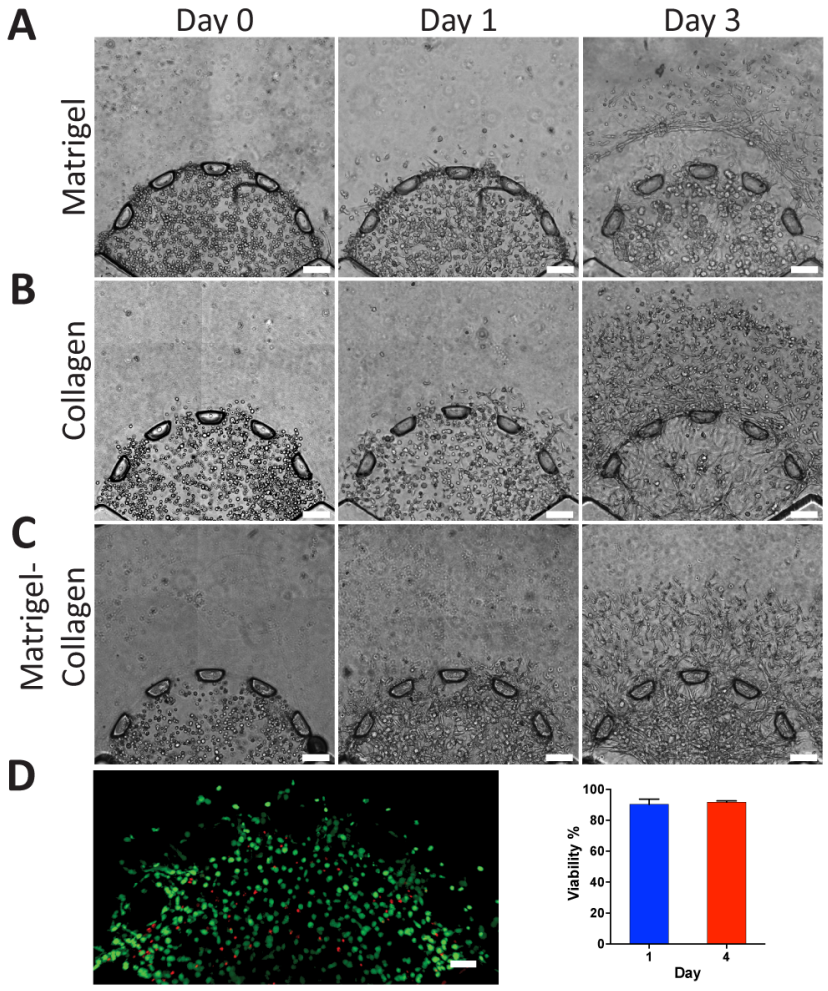

Figure 2.6 Behavior of breast cancer cells within different ECMs.

(A) SUM-159 breast cancer cells were initially encapsulated in Matrigel®. On the first day, the cells demonstrated round morphology and by the third day, the matrix was disrupted (scale bar: 100 µm). (B) Collagen I (2.0 mg/mL) was utilized to encapsulate

cells within the tumor region. The cells demonstrated similar morphology to Matrigel® on the first day. On day 3, cells migrated outside of the tumor region but also exhibited great disruption of the ECM, similarly to Matrigel® (scale bar: 100 μm). (C) A mixed gel of Matrigel®:collagen I (1:1 ratio) was utilized to reduce matrix disruptions. By day 3, the cells successfully migrated out but did not disrupt the tumor as heavily (scale bar: 100 μm). (D) LIVE/DEAD was utilized to assess the viability of the cells on day 1 and 4 within the mixed gel. The cells were highly viable and did not demonstrate any significant change between the two days ($P < 0.05$ calculated from student's T test with more than three devices for each condition, scale bar: 100 μm).

To investigate the survival of the breast cancer cells within the mixed gel (Matrigel®:collagen I) microenvironment, the encapsulated cells were stained with the LIVE/DEAD assay at days 1 and 3. The live cells, which fluoresced green, and the dead cells, which fluoresced red, were counted and compared between the two days (Figure 2.3D). The viability was quantified to be 90.3 ± 3.44 % and 91.7 ± 0.88 % for days 1 and 3 respectively and no statistical difference over the three days. These results suggested that the encapsulation of the cells within the mixed gel did not create a significant impact on cell survival.

2.4.4 Tumor Growth and Dissemination of Invasive Breast Cancer Cells

To understand the effects of EGF on the invasion of the SUM-159 within the spatially organized microenvironment, medium containing EGF (50 ng/mL) was added to the platform daily after an initial 24 h culturing period. The stimulated ((+) EGF) and unstimulated ((-) EGF) cells were tracked for a total of four days (96 h). During the first

24 h (Day 0), the cells adopted round morphologies and were contained within the tumor region (Figure 2.4A). After one day, the cells began to invade into the stroma with a mixture of round and elongated morphologies. Cells were distributed spatially similarly between the two EGF conditions (Figure 2.4B) By day 3 there was a significant difference in tumor dissemination when comparing the stimulated (715 ± 38.0 μm) and unstimulated conditions (556 ± 24.7 μm), demonstrated by a rightward distribution shift by (+) EGF cells along the x-axis (Figure 2.4B). We also calculated the progress of the tumor invasion front over the four day period for both conditions and found that by days 3 and 4, the (+) EGF tumor invaded further than (-) EGF (Figure 2.4C). The invading distance of furthest distal cells from the microposts (Figure 2.4C) were compared daily demonstrating that by days 3 and 4, the (+) EGF tumor invaded further than (-) EGF. Moreover, whole device images taken of the actin cytoskeleton (Appendix Figure A.3) displayed the stark difference between the two conditions in terms of tumor growth and cell invasion. The stimulated cells migrated beyond the stroma and into channels by day 4. In addition, we compared the invasion of SUM-159 breast cancer cells to non-invasive MCF-7 cells. MCF-7 cells developed into clusters of cells near the edge of the tumor region (Appendix Figure A.4A). EGF stimulation enhanced invasion of MCF-7 cells into the stroma (80 ± 8 μm) compared to the control condition without EGF (20 ± 2 μm) on day 2 (Appendix Figure A.4B). However, when comparing to SUM-159 cells, MCF-7 invasion in presence of EGF was significantly lower by almost 10-fold within each day experiment (Appendix Figure A.4C). We also investigated the effect of EGF on proliferation of SUM-159 cells by quantifying the number of cells within the stromal region which revealed increased cell count in the presence of EGF stimulation from day 0

to day 3 (Figure 2.4D and Appendix Figure A.5A). Moreover, expression of Ki-67 proliferative marker was increased in the (+) EGF condition (Appendix Figure A.5B). These findings demonstrated that EGF enhances breast cancer cell invasion within the microengineered 3D platform, consistent with previous studies using 2D assays (S. J. Wang et al., 2004).

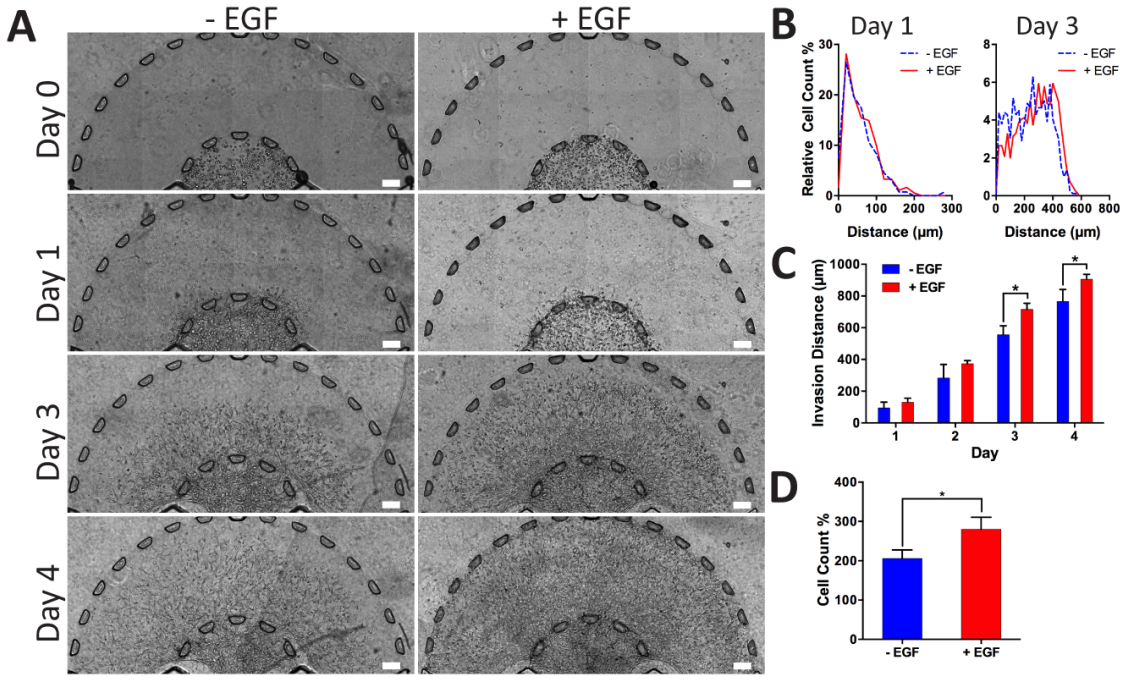

Figure 2.7 Breast cancer 3D invasion assay.

(A) Devices were split into two groups where one group (+ EGF) was introduced to EGF (50 ng/mL) and the other was not exposed to EGF (- EGF). Based on the representative images, (+) EGF showed more proliferation, as indicated by the higher density, and migration by reaching to the outer channels in 4 days. The (-) EGF group demonstrated migratory tendencies but did not have the same invasive profile as (+) EGF. (B) Distribution of cells was quantified for days 1 and 3. The profiles were similar between (-) and (+) EGF for the first day. By the third day, there was a shift in cell distribution

toward the right indicating more cell count further away from the tumor region. Distribution for the fourth day was quantification was not possible due to the high density and overlapping cells (scale bar: 100 μm). (C) Invasion distance of the tumor front was calculated from the radial distances of the furthest cells from the tumor region. (+) EGF exhibited significantly higher invasion by days 3 and 4 ($P < 0.05$ calculated from student's T test with more than three devices for each condition). (D) Number of cells of cells was quantified by counting the amount of cells on days 1 to 3. (+) EGF induced significantly higher cell count ($P < 0.05$ calculated from student's T test with more than three devices for each condition).

In addition to global diffusion through the platform from both media channels, we introduced EGF (50 ng/mL) to a single media channel to localize the chemoattractants asymmetrically through half of the device (Figure 2.5A). The cells were consistently tracked for four days (96 h). We observed no differences in cell migration during the first 24 h of culture. However, by day 2 (Figure 2.5B), there was a significant increase in invasion toward the channel in which we introduced EGF (Figure 2.5C). Such trend was consistent during days 3 and 4. In fact, by day 4, there were cells that had migrated out of the stroma and into the media channels on the EGF side, however, such behavior was not observed on the other side of the stroma (the media only side channel with no EGF (Figure 2.5A). These observations clearly demonstrate the capability of our microfluidic platform to generate competing microenvironments (Figure 2.5C) through introduction of variable regimes of growth factors for invasion studies.

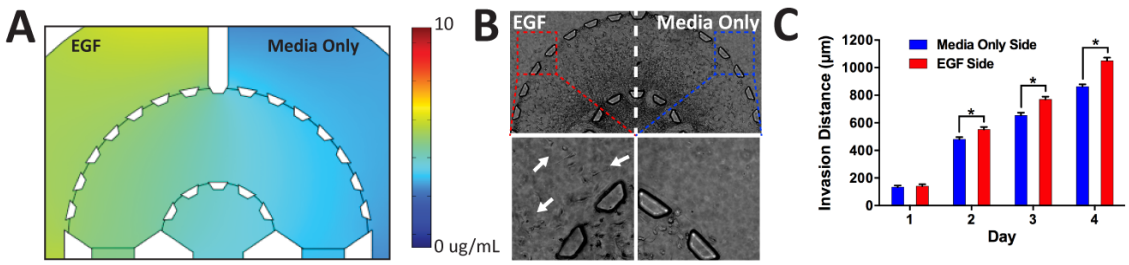

Figure 2.8 Breast cancer 3D invasion assay using asymmetric gradients.
(A) EGF (50 ng/mL) to a single channel while the other contained no supplemented EGF media. We found increased cell gravitation toward the side with EGF (B) Invasion distance of the tumor front was calculated from the radial distances of the furthest cells from the tumor region. (+) EGF exhibited significantly higher invasion by days 2, 3, and 4 ($P < 0.05$ calculated from student's T test with more than three devices for each condition). (C) COMSOL simulation (24 h) of 10 kDa molecule (10 μg/mL) from a single channel through the device demonstrates the concentration gradient.

2.4.5 High Resolution Real-time Imaging of Three-dimensional Cancer Invasion at a Single-cell Level

In comparison to previous real-time migration studies (B. J. Kim et al., 2013; H. Ma, Liu, Qin, & Lin, 2010), our model and technique enabled us to observe the changing morphology of the invading cancer cells at a single-cell level within the 3D matrices, at a high-resolution, using light and fluorescent microscopy. In particular, cells migrated by utilizing thin protrusions probing in front of their cell body and moving their body toward the direction of the protrusions (Figure 2.6A, Appendix Movie D.1 and D.2). Furthermore, these cells appeared to drag their bodies along as the protrusive front moves forward. Using 3D time-lapse imaging (Appendix Movie D.3**)**, we tracked individual cells, which was further analyzed in NIS Elements AR Microscope Imaging Software by

Nikon, to investigate the effects of EGF on 3D tumor cell migration within the initial 24 h of adding EGF (Figure 2.6B). We found a significant increase in average individual cell speed (Figure 2.6C) (0.16 ± 0.006 μm/min) compared to the (-) EGF (0.14 ± 0.006 μm/min) condition. Moreover, we did not see a significant difference in the persistence (Figure 2.6D) for (+) and (-) EGF at 0.32 ± 0.01 and 0.29 ± 0.01 respectively. However, when observing the cell trajectory plots (Figure 2.6B), we noticed migration differences between the cells along the gradient (Figure 2.2), where there were increased cell counts near the y-axis (Figure 2.6B**,** within the pie slice). To investigate this phenomenon, we filtered the cells to only those migrating within ± 30 ° of the gradient (y-axis) in order to isolate the sub-population of cells based on the diffusion gradient (Figure 2.6A) and subsequently compare the average speed and persistence. In doing so, we found that the average speed among filtered cells was still significantly higher for (+) EGF (0.23 ± 0.02 μm/min) compared to (-) EGF (0.17 ± 0.02 μm/min). Furthermore, persistence within the filtered cells was found to be significantly higher for (+) EGF (0.52 ± 0.03) than (-) EGF (0.36 ± 0.03). We continued to culture the cells for two more days with daily media exchanges. The experiment was repeated again between 72 h and 96 h of culture (Figure 2.7A). Consistently, we found a significant increase in average speed of individual cells (Figure 2.7B) for (+) EGF (0.14 ± 0.005 μm/min) compared to (-) EGF (0.11 ± 0.005 μm/min) suggesting that EGF maintained high cell motility over prolonged exposure. Moreover, we noticed a significant difference in the persistence (Figure 2.7C) for (+) and (-) EGF at 0.40 ± 0.02 and 0.29 ± 0.02 respectively. When looking at the filtered cells (Figure 2.7D), we still found that the average speed was significantly higher for (+) EGF at 0.13 ± 0.009 μm/min whereas (-) EGF demonstrated 0.10 ± 0.006 μm/min. However,

the difference in persistence among the filtered cells (Figure 2.7E) was not found to be significant (0.60 ± 0.03 vs. 0.51 ± 0.05) suggesting cells behaving in more of a random walk fashion, at longer duration of culture, as compared to the initial 24 h of EGF stimulation.

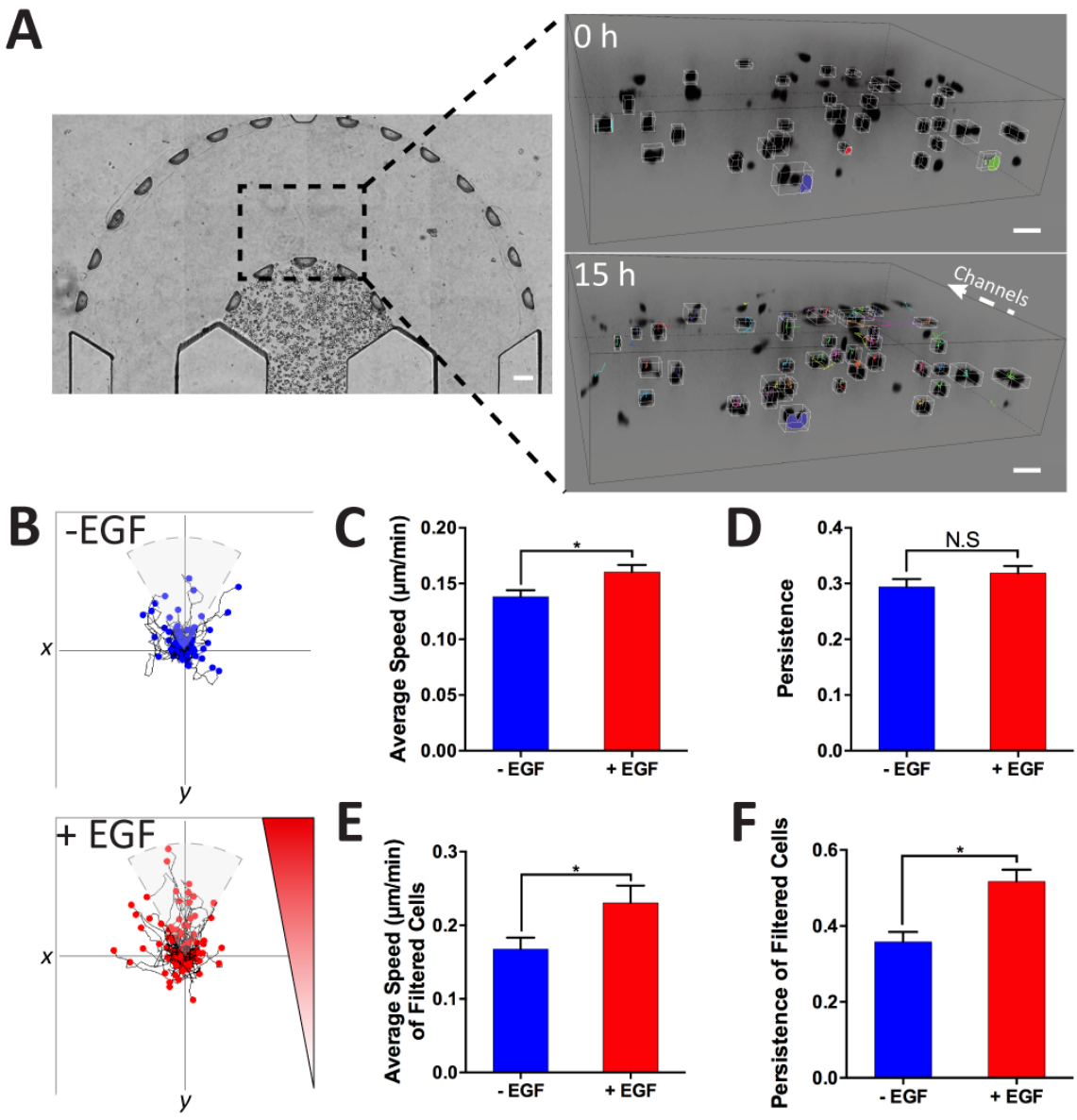

Figure 2.9 Time-lapse analysis of individually invading cells within 24 h of adding EGF.

(A) Dashed box indicates region of interest for time-lapse capture of cell invasion. Frames from a cell invasion movie where the cells are invading throughout the stroma toward the channels (scale bar: 100 µm). (B) The cell trajectories were plotted. (C) (+) EGF cells demonstrated a significant increase in average cell speed but (D) no significant difference for persistence ($P < 0.05$ calculated from student's T test with $n > 50$ from more than three devices for each condition). (E and F) The cells were filtered out for cells following the gradient (y-axis). We found significant increases in cell speed and persistence for (+) EGF ($P < 0.05$ calculated from student's T test with $n > 25$ from more than three devices for each condition).

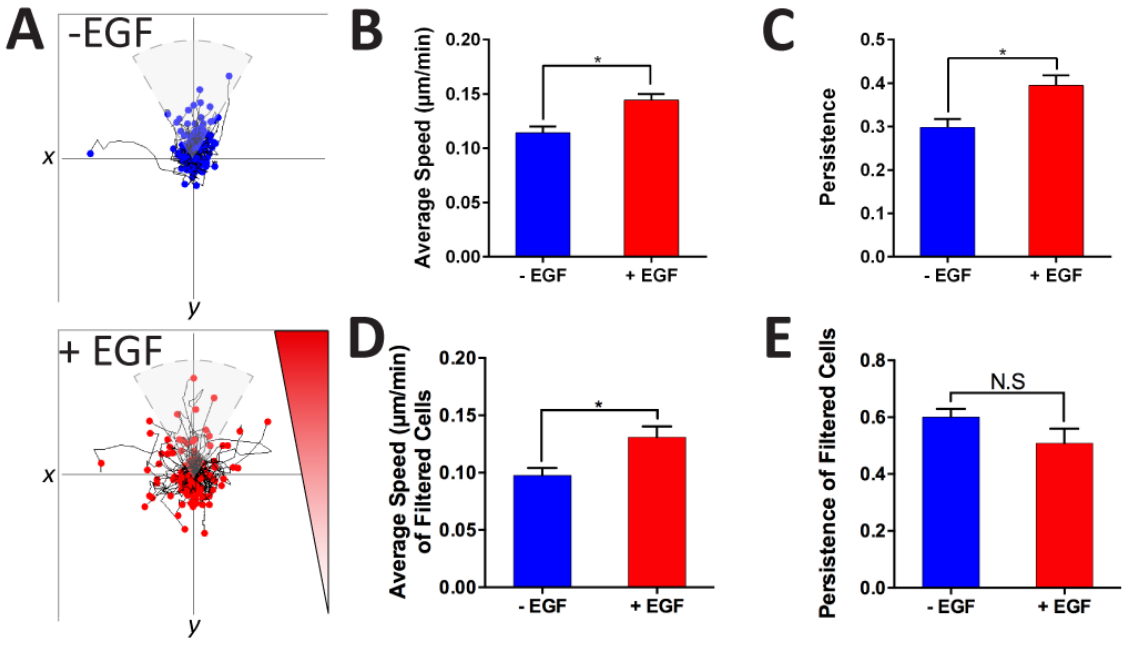

Figure 2.10 Time-lapse analysis of individually invading cells between 72 h and 96 h of EGF addition.

(A) The cell trajectories were plotted. (B and C) (+) EGF cells demonstrated a significant increase in average cell speed and persistence ($P < 0.05$ calculated from student's T test with $n > 50$ from more than three devices for each condition). (D and E) The cells were

filtered out for cells following the gradient (y-axis). We found significant increases in cell speed and but no significant difference in persistence for (+) EGF ($P < 0.05$ calculated from student's T test with $n > 9$ from more than three devices for each condition).

2.4.6 Analysis of EGF Receptors After Long-Term Stimulation

We stained the cells for EGFRs and phosphorylated EGFRs (pEGFRs) after 1, 2, and 4 days of culture in order to visualize the patterning and activation of EGFR in response to EGF stimulation. Interestingly, when observing cells on the first day of culture on both a 2D surface and within the hydrogel matrices (no EGF), EGFRs localized near the cell membrane (Appendix Figure A.6A). After treatment with EGF for 24 hours (Day 2 of culture, Appendix Figure A.6B), we noticed that EGFRs in the (+) EGF condition began to displace from the membrane toward the cell body and became more punctuated. In the (-) EGF condition (Day 2), the location of EGFRs remained similar to the receptors in Day 1 images (Appendix Figure A.6B). However, after 4 days, EGFRs no longer bordered the cell membrane unlike the first days of culture (Appendix Figure A.6B). Moreover, the receptors appeared in a punctate pattern throughout the cell body for both (±) EGF conditions (Figure 2.8A). We normalized the EGFR coverage area to the area of the cell body using actin as a marker for total cell area on Day 4. The EGFR to cell area ratio (Figure 2.8B) was significantly higher in the (-) EGF group. On the other hand, the pEGFR to cell area ratio (Figure 2.8C) was significantly higher in the (+) EGF group. Furthermore, for the (+) EGF group, we found a significantly higher pEGFR to EGFR area ratio suggesting more phosphorylated receptors among the available

receptors. We further examined the reason for why EGFR to cell area ratio was lower in the (+) EGF condition and found that these cells appeared to have clustered or localized EGFR**.** As can be seen in Figure 2.8E, heat maps of relative surface intensity also displayed high clustering of the EGFR near the nucleus in (+) EGF condition while EGFR was seen to be distributed through the cell body in (-) EGF condition. This illustrates that EGFRs are being trafficked within the cell after EGF exposure. Overall, our findings suggest that the migratory phenotype of breast cancer cells, is linked to the activation of EGFRs and further demonstrates successful delivery of EGF to the cells within the 3D microfluidic device.

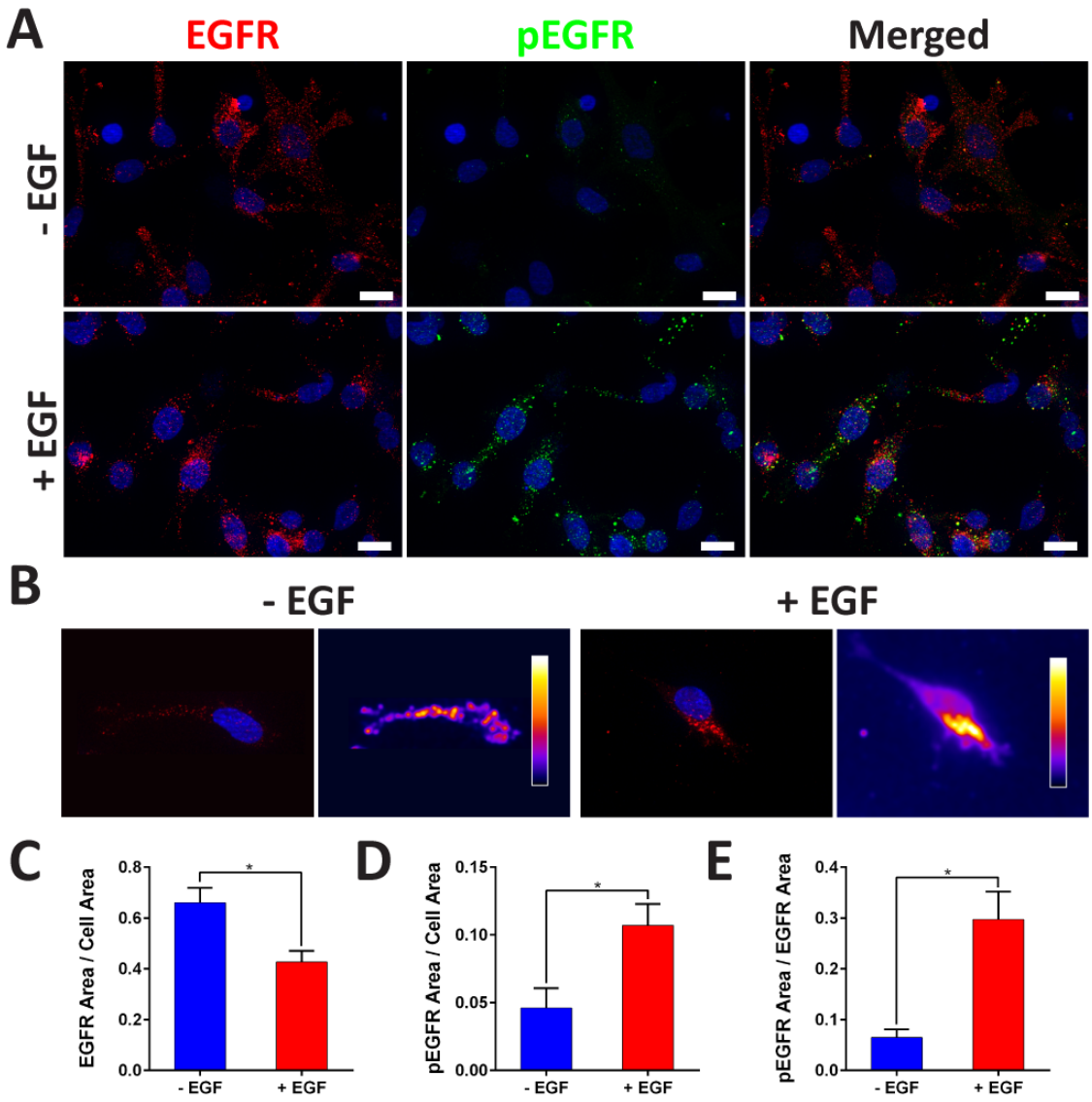

Figure 2.11 Investigation of EGFR and pEGFR.

(A) Cells were stained for EGFR (red), pEGFR (green), and nuclei (blue) (scale bar: 20 µm). (B) (+) EGF demonstrated significantly lower EGFR to cell area ratio. (C and D) (+) EGF displayed significantly higher pEGFR to cell area ratio and pEGFR to EGFR area ratio ($P < 0.05$ calculated from student's T test with $n > 18$ from more than three devices for each condition). (E) Representative images of EGFR clusters with corresponding heat maps of relative intensities.

2.4.7 Cytoskeleton Organization of Invasive Cells

We investigated the changes in the cytoskeleton due to EGF-induced invasion. Upon close inspection, we found that (-) EGF cells were not as spread as the cells within the EGF-stimulated devices. As seen in the Z-projection of the F-actin (Figure 2.9A), more round cells, indicated by the white arrows, were apparent in the (-) EGF group. The actin area, which delineates the area of the cell, (Figure 2.9B) was calculated by thresholding the fluorescent images and dividing the total actin area by the number of cells present in the field of view. This revealed that (+) EGF cells had almost twice the actin area than (-) EGF cells, which is representative of the higher spreading and elongation of cells seen in Figure 2.9B. As previously reported, these cytoskeletal arrangements and changes in morphology are indicative of a shift towards an invasive phenotype (Nikkhah, Strobl, De Vita, & Agah, 2010; Nikkhah, Strobl, Peddi, & Agah, 2009; Nikkhah et al., 2011; Strobl, Nikkhah, & Agah, 2010). Furthermore, specific morphology descriptors (Figure 2.9C) including, aspect ratio (AR), circularity, and roundness, were calculated to divulge the effect of EGF on the cell shape. We limited the analysis to cells that were at the center of the z-stack to avoid the influence of attachment to the top and bottom of the chamber. The ARs of the cells, which indicated polarized length and extension, were significantly higher in (+) EGF (2.33 ± 0.14) than in (-) EGF (1.75 ± 0.08). The extended morphology suggested that EGF played a role in enhancing the migratory phenotype of the breast cancer cells(N. Peela et al., 2016; Sung et al., 2011). Furthermore, the circularity of the cells within the EGF-stimulated devices was nearly half (0.25 ± 0.02) of the circularity for the (-) EGF cells (0.53 ± 0.02). These findings suggested that the protrusiveness or cell extensions were much lower in

unstimulated cells. Moreover, the roundness of the unstimulated cells was 0.66 ± 0.02 compared to 0.53 ± 0.02, which reflected the significantly higher amount of round cells for (-) EGF demonstrated in Figure 2.9A. Interestingly, the distribution of elongated cells were opposite for the two conditions (Figure 2.9D). Specifically, the ARs of the cells were binned into three different groups, high (AR > 2), medium (2 > AR > 1.5), and low (1.5 > AR). As can be seen in Figure 2.9D, 55.8 ± 7.72 % of (+) EGF cells were regarded as high, whereas only 25.2 ± 4.73 % of (-) EGF had high ARs. In contrast, (-) EGF showed the enhanced low ARs and reduced high ARs. For the (-) EGF condition, 59.6 ± 3.49 % of the cells had low ARs in comparison to the 27.2 ± 6.13 % of stimulated cells. There was no significant difference between the medium AR results. Furthermore, we examined the effect of (-) EGF and (+) EGF on protrusiveness (Figure 2.9E). On average, (+) EGF exhibited 3.94 ± 0.34 protrusions per cell whereas (-) EGF demonstrated 1.36 ± 0.13 (Figure 2.9F). Furthermore, the protrusion count per cell was compared with the aspect ratio and the circularity to determine the relationship between cell protrusion and cell morphology under the context of EGF stimulation. These results suggested that ARs and cell protrusions slightly correlated (R-squared = 0.11, $p < 0.001$) prior to EGF stimulation, but upon introduction of EGF the correlation was negligible (R-squared = 0.00, $p < 0.61$). Furthermore, protrusions were correlated with circularity (Appendix Figure A.7) indicating that under (-) EGF condition, the circularity sharply decreased when cell protrusions increased. With EGF stimulation, circularity moderately declined (R-squared = 0.16, $p < 0.001$) with increasing cell extensions where the correlation was weaker than (-) EGF condition (R-squared = 0.45, $p < 0.0001$). This result suggested that

EGF stimulation reduced the correlation between circularity and cell protrusions similarly when looking at ARs and protrusions.

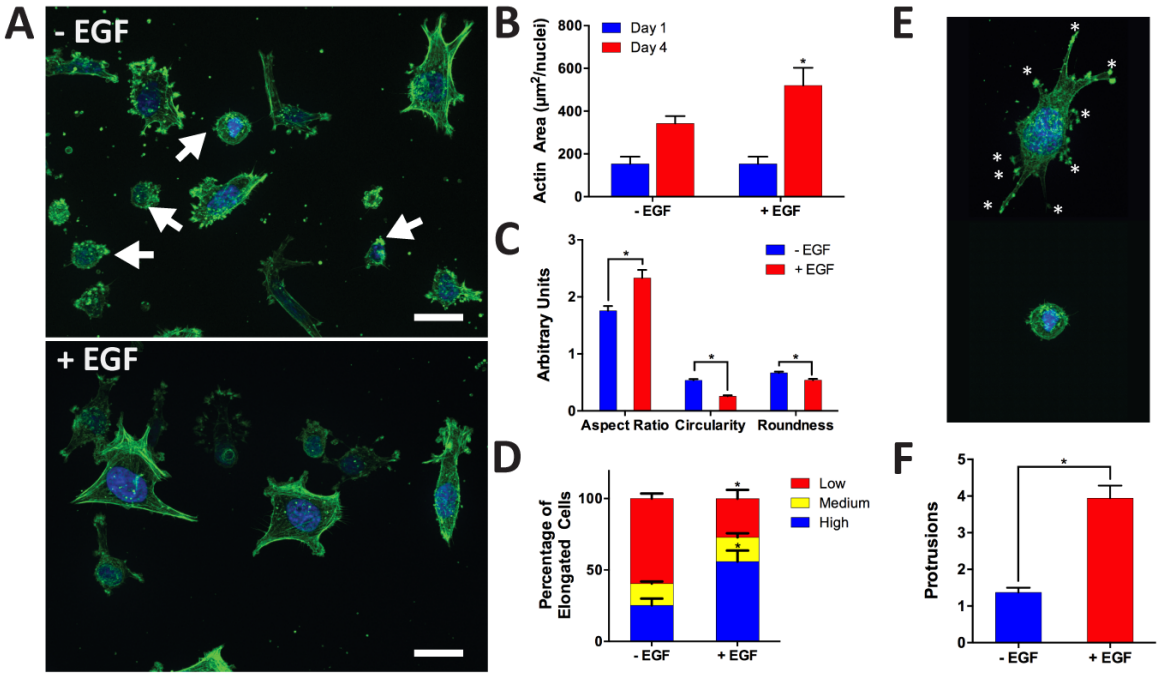

Figure 2.12 Analysis of cell morphology.

(A) Cells were stained for F-actin (green) and nuclei (blue). (-) EGF exhibited more cells with round morphology (white arrows), which was correlated to a less invasive phenotype. (+) EGF appeared to be more protrusive (scale bar: 20 μm). (B) Actin area calculated from thresholded images indicated higher quantities for (+) EGF after 4 days of culture. There was no significant difference between days 1 and 4 for (-) EGF ($P <$ 0.05 calculated from multiple comparisons test with more than three devices for each condition). (C) Cell shape descriptors of the actin-cytoskeleton were quantified using ImageJ software suite (particle analyzer plugin). (+) EGF had significantly higher aspect ratio (AR) and lower circularity and roundness; all of which correlate to a higher invasive phenotype ($P < 0.05$ calculated from student's T test with $n > 70$ from more than three

devices for each condition). (D) AR was reorganized into three categories, low: 1 < AR < 1.5, medium: 1.5 < AR < 2.0, and high 2.0 < AR. Interestingly, (+) EGF contained significantly higher amounts of cells with high ARs whereas (-) EGF contained significantly higher amounts of cells with low ARs. Both groups had no significant difference for the medium category ($P < 0.05$ calculated from student's T test with n > 70 from more than three devices for each condition). (E) Protrusions (white star) were counted for each cell for the two conditions. (F) (+) EGF cells had significantly more protrusions than (-) EGF ($P < 0.05$ calculated from student's T test with n > 70 from more than three devices for each condition).

Further immunostaining, clearly demonstrated microtubule networks in both conditions (Figure 2.10A**)**. We also observed morphology changes between 3D stroma and 2D glass surface. In Figure 2.10B, the red arrow indicates a cell migrating across the 2D plane while the yellow arrow indicates cells exiting the stroma. The morphology of the cells on 2D plane (Figure 2.10B, red arrow) was distinctly different from that of the cells encapsulated within the 3D stroma (Figure 2.10A, Appendix Movie D.4 and D.5) showing that the device can recapitulate 2D and 3D morphologies (Even-Ram & Yamada, 2005; Smalley, Lioni, & Herlyn, 2006). The actin stress fibers (Figure 2.10B, red arrow) spread across the relatively flat cell body with partial local alignment toward the direction of movement. Furthermore, the microtubules exhibited higher amount of fibers and polarization in the same direction. When observing the cells in the 3D stroma (Figure 2.10A, Appendix Movie D.4 and D.5), the cells were less spread, more spherical, and either with or without protrusions. The cells within the stroma presented long

protrusions reaching into the matrix whereas cells on the 2D surface had short and flat protrusions (Appendix Figure A.8**,** white and yellow arrow indicates protrusion and collagen stroma respectively, Appendix Movie D.6). Additionally, in Figure 2.10B, the cells transitioning out of the matrix demonstrated a spherical cell body, similar to cells embedded within the 3D stroma. The flat short protrusions that were reaching out onto the 2D surface were characteristics of cells on glass substrate.

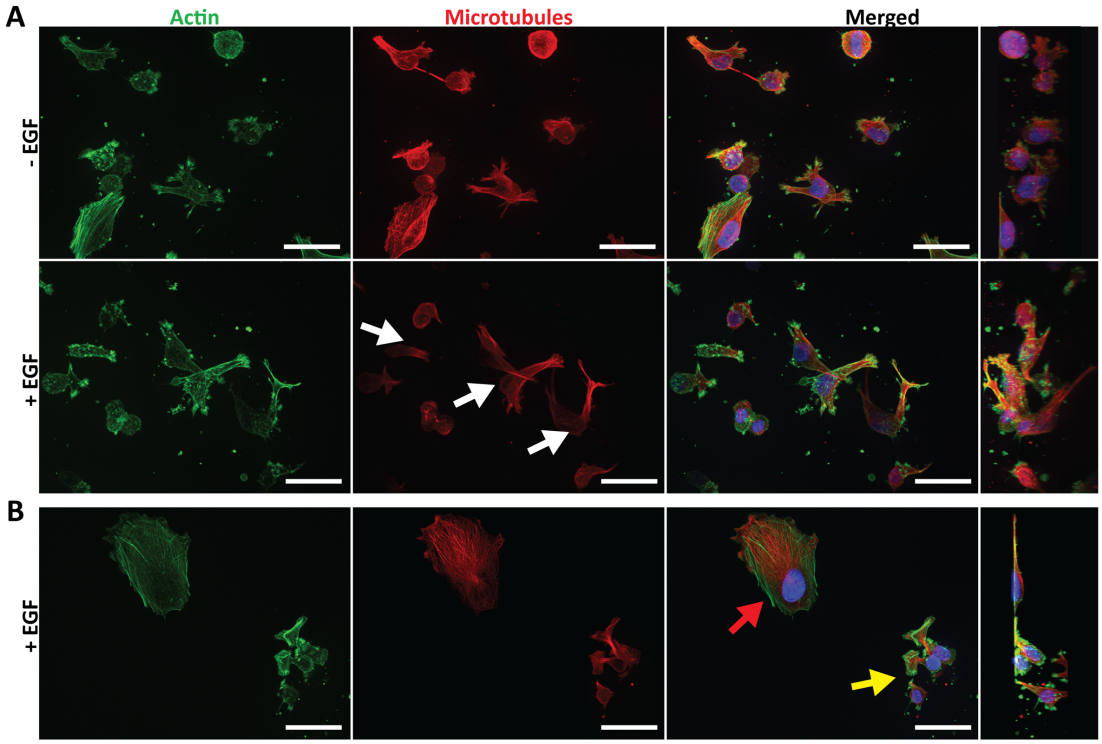

Figure 2.13 3D Analysis of F-actin and microtubules.

(A) Fluorescent staining revealed cell morphology within the 3D matrix. Cells appeared to be round with slight protrusions. Microtubule fluorescence was intense in all directions for (-) EGF, but had a slight affinity toward a single direction (white arrows) in the (+) EGF group. (B) Cell on 2D substrate appeared to be flat comprised of wide lamellipodia (red arrow). Cells moving toward the glass substrate had round cell body but large and wide protrusions (yellow arrow).

2.4.8 CAFs Enhance Breast Cancer Cell Invasion

To incorporate further complexities in the proposed tumor microenvironment, we investigated the invasive response of SUM-159 cells in the presence of CAFs (Figure 2.11A). Specifically, we incorporated the tumor region with only the SUM-159 cells while loading the stroma with only CAFs. In doing so, a 3D tumor-stroma arrangement of breast cancer cells and fibroblasts was successfully generated within the microfluidic device. We observed that over the course of 3 days, SUM-159 cells expressing mCherry were migrating through the surrounding stroma (Figure 2.11B), where the presence of CAFs influenced invasive profile of cancer cells (Figure 2.11C). Specifically, CAFs induced more invasion distance in SUM-159 cells (720 ± 15 μm) as compared to the control condition (564 ± 12 μm) containing no fibroblasts.

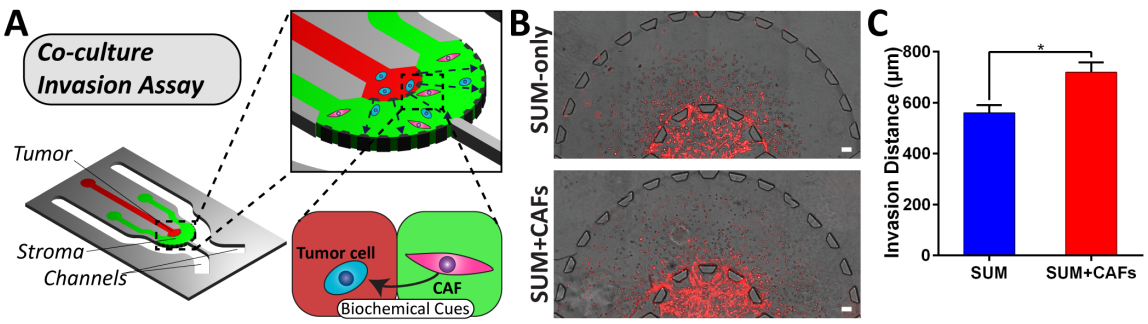

Figure 2.14 Co-culture invasion assay.

(A) Schematic of breast cancer cell and fibroblast interactions. (B) Invading SUM-159 breast cancer cells expressing mCherry (red) into the stroma with or without CAFs, scale bar: 100 μm. (C) Comparison of migration between SUM-159 only and SUM-159 + CAFs groups on day 3. ($P < 0.05$ calculated from student's T test with $n > 6$ from more than three devices for each condition).

2.5 Discussion

Despite significant progress, the majority of microfluidic models lack cell and ECM spatial organization that allows for separate manipulation of side-by-side tumor and stromal regions to assess the roles of microenvironmental factors on 3D cancer invasion, in a real-time fashion (Mosadegh, Saadi, Wang, & Jeon, 2008; Saadi et al., 2006; Sung & Beebe, 2014; S. J. Wang et al., 2004). For instance, work done by Sung et al. provided 3D microenvironment models to spatially compartmentalize different cell types, however the overall objective of the work was not to assess real-time cancer cell invasion in 3D matrix (Sung et al., 2013; Sung et al., 2011). Additionally, these models did not incorporate perfusable channels surrounding the tumor-stroma regions to allow for diffusion of biomolecule gradients of chemotactic factors to the cells. Instead, their model was used to show differences in cell phenotype, which we also demonstrated in our platform. Furthermore, Kim et al., studied invasion in a 3D hydrogel but the model did not offer the ability to separately compartmentalize cancer cells and stromal ECM (B. J. Kim et al., 2013). Moreover, work by Zervantonakis et al., provided insight on the role of tumor-macrophage-endothelial interactions in invasion within a microfluidic tumor model, but was not designed to examine side-by-side arrangement of different 3D ECM components, which is crucial in understanding the invasion process (Farahat et al., 2012; I. Zervantonakis et al., 2010; I. K. Zervantonakis et al., 2012). Our model enabled compartmentalization of tumor and stroma entities, which would allow for fine-tuning and control of heterogeneous ECM and cell components, as well as diffusive barriers (i.e. solid tumors) for nutrient and growth factor transport. Another contribution of our work was real-time high-resolution 3D invasion (in all x, y, z dimensions) and morphology studies at the single cell level.

Cancer cells were compartmentalized within our platform to represent a tumor surrounded by a stromal matrix (Figure 2.1) where biochemical cues (i.e. EGF) diffused from outside of the stoma toward the center of the tumor region (Figure 2.2) (Provenzano et al., 2006). We primarily investigated the cell morphology and tensional homeostatic effect of encapsulating SUM-159 cells within three different matrices namely Matrigel®, collagen I, and 1:1 mixture of Matrigel® and collagen I (Figure 2.3). Our analysis revealed that as the cells migrated and proliferated, they disrupted in the matrix either by proteolytic or tensional effect(Paszek et al., 2005) showing that either collagen I or Matrigel® matrix alone was unable to maintain high fidelity of the tumor-stroma architecture. Furthermore, by mixing collagen I and Matrigel® (1:1 ratio), the combined matrix was able to support continuous migration (from tumor to stroma) and proliferation of the cancer cells with similar morphology compared to Matrigel®-only matrix. Collagen I was chosen for the surrounding stroma matrix where we demonstrated that the two matrices (i.e. Matrigel®:collagen I at 1:1 and collagen I) were not mixed but spatially organized as a stromal (collagen I) component surrounding the tumor region (Matrigel®:collagen I, Figure 2.1). Such capability will enable addition of other cell types (i.e. CAFs) within the stroma region, which have been known to reduce chemoresistance (Sung et al., 2013) as well as enhance tumor growth and invasion (Khamis et al., 2012).

We modulated the invasiveness of breast cancer cells by the introduction of a 3D EGF gradient within the tumor-stroma platform. The encapsulated breast cancer cells migrated (Appendix Movie C.1) in a radial direction outward from the 3D tumor region. EGF was found to heavily influence cell proliferation and invasion distance to which by

day 4, there were stark differences in tumor area coverage between the two studied conditions. The (+) EGF devices exhibited further invasion and increased transitioning from the 3D stroma to the surrounding media channels (Figure 2.4). Moreover, we showed that EGF was also capable of inducing invasiveness in the non-invasive MCF-7 cells (Appendix Figure A.4), however when compared to SUM-159 cells, the level of invasiveness of MCF-7 cells into the collagen stroma was almost 10-fold lower. Our platform also enabled creating competing microenvironments, specifically through introducing EGF in only one of the two segregated channels. SUM-159 cells were attracted to and demonstrated higher invasion to the EGF side (Figure 2.5). Our findings were consistent with those from *in vivo* studies (Patsialou et al., 2009; J. Wyckoff et al., 2004) that demonstrated EGF enhanced invasion within mouse models. However, real-time high-resolution tracking of individual cells and visualization of 3D cell morphology were not possible using *in vivo* models (B. Weigelt, 2014; J. Wyckoff et al., 2004). Moreover, in previous microfluidic models (B. J. Kim et al., 2013; I. K. Zervantonakis et al., 2012) that utilized EGF as a chemoattractant, cell invasion characteristics were not fully captured within a 3D matrix in all x, y and z dimensions.

Our analysis of the real-time imaging (Appendix Movie D.2 and D.3) revealed that the cells increased their individual motility in response to EGF, which confirms that the invasion of the stroma region was not limited to cell proliferation (Figure 2.4D) but also included chemokinesis (Figure 2.6 and 2.7). We found that during the initial 24 h, the whole cell population responded to EGF with increased motility but the overall persistence was not significant. However, when looking only at the filtered cells migrating along the gradient (y-axis) (Figure 2.6D and E), we found significant increases

for individual cell motility and persistence in (+) EGF condition. As expected, there was no difference in persistence for (-) EGF for the whole population of cells as well as the filtered cells (Appendix Figure A.9). This suggests that the population of cells may be heterogeneous in that sub-populations respond to EGF differently (Campbell & Polyak, 2007). Therefore, by analyzing chemotactic responses based on population averages, the end results may fail to account for the aggressive sub-population that can contribute the most to invasion(Hughes-Alford & Lauffenburger, 2012). For longer times (after 72 h), there was no significant difference in persistence toward the gradient (Figure 2.7E) which overall appeared to be more of a random walk. This suggests that over saturation of EGF (72 h) may prolong the overall persistence regardless of the direction (Figure 2.7C). Consistently, several studies have indicated that prolonged exposure to EGF will internalize or localize clusters of EGFRs thus reducing the amount of surface EGFRs (Schulte et al., 2012; Q. Wang, Villeneuve, & Wang, 2005), which we also observed in our results (Figure 2.8). However, none of the previous studies showed prolonged loss of chemotactic responses (i.e. persistence toward the gradient), despite ongoing chemokinesis (i.e. cell speed) in the later stages of invasion, which may be due to saturation of EGFRs (B. J. Kim et al., 2013; Saadi et al., 2006; S. J. Wang et al., 2004). Other studies have also discussed that the effect of EGFR clustering will modify the strength of downstream kinase activity, such as AKT, which may subsequently influence cellular chemotaxis (Mutch, Howden, Jenner, Poulter, & Rappoport, 2014; Schaupp et al., 2014). Moreover, activation of integrins in the presence of EGF has shown to enhance EGFR clustering, which results in Rho responsible for cell contraction during migration (Raftopoulou & Hall, 2004). This could be a potential area of study to investigate the

prolonged spatiotemporal signaling of EGF, in relation to chemokinetic and chemotactic responses, in cancer cells.

Cell morphology analysis, indicated that cells migrating on the glass appeared to have flat and wide protrusions resembling lamellipodia. These cells (Appendix Movie D.7) appeared to follow the characteristic migration steps, which are the exploration and then attachment of the leading edge followed by the detachment and pulling of the rear cell body (Friedl & Wolf, 2003). On the other hand, within 3D matrix, the cells did not clearly exhibit the classical stages of migration (Even-Ram & Yamada, 2005) but instead appeared to entangle inside the matrix with the thin-like protrusions (Appendix Movie D.2), which induced a slow moving crawl. Similarly, F-actin staining of the encapsulated cells (Appendix Figure A.3) revealed thin protrusions surrounding the cell body correlating to what was observed in the migrating cells (Appendix Movie D.2). Consistently, Lämmermann et al. demonstrated elongation and dragging of the cell body, hypothesized that this phenomenon happened in areas of increased spacing between collagen fibers (Lammermann et al., 2008). Similarly to the results found with our device, Fraley et al. showed several protrusions extending from migrating cells in 3D matrices but did not show wide lamellipodia in 3D. Furthermore, they suggested that the cells utilized these protrusions to probe the surrounding matrix which led to correlating the extent and amount of protrusions to cell motility in 3D (Fraley et al., 2010). We further observed noticeable deformation of the collagen matrix overtime in the device, which was the driving factor to producing a suitable matrix composition for the encapsulation of the invasive cancer cells. When closely observing the migrating cells, there were some cells that tended to follow in the tracks of another cell. This observation

was in line with previous work by Gaggioli et al. who studied invasion inducing-microtracks (Gaggioli et al., 2007). This behavior would require further analysis to elucidate the mechanisms of this migratory phenotype.

Stromal cells, such as fibroblasts, endothelial cells, and immune cells, have been demonstrated to heavily influence cancer invasion and therapy (Kalluri & Zeisberg, 2006; B. Weigelt, 2014). In particular, CAFs enhances cancer survival and invasion through cell-cell signaling (Kalluri & Zeisberg, 2006). In our model, we showed that in the presence of CAFs, SUM-159 cells responded by increasing their migration distance compared to control condition (no CAFs) (Figure 2.11C). Based on previous literature and our own experiments, we believe that CAFs are potentially secreting chemoattractants (Orimo et al., 2005) such as stromal cell-derived factor 1α (SDF-1α or CXCL12) that promote breast cancer invasion. This phenomenon creates a unique opportunity for future studies to mechanistically assess the influence of paracrine signaling and the resulting effects within a heterogeneous population of cells on cancer invasion using our proposed platform.

Taken together, our microfluidic platform demonstrated the capability of studying tumor growth and cancer cell migration at a single cell level with the advantage of direct control over spatial cell-ECM, cell-cell and cell-ligand interactions. In our future studies, we aim to incorporate stromal cells (i.e. cancer associated fibroblasts) surrounding the tumor region for more physiologically relevant invasion studies.

2.6 Conclusions

In this work, a new 3D microfluidic platform, designed with separate tumor-stroma entities, was developed to recapitulate 3D cancer cell invasion. Our platform enabled, precise control over cell-ECM and cell-growth factor interactions. We specifically investigated the invasion enhancing effects of EGF and validated the platform as a real-time functional assay for fundamental biological processes (i.e. cell invasion, cellular signaling). Our unique approach allowed for visualization and quantification of invasion and morphology changes, at a single cell level, which was not possible in conventional Transwell assays, 3D macroscale hydrogels, and animal models. We spatially organized a high density of SUM-159 breast cancer cells within a confined 3D tumor region composed of Matrigel® and collagen type I. A stromal matrix of collagen type I surrounded the tumor region, which allowed diffusion of EGF through the stroma into the primary tumor. On a global level, we observed enhanced invasiveness of the breast cancer tumor front when stimulated with EGF. At a single-cell level, we performed real-time 3D migration, which confirmed the increased motility and persistence of cells due to EGF stimulation. Moreover, we showed changes in persistence and migration at different time frames, where we observed that initially a subset of cells migrated preferentially toward the gradient. However, after prolonged exposure to EGF, we found no difference in persistence between the EGF condition and the control despite still increasing cell motility due to EGF. Subsequently, we found higher EGFR clustering within the cell after 4 days of EGF exposure suggesting possible receptor saturation(Schulte et al., 2012; Q. Wang et al., 2005), which could explain the lowered chemotactic responses at later time points We observed cytoskeletal and morphological changes in the EGF-stimulated devices, where the cells demonstrated a more invasive phenotype (i.e. increased aspect

ratio and reduced circularity) with higher protrusion counts. Lastly, we investigated the co-culture of SUM-159 cells and CAFs within the tumor and stroma region respectively resulting in enhanced SUM-159 invasion. Together, this demonstrates the ability of our device to visually observe a combination of cell migration, morphology, survival, and proliferation changes, which provides a valuable tool that recapitulates 3D tumor-stroma interaction and invasion in a single platform.

Our future studies will be focused on adding complexities to this process by studying heterotypic cell interactions such as the understanding the diverse roles of CAFs within the stroma region. We further plan to take advantage of our device to investigate and image real-time changes in cell morphology and migration under different therapeutics regimens such as suberoylanilide hydroxamic acid (Strobl et al., 2010), nocodazole (Nikkhah et al., 2010), paclitaxel (Loessner et al., 2010), etc. Moreover, we aim to manipulate the cell-cell interactions to study how the heterotypic dialogue affects drug resistance.

CHAPTER 3

AIM 2: Study the influence of patient-derived CAFs on cancer cell invasion and gene expression profile and determine a possible mediator of invasion due to tumor-stroma interactions.

3.1 Abstract

Tumor-stroma interactions significantly influence cancer cell metastasis and disease progression. These interactions are partly comprised of crosstalk between tumor and fibroblasts, but key molecular mechanisms within the crosstalk governing cancer invasion are still unclear. Here we develop a 3D in vitro organotypic microfluidic to model tumor-stroma interaction by directly juxtaposing tumor and stroma regions to mimic the spatial organization of the tumor microenvironment. We co-culture breast cancer and patient-derived fibroblast cells in the tumor and stroma regions respectively and combine functional assessment of cancer invasion, like migration and proliferation, with transcriptome profiling to unveil the molecular influence of tumor-stroma interactions on cancer invasion. Through this work, we uncovered a novel gene of interest, *GPNMB*, and unveiled that CAFs enhanced breast cancer invasion by up-regulating the expression of GPNMB on breast cancer cells resulting in increased migration speed. Overall, these results demonstrate the ability of our model to recapitulate patient specific tumor microenvironment to investigate cellular and molecular consequences of tumor-stroma interactions.

3.2 Introduction

Tumor-stroma interactions significantly influence cancer cell metastasis and disease progression (Kalluri, 2016). These interactions in part comprise of heterotypic crosstalk between tumor and stromal cells, however, the mechanism and functional consequences of the interactions on cancer invasion are still unclear (Kalluri, 2016). Cancer-associated fibroblasts (CAFs) stand out as the most abundant non-cancer cell type due to their ubiquitous nature within the tumor-stroma microenvironment, which allows them a unique position to significantly influence cancer invasion (Kalluri, 2016; Ohlund et al., 2014; Tchou & Conejo-Garcia, 2012). Ongoing studies have demonstrated that the presence of CAFs have promoted invasion of many different cancers, such as breast, prostate, ovarian, colon, and non-small cell lung cancer (Kalluri, 2016). Particularly, breast cancer has been known to harbor many CAFs within their tumor microenvironment (Kalluri, 2016; Orimo et al., 2005). Further, triple negative breast cancers (TNBCs), which do not express estrogen, progesterone, and Her2-neu receptors, lack effective targeted therapies. However, there is ample evidence that interactions between TNBC and the tumor microenvironment do play crucial role in breast cancer progression (Orimo et al., 2005; Tchou & Conejo-Garcia, 2012). As such, understanding and targeting the crosstalks between cancer and CAFs within the tumor microenvironment is a novel treatment strategy for breast cancer, shifting away from the neoplastic cell-centric to a tumor-stroma paradigm.

To unveil the cellular and molecular basis of cancer invasion in response to CAFs, a significant effort has been devoted to developing tumor models allowing complex tumor-stroma interactions. Although, *in vivo* models play a crucially important role in studying the cellular and molecular basis of disease progression, they suffer from lack of

high resolution observation and analysis of cell-cell interactions as well as precise control over critical parameters, like manipulating stromal cells, in the tumor microenvironment (B. Weigelt, 2014). Importantly, this lack of precise control creates challenges to determining the cause and effect relationships within the heterotypic dialogues between cancer and stromal cells like CAFs (B. Weigelt, 2014). Furthermore, there are crucial molecular and cellular differences between humans and mice limiting the scope for animal models to recapitulate human diseases (Mak et al., 2014). To overcome some of these problems, conventional co-culture *in vitro* platforms, including transwell migration assays as well as 3D spheroid-based models, have been widely utilized to perform biological studies for cancer invasion (Gaggioli et al., 2007; Glentis et al., 2017; Tyan et al., 2011). Still, these models are often oversimplified and do not replicate proper organotypic arrangement of the tumor-stroma architecture due to random mixing of cells. This limits the available analyses to proliferation, morphology, and protein expression as opposed to precise spatial organization of cells which could enable assessment of migration metrics (i.e. distance, speed, persistence) (dit Faute et al., 2002; S. A. Kim, Lee, & Kuh, 2015; Orimo et al., 2005; Yang et al., 2015). Importantly, these models are often end-point assays that do not allow real-time observations of dynamic tumor-stroma interactions at cellular and molecular levels.

Recently, there have been a significant thrust to use microfluidics to develop complex 3D tumor models, with precise control over cell-cell, cell-matrix and cell-soluble factor interactions (D. Truong et al., 2016). Various microfluidics integrated with hydrogel-based 3D matrices allow the study of different steps of the metastatic cascade such as invasion, intravasation, and extravasation within a well-controlled tumor

microenvironment (Nagaraju et al., 2018; N. Peela, Barrientos, Truong, Mouneimne, & Nikkhah, 2017; N. Peela, Truong, et al., 2017; D. Truong et al., 2016). Since tumor progression is a complex and dynamic process, our group developed a tumor invasion model of breast cancer on the premise of utilizing and understanding chemoattractants and paracrine signaling (Nagaraju et al., 2018; N. Peela, Barrientos, et al., 2017; D. Truong et al., 2016). We studied the effects of EGF on breast cancer cell invasion, providing quantitative data on real-time invasion at a single-cell level in 3D, cancer cell phenotype, and EGF receptor activation (D. Truong et al., 2016). However, the analyses were limited to cell-based functional assessments, such as migration or proliferation, and did not integrate transcriptome profiling to better inform the influence of stromal factors on cancer invasion. In that work, stromal cells were also represented by simple biomolecule cues, such as EGF, or immortalized cell lines. In regards to other works, the impact of their studies using complex *in vitro* models in the context of breast cancer were also limited due to lack of CAF co-culture or the use of non-mammary cells, such as 3T3 or dermal fibroblasts, rather than using patient-specific CAFs (Nikkhah et al., 2011; Strobl et al., 2010). Thus, there is a crucial need to develop a patient-specific and physiologically relevant tumor-stroma model to understand the extent of the molecular and cellular influence of stromal CAFs on cancer invasion.

In this present study, we incorporated breast cancer patient-derived CAFs and NFs into our *in vitro* organotypic microfluidic model of breast tumor-stroma interactions to investigate the interplay between fibroblasts and breast cancer cells (Figure 1.1A and Appendix Figure B.1). Using this 3D co-culture model, we found that the interaction between invasive SUM-159 breast cancer cells and mammary fibroblasts had distinct

consequences on cancer migratory behavior depending on the fibroblast phenotype (i.e. CAFs or NFs). From there, we paired our functional assessments with transcriptional profiling to evaluate the molecular changes during cancer invasion. Here, we uncovered a novel gene of interest, glycoprotein non-metastatic B (*GPNMB)*, and unveiled that CAFs enhanced breast cancer invasion through up-regulation of GPNMB on breast cancer cells.

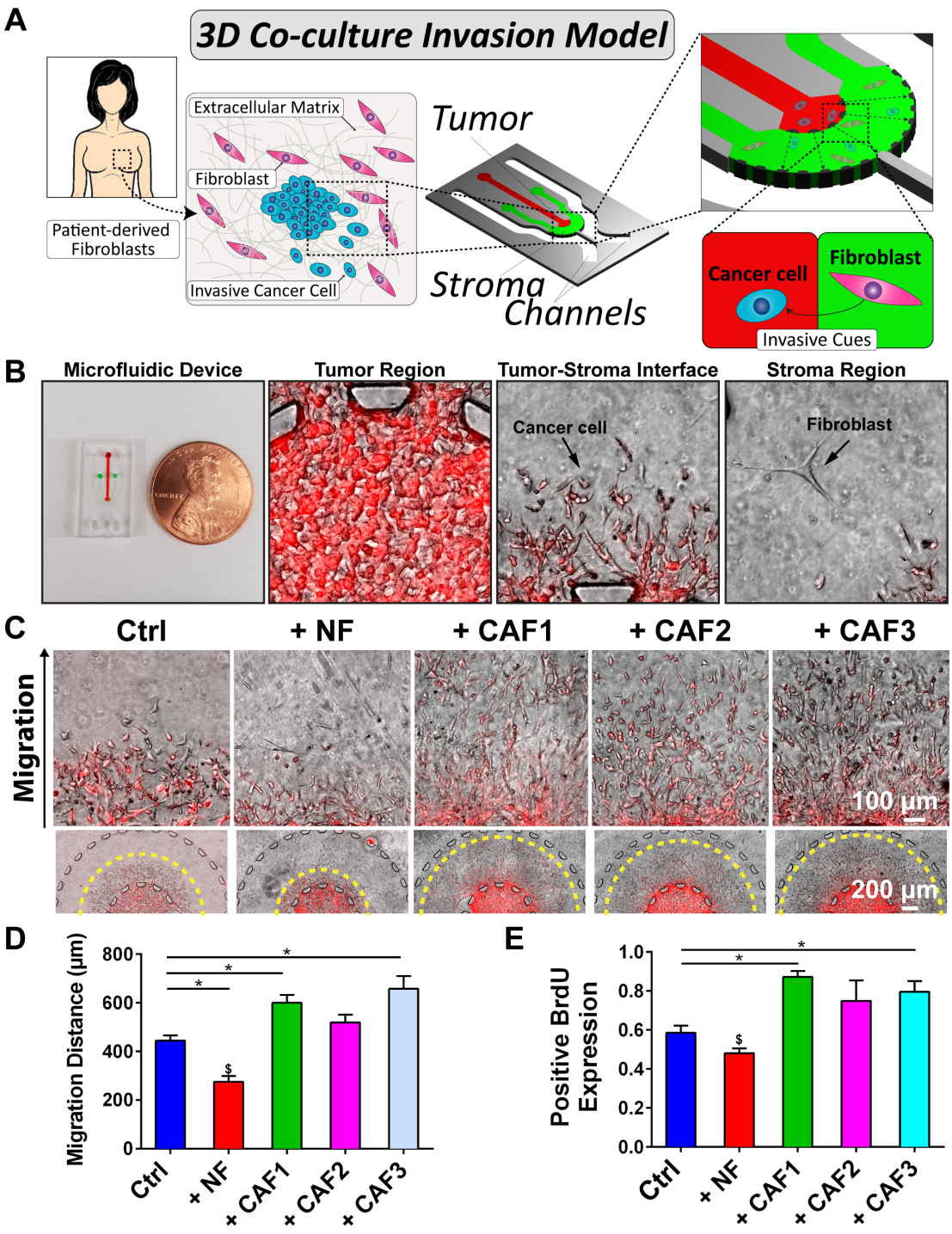

Figure 3.15 3D organotypic co-culture invasion assay.

(A) Fibroblasts were derived from patient biopsies. SUM-159 breast cancer cells were cultured in the tumor (red) region while fibroblasts (NFs or CAFs) were cultured in the

stroma (green). (B) Microfluidic device shown next to a penny depicting the size of the platform. The tumor region of the platform demonstrates a dense amount of cancer cells. The tumor-stroma interface within the device shows migrating cancer cells. Fibroblasts are shown within the stroma region. (C) Magnified images of cancer migration in the presence of fibroblasts alongside images of the tumor-stroma regions. (D) + CAF1 and + CAF3 migration was significantly higher than Ctrl while + NF was lower than all groups. (E) + CAF1 and + CAF3 had increased expression of BrdU compared to Ctrl. + NF was significantly lower than CAF co-cultures. * denotes significant difference and $ denotes a significantly different group for $p < 0.05$.

3.3 Materials and Methods

3.3.1 Microfluidic design and fabrication

The microfluidic platform design and fabrication was established in our previous studies (D. Truong et al., 2016). Briefly, SU8-2075 (MicroChem) was spun onto a silicon wafer for a final height of approximately 200 μm. A patterned wafer was created by placing the silicon wafer underneath the mask containing the microfluidic design and exposing them to UV followed by developing the wafer. Polydimethylsiloxane (PDMS, Sylgard 184 Silicon Elastomer Kit, Dow Corning) was then poured on to the pattern SU-8 wafer and baked for 1 h at 80 °C. Afterwards, the PDMS containing the patterns of the device was peeled from the silicon wafer. Next, the PDMS was processed by cutting out individual microfluidic device and punching the inlets and outlets with biopsy punches. Next, these devices were treated with oxygen plasma (PDC-32G, Harrick Plasma) and were then bonded to glass with channel side facing down to create a sealed cell culture

environment and sterilized using an autoclave. To enhance attachment of collagen to the microfluidic devices, 1 mg/mL poly-d-lysine (PDL, Sigma-Aldrich) was injected into the cell culture regions and incubated at 37 °C for 1 h and then washed with deionized (DI) water. Next, 0.1% (v/v) glutaraldehyde (GA, Sigma-Aldrich) solution was introduced incubated at room temperature for 1.5 h. Finally, the devices were washed 4 times with DI water and placed in an 80 °C oven overnight to render the surfaces hydrophobic.

3.3.2 Fibroblast Isolation

CAFs were selected from regions adjacent to the tumor mass. Collagenase I (1 mg/mL, Worthington) and hyaluronidase (125 U/ml, Sigma-Aldrich) were used to digest the tissues at 37 ºC in DMEM) and 10% fetal bovine serum (FBS). Following this, a cell strainer was used to isolate cells from the dissociated tissues and re-suspended in complete DMEM. Fibroblasts were grown in complete DMEM and passaged three times before use.

3.3.3 Cell culture

In order to model 3D migration, SUM-159 breast cancer cells was chosen as a suitable cell type due to their readiness to invade 3D hydrogels(Sabeh et al., 2009). The mCherry-labeled SUM-159 breast cancer cells, provided by Mouneimne lab, were cultured in SUM specific media (Ham's F-12 with L-glutamine and supplemented with 5% heat inactivated fetal bovine serum (FBS), 1% penicillin-streptomyocin, 1 μg/ml hydrocortisone, and 5 μg/ml insulin). NFs were obtained from ZenBio. CAFs were isolated from breast tissue. mCherry-labeled MDA-MB-231 and MCF7 were provided by

the Mounmeine Lab. The cells were maintained in complete Dulbecco's Modified Eagle Media (DMEM supplemented with 10% heat inactivated fetal bovine serum (FBS), 1% L-glutamine, and 1% penicillin-streptomyocin).

3.3.4 Fibroblast Characterizations

Scratch assay was performed by seeding fibroblasts into a 24-well plate and allowing cells to become confluent. Afterwards, a pipette tip was used to scratch the monolayer in straight line down the center. The wells were washed 3 times with PBS prior to imaging. Images were taken at 0 and 24 h. NIH ImageJ was used to quantify the gap closure.

alamarBlue® was performed according the manufacturer's instructions. Briefly, 4000 cells were seeded per well within a 96-well plate. alamarBlue® reagent was added on days 0, 1, 3, and 5 at a ratio of 1:10 to cell culture media. The fluorescence intensity was read using a plate reader at 560 nm excitation and 590 nm emission. Values were calculated as a relative intensity based on the day 0 samples.

To characterize fibroblasts in 3D microenvironment, we used our microfluidic model based on our previous publications(D. Truong et al., 2016). Briefly, a 1:1 mixture of Matrigel® to collagen type I (2.0 mg/mL) was injected into the tumor region of the microfluidic chip and polymerized by placing the devices into the humidified cell culture incubator at 37 °C. After 2 min within the incubator, the devices were taken out and subsequently a 2.0 mg/mL collagen type I solution containing 50,000 cells/ml was injected into the stroma region. The collagen was polymerized within the humidified incubator at 37 °C for 8 min and flipped every min. Next, SUM media was added into the

channels of each device and the microfluidic chips were placed into the cell culture incubator. Media was exchanged daily. Fibroblasts were imaged daily and migration was measured based on final and initial location of the fibroblasts.

3.3.5 3D Co-culture Microfluidic Invasion assay

The invasion assay was based on our previous publications(D. Truong et al., 2016). Briefly, a 1:1 mixture of Matrigel® to Collagen I (2.0 mg/mL) was added to the cells to create a mixed hydrogel cell solution (final concentration of Collagen I at 1 mg/mL) with a density of 15 million cells/mL. The mixed hydrogel cell solution was injected into the tumor region of the microfluidic chip and polymerized within the cell culture incubator at 37 °C. These devices were flipped every minute to create a homogenous distribution of cells 3D hydrogel. After 2 min within the incubator, the devices were taken out and subsequently a 2.0 mg/mL collagen type I solution was injected into the stroma region. For co-culture with CAFs, 50,000 cells/mL were encapsulated in the collagen type I solution. The collagen was polymerized within the humidified incubator at 37 °C for 8 min and flipped every min when fibroblasts were encapsulated. SUM-159 cell media was added into the channels and the devices were put in the cell culture incubator. Media was exchanged daily.

3.3.6 Proliferation assay

Click-iT™ EdU Alexa Fluor™ 488 Imaging Kit (ThermoFisher) was used to assess proliferation by following manufacturer's protocol. 10 μM of EdU was added to the cell culture media in the microfluidic on day 2 of culture. Cells were incubated

overnight for 16 h before fixation. Next, cells were permeabilized and blocked prior to EdU activation. Then EdU was tagged using Click-iT™ reaction cocktail before imaging. EdU to nuclei ratio was defined as the proliferative metric.

3.3.7 Time-lapse imaging

To perform time-lapse imaging, mCherry-labeled SUM-159 cells were mixed together with normal SUM-159 at a ratio of 1:9 prior to the invasion assay. The devices were placed inside a custom miniature incubator (TC-MWP, Bioscience Tools) at 37 °C and 5% CO_2. Fluorescent time-lapse imaging was performed using a fluorescent microscope (Zeiss Axio Observer Z1, Zeiss) equipped with the Apotome.2 and a 10x objective. The Apotome.2 utilized structural illumination technique to create optical sections of our devices to reduce scattered light and to generate high-resolution Z-stacked fluorescent 3D images. The time interval was set to 45 min. Time-lapse images were taken on day 2 of the invasion assay for 12 h overnight followed by migration metric quantifications.

3.3.8 Immunofluorescent staining

For immunofluorescent staining, the cells were fixed by adding warmed 4% paraformaldehyde into the channels of the microfluidic chip for 30 min. The devices were then washed twice with PBS-glycine (100 mM glycine in PBS) for 10 min at room temperature. This was followed by a single wash using PBS-Tween (0.05% (v/v) Tween-20 in PBS). Next, immunofluorescent (IF) buffer (0.2% (v/v) Triton X-100, 0.1% (v/v) BSA (radioimmunoassay grade), 0.05% Tween 20, 7.7 mM NaN_3 in PBS), 10% (v/v)

goat serum was added into the channels and incubated at room temperature for 1.5 h. Primary antibodies, vimentin (ab92547, abcam), αSMA (ab7817, abcam), pan-cytokeratin (MA5-13203, ThermoFisher), and anti-BrdU (G3G4 (anti-BrdU) was deposited to the DSHB by Kaufman, S.J.) was diluted at in IF buffer and kept at 4 °C overnight. Afterwards, the microfluidic channels were washed with IF buffer. Then, the secondary antibody (Alexa Fluor, Thermo Fisher Scientific) diluted in IF buffer was added for 45 min at room temperature in the dark. The devices were washed once with IF buffer and twice with PBS-Tween at room temperature. Afterwards, the nuclei and F-actin fibers were stained by using 4',6-diamidino-2-phenylindole (DAPI, Invitrogen) (1:1000) and Alexa Fluor® 488 Phalloidin (Invitrogen) (1:40) overnight at 4 °C. The devices were washed before imaging.

3.3.9 Western blotting

Western blotting was performed as described. Briefly, cells were scraped, lysed using NP-40 buffer and protease inhibitors, and boiled prior to running. SDS-polyacrylamide gel electrophoresis (SDS-PAGE) was used to separate protein by molecular weight. Proteins were transferred to PVDF membrane and subjected to antibodies for analysis. Primary antibodies include anti-αSMA (ab7817, abcam), anti-GPNMB (ab125898, abcam), anti-Vinculin (ab18058, abcam), and anti-GAPDH (sc-365062, Santa Cruz). Blots were imaged using Odyssey® CLX imaging system (Li-Cor) and analyzed in Image Studio™ Software (Li-Cor).

3.3.10 Gene expression profiling

mCherry-labeled SUM-159 breast cancer cells interacted with fibroblasts within the microfluidic device for 3 days. Collagenase (2 mg/mL) was injected into the media channel and allowed to incubate for 30 minutes. Physical agitation was used to release cells from the ECM. Cell mixtures were centrifuged and collagenase was replaced with cell culture media. BD FACSAria II (BD Biosciences) at the Barrow Neurological Institute was used to separate SUM-159 cells from fibroblasts. Cells were sorted directly into RNA lysis buffer and then RNA was extracted using the Quick-RNA™ Microprep kit (Zymo Research). RNA-Seq library prep was performed using Kapa RNA kit. Next generation sequencing was done using a hiSeq 3000, from which we obtained > 30 million 1x50 bp reads to measure gene expression level. The reads were aligned by STAR(Dobin & Gingeras, 2015) and the TPM (transcripts per million reads) were compared in the edgeR package (Robinson, McCarthy, & Smyth, 2010).

3.3.11 Breast Cancer Dataset Analysis

cBio (www.cbioportal.org) was used to query The Cancer Genome Atlas Breast Invasive Carcinmoa (TCGA-BRCA) for alteration and expression of *GPNMB*. Breast cancer patient gene expression datasets were obtained from GEO (www.ncbi.nlm.nih.gov/geo). mRNA expression of *GPNMB* from tissues were obtained from accession nos. GSE3744(Richardson et al., 2006), GSE14548(X. J. Ma, Dahiya, Richardson, Erlander, & Sgroi, 2009), and GSE9014(Finak et al., 2008). Survival data was queried from Geneanalytics tool (http://geneanalytics.duhs.duke.edu). Low and high expression of *GPNMB* were distinguished using lower and upper quartiles respectively. Correlation

analysis of *GPNMB* expression and tumor staging was obtained through Oncomine (www.oncomine.org) (Rhodes et al., 2004).

3.3.12 Vectors and Gene Transduction

shRNA clone set against Human GPNMB (NM_001005340.1, GeneCopoeia™, HSH000547-LVRU6MP) were used to produce GPNMB knockdown lines. A scrambled shRNA was used to produce the shCtrl (GeneCopoeia™, CSHCTR001-LVRU6MP). Lenti-Pac HIV Expression Packaging Kit (LT001, GeneCopoeia™) was used to transduce the SUM-159 breast cancer cells based on manufacturer's protocol.

3.3.13 Imaging analysis

Phase-contrast images of the invasion assay were acquired once every day using 4 x 3 tiles with a 10x objective. To quantify the invading edge of the tumor (i.e. the invading tumor front), the cells on the periphery were measured by considering the most distal points of the most distal cells. In this case, only the cells at the edge of the tumor (i.e. cells that have traveled the highest distance from the tumor region from each degree) were included in the quantification.

Real-time analysis was conducted using CellTracker software(Piccinini, Kiss, & Horvath, 2015). Speed (defined as distance over time) and persistence (defined as euclidean distance over accumulated distance) were utilized to quantify cell migration metrics.

Shape descriptors (area, circularity, aspect ratio, and protrusiveness) were used to describe the cell shape for cancer cells and fibroblasts based on the actin cytoskeleton.

We used the particle analyzer plugin within the NIH ImageJ suite to quantify cell shape based on the actin images.

Protein signals were quantified in NIH Image J consistent to previous literature(Acerbi et al., 2015). Staining protocol and image capture settings were kept consistent for all samples/ Image fluorescent intensity integrated density per cell was used to quantify the protein signal.

3.3.14 Statistical analysis

All measurements were compiled from three or more independent devices or replicates for each experimental condition and repeated at least three times. Reported measurements are shown as average ± standard error of mean. The data were compared using unpaired t-test, paired t-test, multiple comparisons test with corrections, and correlation analysis as appropriate within the GraphPad Prism software (GraphPad Software). Volcano plots and heatmaps were generated using R (Kolde, 2015; R Development Core Team, 2010).

3.4 Results

3.4.1 Isolation and characterization of patient-derived CAFs

We isolated CAFs from breast tumor tissue samples of three different patients varying in hormone and Her2 receptor status from the Mayo Clinic (Phoenix, AZ) (Appendix Table E.1). We obtained NFs from reduction mammoplasty. Next, CAFs are routinely identified through expression of alpha smooth muscle actin (αSMA), contractile stress fibers, and vimentin(Ohlund et al., 2014). Immunofluorescent (IF) images of both

NFs and CAFs showed positive staining for vimentin and negative expression of cytokeratin demonstrating the overall purity of the fibroblast populations (Appendix Figure B.1A). CAFs expressed significantly higher αSMA levels (Appendix Figure B.1B). We further corroborated the IF results with western blotting (Appendix Figure A.1C and D), demonstrating that the quantified levels of αSMA were indeed higher in CAFs than NFs.

Differences between CAFs and NFs also extended to morphology(Kalluri, 2016). Generally, NFs were smaller and more spindle shaped, while CAFs were larger and polygonal with actin stress fibers (Appendix Figure B.2A) (Evans, Tian, Steadman, & Phillips, 2003). Based on morphometric analyses, all three CAFs demonstrated larger cell spreading area and aspect ratio compared to NFs, where the differences for CAF2 and CAF3 but not CAF1 were statistically significant (Appendix Figure B.2B and C). Next, we analyzed the 2D migration of the fibroblasts using a scratch wound healing assay (Appendix Figure B.2D), and found that NFs and CAFs migrated similarly (Appendix Figure B.2E). Overall, these results indicated that CAFs shared general characteristics with NF in 2D culture, but were heterogeneous in their morphology and αSMA expression.

3.4.2 Stromal CAF and NF behavior within a 3D matrix

To examine the cell morphology and behavior of NF and CAFs in 3D culture, the fibroblasts were cultured in the stroma region of the 3D microfluidic platform. All fibroblast populations showed elongated morphology (Appendix Figure B.3A and B). Time-lapse image analysis demonstrated that fibroblasts were mostly stationary for 3

days, and no statistical difference was observed between the migratory activities of NF and CAF similar to the 2D wound healing assay (Appendix Figure B.3C). Both NF and CAF1 exhibited significantly lower cell area than CAF2, while CAF3 was not statistically different to any other fibroblasts (Appendix Figure B.3B and D). Interestingly, no difference was found for cell aspect ratio in 3D suggesting less morphological heterogeneity in 3D culture (Appendix Figure B.3E).

3.4.3 Fibroblasts differentially influence breast cancer cell invasion

To investigate the influence of patient-derived CAFs on migration and proliferation of invasive breast cancer cells, we utilized 3D tumor-stroma microfluidic as a co-culture system (Figure 3.1B) (D. Truong et al., 2016). SUM-159 breast cancer cells, which were derived from invasive ductal carcinoma of a TNBC patient, were chosen for their propensity to migrate within a 3D hydrogel(L. Ma, Teruya-Feldstein, & Weinberg, 2007; N. Peela, Barrientos, et al., 2017; D. Truong et al., 2016). SUM-159 cells in the tumor region were observed over 3 days invading into the stroma region of the microfluidic either with or without fibroblasts (Figure 3.1C, Appendix Figure B.4). We found a significant increase in migration distance for CAF1 (+ CAF1) and CAF3 (+ CAF3) but not with CAF2 (+ CAF2) when compared to the mono-culture condition (Ctrl) (Figure 3.1D). Notably, the NF co-culture (+ NF) had significantly lower migration compared to all CAF co-cultures and the Ctrl (Figure 3.1D). In parallel, we investigated cancer cell proliferation influenced by fibroblasts. The + NF condition had a lower fraction of BrdU-positive SUM-159 cells compared to the three CAF co-cultures indicating less proliferation in NF co-culture (Figure 3.1E). On the other hand, we

observed a significant increase in BrdU expression for + CAF1 and + CAF3 versus the Ctrl, and for + CAF2 to a lesser extent. In summary, NFs demonstrated a suppressive effect on cancer cell invasion and proliferation, while CAF1 and 3 exhibited an invasion- and proliferation-promoting activities. Taken together, this suggests that fibroblasts of different microenvironmental origin (i.e. patients) and phenotype, although all were mammary derived, could exert distinct effects on invasion and proliferation of cancer cells in 3D culture conditions.

We also investigated MDA-MB-231, another TNBC cell line, but derived from pleural effusion, and MCF7 cells, which are also pleural effusion-derived but less invasive(L. Ma et al., 2007). We asked if CAFs had a similar influence on migration for these breast cancer cell lines. The CAF3 population was utilized as it demonstrated the highest increase in SUM-159 cell migration (Figure 3.1D). We observed that both MCF7 and MDA-MB-231 cells showed propensity to migrate into the 3D stroma but MCF7 had far less migration capacity. Importantly, adding CAFs into the stroma influenced both MCF7 and MDA-MB-231 cells by significantly enhancing their 3D invasive capacity into the stroma similar to SUM-159 cells (Appendix Figure B.5A and B). Consistent with the literature, MDA-MB-231 had less invasive capacity as compared to SUM-159 cells(C. Bao et al., 2016). Taken together, this suggests that patient-derived CAFs promoted invasion of broad types of breast cancer cell lines.

3.4.4 Real-time analysis of cell migration reveals bi-directional cancer-fibroblast crosstalk

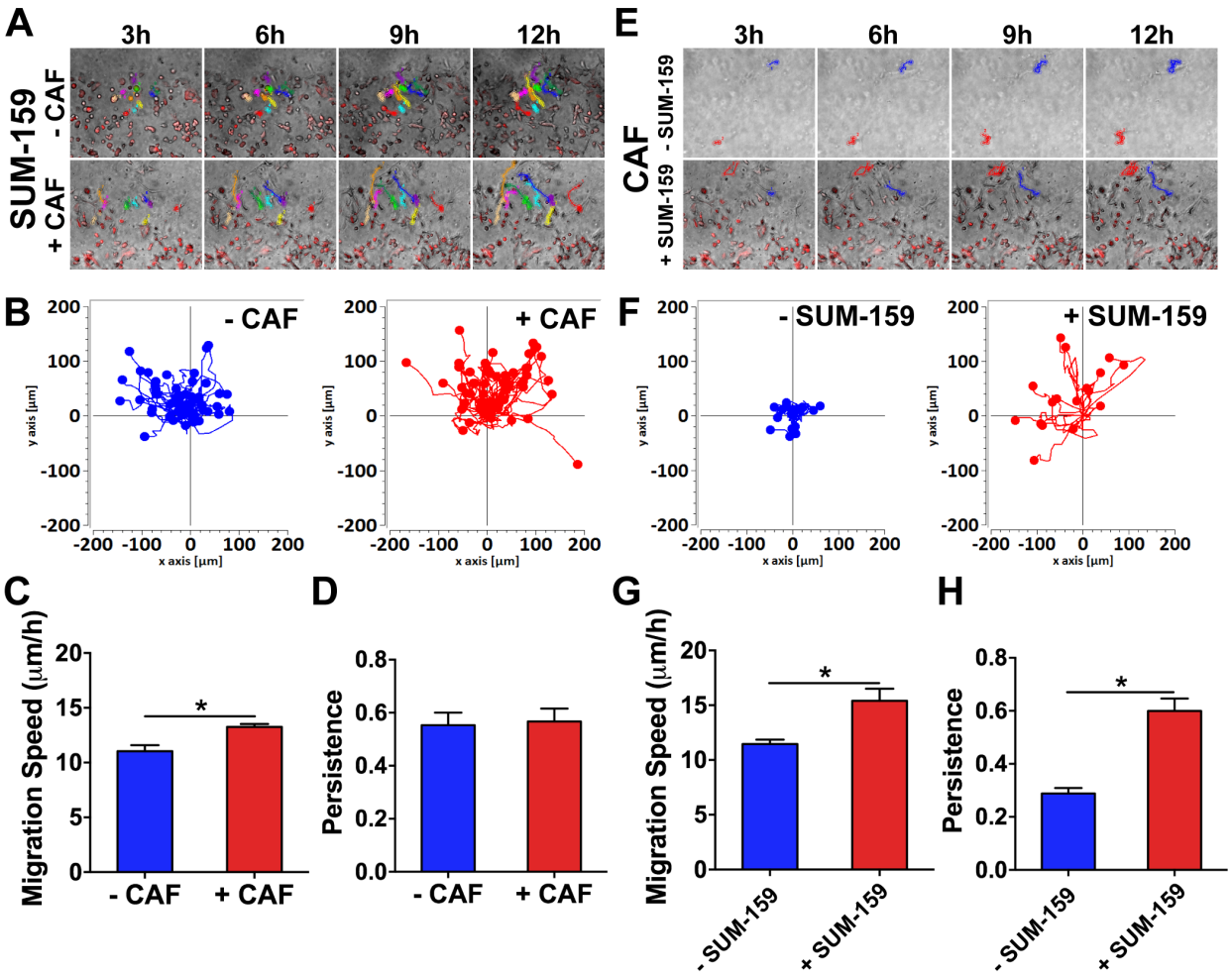

Figure 3.16 Real-time analysis of cell migration.

(A) SUM-159 migration tracked over 12 h in presence of absence of CAFs. (B) Overlay of all migration tracks showed SUM-159 cells migrated further in presence of CAFs. (C, D) CAFs significantly enhanced migration speed of SUM-159 cells but not for persistence. * denotes significant difference for $p < 0.05$. (E) CAF migration tracked over 12 h in presence of absence of SUM-159 cells. (F) Overlay of all migration tracks showed CAFs migrated further in presence of SUM-159 cells. Presence of SUM-159 cells significantly enhanced both (G) migration speed and (H) persistence of CAFs. * denotes significant difference for $p < 0.05$.

To investigate the migration of cancer cells in real-time, at a single cell level, within our co-culture system, we measured the influence of CAFs on SUM-159 migration speed using CAF3. We traced cell migration tracks and quantified the migration speed observing that the presence of CAFs significantly enhanced migration speed of SUM-159 cells (Figure 3.2A-C, Appendix Movie D.8 and D.9). However, there was no statistical difference for persistence of migration (Figure 3.2D). Surprisingly, CAFs, which were largely stationary in the absence of cancer cells (Appendix Figure B.3A), showed enhanced migration behavior when co-cultured with migrating cancer cells (Figure 3.2E and F, Appendix Movie D.10 and D.11). Quantification indeed showed that presence of SUM-159 cells significantly promoted both migration speed and persistence of CAFs (Figure 3.2G and H). Taken together, these analyses demonstrated the presence of a bi-directional crosstalk between cancer and fibroblast cells mutually influencing their migratory behaviors of both SUM-159 cells and CAFs.

3.4.5 Morphometric analysis of SUM-159 cells co-cultured with fibroblasts

As morphology is closely linked to cell migratory behavior, we utilized shape descriptors to analyze the morphology of cancer cells by assessing the cell area, circularity, aspect ratio, and protrusiveness of SUM-159 cells that have migrated into the stroma (Figure 3.3A and B) (Yu, Lim, Xiong, Tan, & Shim, 2013). Only CAF3 but no other fibroblast population significantly increased cell area and decreased circularity of the SUM-159 cells (Figure 3.3C and D). We found significant lowered aspect ratio between + NF vs. + CAF1 and + NF vs. + CAF2 (Figure 3.3E). Protrusiveness was

measured using the inverse of solidity and we found that SUM-159 cells showed significantly higher levels of protrusion in CAF co-cultures than the Ctrl and + NF (Figure 3.3F). To summarize the phenotypic influence (i.e. changes in morphology, proliferation, and migration) of the heterogeneous fibroblast population and SUM-159 cells, we performed a hierarchical clustering on the morphological and behavioral measurements (Figure 3.3G). The analysis showed that CAF co-culture conditions clustered together and that + CAF3 was separated from + CAF1 and + CAF2, agreeing with the data showing that + CAF3 exerted the largest influence in cell migration compared to the other two CAF isolates.

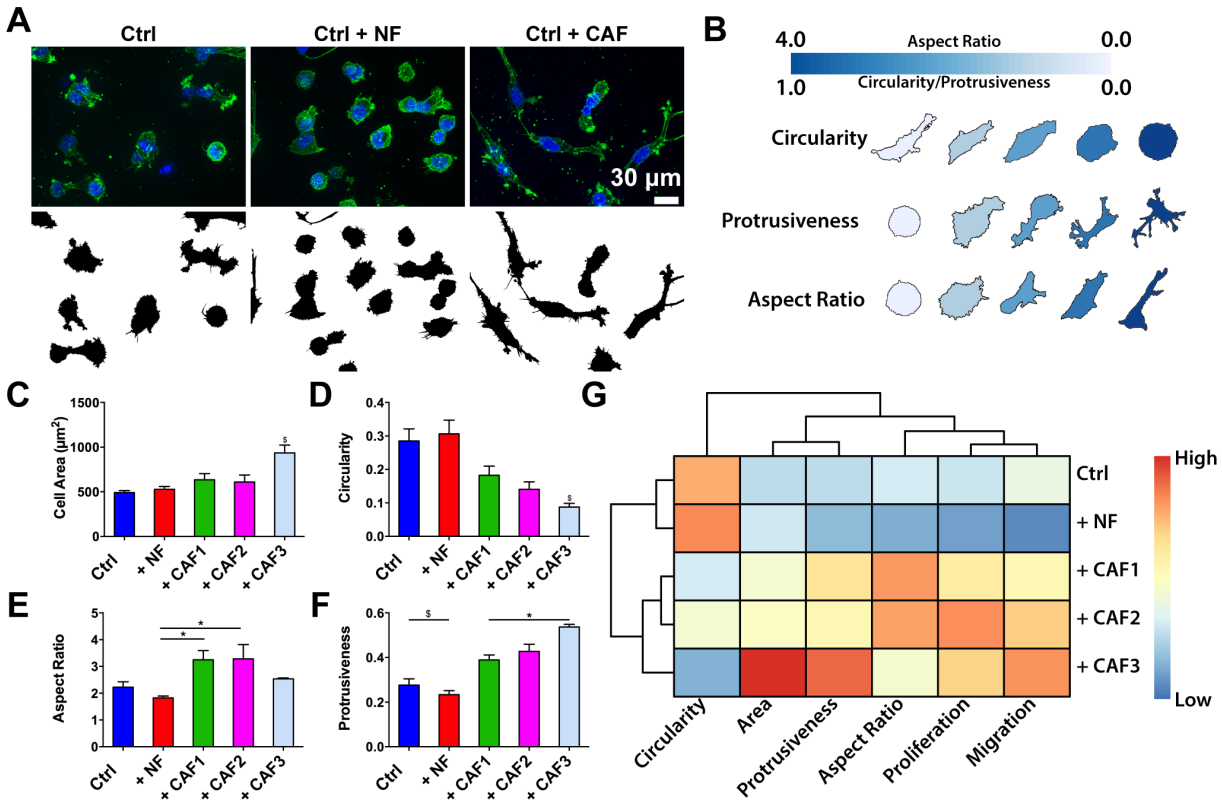

Figure 3.17 Morphometric analysis of SUM-159 cells after co-culture.

(A) Depiction of cancer cell shape during co-culture with fibroblasts. (B) Morphometric key for the analysis circularity, protrusiveness, and aspect ratio. (C-F) Graph comparing different cell shape descriptors. * denotes significant difference for $p < 0.05$. $ denotes significantly different groups for $p < 0.05$. (G) Unsupervised clustering revealed Ctrl and NF co-culture as more similar than the CAF co-cultures.

3.4.6 Gene expression profiles of SUM-159 cells upon tumor-stroma interaction

To couple our functional assessments (i.e. migration, proliferation, morphology) with molecular changes, we performed RNA-seq on sorted populations of SUM-159 cells extracted from the microfluidic device after co-culture with fibroblasts. Multi-dimensional scaling (MDS) analysis on total expression profiles showed that SUM-159 cells in NF and CAF co-cultured conditions separated away from the mono-cultured cells (Ctrl, Figure 3.4A). Furthermore, + CAF1, 2, and 3 clustered together indicating that SUM-159 cells in CAF co-cultures share a similar transcriptional profile distinct from the + NF condition, concordant with our functional assessments (Figure 3.3G). By an ANOVA-like test, we identified 280 differentially expressed genes (DEGs, fold change ≥ 1.5 and FDR < 0.05 in any pairwise comparison) across all conditions. Hierarchical clustering on the expression profiles (Figure 3.4B) resulted in an identical grouping pattern as the MDS analysis (Figure 3.4A). We then compared Ctrl vs. all fibroblast co-culture conditions, and identified 149 DEGs (92 up and 57 down, fold change ≥ 1.5 and FDR < 0.05). These genes represented a common set of transcriptional changes elicited by any fibroblasts, and were associated with Pathways in Cancer, Focal Adhesion, and PI3K-Akt signaling pathway. We next compared the expression profiles of Ctrl vs. NF as

well as Ctrl vs. CAF co-cultures to identify DEGs uniquely regulated by either NFs or CAFs, and found 108 DEGs in the NF co-culture (70 up and 38 down, fold change ≥ 1.5 and FDR < 0.05, Figure 3.4C) and 175 DEGs in CAF co-cultures compared to mono-culture (118 up and 57 down, fold change ≥ 1.5 and FDR < 0.05, Figure 3.4C). KEGG pathway analysis revealed enrichment for cell adhesion, collagen fibril organization, and extracellular matrix organization-related terms for Ctrl vs. CAFs, while inflammatory response, response to liposaccharide, and leukocyte migration-related terms were enriched in Ctrl vs. NFs (Figure 3.4D). Finally, we identified 22 unique DEGs between NF and CAF co-cultures that could potentially play a role in cancer invasion (FDR < 0.05, Appendix Table E.2), including *VAMP1, GPNMB, BGN,* and *CEND1,* which were up-regulated in the CAF co-cultures, and *RGS16, SOCS3, CXCL8, SAA2,* and *IL6*, which were expressed higher in NF co-culture.

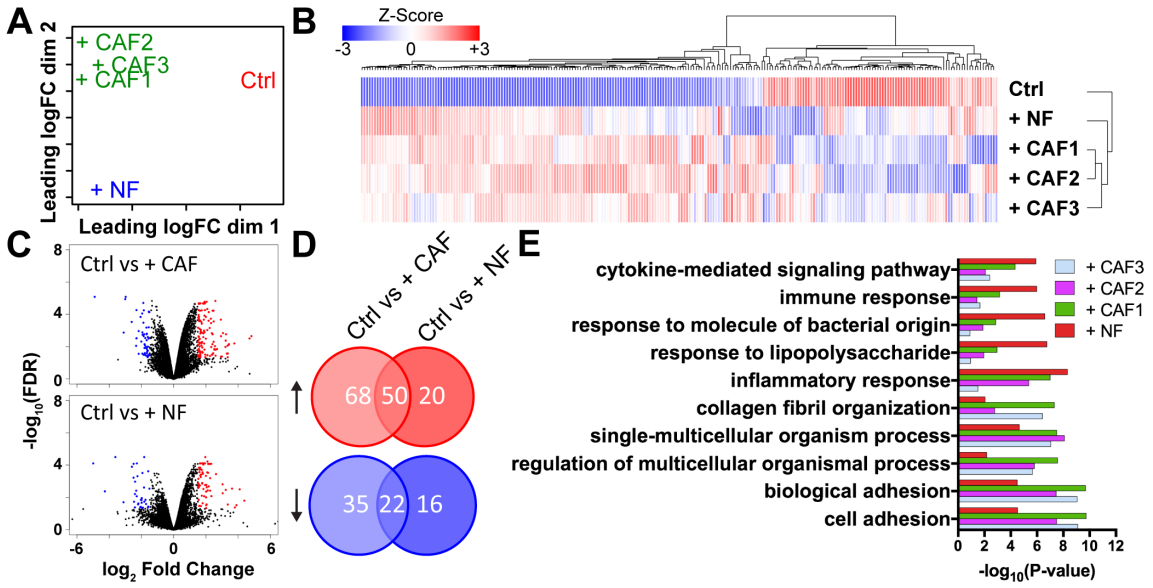

Figure 3.18 Gene expression profiling of SUM-159 breast cancer cells after interacting with fibroblasts.

(A) Multi-dimensional scaling of gene expression profile revealed that cancer cells in CAF co-cultures shared a similar transcriptional profile distinct from the + NF condition (B) Heatmap of 280 differentially expressed genes (DEGs, fold change ≥ 1.5 and FDR < 0.05 in any pairwise comparison) across all conditions. (C and D) Volcano plots and Venn diagrams show Ctrl vs + CAF (118 up and 57 down, fold change ≥ 1.5 and FDR < 0.05) and Ctrl vs + NF (70 up and 38 down, fold change ≥ 1.5 and FDR < 0.05). (E) Top 5 GO terms from Ctrl vs CAF or NF co-cultures.

3.4.7 Clinical relevance of glycoprotein non-metastatic B in cancer

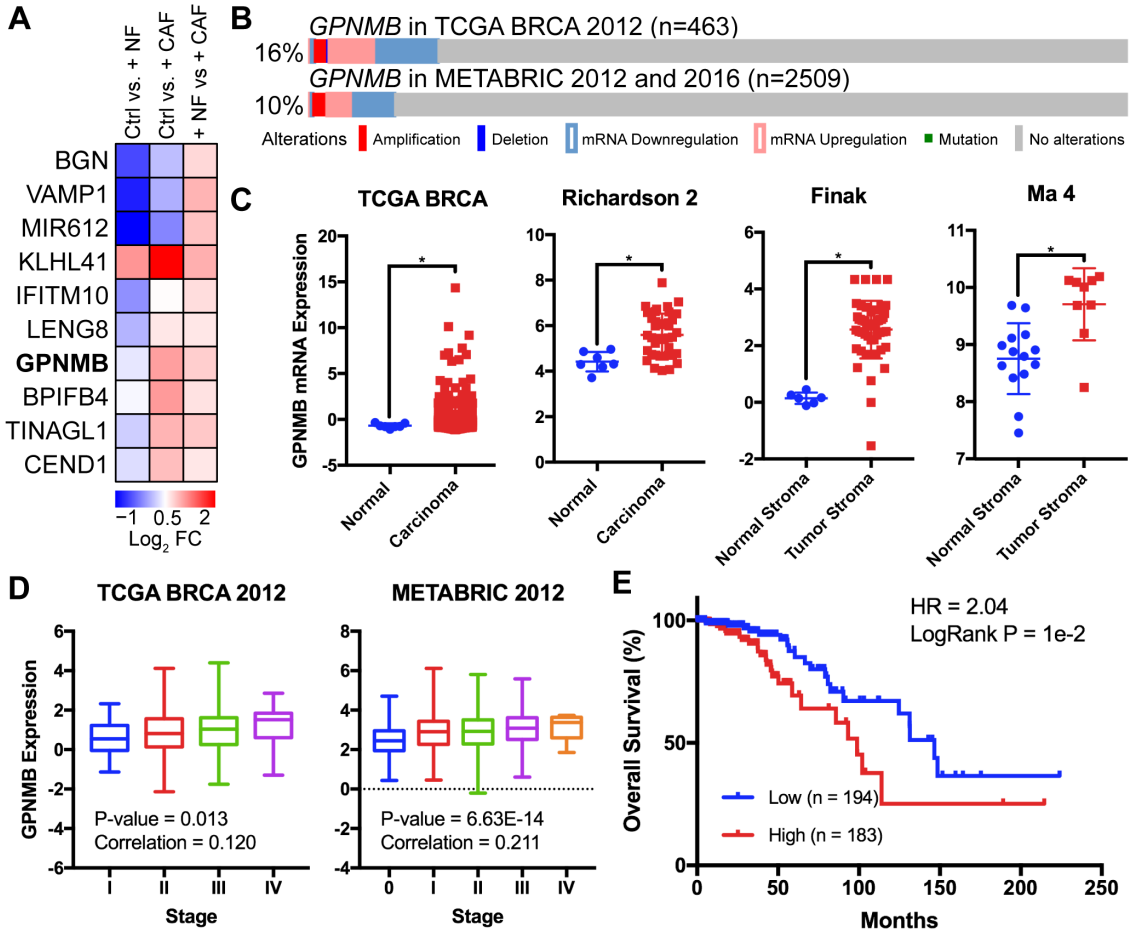

Figure 3.19 Clinical relevance for GPNMB.

(A) Heat map of top 10 DEGs when comparing NF and CAF co-cultures. (B) Incidence of *GPNMB* alterations in two different cohorts from public datasets(Cancer Genome Atlas, 2012; Cerami et al., 2012; Curtis et al., 2012; Gao et al., 2013; Pereira et al., 2016). (C) *GPNMB* expression from TCGA-BRCA in breast cancer compared to normal. * denotes significant difference for $p < 0.05$; unpaired t-test(Finak et al., 2008; X. J. Ma et al., 2009; Richardson et al., 2006; Zhou et al., 2012). (D) *GPNMB* expression positively correlated with tumor stage (Cancer Genome Atlas, 2012; Curtis et al., 2012). (E) Kaplan–Meier analysis of overall survival from TCGA-BRCA data sets. HR, 2.04; P = 1e-2. High expression of *GPNMB* was correlated to poorer patient prognosis using TCGA data (Cancer Genome Atlas, 2012).

As we found striking differences in CAF co-cultures compared to Ctrl (mono-culture of SUM-159 cells), we asked which of the up-regulated genes could play a role for the enhanced migration in SUM-159 cells in co-culture with CAFs (Figure 3.5A, **Table S8**). We investigated *GPNMB* as one of the possible mediator of promoting invasion. *GPNMB* encodes for a cell surface transmembrane glycoprotein that is highly expressed among many cancers, including breast cancer. It has also been implicated in tumor invasion, angiogenesis, cell adhesion, and immune suppression(April AN Rose et al., 2010). To determine whether *GPNMB* may play a tumor-promoting role in breast cancer, we evaluated two large publically available datasets (METABRIC and TCGA) for mutations, copy-number variations and changes in expression(Cancer Genome Atlas, 2012; Cerami et al., 2012; Gao et al., 2013; Pereira et al., 2016). We found that alterations occurred in 10 and 16% of breast cancer patients, respectively, in two data sets

(Figure 3.5B). mRNA overexpression in breast carcinoma was significantly increased in TCGA and other data sets, when compared to the normal tissue controls (Figure 3.5C). Additionally, the TNBC-related subtypes (i.e. basal-like and claudin-low) expressed higher levels of *GPNMB* than other subtypes (Appendix Figure B.6A**)**. Next, expression of *GPNMB* also positively correlated with tumor stage (Figure 3.5D). To determine the impact of *GPNMB* overexpression, we next investigated the effect on patient survival. Analysis of the public breast cancer data sets from TCGA-BRCA and web-based GeneAnalytics revealed that high expression of *GPNMB* correlated with poorer metastasis-free and overall survival (Figure 3.5E and Appendix Figure B.6B and C). Taken together, these data provided important evidence for the potential clinical relevance of *GPNMB* in breast cancer.

3.4.8 Role of GPNMB in tumor-stroma interaction and SUM-159 cancer cell migration

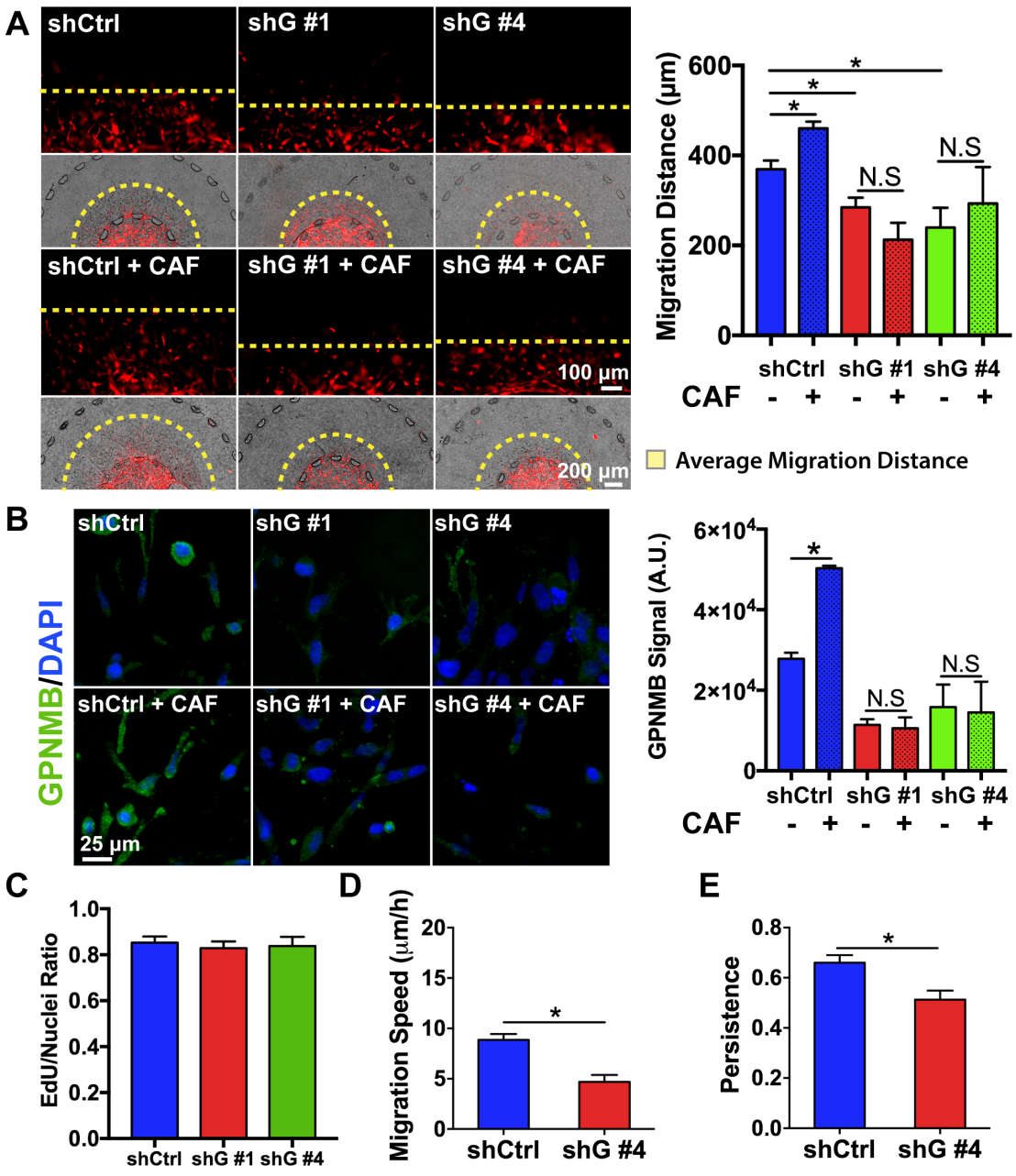

Figure 3.20 Functional study of GPNMB in tumor-stroma interactions.

(A) Migration distance was lowered in GPNMB knockdown lines compared to the control. CAF co-culture increased migration of control knockdown, but did not increase migration of GPNMB knockdowns. * denotes significant difference for $p < 0.05$. (B) CAF co-culture increased IF expression of GPNMB in shCtrl cells, but did not increase

IF expression of GPNMB in shG knockdown lines. * denotes significant difference for $p < 0.05$. (C) No difference was found in proliferation using EdU assay. (D, E) GPNMB knockdown significantly reduced migration speed and persistence of SUM-159 cells. * denotes significant difference for $p < 0.05$.

We first validated for expression of GPNMB in our cell lines. Western blotting demonstrated that GPNMB was indeed expressed highly in SUM-159 and MDA-MB-231 cells and lowly in MCF7 and MCF10A cells corroborating prior studies (Appendix Figure B.7A) (Smuczek et al., 2017). Next, to study the role of GPNMB in the context of tumor microenvironment, we assessed the expression of GPNMB in SUM-159 cells in mono- or co-culture with CAFs (CAF3). IF imaging revealed punctate expression throughout the cell body of SUM-159 cells while quantification of the IF signal demonstrated a significant increase GPNMB expression in SUM-159 cells of the CAF co-culture agreeing with the RNA-seq data (Appendix Figure B.7B**)**. Next, we knocked down GPNMB using two independent short hairpin RNAs (shRNA) on SUM-159 breast cancer cells and characterized the resulting invasive phenotype of GPNMB knockdown lines (shG). Successful knockdown was confirmed by a western blot (Appendix Figure B.8A) and IF images of 2D culture demonstrated qualitatively less punctuates compared to shG cells (Appendix Figure B.8B). Proliferation of shG lines were significantly attenuated as compared to the shControl (shCtrl) line in 2D cultures (Appendix Figure B.8C). We also observed reduced cell spreading area and higher circularity on a 2D substrate, which was correlated to reduced invasive capacity (Appendix Figure B.8D and E), but no difference among the knockdown lines was found in adhesion to collagen

substrate (Appendix Figure B.8F). Then, we asked whether GPNMB is crucial for breast cancer cell migration in a 3D hydrogel-based stroma using our microfluidic model. It was observed that GPNMB knockdown significantly decreased 3D migration of SUM-159 breast cancer cells (Figure 3.6A). When we co-cultured with CAFs (CAF3), we found a significant increase in migration into the stroma for only the shCtrl line but not for the shG knockdown lines (Figure 3.6A). Next, we examined expression change of the GPNMB protein in SUM-159 cells by IF when in presence of CAFs and found an increase in expression for the shCtrl line but found no significant difference for the shG lines (Figure 3.6B). Then we asked if the slower migration of shG cells was due to either reduced cell proliferation, cell migration speed, or both. EdU assay was used to measure cell proliferation, and we found no significant difference between the shCtrl and shG lines (Figure 3.6C). On the other hand, time-lapse imaging of cell migration in 3D revealed that GPNMB knockdown significantly attenuated migration speed by nearly half and migration persistence to a lesser extent when compared to the control knockdown (Figure 3.6D and E, Appendix Movie D.12 and D.13). This suggested that the decreased migration distance into the 3D stroma for the GPNMB knockdown lines was likely due to attenuated cell migration speed. Taken together, these data demonstrated that GPNMB plays a key role in enhancing cancer invasion in 3D by affecting cell migration speed and that co-cultured CAFs induced GPNMB expression in cancer cells.

Despite the significance of tumor-stroma interactions in early steps of cancer metastasis, not many models have studied and paired the functional assessments to molecular changes in cancer cell invasion in a suitable and relevant tumor microenvironment (Kalluri, 2016; B. Weigelt, 2014). In this work, we aimed to take a

significant step forward by developing an innovative organotypic tumor microenvironment model with configurable tumor and stroma regions coupled with integrated molecular and cellular studies on the influences of patient-derived fibroblasts on breast cancer invasion. The 3D microfluidic co-culture system contained side-by-side tumor and stroma regions to resemble the architecture of the early tumor microenvironment. This spatial organization enabled bi-directional crosstalk between the cancer cells and stromal cells, while still allowing imaging-based quantifications such as migration and proliferation. Most importantly, our model also addressed the limitations of previous systems, which only used functional assessments (i.e. cell migration and proliferation), by incorporating RNA-seq to profile the transcriptome of the cancer cells in co-culture with patient-derived fibroblasts to better dissect the molecular mechanisms and provide insights in tumor-stroma crosstalk during invasion.

3.5 Discussion

We demonstrated that interaction between invasive breast cancer and mammary fibroblasts led to distinct consequences on cancer cell migration behavior depending on the fibroblast phenotype. NFs with lower expression of αSMA showed a tumor suppressive behavior compared to CAFs with higher levels of αSMA. Despite that patient-derived CAFs showed no difference in αSMA expression among themselves in 2D, only CAF1 and CAF3 significantly promoted migration and proliferation and CAF2 to a lesser extent suggesting further CAF heterogeneity beyond αSMA levels (Kalluri, 2016). Owing to the complexity in fibroblast heterogeneity, previous studies have proposed that fibroblasts could be subdivided into categories based on their functional

heterogeneity, like tumor-straining or tumor-promoting (Kalluri, 2016; Ohlund et al., 2014). The NFs that we examined showed tumor-restraining properties which indeed corroborated with prior studies (Sadlonova et al., 2007). On the other hand, we demonstrated that two of three patient-derived CAFs, including CAFs from a TNBC patient, exhibited tumor-promoting behavior. Therefore, we envision that the changes in SUM-159 behavior when in co-culture with fibroblasts were due to the differences in fibroblast phenotype and their microenvironmental origin.

One interesting consequence of tumor-stroma interactions that was revealed through our model was the possibility of a bi-directional crosstalk between SUM-159 cells and fibroblasts influencing migration of both cell types. Specifically, real-time analysis of CAF migration demonstrated increased cell motility and persistence in presence of SUM-159. In reverse, SUM-159 cells also expressed enhanced migration speed in presence of CAFs. Previous studies have used cancer-conditioned media by adding to fibroblasts also showed enhanced elongation and migration of these cells in scratch assays (Henriksson et al., 2011; Karagiannis et al., 2014). Building upon these studies, our work incorporated both cancer cells and fibroblasts in a 3D matrix to reveal this reciprocal effect on cell motility instead of utilizing conditioned media to simulate cell-cell signaling.

Many studies have indicated that the shape of the cell carries information determining the cell behavior, such as invasiveness(Yu et al., 2013). Here we showed that SUM-159 cells alone or when in co-culture with NFs demonstrated higher circularity as well as lower protrusiveness, area, and aspect ratio compared to when co-cultured with CAF populations. We connected the shape changes of the cancer cells to invasive

behavior by demonstrating that the increase in migration and proliferation of SUM-159 cells correlated with increases in aspect ratio and protrusiveness. These results build upon the growing body of literature that have previously reported the relationship between protrusive activity and invasion (Mouneimne et al., 2012). Taken together, this suggested that the CAF isolates within our system promoted invasive morphology and migratory behavior of breast cancer cells (Kalluri, 2016; Yu et al., 2013).

To screen for molecular influences on cancer migration due to the stromal fibroblasts (i.e. both CAFs and NFs), we profiled the transcriptome of the cancer cells and performed bioinformatics analyses. Within the NF co-culture, we found higher expression of genes related to inflammatory responses, such as *CXCL8*, *ILR2,* and *IL6*. A recent paper by Camp *et al.* co-cultured basal-like cancer cells (i.e. SUM-159) with immortalized fibroblasts obtained from reduction mammoplasty similar to NFs in our study (Camp et al., 2011). Consistently, they showed up-regulated immune responses, such as *IL6, CXCL8, STAT1, CXCL1,* and *ILR2*, corroborating our results. In addition, we found over-expression of Regulator of G protein signaling 16 (*RGS16)* within NF co-culture. *RGS16* is a possible tumor suppressor gene down-regulating cancer migration and proliferation (Carper et al., 2013). On the other hand, CAF co-culture over-expressed genes related to cell adhesion, like *BGN, GPNMB,* and *IFITM10*. The gene *BGN* encodes for biglycan, a small leucine-rich repeat proteoglycan found within the ECM, which has been demonstrated to be up-regulated within the breast tumor stroma (Casey et al., 2009). *GPNMB* has been associated with poor prognosis within basal/triple-negative subtype of breast cancers (April AN Rose et al., 2010). Prior research has implicated *GPNMB* in tumor invasion, angiogenesis, cell adhesion, and immune suppression for melanoma,

breast, prostate, pancreatic, and lung cancers (Fiorentini et al., 2014; Oyewumi et al., 2016; A. A. Rose et al., 2007). Therefore, of the genes we screened for, we chose *GPNMB* as a possible mediator of cancer invasion in our model. Previous studies have mainly utilized transwell and colony forming assays to assess the influence of GPNMB in tumor invasion (A. A. Rose et al., 2007). We intended to clarify the role of GPNMB in 3D cancer migration and tumor fibroblast interactions. Using our 3D model, we confirmed that GPNMB knockdown reduced breast cancer cell invasion within a 3D hydrogel-based stroma, suggesting its requirement for efficient migration in a 3D microenvironment. We showed through time-lapse imaging that the decrease in migration distance was due to attenuated cell migration speed in the 3D matrix. Our work is the first time that it was shown that GPNMB contributed to breast cancer cell migration speed in 3D culture. In prior works, GPNMB has been demonstrated to engage integrins and MMPs which are crucial for 3D migration (Even-Ram & Yamada, 2005; Fiorentini et al., 2014; Maric et al., 2015; A. A. Rose et al., 2007). We did indeed observe similar association between GPNMB and integrins and MMPs in our RNA-seq data (**Table S9**). GPNMB interaction with integrin was also shown to activate SRC and FAK signaling, which regulate cell migration (Maric et al., 2015; Smuczek et al., 2017). Our results taken together with the current findings suggested that GPNMB plays a crucial role in cancer invasion in 3D microenvironment.

The influences of GPNMB on invasion has mainly been studied using a neoplastic-cell centric approach. To identify the involvement of the tumor microenvironment, we specifically asked whether CAFs promoted invasion of cancer cells through a GPNMB-dependent manner. Using the CAF co-culture model, we showed

through IF that patient-derived CAFs residing in the biomimetic stroma enhanced protein expression of GPNMB on breast cancer cells validating the RNA-seq data. Furthermore, knockdown of GPNMB of SUM-159 cells in the co-culture model blunted the effect of CAFs on promoting invasion. To the best of our knowledge, tumor-stroma interaction through GPNMB has not been explored before. In a similar study to ours, Le bras *et al*. established a 3D organotypic co-culture model using a collagen matrix, human esophageal epithelial cells, and human skin fibroblasts and demonstrated enhanced tumor proliferation and growth (Le Bras et al., 2015). Concordant with our work, gene expression analysis revealed more than a 1.5 fold-increase in GPNMB compared to non-invasive cultures. However, studying the role of GPNMB was not the focus of that study. To that end, our work adds to the growing body of literature implicating GPNMB in promoting tumor invasion and progression, while supporting that GPNMB expression is enhanced through tumor-stroma interactions between breast cancer and CAFs (Even-Ram & Yamada, 2005; Fiorentini et al., 2014; Maric et al., 2015; A. A. Rose et al., 2007). There are some potential mechanisms by which CAFs could induce GPNMB expression in cancer cells. Smuczek *et al*. showed that C16, a laminin-111 subunit, could enhance GPNMB expression and promote MDA-MB-231 cell migration (Smuczek et al., 2017). It was suggested that C16 was produced through cell-induced proteolysis of the ECM through MMP9 and MMP9 has been shown to be secreted by CAFs (Siqueira et al., 2016; Stuelten et al., 2005). In a separate study, GPNMB was upregulated in hepatocellular carcinoma by colony-stimulating factor 1, which is a known factor secreted from fibroblasts (Teng et al., 2016; Tian et al., 2013). Taking these prior findings with our results indicate that either directly through paracrine signaling or

indirectly by enzymatic release of bound peptides from ECM, GPNMB could be induced through tumor-stroma interactions.

3.6 Conclusions

In conclusion, we engineered a 3D organotypic microfluidic co-culture system to represent the breast tumor microenvironment by juxtaposing 3D tumor and stroma regions in order to study the molecular and cellular influence of patient-derived fibroblasts on breast cancer invasion. We found clear evidence that interactions between invasive SUM-159 breast cancer cells and mammary fibroblasts displayed distinct consequences on cancer migratory behavior depending on the fibroblast phenotype. Particularly, NFs expressed a tumor-suppressive behavior shown by reduction in migration, proliferation, and cell aspect ratio. On the other hand, two of the three CAFs studied demonstrated tumor-promoting behavior while the other to a lesser extent. Through transcriptome profiling of the SUM-159 cells, we found that NF co-cultures were enriched for inflammatory pathways while CAF co-cultures were enriched cell adhesion and ECM. This led to the observation that CAFs enhanced breast cancer invasion within a 3D microenvironment by inducing the expression of a novel gene of interest, GPNMB, in breast cancer cells resulting in increased invasion speed. Importantly, knockdown of GPNMB led to blunting the effect of CAFs on promoting cancer invasion. Overall, we propose that this organotypic microfluidic model has potential to tease out and understand key molecular pathways in tumor-stroma interactions for discovering druggable targets for inhibiting cancer invasion. In future studies, we intend to correlate the changes in gene expression to the molecular

differences in fibroblasts to predict how distinct patient-specific tumor microenvironments could influence cancer progression.

CHAPTER 4

AIM 3: Use a microfluidic platform of the GSC vascular niche to study the influence of endothelial cells (ECs) on patient-derived GSC behavior and identify signaling cues that mediate their invasion and phenotype.

4.1 Abstract

Glioblastoma (GBM) is one of the deadliest forms of cancer. Despite many treatment options, prognosis of GBM remains dismal with a 5-year survival rate of 4.7%. Even then, tumors often recur after treatment. Tumor recurrence is hypothesized to be driven by glioma stem cell (GSC) populations which are highly tumorigenic, invasive, and resistant to several forms of therapy. GSCs are often concentrated around the tumor vasculature, referred to as the vascular niche, which are known to provide microenvironmental cues to maintain GSC stemness, promote invasion, and resistance to therapies. In this work, we developed a 3D organotypic microfluidic platform, integrated with hydrogel-based biomaterials, to mimic the GSC vascular niche and study the influence of endothelial cells (ECs) on patient-derived GSC behavior and identify signaling cues that mediate their invasion and phenotype. The established microvascular network enhanced GSC migration within a 3D hydrogel, promoted invasive morphology as well as maintained GSC proliferation rates and phenotype (Nestin, SOX2, CD44). Notably, we compared migration behavior to *in vivo* mice model and found similar invasive morphology suggesting that our microfluidic system could represent a physiologically relevant *in vivo* microenvironment. Moreover, we confirmed that CXCL12-CXCR4 signaling is involved in promoting GSC invasion in a 3D vascular microenvironment by utilizing a CXCR4 antagonist (AMD3100), while also

demonstrating the effectiveness of the microfluidic as a drug screening assay. Our model presents a potential *ex vivo* platform for studying the interplay of GSCs with its surrounding microenvironment as well as development of future therapeutic strategies tailored toward disrupting key molecular pathways involved in GSC regulatory mechanisms.

4.2 Introduction

Glioblastoma (GBM) is one of the most common and deadliest forms of brain cancer in adults. Despite aggressive treatment, including surgery, radiation and chemotherapy, prognosis for GBM patients remains dismal with a 5-year survival rate of 4.7% (Omuro & DeAngelis, 2013). These tumors almost always recur within a few months after treatment. Tumor recurrence is hypothesized to be driven in part by glioma stem cell (GSC) populations within the primary brain tumor (S. Bao et al., 2006; Lathia et al., 2011). GSCs have similar properties to neural stem cells − they can self-renew and differentiate into several neuro-glial lineages leading to intratumoral heterogeneity (Lathia, Mack, Mulkearns-Hubert, Valentim, & Rich, 2015). Importantly, GSCs are also highly tumorigenic, invasive, and resistant to several forms of therapy (Sundar, Hsieh, Manjila, Lathia, & Sloan, 2014). As such, GSCs evade conventional therapies that target bulk populations of cancer cells allowing these cells to survive and regenerate the tumor (Venere, Fine, Dirks, & Rich, 2011).

GSCs are often concentrated near specific niches around pre-existing blood vessels, referred to as the perivascular niche and around necrotic areas known as the peri-necrotic or hypoxic niches (Calabrese et al., 2007; Li et al., 2009; Sharma & Shiras,

2016). These specialized niches shelter, maintain, and regulate GSC stem phenotypes, invasion, and therapeutic resistance (Hambardzumyan & Bergers, 2015). Previous studies have shown that cell-cell interactions within the perivascular niches, which involve soluble factors released by endothelial cells (ECs) of the nearby blood vessels, lead to self-renewal of GSCs and propagation of the brain tumor *in vivo* (Calabrese et al., 2007). Different signaling pathways have been implicated in GSC-EC interactions, such as Notch, TGFβ, nitric oxide, and sonic hedgehog (SHH) (Sharma & Shiras, 2016). Targeting some of these signaling pathways have resulted in reduced tumor growth (Charles et al., 2010; Zhu et al., 2011). Therefore, disruption of vascular niches could serve as a potential therapeutic strategy for GBM. In that regard, it is important to identify specific signaling pathways within the niches that support GSC self-renewal and propagation.

The CXCL12-CXCR4 signaling axis regulates cell migration and proliferation during normal development in several tissues including the brain (Wurth, Bajetto, Harrison, Barbieri, & Florio, 2014). However, high levels of the chemokine receptor CXCR4 is overexpressed in gliomas and its expression level is correlated with tumor grade and poor prognosis (Bian et al., 2007). Expression of CXCL12 was also found to be highly expressed in the endothelium surrounding GBM whereas normal brain tissue lacked CXCL12 expression (Rao et al., 2012). As such, CXCL12-CXCR4 signaling axis has been described to play a central role in tumorigenesis of GBM along with several other human cancers, such as breast, colon, pancreatic, ovarian, and prostate (Ehtesham, Mapara, Stevenson, & Thompson, 2009; Orimo et al., 2005; Scotton et al., 2002; Taichman et al., 2002; Z. Wang et al., 2008; Zeelenberg, Ruuls-Van Stalle, & Roos,

2003). Importantly, inhibition of the CXCL12-CXCR4 signaling using AMD3100 has resulted with some success in tumor regression *in vivo* (Redjal, Chan, Segal, & Kung, 2006). However, it is still unclear if GSC-EC interaction enhances GSC migration within the vascular niche and if this effect is mediated by CXCL12-CXCR4 interaction.

To better understand the role of the vascular niche and cell-cell signaling, such as CXCL12-CXCR4, that govern GBM tumorigenesis, an appropriate model with well-controlled architecture is needed to recapitulate the components of the *in vivo* tumor microenvironment. Conventional *in vitro* platforms, such as transwell assays and spheroid models, have been widely utilized to perform biological studies and drug screening (Britta Weigelt et al., 2014). However, transwell systems are end-point assays that do not allow real-time observations of dynamic cellular interactions (S. A. Kim, Lee, & Kuh, 2015; Yang et al., 2015). In addition, these conventional assays often require a large population of cells, which may be problematic for patient-derived cells. Most importantly, these models do not fully recapitulate the complex *in vivo* tumor microenvironment leading to non-physiologically relevant cell behavior (Hutmacher et al., 2010). Therefore, there have been significant innovations in the use of microscale tissue-engineered technologies to develop complex 3D tumor models across different types of cancer, with precise control over cell-cell, cell-matrix and cell-soluble factor interaction (Chonan, Taki, Sampetrean, Saya, & Sudo, 2017; Jeon et al., 2015; Ngo & Harley, 2017; N. Peela, Barrientos, et al., 2017; N. Peela et al., 2016; N Peela, Truong, Barrientos, Mouneimne, & Nikkhah, 2016; N. Peela, Truong, et al., 2017; D. Truong et al., 2016; Britta Weigelt et al., 2014). While these 3D models have had great success in interrogating tumor responses to the microenvironment, few have studied GBM and even

less in the context of the vascular niches (i.e. tumor-vascular interactions) within a 3D platform (Ayuso et al., 2016; S. Kim, Lee, Chung, & Jeon, 2013). While these 3D models have had great success in interrogating tumor responses to the microenvironment, few have studied GBM and even less in the context of the vascular niches (i.e. tumor-vascular interactions) within a 3D platform (Ayuso et al., 2016; S. Kim et al., 2013). For instance, a 3D *in vitro* model of the perivascular niche was developed by Infanger et al. to study GSC behavior using 3D hydrogels. However, in this model, GSCs and ECs were not co-cultured together simultaneously and EC-conditioned medium was used to simulate paracrine signaling (Infanger et al., 2013). On the other hand, a 3D microfluidic device was used to study glioma invasion influenced by ECs. The GSCs and ECs were seeded as 2D monolayers separated by a 3D collagen layer in between, which did not truly represent the 3D GBM microenvironment (Chonan et al., 2017). With recent attempts in modeling vasculature in 3D, there have also been notable advances in developing vascular networks with increasing physiological relevance within 3D hydrogels (Jeon et al., 2015; S. Kim et al., 2013; H. Lee, Park, Ryu, & Jeon, 2014; Nagaraju et al., 2018). However, much of the focus have not been on GBM or patient-derived GSCs. Additionally, those studying GBM were specifically investigating the influence of GBM on tumor-associated angiogenesis, such as the work from Cui et al, which highlighted the importance of macrophage-associated immunosuppression during GBM angiogenesis, and not the changes in GSC invasion and stem phenotype within the context of a vascular niche, which is the focus of our study (Cui et al., 2018; H. Lee, Park, et al., 2014).

We previously developed microfluidic technologies comprising of 3D hydrogel-based layers for multi-culturing of tumor and stromal cells side-by-side to mimic the

architecture of the native tumor microenvironment (N. Peela, Barrientos, et al., 2017; D. Truong et al., 2016). We have investigated breast cancer cell invasion in response to signaling cues and stromal cells, such as cancer-associated fibroblasts and ECs (N. Peela, Barrientos, et al., 2017; D. Truong et al., 2016). In this study, we describe the design, biological validation, and use of our microfluidic platform as a new *in vitro 3D* organotypic model for GSC invasion in the context of a vascular niche (Figure 4.1A). We formed a spontaneously assembled 3D vasculature within our platform, and then incorporated patient-derived GSCs within the core of the tumor region. The novelties of our model enabled the interaction of patient-derived GSCs and a 3D microvascular network which has not been described in previous studies. We specifically investigated the effect of GSC-EC interactions within our microfluidic on GSC proliferation, invasion, and stem phenotype. Importantly, in parallel to our *in vitro* experiments, we utilized a patient-derived xenograft (PDX) *in vivo* model to evaluate the physiological relevance of our microfluidic platform. Indeed, we observed similar GSC invasive behaviors between the two systems in terms of GSC migration, morphology, and proximity to the vasculature. Lastly, to determine the influence of CXCL12-CXCR4 signaling on EC-mediated GSC invasion, we tested the effect of AMD3100, a CXCR4 antagonist, within our *in vitro* microfluidic model. As such, our study presents a physiological relevant 3D organotypic model of GSC invasion for investigating the interaction between GSC and the surrounding microenvironment.

4.3 Materials and Methods

4.3.1 Microfluidic device fabrication

The microfluidic platform was designed using CAD software, and transferred onto a transparent mask. The design consisted of three concentric semicircles comprising of tri-layer tumor, stroma, and vasculature regions with diameters of 1, 2, and 3 mm with heights of 200 μm. The intraregional distance between the concentric semicircles was 1 mm. Trapezoidal microposts were spaced evenly at 100 μm bound each region. The microposts were configured to separate the regions, while also enabling interactions between the regions by allowing exchange of media, biomolecules, and cells throughout the platform. To create a master mold of the devices, SU8-2075 (MicroChem) was spun to height of 200 μm onto a silicon wafer after which, the wafer was exposed to UV through the mask placed on the wafer forming the primary mold. The surfaces of the silicon wafer were made hydrophilic by treatment with methyltrichlorosilane (MTCS, Sigma-Aldrich). Next, polydimethylsiloxane (PDMS, Sylgard 184 Silicon Elastomer Kit, Dow Corning) was poured over the wafer and cured for 1.5–2 h at 80 °C. The PDMS cast was then peeled from the micro-patterned mold. Individual devices were then cut from the cast using a razor, and inlet and outlet holes were hollowed out using biopsy punch. PDMS device casts were then bonded to 18 mm^2 glass slides to form the channels of the microfluidic. Before bonding, devices and glass slides were cleaned with ethanol and pressurized nitrogen gas and subjected to oxygen plasma (PDC-32G, Harrick Plasma) to produce hydrophilic surfaces on both the devices and the glass. PDMS device casts were then joined to glass slides with the channel side facing down and placed in oven at 80 °C overnight to secure bonding. Next, device sterilization was performed by one treatment in the liquid autoclave and a subsequent treatment by dry autoclave. Finally, devices were placed in the oven at 80 °C overnight to dry completely.

To enhance attachment of the hydrogels (i.e. Matrigel and Fibrin) to the 3D cell culture regions, poly-d-lysine (1 mg mL^{-1}) (PDL, Sigma-Aldrich) was injected into the cell culture region and incubated at 37 °C for 1 h, then washed with deionized (DI) water. Glutaraldehyde (1% (v/v)) (GA, Sigma-Aldrich) was then added to the culture region and incubated for 1.5–2 h at room temperature, then washed 4–5 times with DI water to remove excess GA. The devices were then placed in the oven at 80 °C overnight to restore the hydrophobicity of the channels. Hydrophobicity enabled microposts to contain a hydrogel within the culture regions before it can polymerize and attach to the inner surface (C. P. Huang et al., 2009).

4.3.2 Cell culture

Patient samples used for this research were provided by the Biobank Core Facility at St. Joseph's Hospital and Medical Center and Barrow Neurological Institute (BNI), Phoenix, Arizona. The samples were de-identified and conformed to the Biobank Institutional Review Board (IRB) protocol. Patient-derived cell line GB3 was established from resected primary GBM tumor tissue at BNI. Briefly, tumor tissue was processed using the Gentle MACS Dissociator and Tumor Tissue Dissociation kit (Miltenyi Biotec Inc.). Cells were expanded as neurospheres in tissue culture dishes coated with poly-(2-hydroxyethyl methacrylate) (Sigma-Aldrich) or grown adherent on laminin (Fisher Science), in neural stem cell (NSC) medium consisting of DMEM and F12-Glutamax supplemented with B27 and N2 (Fisher Science), in the presence of 20 ng ml^{-1} EGF and 20 ng ml^{-1} FGF2 (EMD Millipore). To generate GB3-RFP cell line, GB3 cells were transduced with pre-made lentiviral particles (Amsbio) expressing RFP-Luc (GB3-RFP)

and were selected using blasticidin (2 μg ml^{-1}). Human umbilical vein endothelial cells (HUVECs) were obtained from Lonza and cultured in EGM-2 (Endothelial Growth Medium, Lonza) and passaged at 70-80%.

4.3.3 Vasculogenesis in the microfluidic device

To model vasculogenesis within our microfluidic platform, HUVECs were dislodged from culture flasks using trypsin-EDTA and centrifuged. Next, 5 mg mL^{-1} bovine fibrinogen (Sigma-Aldrich) dissolved in Dulbecco's phosphate buffered saline (DPBS, Gibco) was used to make the fibrinogen solution. Bovine thrombin (Sigma-Aldrich) was dissolved in DPBS to create 4 U ml^{-1} thrombin solution. Fibrinogen and thrombin solutions were then filter sterilized (Denville scientific). HUVECs were added to the fibrin solution (5 mg ml^{-1} fibrinogen plus 4U ml^{-1} thrombin) to form a hydrogel with the final cell density of 20 million cells ml^{-1}. The mixture was then immediately injected into the vascular region (third layer, Figure 4.1B) of the device and the devices were incubated at room temperature for 10 min to promote fibrin polymerization. After hydrogel polymerization, EGM-2 (endothelial growth medium supplemented with additional 50 ng ml^{-1} VEGF) was added to each device and the platforms were kept in the incubator (humidified, 37 °C, 5% CO2). Cell culture medium was exchanged every 24 h throughout vasculogenesis (3 d).

4.3.4 Co-culture invasion assay

To study GSC-EC interactions, GB3-RFP cells, referred to as GB3 hereafter, were added to the devices after vasculogenesis. GB3 cells were dissociated, centrifuged, and

then the cells were directly suspended in pure Matrigel® with a final cell density of 15 million cells ml^{-1}. The cell–hydrogel solution was mixed and injected into the tumor region of the device (Figure 4.1B). The devices were then incubated (humidified, 37 °C, 5% CO2) for 3 min. Subsequently, Matrigel® was injected into the stroma region followed by 5 min of incubation allowing hydrogel polymerization. Cell culture medium was added afterwards and exchanged daily. Invasion distance was measured by drawing lines from the microposts to the edge of leading cells and then averaging at least 10 lines. Extensions from the cell body were measured by drawing a line from the front edge of nucleus to the end of the extension. Click-iT EdU Alexa Fluor 488 Imaging Kit (Thermo Fisher) was used to assess proliferation in invasion assay.

4.3.5 In vivo animal Experiments

Animal husbandry was performed according to the guidelines of St. Joseph Hospital and Medical Center and Barrow Neurological Institute under the Institutional Animal Care and Use Committee–approved protocol. Five- to six-week-old IcrTac:ICR-Prkdcscid mice were used for in vivo orthotopic transplant of fluorescently-tagged GB3 cells. For orthotopic transplants, 2 μL of dissociated cells at a density of 50,000 cells μL^{-1} were injected in the right hemisphere (stereotactic coordinates AP 0, ML -2, DV -2.5), as described previously (Ligon et al., 2007; S. Mehta et al., 2011). 8 weeks after injection, tumor-bearing mice were euthanized with a lethal intraperitoneal injection of 2.5% Avertin (2,2,2-Tribromoethanol, Sigma-Aldrich; T48402; *tert*-Amyl alcohol, Sigma-Aldrich, A1685). Tissues were fixed through intracardial perfusion with Ringer's solution (Electron Microscopy Sciences; 11763-10) supplemented with 40 mM $NaNO_2$, 2 mM

$NaCHO_3$, and 50 IU mL^{-1} heparin, followed by ice-cold 4% paraformaldehyde (PFA) in 0.1 M phosphate buffer (PB). Brains were subsequently cryoprotected with incubation in a solution of 30% sucrose in PB for 48 hours before being frozen and cut into 40 µm coronal sections using a cryostat (Microm HM550, Thermo Scientific).

4.3.6 Immunostaining within the microfluidic device

Cells within microfluidics were fixed in 4% PFA following 3 days after co-culture by removing cell culture medium and exchanging for 4% PFA before applying a gentle negative pressure to other well to create flow. Devices were then incubated for 30 min at room temperature (RT). After incubation, the samples were rinsed twice with PBS-glycine (100 mM glycine in PBS) incubating for 10 min at RT and washed with PBS-Tween (0.05% (v/v) Tween-20 in PBS) for another 10 min at room temperature to permeabilize the cells. Following permeabilization, the samples were blocked with immunofluorescence buffer and 10% goat serum (GS) (IF buffer: (0.2% (v/v) Triton X-100, 0.1% (v/v) BSA (radioimmunoassay grade), 0.05% Tween 20, 7.7 mM NaN_3 in PBS) for 2 h to inhibit nonspecific binding of antibodies. Primary antibody was diluted in PBS-tween and then added to the blocked samples and kept at 4 °C overnight. Devices were kept in petri dishes and wrapped in parafilm to avoid evaporation. Then, devices were washed with IF buffer three times each at 20 min intervals at room temperature. Species-matching Alexa-conjugated secondary antibodies were used at 1:500 dilution (Invitrogen). After adding the mixture to each sample, the devices were incubated at room temperature for 1 h. The devices were then washed once with IF buffer for 20 min followed by two times washing with PBS-Tween-20 for 10 min. 4',6-diamidino-2-

phenylindole (DAPI, Invitrogen) (1:1000) was added to the devices to counterstain nucleus. Following staining, the devices were finally washed with PBS–Tween-20 three times each at 10 min intervals. The following primary antibodies were used: mouse anti–Ki-67 (1:100, Dako), rabbit anti-Sox2 (Cell Signaling, 1:100), mouse CD-31 (10 μg mL^{-1}, P2B1, Developmental Studies Hybridoma Bank, DHSB), mouse anti-Nestin (1:200, Abcam), rabbit anti-CD44 (Cell signaling, 1:400), rabbit anti-GFAP (Millipore, 1:500), rabbit anti-pCXCR4 (Cell Signaling, 1:100).

4.3.7 Immunohistochemistry of in vivo tissue sections

Immunohistochemistry was performed on free-floating sections. When antigen retrieval was necessary, tissues were treated for 45 minutes in citrate buffer (pH 6) at 80°C. To block unspecific staining when mouse-raised primary antibodies were used, we initially incubated sections with goat anti-mouse and goat anti-rabbit IgG (Jackson ImmunoResearch) 1:50 in 0.1 M PB 0.4% Triton-X (PBTx). After a permeabilization and blocking incubation for 2 hours at RT in PBTx supplemented with 10% heat-inactivated GS, the sections were incubated with the primary antibodies for 12 hours at 4°C in PBTx, 2% GS. Incubation with secondary antibodies was performed for 2 hours at 4°C in PBTx, 2% GS. Nuclear counterstaining was achieved with DAPI (0.5 μg/mL). The following primary antibodies and dilutions were used: mouse anti–Ki67 (1:100, Dako), rabbit anti-RFP (1:100, Abcam), rabbit anti-Sox2 (Cell Signaling, 1:100). For blood vessel staining, sections were incubated with DyLight-488 Tomato Lectin (Vector Lab) for 1hr RT at 1:1000. Coverslips were mounted using Pro-long Gold (Vector Lab).

4.3.8 Imaging

Microfluidic devices were imaged using fluorescence microscopy (Zeiss Axio Observer Z1 with the Zen Pro software suite) equipped with Apotome.2 (Zeiss) at 20x and 40x magnification. Fluorescent brain tissue sections were imaged using a Leica SPE Confocal microscope at 20x magnification (1.2 micrometer stacks). Analysis and 3D reconstructions were performed with Imaris (Bitplane).

4.3.9 Statistical Analysis

For all analyses, values were obtained from at least three independent experiments ($n > 3$) with 2–3 technical replicates each. Data are expressed as average ± standard deviation or average ± standard error of mean. When only two conditions, we utilized an unpaired two-tailed Student's t-test. Two-way ANOVA with Sidak multiple comparison tests were used when comparing more than two conditions and statistical significance defined as $p < 0.05$. Statistical analyses were performed within the GraphPad Prism software (GraphPad Prism 6).

4.4 Results

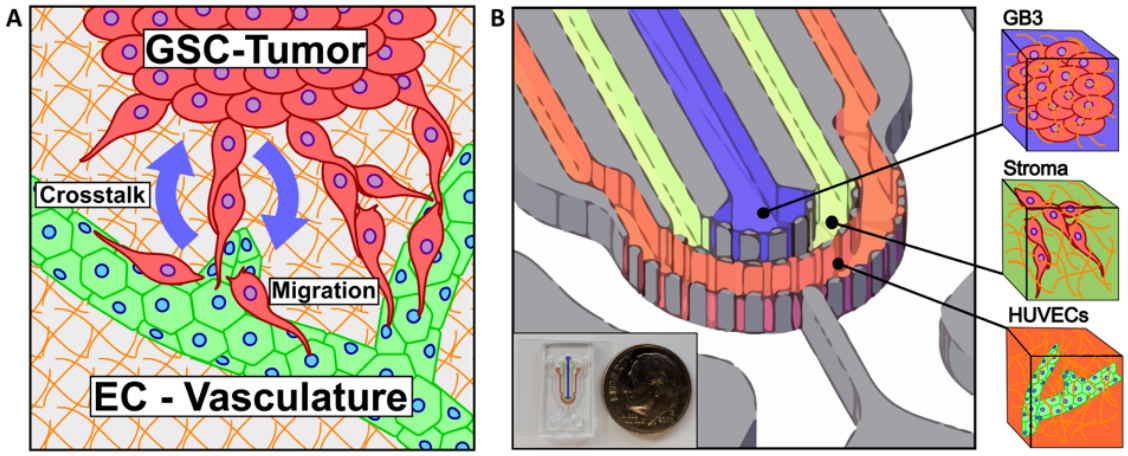

Figure 4.21 Schematic of GSC-EC interaction.

(A) Schematic of the vascular niche within the GBM tumor microenvironment demonstrating GSC (red) migration in response to ECs (green). (B) The 3D schematic and photograph of the microfluidic platform is showing the different regions for cell culture and migration. Blue represents the tumor region housing the GB3 and red represents the vasculature region containing the HUVECs. The green region in the middle enables GB3 migration toward the microvascular network.

4.4.1 Formation of vasculature within the microfluidic model

We first established and tested the formation of a 3D microvascular network within our microfluidic model prior to incorporating GSCs within the tumor region (Figure 4.1B). To establish the microvascular network, we utilized fibrin as the candidate ECM for encapsulating the HUVECs. Fibrin has been widely used to model the tumor vasculature as it promotes physiologic vasculogenesis (Jeon et al., 2015; H. Lee, Park, et al., 2014). Importantly, fibrin has been well-documented to be deposited near tumor-associated vasculature for different cancers including those of the brain functioning as a source of growth factors for angiogenesis and cell recruitment (Bardos, Molnar, Csecsei,

& Adany, 1996; Harold F Dvorak, 1986). Additionally, in our previous extensive characterization, we demonstrated the suitability of fibrin for physiologic vasculogenesis (Nagaraju et al., 2018). So, we embedded HUVECs in a fibrin gel and injected them within the outer layer of the microfluidic to enclose the tumor and stroma layers. The process of microvascular network formation occurred over the course of 3 days in culture. As seen in Figure 4.2A, the phase-contrast images demonstrated the formation of branched microvascular network within the microfluidic platform. The HUVECs began to elongate and connect within the first day of culture. By the third day, vessel-like structures could be seen similar to our prior publication (Nagaraju et al., 2018). Notably, fluorescent 70-kDa dextran flowed into the vasculature, demonstrating open lumens of the microvascular network (Figure 4.2B). CD31 staining confirmed the microvascular phenotype and the cross-sectional view clearly showed the formation of lumen (Figure 4.2C).

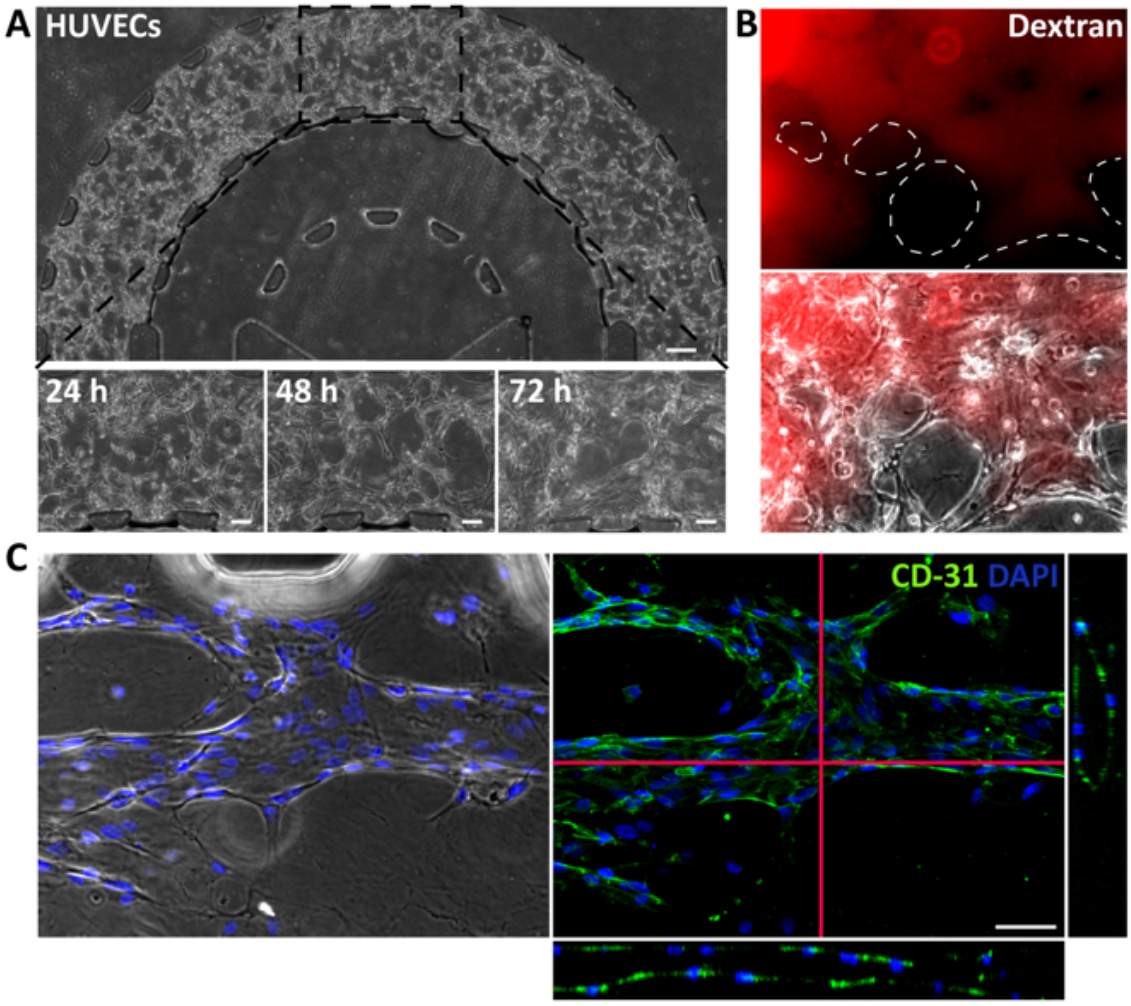

Figure 4.22 Successful formation of 3D microvascular network within the microfluidic platform.

(A) Phase-contrast images of HUVECs forming microvascular network over 3 days of culture; Scale bar: 100 µm top image and 50 µm for bottom row. (B) Fluorescent dextran perfused into the media channels demonstrating open lumens within microvascular network. (C) CD-31 stain confirming the morphology of vessels within microfluidic device. Cross-sectional view (red lines) demonstrating hollow lumen of the vessels; Scale bar: 50 µm.

4.4.2 Phenotype of GSCs in the microfluidic model

We utilized GB3 GSCs, a patient-derived cell line established from resected primary GBM tumor at the Barrow Neurological Institute (BNI). GB3 GSCs have previously been shown to be highly invasive within 2D *in vitro* transwell assays as well as *in vivo* mice models (Singh et al., 2016). When cultured within 3D hydrogels, these cells demonstrated expression of Nestin, SOX2, and CD44, and the ability to maintain self-renewal which are classical GSC markers (Heffernan et al., 2017). However, the phenotype of patient-derived GB3 cells within the 3D microenvironment in presence of vasculature has not been assessed. Therefore, prior to invasion analysis, we confirmed the expression of specific proteins related to stemness and different neural lineages of the GSCs within our microfluidic model through immunofluorescent staining. While GSCs are typically cultured in serum-free condition, the co-culture with HUVECs requires further optimization of medium conditions. HUVEC growth requires media containing 2% fetal bovine serum (FBS) along with additional growth factors which may influence invasion and phenotype of the GSCs in the co-culture condition. Therefore, we designed experiments with different media composition to conduct our biological studies. The culture media were comprised of: NSC medium, NSC medium supplemented with 5% FBS (NSC +), and EGM-2.

To establish working microfluidic model, we first formed the microvascular network within the model for 3 days. Next, we utilized Matrigel® as it is compatible with 3D culture and rich in laminin, which is important ECM component of the GSC microenvironment (Rape, Ananthanarayanan, & Kumar, 2014; Xiao, Sohrabi, & Seidlits,

2017). Patient-derived primary GSCs were encapsulated within Matrigel® and introduced into the primary tumor region of the platform. Subsequently, Matrigel® was added into the second layer (i.e. stroma) of the device to surround and enclose the tumor region. Within different medium compositions, we examined the expression of Nestin, SOX2, GFAP, and CD44 markers in the GSCs embedded in Matrigel® within the second layer of the microfluidic platform in the presence of microvascular network. Nestin, which is an intermediate filament and a neural progenitor marker, was expressed in the GSCs (Figure 4.3A). We did not detect expression of astrocytic marker, GFAP (Figure 4.3B), while the transcription factor SOX2, a marker for pluripotency and self-renewal (Figure 4.3C) (Guo et al., 2011), was widely expressed in GSCs. Moreover, CD44, a receptor for hyaluronic acid which is highly expressed in malignant GBM (Breyer et al., 2000), was clearly shown on the membrane of the GSCs (Figure 4.3D). These results from our 3D microfluidic model are consistent to prior publications which suggests that the GSCs maintain stemness and GBM phenotype markers in presence of the vasculature (Heffernan et al., 2017; Singh et al., 2016).

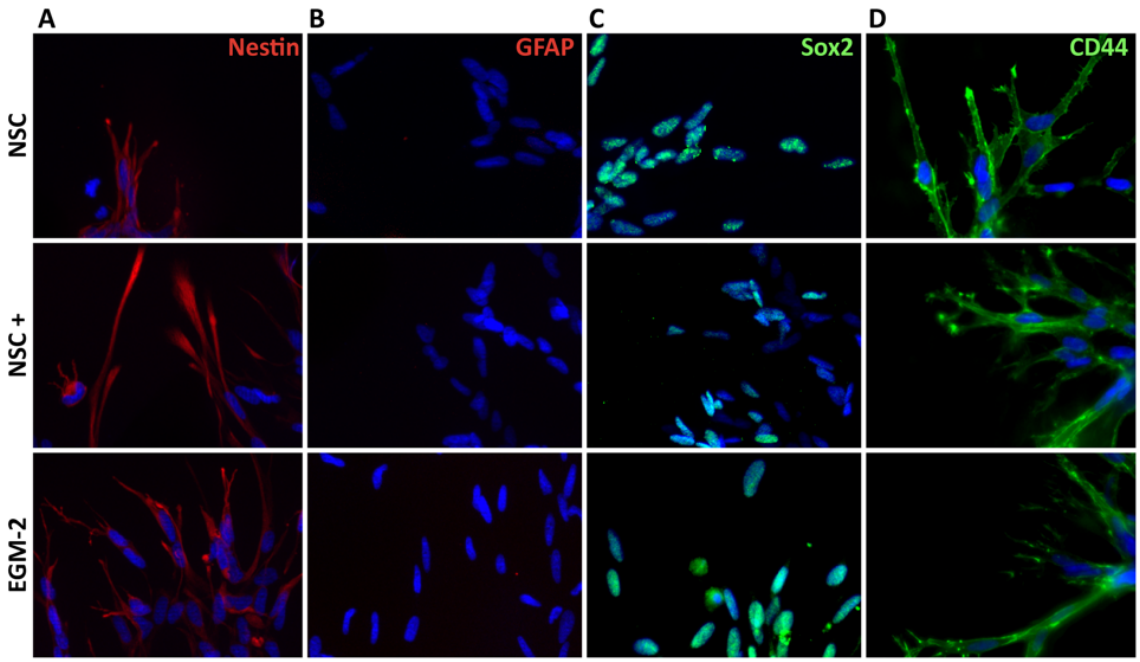

Figure 4.23 GB3 GSCs demonstrated stem phenotype within the 3D microfluidic device. (A) GSCs demonstrated positive staining for Nestin and (B) negative for GFAP while (C and D) SOX2 and CD44 were positively expressed in GSCs within different medium compositions.

4.4.3 Invasion of GSC in presence of the 3D microvascular network

We intended to find out if the formed vasculature influenced the invasion distances of GSCs within a 3D microenvironment. As previously described, we introduced different medium conditions in our microfluidic model. Within the first day of culture, we observed that GSCs did not form spheroids but demonstrated elongated and branching morphology under all the conditions. Additionally, GSCs exhibited propensity to migrate into the stroma as chains of cells (Figure 4.4). We compared invasion of GSC between mono-culture (- HUVECs) and co-culture with HUVECs (+ HUVECs) for the three different media conditions (Figure 4.4A). Co-culture with HUVECs led to

significant invasion of GSC in the NSC medium (Figure 4.4B; - HUVECs 52.8 ± 11.3 μm and + HUVECs 262.4 ± 39.2 μm) and NSC + medium (Figure 4.4B; - HUVECs 170.5 ± 21.0 μm and + HUVECs 319.4 ± 60.6 μm). On the other hand, we found no difference between mono- and co-culture conditions in EGM-2 (Figure 4.4B; - HUVECs 310.7 ± 22.4 μm and + HUVECs 318.3 ± 29.24 μm). This suggests that EGM-2 may contain cytokines that elicit a strong invasion response in GSCs thereby shielding the influence of HUVECs on invasion. Conversely, since there was a significant increase in GSC migration upon co-culture in both NSC and NSC + medium conditions, this suggests that HUVECs do play a role in enhancing invasion of GSCs within the 3D tumor-vascular microenvironment.

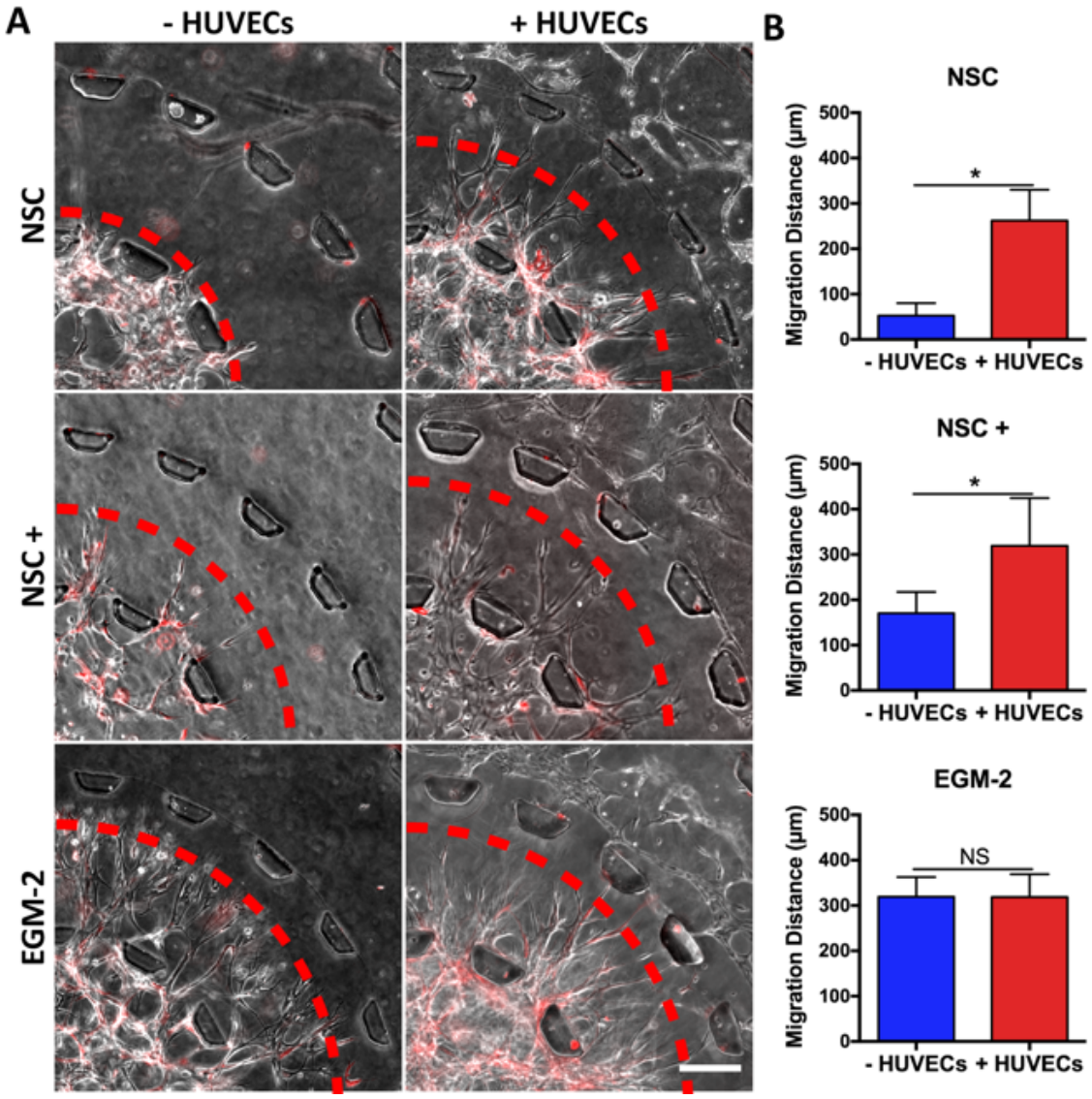

Figure 4.24 GSC invasion in under different medium conditions within the 3D microfluidic model.

(A) Phase-contrast image of GSC (red) invading in the presence of HUVECs in different medium conditions. Red dashed line delineates average migration boundary; Scale bar: 200µm. (B) Quantification of invasion distance for each condition (* denotes $p < 0.05$; Student's T-test; $n > 3$ for each data set).

Based on the phase-contrast images of the invasion assay on day 3, we also noticed morphological differences in how GB3 GSCs invaded when co-cultured with HUVECs. Cell membrane protrusions or extensions from the cell body were observed within the GSCs (Figure 4.5A), which have been attributed to invasive phenotype in GBM (Jensen et al., 2016; Osswald et al., 2015). We measured the extensions of the leading GSCs and compared within different medium conditions. As seen in Figure 4.5A, the migrating GSC exhibited more elongated extensions from the cell body when co-cultured with HUVECs, which was correlated with their invasive response (Figure 4.4). This is indeed also consistent with previous *in vivo* studies on invasive morphology of the GSCs (Osswald et al., 2015). Quantifications of the extensions demonstrated that GSCs had a significant increase in extension length upon co-culture with HUVECs within each medium condition (Figure 4.5B; NSC: - HUVECs 70.8 ± 16.5 μm and + HUVECs 106.5 ± 20.6 μm, NSC +: - HUVECs 60.0 ± 5.4 μm and + HUVECs 104.5 ± 19.0 μm, and EGM-2: - HUVECs 84.2 ± 14.9 μm and + HUVECs 129.8 ± 26.8 μm) corroborating the observations from phase-contrast images (Figure 4.5A). We also speculated that, apart from the migration distance (Figure 4.4), the presence of vascular network may influence the density of migrating cells within the stromal region. Therefore, we utilized two metrics, number of cells in a migrating chain as well as number of cells in a field of view (FOV) within the stroma, to quantitatively discern the density of migrating cells. For co-culture with HUVECs in the NSC medium condition, there were significantly increased numbers of nuclei per chain of migrating cells (Figure 4.5C; - HUVECs 2.8 ± 0.9 and + HUVECs 5.6 ± 1.5) and within a FOV in the stroma (Figure 4.5D; - HUVECs 9.6 ± 6.1 and + HUVECs 32.2 ± 9.2) as compared to mono-culture. On the other hand, no

significant difference between mono- and co-culture conditions was found in either NSC + or EGM-2 media (Figure 4.5C and D). As such, the microfluidic model was capable of monitoring GSC invasive behaviors in terms of migration distance and morphology under different medium conditions in the absence and presence of a functional 3D vasculature.

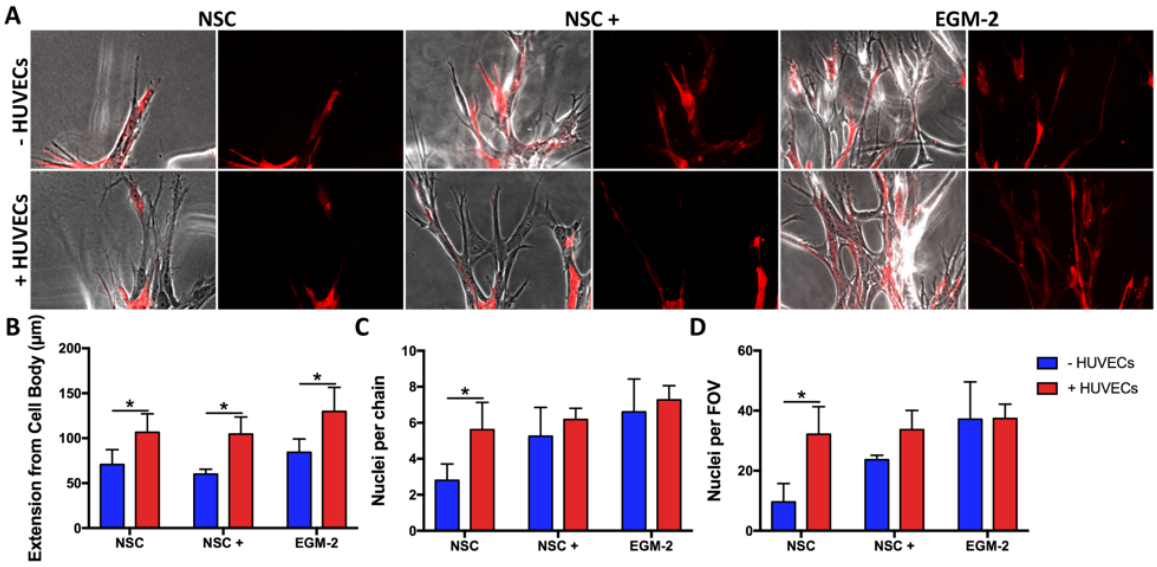

Figure 4.25 GSCs demonstrated elongated morphology during invasion.

(A) Phase-contrast and fluorescent images of GSC invading into the stroma exhibiting extensions from cell bodies. (B) Quantification of the extensions in each medium condition. (C) Quantification of the nuclei per chain in each medium condition. (D) Quantification of the nuclei per FOV in each medium condition. (* denotes $p < 0.05$; 2-way ANOVA with Sidak post-hoc test; $n > 3$ for each data set).

In addition to assessing GSC invasion distance and morphology, we investigated the behavior of the formed vessels under different media compositions. Consistent to our prior publication (Nagaraju et al., 2018), we measured the diameter of the vessels (Appendix Figure C.1A; NSC: 55 ± 5 μm, NSC +: 63 ± 14 μm, EGM-2: 48 ± 9 μm) and the length between junctions (Appendix Figure C.1B; NSC: 267 ± 71 μm, NSC +: 276 ±

103 μm, EGM-2: 247 ± 42 μm) (Nagaraju et al., 2018). We found slight differences between the different media compositions but none were statistically significant. Furthermore, we did not observe extensive angiogenesis over the three-day time-period of our assay.

4.4.4 Effect of vasculature on GSC proliferation

As the vascular microenvironment had been demonstrated to maintain proliferation of GSCs (Calabrese et al., 2007), we asked if the microvascular network within our model played a similar role on GB3 proliferation. In mono- and co-culture conditions, we utilized Ki-67, in addition to pulsing with EdU for 24 h, to assess the proliferation of GSCs. As shown in Figure 4.6, we observed expression of Ki-67 and EdU suggesting that the GSCs divided within the microfluidic platform. However, regardless of the medium conditions, we did not observe a significant difference in proliferative markers between mono- and co-culture conditions. This suggests that HUVECs within this model did not influence GSC proliferation. Moreover, this also suggests that the invasion responses of the GB3 cells were more likely due to migration speed and elongation of cells rather than proliferation (Figure 4.4).

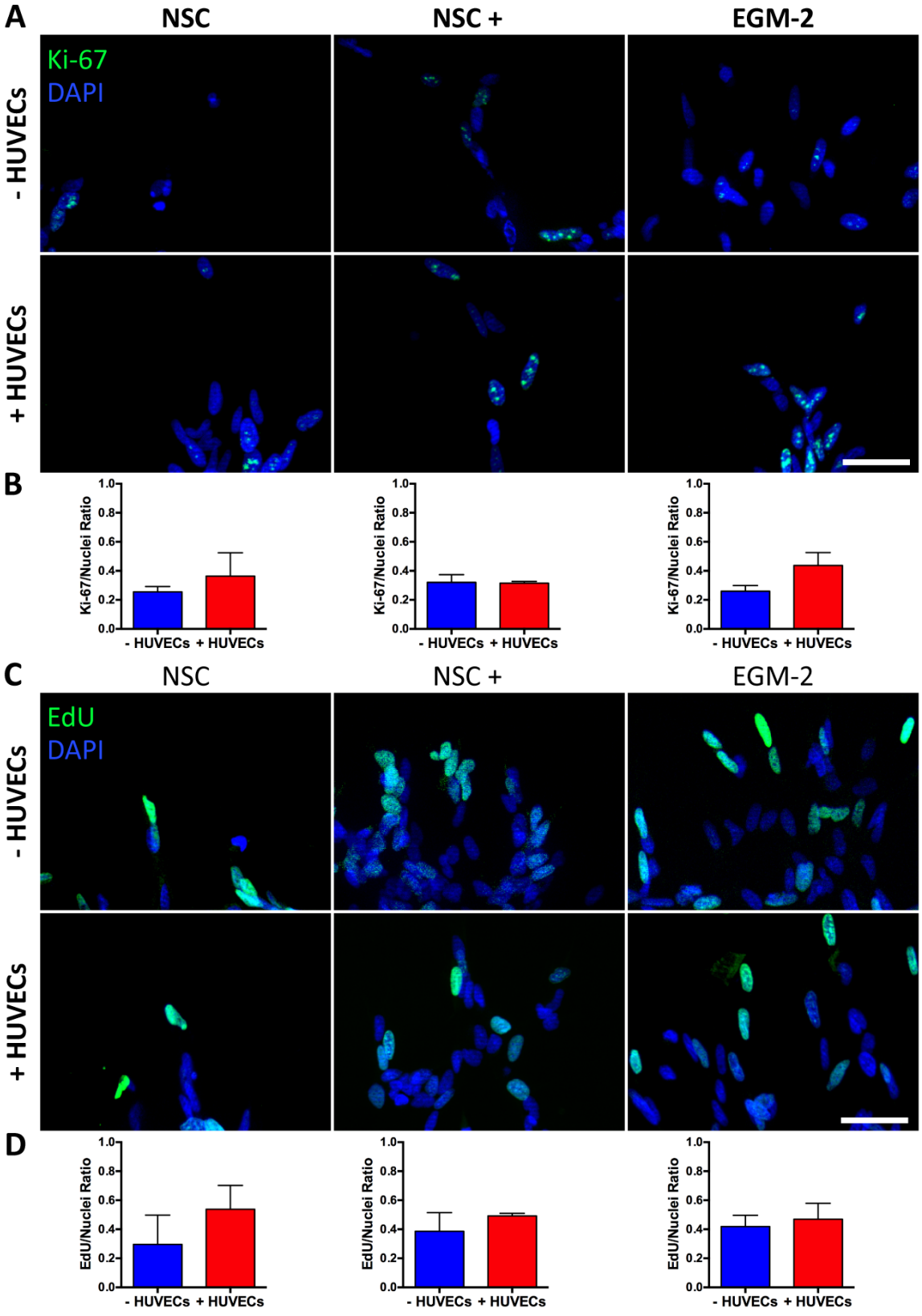
A
NSC
NSC +
EGM-2
Ki-67
DAPI
- HUVECs
+ HUVECs
B
Ki-67/Nuclei Ratio
1.0
0.8
0.6
0.4
0.2
0.0
- HUVECs + HUVECs
C
NSC
NSC +
EGM-2
EdU
DAPI
- HUVECs
+ HUVECs
D
EdU/Nuclei Ratio
1.0
0.8
0.6
0.4
0.2
0.0
- HUVECs + HUVECs

Figure 4.26 GSC proliferated within the 3D microfluidic model.

(A) Immunofluorescence staining of Ki-67 proliferative marker; Scale bar: 50 µm. (B) Quantification of Ki-67/Nuclei ratio of each medium condition. (C) Immunofluorescence staining of EdU incorporation into nuclei; Scale bar: 50 µm. (D) Quantification of EdU/Nuclei ratio of each medium condition.

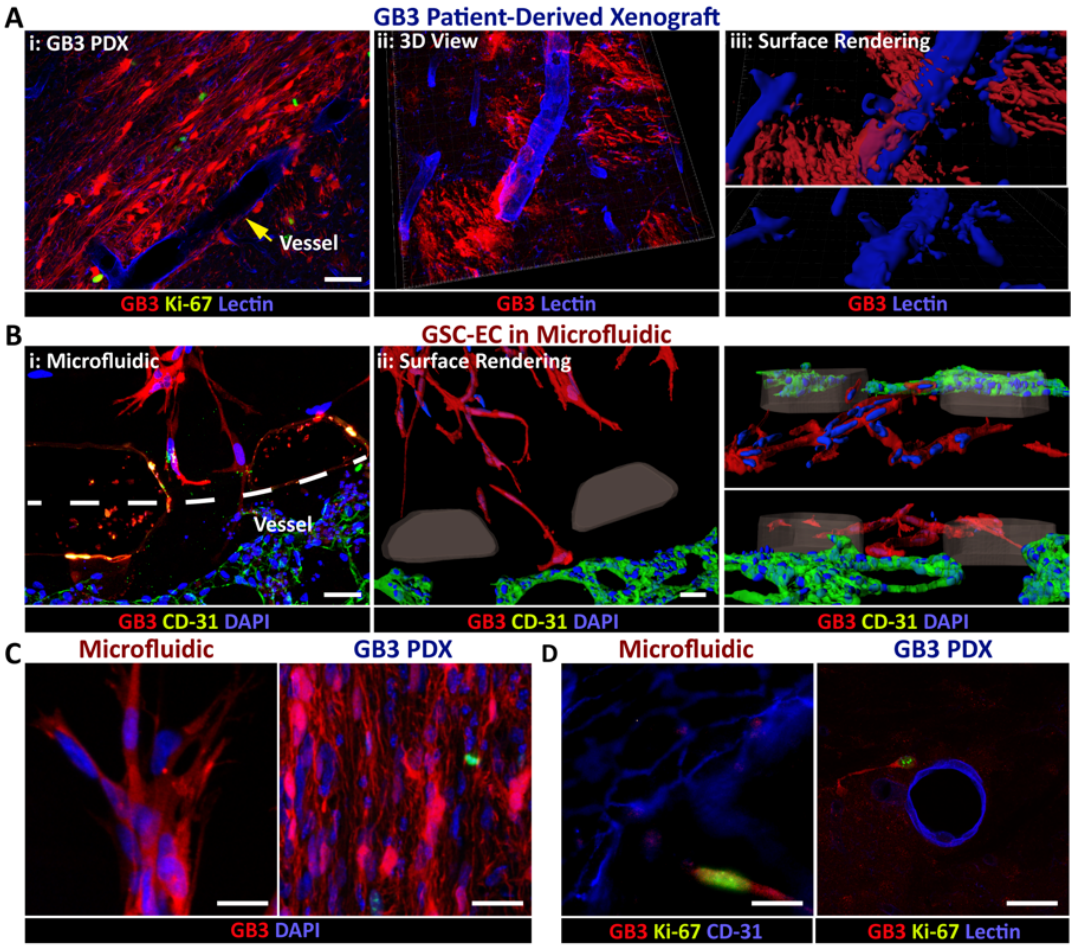

Figure 4.27 GSC invasion in microfluidic and PDX models.

(A) i: GSCs (red) shown migrating toward vasculature (blue, Lectin) within the *in vivo* model; Scale bar: 50 µm. ii: 3D view of tissue-slices of the *in vivo* model demonstrating GB3 migrating along vessel. Iii: surface rendering of migrating GSCs showing the cells

establishing contact with the vasculature. (B) i: Immunofluorescence staining of invading GSCs (GB3, red) near vasculature (CD-31, green) in microfluidic model. The white dashed line demarcates the border between the stroma and the vascular regions. ii: Surface rendering with multiple views of migrating GSCs (red) within the microfluidic model; Scale bar: 40 μm. (C) Comparison of chain-like migration between the two models; Scale bar: 25 μm. (D) Comparison of proliferating GSC (green, Ki-67) near vessel in both models; Scale bar: 25 μm.

4.4.5 Comparison of the microfluidic platform of GSC invasion to in vivo PDX model

In parallel to our *in vitro* studies, we utilized a PDX model to investigate GSC invasive behavior *in vivo* to confirm the physiological relevance of our microfluidic platform. Notably, side-by-side validation of microfluidic models of GSC-EC interactions and *in vivo* PDX model had not been performed in prior microfluidic systems. (Chonan et al., 2017; H. Lee, Park, et al., 2014). Fluorescently-tagged GB3 cells orthotopically transplanted in mice, demonstrated migration near and along blood vessels (Lectin, blue) within the mouse brain (Figure 4.7Ai), appeared comparable to the behavior of GSCs in our microfluidic model (Figure 4.7Bi). Based on 3D and surface renderings of the tissue slices, we could clearly observe cells migrating along the vessels, consistent to other studies (Figure 4.7Aii and iii) (Watkins et al., 2014). Similarly, within the microfluidic model, GSCs could be observed migrating in 3D space while also establishing contact with the vasculature (CD-31, green) through the 3D surface renderings of the cells (Figure 4.7Bii and Appendix Movie D.14). Additionally, we observed similar chain-like migration within the *in vivo* PDX model that resembled the

migratory behavior of cells within the co-culture microfluidic model (Figure 4.7C). We noticed long protrusion-like extensions in both systems consistent to other studies, which have been associated with invasive phenotype as well as resistance to radiotherapy of the GSCs (Gritsenko, Leenders, & Friedl, 2017; Osswald et al., 2015). The expression of proliferation marker, Ki-67, was observed near vessels in both the microfluidic and *in vivo* model (Figure 4.7D). The microfluidic model could also enable in-depth visualization of the 3D vasculature as shown in Appendix Figure C.2A. The surface renderings clearly depicted the inner membrane of the vasculature providing potential for high-resolution observation of cell-cell interaction at a single-cell level (Appendix Figure C.2B, C and Appendix Movie D.15). Taken together, these evidences showed that our microfluidic model reliably represented GSC invasion *in vivo* in the context of a vascular niche. Importantly, our *in vitro* microfluidic assay only took 6 days to conduct our studies, which could provide faster and higher throughput for multiple analyses as well as high-resolution observation of cell-cell interactions prior to *in vivo* studies.

4.4.6 Effect of AMD3100 on GSC invasion within microfluidic model

High expression of chemokine receptor CXCR4 is a hallmark of malignant GBM (Bian et al., 2007). As such, CXCL12-CXCR4 interaction has been previously implicated in malignant GBM invasion (Ehtesham et al., 2009). However, previous studies have not assessed the expression of this signaling axis in a 3D tumor-vascular niche model. We demonstrated in our model that the presence of the 3D microvascular networking consisting of HUVECs promoted migration of GSCs. Additionally, since HUVECs have previously been shown to be a source of CXCL12 (Faber et al., 2014; Grasman &

Kaplan, 2017). We hypothesized that CXCR4-CXCL12 signaling axis may be involved in the migration of GSCs when in presence of HUVECs. AMD3100 has been used to inhibit CXCR4 and disrupt neural stem cell and GBM cell migration (C. Liu et al., 2013; J. M. Liu et al., 2017; Wurth et al., 2014). Therefore, we utilized this drug to study the influence of CXCL12-CXCR4 on GSC invasion in the context of 3D *in vitro* vascular microenvironment.

We chose the NSC medium condition due to the strong invasion response of GSCs in presence of HUVECs (Figure 4.3 and 4.4). HUVECs have previously been demonstrated to be a source of CXCL12 *in vitro* using ELISAs (Faber et al., 2014; Grasman & Kaplan, 2017). Therefore, we primarily validated signaling of CXCL12-CXCR4 axis by staining for the phosphorylated active form of CXCR4 (pCXCR4) in GSCs (Warrington et al., 2007). In absence of the microvascular network, pCXCR4 showed a diffuse pattern and was not localized to the nucleus (white arrows in Figure 4.8A). In presence of the microvascular network, pCXCR4 showed a punctate pattern and was localized to nucleus (white arrows in Figure 4.8A), providing additional evidence for CXCR4 activation by CXCL12 in our model (L. Wang et al., 2009).

We introduced AMD3100 at a concentration range between 0 and 100 μM after 24 h of establishing the model (C. Liu et al., 2013). The cells were maintained in AMD3100 for 48 h while we assessed their invasion response (Figure 4.8B). In mono-culture condition (- HUVECs) by day 3, the cells invaded in all drug treated concentrations but there were no significant differences in the invasion distances (Figure 4.8C, blue line; 0 μM: 98.1 ± 20.1 μm, 1 μM: 69.4 ± 27.58 μm, 10 μM: 52.9 ± 13.1 μm, and 100 μM: 59.0 ± 0.5 μm). However, in the presence of HUVECs on day 3 (+

HUVECs), we observed that invasion distance for 0 μM AMD3100 was significantly higher than all other concentrations with 1 μM being significantly higher than 100 μM (Figure 4.8C, red line; 0 μM: 285.1 ± 65.4 μm, 1 μM: 162.1 ± 42.4 μm, 10 μM: 137.5 ± 65.3 μm, and 100 μM: 69.9.0 ± 15.9 μm). We observed a decreasing trend in invasion response with increasing AMD3100 concentration (Figure 4.8C). The enhanced invasion response due to presence of the 3D microvascular network could be abrogated to mono-culture (- HUVECs) migration levels through treatment with AMD3100 by disrupting CXCL12-CXCR4 signaling (i.e. 100 μm). Interestingly, we did not observe a significant difference between mono- and co-culture even in presence of AMD3100 within the EGM-2 condition (Appendix Figure C.3). This suggests that there may be other cytokines other within EGM-2 apart from CXCL12 that may influence GSC invasion. In that regard, when utilizing NSC medium condition, our findings demonstrated that CXCL12-CXCR4 is involved in EC-mediated invasion of GSC within the 3D tumor model.

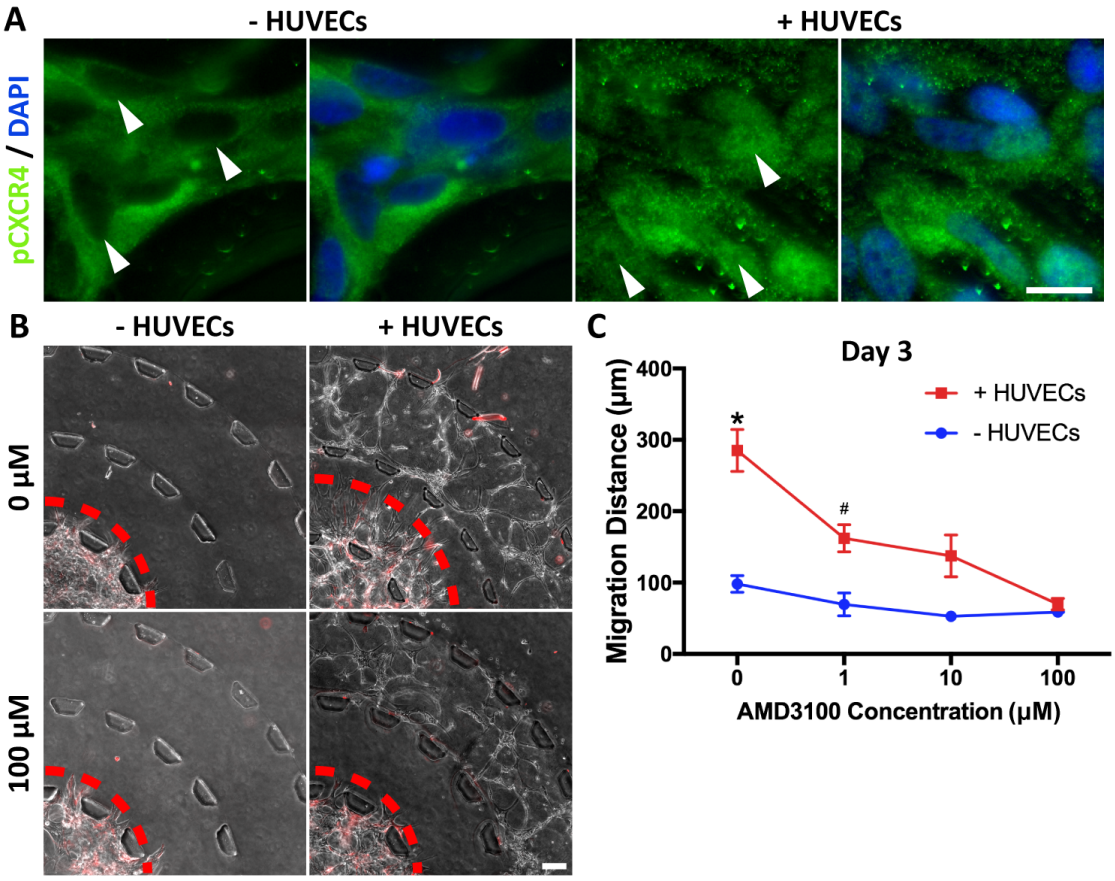

Figure 4.28 CXCL12-CXCR4 signaling in GSC-EC interaction.

(A) Immunofluorescence imaging of pCXCR4 in presence of microvascular network. White arrow denotes absence and presence of nuclear localization in mono- and co-culture respectively; Scale bar: 20 µm. (B) Phase-contrast image of GSC (red) invading in presence of HUVECs in different concentrations of AMD3100. Red dashed line delineates average migration boundary; Scale bar: 100 µm. (C) Quantification of invasion distance for each condition (* denotes a significantly different group for $p < 0.05$; # denotes a significant difference between 1 µM and 100 µM for $p < 0.05$; 2-way ANOVA with Sidak post-test; $n > 3$ for each data set).

4.5 Discussion

In GBM, a sub-population of cells with stem-like properties, GSCs, have been shown to be one of the major drivers for tumor recurrence, invasion of normal brain parenchyma and resistance to therapies (Lathia et al., 2011; Sundar et al., 2014). Recent investigation on the tumorigenic influence of the microenvironment has added further layers of complexity to understanding GSC biology and behavior (Hambardzumyan & Bergers, 2015). These specialized niche microenvironments provide safe harbor to GSCs making these cells difficult to therapeutically target. Importantly, the niches provide extrinsic cues that promote GSC growth and invasion and preserve the stem cell phenotype. In an elegant study by Calabrese *et al.,* GSC-EC interactions *in vivo* within the vascular niche was implicated as a key driver of tumor growth (Calabrese et al., 2007; Sharma & Shiras, 2016). Several signaling pathways with important roles in normal neural stem cell maintenance and growth, such as Notch, TGFβ, hypoxia-inducible factors (HIFs), and SHH have also been shown in GSC-EC interactions (Bruna et al., 2007; Sharma & Shiras, 2016; Yan et al., 2014; Zhu et al., 2011). These studies highlight the complex intercellular interactions that occur within the components of the vascular niche and GSCs that regulate whether GSCs remain quiescent, proliferate, transdifferentiate into pericytes or endothelial cells, or invade along existing blood vasculature (Lathia et al., 2015). Hence, further investigations are required into the GSC-niche interactions to unveil novel targets that could be used to disrupt the regulatory pathways that promote tumorigenesis.

Despite the significance of GSC-EC interactions within the niches, there are few *in vitro* models that could provide a 3D suitable biomimetic microenvironment for studying the influence of vascular niche components on GSC invasion. *In vivo* models are

often too complex presenting challenges in determining the cause and effect relationships between the microenvironmental cues and tumor cell behavior (Britta Weigelt et al., 2014). In addition, reduced spatial-temporal resolution of real-time events such as invasion speed within *in vivo* models pose additional difficulties, resulting in end-point analyses (Britta Weigelt et al., 2014). More complex *in vitro* systems consisting of higher dimensionality (i.e. 3D), microfluidics, and cell-laden hydrogels, have been developed to bridge this gap to better recapitulate the GBM microenvironment while providing better control over the microenvironmental cues (Britta Weigelt et al., 2014). For instance, Infanger *et al*. developed a 3D *in vitro* model of the perivascular niche by utilizing 3D scaffolds and EC-conditioned medium. EC-conditioned medium was collected from a 3D scaffold and then was subsequently added to GSC cultures. They found that the EC-conditioned medium maintained SOX2 and Nestin expression in GSCs. However, simultaneous co-culture of GSCs and ECs required random mixing of the two cell-types within the 3D scaffold which limited an organotypic architecture and quantitative assessment of migration. Therefore, they utilized a transwell assay instead to study migration in response to EC-conditioned medium (Infanger et al., 2013). On the other hand, to overcome the limitations of transwell assay, Chonan *et al*. created a 3D microfluidic device to study glioma invasion influenced by ECs. The two cell types were seeded as monolayers in two adjacent channels separated by a 3D collagen layer in between. They observed that glioma cells demonstrated increased invasion capacity near the monolayer of ECs. In this model, ECs were seeded as a monolayer, which did not represent a native-like 3D vasculature of the brain microenvironment (Chonan et al., 2017). In that regard, the relevance of our work lies in providing a 3D physiological

relevant *in vitro* model of GSC-EC interaction by spatially organizing GSCs near a 3D microvascular network with the possibility of adding additional cell types, such as astrocytes or pericytes. This enables us to engineer an organotypic architecture and to investigate the dynamic influence of the microvascular network on GSC invasion and phenotype. Importantly, we paired our *in vitro* study on GSC invasion with an *in vivo* PDX model to benchmark the physiological relevance of our microfluidic system. Therefore, aside from fundamental biological studies, the results of this study will also have implications for drug screening of therapeutics targeting GSC-EC interactions within niche microenvironments.

The microfluidic model, presented herein is based on a well-established 3D microvascular network that further enables detailed study of GSC invasion into a stroma-like region. This model also overcomes the limitation of prior work by introducing patient-derived GSCs after formation of the microvascular network instead of introducing both cell-types at the same time (Nagaraju et al., 2018). HUVECs require serum to develop into a 3D microvascular network which has been well-established by many groups (Jeon et al., 2015; S. Kim et al., 2013). GSCs are cultured in serum-free conditions as addition of serum induces differentiation. To avoid prolonged exposure to serum, we leveraged the design of our microfluidic platform to first establish a microvascular network using EGM-2 as the culture medium. Then we introduced GSCs into the microfluidic platform while exchanging EGM-2 for another medium, such as NSC, for the co-culture experiments.

We studied the influence of different medium compositions (i.e. NSC, NSC+, and EGM-2) on GSC phenotype within the co-culture assay. Expression levels of SOX2,

Nestin, and CD44 were positive in GSCs across all medium conditions. In addition to these markers, we investigated expression of GFAP, which is an astrocytic maturation marker used to identify differentiated GSCs. As others have shown, GFAP expression is inversely correlated to SOX2 (Y. Kim et al., 2012). Consequentially, since the GSCs within our microfluidic device were positive for SOX2, we found negative staining for GFAP. Heffernan *et al*. utilized the same cell line, GB3, grown in serum-supplemented medium for 14 days which eventually resulted in expression of GFAP (Heffernan et al., 2017). As the microfluidic assay was run for 3 days, it is possible that a longer time-period in either the EGM-2 or NSC + media (both containing serum) may result in positive expression of GFAP. Overall, the expression of these markers, (i.e. SOX2, Nestin, and CD44), suggested that the microfluidic model could recapitulate the classical hallmarks of GBM (Wakimoto et al., 2012).

Utilizing our 3D organotypic microfluidic model, we tested the influence of the microvascular network on patient-derived GSC invasive behavior under different medium conditions. We observed that microvascular network promoted protrusive morphology in all medium conditions suggesting transition to an invasive phenotype. Osswald *et al.* described these long protrusions as infiltrating into normal brain tissue during invasion (Osswald et al., 2015). Interestingly, we also observed chain migration of GSCs into the stroma, which is often associated with neural stem cells migrating from the subventricular zone (Lois, Garcia-Verdugo, & Alvarez-Buylla, 1996). This type of migration pattern has been described previously for glioma but only in certain settings (Deisboeck et al., 2001; Sander & Deisboeck, 2002). For instance, U87 and U251N glioma cells were observed in a 2D *in vitro* ring migration assay, but instead of migrating

as chains, the cells moved individually (Chen & Nalbantoglu, 2014). However, in separate study by Gritsenko *et al.,* when the same cells were cultured as multicellular spheroids on a basement membrane-like ECM, the cells exhibited the same chain-like migration, as we observed, suggesting the influence of ECM proteins on their migratory behavior (Gritsenko et al., 2017). Similarly, Grundy *et al.* cultured patient-derived GBM lines on 2D substrates demonstrating individual cell migration when the cells were cultured in 3D Matrigel® (Grundy et al., 2016). They observed chain migration consistent to our study. These evidences suggested that the chain-like migratory phenotype is dependent on the ECM as well as the 3D microenvironment, which we created in our microfluidic model. Importantly, we observed similar chain-like migration within the *in vivo* PDX model in brain tissue sections, which was also comparable to other studies in literature (Gritsenko et al., 2017). Taken together, this provides further evidence that our microfluidic platform is a suitable model to study the migratory behavior of GSCs in a 3D microenvironment.

As we observed in our PDX model, the GSCs migrated near or along vasculature of the mouse brain. To investigate whether 3D vasculature influenced GSC invasion distance, we performed co-culture invasion experiments within our *in vitro* microfluidic model. Interestingly, NSC medium did not promote invasion in mono-culture. However, in the presence of the microvascular network, we observed significant invasion of GSCs using the NSC medium as opposed to EGM-2 that showed no difference between mono- and co-culture. Firstly, this suggests that EGM-2, which contains both serum and additional growth factors, influenced GSC invasion regardless of the presence of the microvascular network. This essentially masks the influence of the microvascular

network and confounds the experimental interpretation. On the other hand, using the NSC medium, we could identify that the microvascular network promoted invasion of GSC thereby allowing us to further investigate the signaling between ECs and GSCs. As such, our findings report the influence of medium composition on GSC-EC interaction.

In our experiments, we did not find a significant change in proliferation rate of GSCs in presence of vasculature. A similar study was performed by co-culture of neurospheres with human brain microvascular ECs (hBMECs), showing that there was no difference in proliferation measured through both PCNA and Ki-67 between the mono- and co-culture conditions. Expression of CD133, a marker for self-renewal, was increased in the presence of hBMECs, which suggested that there was only an increase in self-renewal capacity of the cells but not proliferation (Zhu et al., 2011). Similarly, Galan-Moya *et al*. compared the amount of proliferative and quiescent cells in control medium and EC-conditioned medium on GSCs and found no difference in the ratio of proliferative to quiescent cells (Galan-Moya et al., 2011). However, like the study by Zhu *et al*., they also found that the EC-conditioned medium maintained self-renewal of the GSCs confirmed by expression of Nestin and SOX2. Consistently, we also observed expression of Nestin and SOX2 when GSCs were in presence of the 3D microvascular network. Additionally, we demonstrated increased density of migrating GSCs. However, since we did not observe a statistical increase in proliferation, we propose that this increase is due to enhanced migration speed of GSC.

The CXCL12-CXCR4 signaling axis has also been shown to be important in GBM invasion and tumorigenesis (Bian et al., 2007; Ehtesham et al., 2009; Jiang, Zhou, Guan, Wang, & Liang, 2013). Since CXCL12 has been also positively detected in ECs

within GBM tumor tissue, it is suggested that GSC-EC interaction through CXCL12-CXCR4 may play a role in GBM invasion (Rao et al., 2012; Salmaggi et al., 2004). To that end, we probed for pCXCR4, the phosphorylated form of CXCR4, as a measure of CXCR4 activation. We observed punctate staining for pCXCR4 in GSCs co-cultured with HUVECs but a diffuse staining in GSCs cultured alone, indicating more activated CXCR4 activation in co-culture. Moreover, we noted nuclear localization of pCXCR4 as additional evidence for activated CXCL12-CXCR4 signaling in the co-culture condition (Patsialou et al., 2009). Treatment with AMD3100, a CXCR4 antagonist, we observed a decreasing trend in GSC invasion in co-culture as a function of drug concentration. In fact, this was not observed in mono-culture of GSCs. This distinction highlights the importance of multi-culture 3D microenvironment in drug responsiveness of the GSCs. However, the cells did not respond to AMD3100 treatment in EGM-2 condition. As such, we hypothesized that EGM-2 promoted GSC invasion in a CXCL12-CXCR4 independent manner due to the growth factors and cytokines, including insulin-like growth factor, in EGM2 which has been previously shown to be a strong mediator of GBM invasion *in vitro* (Brockmann et al., 2003; Schlenska-Lange, Knupfer, Lange, Kiess, & Knupfer, 2008). This behavior further highlights the critical role of medium composition in establishing a reliable model for molecular and cellular level analysis of GSC invasion.

As we experimentally confirmed, CXCL12-CXCR4 signaling was crucial to GSC invasion in a vascular microenvironment. GSC survival and growth have been also shown to be dependent on the specialized niche microenvironments, such as hypoxic and perivascular (Hambardzumyan & Bergers, 2015). These niche microenvironments can further protect GSCs from chemo- and radiotherapy. Therefore, GSC-EC interactions

may also regulate resistance to radiotherapy. For instance, Brown *et al.* demonstrated that co-culture of HUVECs and U87 glioblastoma increased expression of ataxia telangiectasia mutated (ATM), a DNA damage response protein, which led to resistance to radiation-mediated apoptosis (Brown et al., 2004). Therefore, based on our study and the findings of others, combination of AMD3100 ad chemo- or radiotherapy could be a potential basis for GBM treatment as it has been tested in U251 GBM immortalized cell line in nude mice (Kioi et al., 2010). However, further investigation is required to assess how patient-derived GSC growth and invasion is affected as compared to high passage, immortalized cell lines that are used in most of the previous studies (S. Bao et al., 2006; Evers et al., 2010; Omuro & DeAngelis, 2013). Recently, Heffernan *et al.* studied the effects of radiotherapy on patient-derived GSCs, GB3 and GB7. The GSCs exhibited a dose response when grown as neurospheres, but demonstrated radioresistance when encapsulated in a 3D hydrogel (Heffernan et al., 2017). Therefore, the proposed 3D co-culture model presented herein could be used to study the effect of the vascular niche on radioresistance as part of future work.

Investigating tumor-associated angiogenesis due to GSCs was one of the future goals of our study using the microfluidic assay. Based on the current experimental settings, we did not observe statistically significant differences in vascular morphology based on different media compositions. Furthermore, we did not observe extensive angiogenesis over the three-day time-period of our assay. We contend that it may take longer to observe extensive angiogenesis (i.e. > 7 days) as demonstrated by other works (H. Lee, Park, et al., 2014) or that addition of brain ECs (instead of HUVECs) or other stromal cells, such as pericytes may influence vascular sprouting (J. Kim et al., 2015). In

this regard, addition of these new elements is the subject of our future work based on the developed assays.

Targeting the tumor angiogenesis in GBM is another option that is being explored clinically (Gerstner & Batchelor, 2012; K. Lee et al., 2009). However, many studies have reported that tumors treated with only Bevacizumab (Avastin®), a VEGF inhibitor, all eventually relapse (Wick et al., 2017). One caveat of disrupting angiogenesis is driving the tumors toward a hypoxic niche which could in turn promote invasiveness by co-opting native brain blood vessels (Hambardzumyan & Bergers, 2015; Rubenstein et al., 2000). In that regard, our microfluidic model of GSC-EC interaction could provide a quick and economical method as a drug screening assay to study the consequences of disrupting the vasculature on GSC invasive behavior.

Furthermore, future work will focus on improving our 3D organotypic *in vitro* microfluidic model by incorporating additional elements of the vascular niche. In this study, we utilized Matrigel® as the ECM component of model due to it containing 60% laminin, 30% collagen IV, and 8% enactin in addition to growth factors found in tumor vascular microenvironment (Rape et al., 2014; Xiao et al., 2017). However, in our future studies, we aim to utilize and characterize other types of hydrogels, such as hyaluronic acid (HA), which is a main ECM component of the brain. Our current work was also the first step to establish and validate a successful model of GSC-vascular interactions for biological studies. However, we acknowledge that stromal cells play critical roles in the microenvironment (Shwetal Mehta, 2018). For instance, pericytes are known to interact and mature the vasculature while astrocytes maintain hemostasis of the microenvironment, however, the roles of both cells along with neurons and

oligodendrocytes in GSC invasion behavior are still active areas of research (Audia, Conroy, Glass, & Bhat, 2017). Therefore, our future work, will involve fine-tuning and adding higher levels of complexities to our tumor microenvironment model by addition of stromal cells, including pericytes, smooth muscle cells, and additional glial cells.

4.6 Conclusions

We developed a 3D organotypic *in vitro* microfluidic model incorporated with a microvascular network to study the influence on patient-derived GSC and EC interaction on invasion and tumor behavior. Additionally, we have improved upon current *in vitro* platforms by first establishing a microvascular network prior to introducing the patient-derived GSCs. This avoids the confounding influence of vasculogenesis on the invading cancer cells allowing us to focus more on cell-cell interaction and role of the established vasculature on the migrating GSCs. Notably, we compared our microfluidic system to a PDX model using the same cells, finding similar invasive behaviors between the two models. In our experiments, we found evidence that the established microvascular network enhanced GSC invasion and promoted invasive morphology as well as maintained cell proliferation rates and classical GSC phenotype. Furthermore, we confirmed that CXCL12-CXCR4 signaling is involved in promoting GSC invasion within a vascular microenvironment while also demonstrating the effectiveness of this microfluidic model as a drug screening platform. Importantly, most of our experiments focused on utilizing NSC medium which did not contain serum and thereby allowed us study GSC-EC interactions in an unbiased experimental condition. As such, future studies using our model could incorporate collection of conditioned media from these

experiments to probe for additional possible paracrine signaling cues mediating GSC invasion. Indeed, this would have proven difficult if serum were included in the medium, such as in EGM-2, and within *in vivo* models which could contain confounding factors from other cells and microenvironmental cues. Further work will also involve fine-tuning the microenvironment, such as by incorporation of brain-mimetic hydrogels, patient-derived brain microvascular ECs, pericytes, smooth muscle cells, and additional glial cells. Taken together, this model presents a potential platform for studying the interplay of GSCs with its surrounding microenvironment as well as development of future therapeutic strategies tailored toward disrupting key molecular pathways involved in GSC regulatory mechanisms.

CHAPTER 5

CONCLUSIONS AND FUTURE DIRECTIONS

This final chapter discusses the achievements that we have made with each of the specific aims while providing insights and opportunities for future directions.

5.1 Significance and Contributions

5.1.1 Specific Aim 1

In this chapter, we described the development of a microfluidic system that was used as a model for 3D chemotactic tumor-stroma invasion. We designed the microfluidic platform to enable side-by-side positioning of 3D hydrogel-based matrices to create a dual matrix architecture extending in a continuous manner. Firstly, this enabled us to establish distinct regions of tumor and stroma cell/ECM compositions similar to the *in vivo* tumor microenvironment. Next, it allowed cellular invasion from one 3D matrix to another with a clear demarcated tumor invasion front, that enables quantitative analysis of the progression of cancer cells migrating into the biomimetic stroma at a tissue or single-cell level. In this chapter, we asked how a transient gradient of EGF through the stroma region of our device affected the cancers cells within the tumor region. We demonstrated through 3D tracking of cells at the single-cell level showed increased cellular migration speed and persistence. Subsequently, we observed an increase in EGF receptors, cell aspect ratio, and protrusive activity under EGF treatment. Overall, these findings demonstrated the unique ability of our model to quantitatively analyze 3D chemotactic invasion, both globally by tracking the progression of the invasion front, and at the single-cell level by examining changes in cellular behavior and morphology using high-resolution imaging.

In this chapter, for the first time, the influence of EGF was studied in a model containing two separated matrices on cancer migration speed and proliferation. Further, we utilized SUM-159 cells, a triple-negative breast cancer cell line, as our model which has not been tested for their invasive response to EGF. Our work demonstrated they indeed responded to EGF by increasing cell motility speed in a 3D ECM. In addition, we demonstrated that our microfluidic model was compatible with both phase-contrast and fluorescent time-lapse imaging which is crucial for feasible analysis for cell motility. Taken together, this chapter showed that we developed a novel platform capable of recapitulating 3D tumor-stroma interactions for studies of real-time cell invasion and morphological changes within a single platform.

5.1.2 Specific Aim 2

This chapter described the use of the microfluidic platform developed in Specific Aim 1 as a 3D in vitro organotypic model of tumor-stroma interaction with patient-derived fibroblasts incorporated within the stroma region. As tumor-stroma interactions significantly influence cancer cell metastasis and disease progression, we hypothesized that adding CAFs to our model would enhance the invasion of cancer cells. From there, we intended to interrogate the molecular influence of tumor-stroma interactions on cancer invasion. Using this approach, we combined functional assessment of cancer invasion, like migration and proliferation, with transcriptome profiling. Our model demonstrated that CAFs were able to promote cancer invasion corroborating results from clinical findings and other works. Once we established our invasion model, we utilized transcriptome profiling to interrogate possible molecular pathways derived from CAF

signaling that could influence cancer invasion. Through this work, we uncovered a novel gene of interest, *GPNMB*, and utilized function knockdown through short hairpin RNA to unveil that CAFs enhanced breast cancer invasion. We asked if the enhanced invasion due to increased proliferation or cell motility and through a series of experiments, we determined that GPNMB modulated migration speed and not proliferation.

In this chapter, for the first time, a microfluidic model was utilized as a biomimetic model tumor-stroma interactions using patient-derived fibroblasts as opposed to cell lines. In addition, transcriptome profiling was utilized to uncover a possible mediator of cancer invasion, *GPNMB*, which was corroborated with clinical findings and other literature. For the first time, CAFs were linked to expression of *GPNMB* in breast cancer cells. Additionally, GPNMB was studied in a 3D microfluidic model and we determined that GPNMB influenced cell migration speed and not proliferation. Overall, these results demonstrated the ability of our microfluidic model to recapitulate patient specific tumor microenvironment to investigate cellular and molecular consequences of tumor-stroma interactions.

5.1.3 Specific Aim 3

In chapter 4, we developed a new organotypic model based on our microfluidic technology to study glioblastoma (GBM). GBM is one of the deadliest forms of cancer. While there are many treatment options, prognosis of GBM still remains dismal as the 5-year survival rate is approximately 4.7%. Furthermore, tumors can recur after treatment. Tumor recurrence is hypothesized to be driven by glioma stem cells (GSC), a sub-population within GBM, which are highly tumorigenic, invasive, and resistant to several

forms of therapy. GSCs are concentrated around the tumor vasculature, referred to as the vascular niche, which provides microenvironmental cues mediating GSC stemness, invasive behavior, and resistance to therapies. As such, the fabricated 3D organotypic microfluidic platform was used in this chapter to mimic the GSC vascular niche and study the influence of endothelial cells (ECs) on patient-derived GSC behavior while identifying signaling cues that may mediate GSC invasion and phenotype. We established a 3D microvascular network within this model which led to enhanced GSC migration, promoting invasive morphology as well as maintaining GSC proliferation rates and stem phenotype. Notably in this chapter, we compared the migration behavior of GSCs in our microfluidic model to *in vivo* mice model and found evidence suggesting that our microfluidic system could represent a physiologically relevant *in vivo* microenvironment. In this chapter, we also confirmed that CXCL12-CXCR4 signaling was involved in promoting GSC invasion within a 3D vascular microenvironment.

In this chapter, for the first time a model of patient-derived GSCs within a vascular niche was developed using microfluidics. We took advantage of the different culture regions within this model to spatially arrange GSCs near a microvascular environment to resemble the *in vivo* situation. Further, we provided validation of this model by comparison with a PDX model of the same patient-derived GSCs, which has seldom been performed in previous works. We also corroborated literature data suggesting that CXCL12 signaling was mediating GSC invasion within a vascular niche, demonstrating that our model could represent relevant GSC behavior. Overall, our model presents a potential *ex vivo* platform for studying the interplay of GSCs with its surrounding microenvironment as well as development of future therapeutic strategies

tailored toward disrupting key molecular pathways involved in GSC regulatory mechanisms.

5.1.4 Contributions

Below we list the outcomes and contributions of our works in peer-reviewed journal articles and conference posters and presentations as well as patents.

Journal Articles:

1. **Truong, D.,** Kratz, A., Park, J.G., Nguyen, T., Barrientos, E.S., Saini, H., Pockaj, B.A., Mouneimne, G., LaBaer, J., Nikkhah, M., (2018). "Human Organotypic Microfluidic Model to Investigate the Interplay Between Patient-derived Fibroblasts and Breast Cancer Cells", *Minor Revisions.*
2. **Truong, D.**, Fiorelli, R., Barrientos, E. S., Luna Melendez, E., Sanai, N., Mehta, S., & Nikkhah, M. (2018) A Three-Dimensional (3D) Organotypic Microfluidic Model for Glioma Stem Cell – Vascular Interactions. *Biomaterials*. In press.
3. Nagaraju, S.*, **Truong, D.***, Mouneimne, G., & Nikkhah, M. (2018). Microfluidic Tumor–Vascular Model to Study Breast Cancer Cell Invasion and Intravasation. *Advanced healthcare materials.* **** indicates equal contribution.***
4. Peela, N., Barrientos, E. S., **Truong, D.**, Mouneimne, G., & Nikkhah, M. (2017). Effect of suberoylanilide hydroxamic acid (SAHA) on breast

cancer cells within a tumor-stroma microfluidic model. *Integrative Biology, 9(12), 988-999.*

5. Peela, N.*, **Truong, D.***, Saini, H.*, Chu, H, Mashaghi, S., Ham, SL., Singh, S., Tavana, H., Mosadegh, B & Nikkhah, M. (2017). Innovations in Advanced Biomaterials and Microengineering Technologies Towards Recapitulating the Stepwise Process of the Metastatic Cascade. *Biomaterials, 133,* 176-207. *17% acceptance rate.* **** indicates equal contribution.***
6. **Truong, D.,** Puleo, J., Llave, A., Mouneimne, G., Kamm, R. D., & Nikkhah, M. (2016). Breast Cancer Cell Invasion into a Three Dimensional Tumor-Stroma Microenvironment. *Scientific Reports*, *6*.

Conference Presentations:

1. **Truong, D.,** Kratz, A., Park, JG., Barrientos, E., Nguyen, T., Saini, H., Pockaj, B., Mouneimne, G., & Nikkhah, M., "Gene-expression Profiling of Patient-Derived Fibroblast and Breast Cancer Interactions in a Three-Dimensional (3D) Organotypic Microfluidic Platform" Annual Biomedical Engineering Society (BMES) Meeting, Atlanta, GA October 15-20, 2018

2. **Truong, D.,** Saini, H., Kratz, A., Barrientos, E., Nguyen, T., Pockaj, B., & Nikkhah, M., "The Influence Of Patient-Derived Fibroblasts On Breast

Cancer Invasion Profile Within A Microfluidic Platform" Annual Biomedical Engineering Society (BMES) Meeting, Phoenix, AZ October 11-14, 2017

3. Nagaraju, S., **Truong, D.,** & Nikkhah, M., "Tri-layer Microfluidic Platform for Studying Tumor Angiogenesis and Cancer Cell Intravasation" Annual Biomedical Engineering Society (BMES) Meeting, Phoenix, AZ October 11-14, 2017
4. **Truong, D.,** Nagaraju, S., & Nikkhah, M., "Microfluidic device to study Tumor-Stromal Interactions", Invited Presentation at University of Arizona Cancer Center, Tucson, AZ May 11, 2017
5. **Truong, D.,** Barrientos, ES., Puleo, J., Mouneimne, G., & Nikkhah, M., "Microengineered Tumor-Stroma Platform Investigating the Biochemical Influence of Stromal Fibroblasts on Breast Cancer Invasion" Annual Biomedical Engineering Society (BMES) Meeting, Minneapolis, MN October 5-8, 2016
6. **Truong, D.,** Puleo, J., Llave, A., Mouneimne, G., Kamm, R. D., & Nikkhah, M., "Three-dimensional (3D) Invasion of Breast Cancer Cells in a Well-Defined Tumor-Stroma Platform," NanoEngineering for Medicine and Biology Conference (ASME NEMB), Houston, TX, February 20-24, 2015

Conference Posters:

1. **Truong, D.**, Fiorelli, R., Barrientos, E. S., Luna Melendez, E., Sanai, N., Mehta, S., & Nikkhah, M. “Interrogating Glioma Stem Cell – Vascular Interactions Using a Three-Dimensional (3D) Organotypic Microfluidic Model” Annual Biomedical Engineering Society (BMES) Meeting, Atlanta, GA October 15-20, 2018
2. **Truong, D.**, Saini, H., Kratz, A., Barrientos, ES., Nguyen, T., Pockaj, BA., & Nikkhah, M., "Microengineered Tumor-Stroma Platform Investigating the Effect of Patient-Derived Stromal Fibroblasts on Breast Cancer Cells”, 2017 ARCS Foundation Phoenix Scholar Awards Dinner, Phoenix, AZ, April 21, 2017
3. **Truong, D.**, Saini, H., Kratz, A., Barrientos, ES., Nguyen, T., Pockaj, BA., & Nikkhah, M., "Microengineered Tumor-Stroma Platform Investigating the Effect of Patient-Derived Stromal Fibroblasts on Breast Cancer Cells”, ASU Molecular, Cellular and Tissue Bioengineering (MCTB) Symposium, Tempe, AZ, April 1, 2017
4. Nagaraju, S., **Truong, D.,** & Nikkhah, M., “Three-Dimensional Microfluidic Platform to Study the Role of Stromal Cells in Tumor Angiogenesis,” Annual Biomedical Engineering Society (BMES) Meeting, Minneapolis, MN, October 5-8, 2016
5. Peela, N., **Truong, D.**, Barrientos, ES., Mouneimne, G., & Nikkhah, M., “Evaluation of Anti-Cancer Drug Suberoylanilide Hydroxamic Acid (SAHA) on Cancer Cell Phenotype In A Three-Dimensional (3D) Breast

Tumor-Stroma Platform," MicroTAS 2016, Dublin, Ireland, October 9-13, 2016.

6. **Truong, D.,** Puleo, J., Llave, A., Mouneimne, G., Kamm, R. D., & Nikkhah, M., "Microengineered Breast Cancer Invasion Platform," Annual Biomedical Engineering Society Meeting, Tampa, FL, October 7-10, 2015
7. **Truong, D.,** Puleo, J., Llave, A., Mouneimne, G., Kamm, R. D., & Nikkhah, M., "Microengineered Breast Cancer Invasion Platform," AZBIO Awards 2015, Phoenix, AZ, October 1, 2015

Patents:

1. Nikkhah, M. & **Truong, D**. (2018). *U.S. Patent App. 2018/052151*. Washington, DC: U.S. Patent and Trademark Office.
2. Nikkhah, M., Kamm, R. D., & **Truong, D**. (2016). *U.S. Patent No. 10,017,724*. Washington, DC: U.S. Patent and Trademark Office.

5.2 Project Challenges

During this dissertation, there were several challenges that we overcame or addressed to the best of our ability. For instance, quantification of protein or gene expression is an integral part of studying cancer biology. Although the microscale nature of microfluidics enables low input of cells, this creates a disadvantage for using conventional techniques such as western and Northern blots. This led us to explore

different options of exploring molecular changes within cells. For example, in Chapter 2, we quantified activated EGFRs as a ratio between the phosphorylated form vs the non-phosphorylated form. Receptors were identified using immunofluorecent staining and quantifications were based on their count. In chapter 3, to measure relative protein expression, we followed an established technique to quantify fluorescent intensity. As the differences in the intensity was large between the positive and negative expressing cells, we felt comfortable that this method was justifiable (Acerbi et al., 2015). If the differences in expression were much smaller, we would explore options for more precise measurements such as utilizing a fluorescent standard. Another possible technique that is currently being explored in our lab is In-Cell Western™ assay (ICW). ICW utilizes a laser scanner equipped with filters to measure protein expression using the near and far-infrared secondary antibodies (Paguirigan, Puccinelli, Su, & Beebe, 2010). ICW offers significant benefits over conventional immunofluorescent microscopy. For instance, immunofluorescent microscopy requires separate images for each sample which could influence the number of settings that must be held identical between conditions. In comparison, several microfluidic devices could be imaged in one scan, which maintains the same exposure setting for all samples for better consistency during the analysis.

Another challenge we faced in this work are patient variation and molecular subtyping of the patient-derived fibroblasts. Although we observed cancer cell migration differences due to the different patient-derived fibroblasts, not all the differences between cancer cell migration could be explained using α-SMA and vimentin. For instance, Chapter 3 of this dissertation showed that CAF1 and CAF3 promoted more migration than CAF2 but the expression of α-SMA was similar between these three CAF

populations. Fibroblast activation protein (FAP) is another useful protein that is used to identify CAFs within the tumor microenvironment (Kalluri, 2016). In addition, fibroblast-specific protein-1 (FSP-1) is another widely used marker of CAFs (Kalluri, 2016). Prior studies have shown that α-SMA expression correlated well with advanced tumors and both α-SMA and FSP-1 correlated with shorter overall survival rates (Ha, Yeo, Xuan, & Kim, 2014). On the other hand, FAP did not correlate clinicopathologic parameters. Therefore, in addition to characterization of the patient-derived fibroblasts used in this study, other markers such as FAP and FSP-1 could be used to explain the differences between the CAF populations. Furthermore, if available, RNA-sequencing could be used to provide transcriptome profiling which would provide a broad characterization of the CAFs.

5.3 Future Directions

5.3.1 Microengineering the tumor microenvironment

Microengineered models have provided significant advantages over conventional 3D and *in vivo* models as they enable better control over the biochemical and biophysical properties that influence cancer invasion. The microfluidic model developed in Chapter 2 demonstrated a biomimetic tumor microenvironment with ability to control cell/ECM composition and observe dynamic cancer cell migration in 3D. However, there is still room for development to better interrogate the influences of the tumor microenvironment on cancer invasion. For instance, there are very few models that are being used to study the combinatory effect of several stromal components (e.g. immune cells and CAFs) on cancer cell invasion (I. K. Zervantonakis et al., 2012). There is much information on how

individual stromal cells, such as CAFs, endothelial cells, macrophages, influence cancer invasion but the integrated influence of several stromal cells is still unknown. However, microengineered technologies offer the ability to better recapitulate the *in vivo* tumor microenvironment by embedding one or more cell type within 3D ECM with spatial arrangement similar to the *in vivo* situation. As such, there is a need for more complex models of cancer that can approach a feasible representation of the *in vivo* tumor microenvironment for better prediction of cancer behavior (Britta Weigelt et al., 2014).

In addition to understanding the influences of stromal cells, cell-ECM interactions are another aspect of cancer progression that has not been well studied within microengineered models (Y. L. Huang, Segall, & Wu, 2017). ECM remodeling is important during development while also being indispensable for cancer progression (Lu, Weaver, & Werb, 2012). In normal physiology, the ECM is integral in modulating cell behavior by biophysical and biochemical methods. Mechanically, the ECM acts as a scaffold for supporting tissue architecture, a barrier for compartmentalizing cells and soluble factors, and anchorage sites/migration tracks for cell movement (Egeblad, Rasch, & Weaver, 2010). Chemically, the ECM can sequester a myriad of growth factors and cytokines that direct cell behavior through ligand-receptor interactions. Furthermore, changes to the ECM properties are intertwined and affect multiple characteristics of the ECM, such as stiffness, fiber density/architecture, and cell adhesive moieties (Kraning-Rush et al., 2013). Alterations of the ECM are dynamic and are also influenced by cell behavior. In that regard, alterations of the ECM due to cell-ECM interactions are reciprocal, thus linking the behavior of cells and ECM dynamics (Lu et al., 2012).

It has been well-documented in clinical studies that abnormal ECM dynamics is a classical hallmark of cancer. For instance, stiffening of the ECM in breast cancer is now a prognostic and risk factor for patients (Casey et al., 2009; Paszek et al., 2005). ECM remodeling enzymes, like MMPs, are other factors that are deregulated during cancer progression leading to changes in ECM architecture, topography, and composition (Acerbi et al., 2015). These alterations change the expression of ECM components to cells facilitating tumor growth and progression. However, the complex nature of the tumor microenvironment hinders the ability to decouple the components that contribute to cancer progression. As such, microfluidics have emerged as a tool with significant advantages in building a biomimetic tumor microenvironment using a bottom-up approach (Sung & Beebe, 2014). Tissue engineering approaches could design biomaterials based on ECM components while microfluidics enable well-defined spatial and temporal modeling of cells, ECM, and biochemical cues to build better predictive models of cancer drug screening (N. Peela, Truong, et al., 2017).

5.3.2 Characterization of the secretome in microfluidic models of the tumor microenvironment

Cell signaling is a crucial aspect of biology providing a method for cells to share information and coordinate cell activities. Secretion of soluble factors is a key part of cellular communication and that disruption or deregulation of this could lead to diseases like cancer. Traditional biological experiments have utilized conditioned media as a way to simulate cell-cell signaling *in vivo* but with the advent of microengineered models, like microfluidics, a biomimetic tumor microenvrionemnt could be created to study cell-cell

signaling. However, much of the focus on microfluidic-based tumor models has been on imaging-based assays for cell migration, proliferation, apoptosis, or morphology studies. On the other hand, studies involving soluble factors often only involve a single growth factor or indirect methods using gene expression or perturbing with inhibitors and observing the resulting phenotypic changes. While these methods have provided interesting and significant results, direct characterization or study of multiple signaling factors and biochemical pathways are not as sufficient. As such, characterization of the secreted factors during cell-cell signaling of microfluidic-based tumor models still need further research.

In recent years, progress has been made with coupling microfluidics with mass spectrometry (MS) (Feng, Liu, Li, & Liu, 2015). MS is a method which ionizes sample molecules to identify proteins based on mass to charge ratios. This technique has had widespread use in drug discovery and diagnostics. While a majority of microfluidic chips that have been coupled with MS (Chip-MS) had a focus on diagnostics and biomarkers using liquid samples, some have been developed with cell culture in mind to probe a biomimetic tumor microenvironment (Feng et al., 2015). For instance, Chin et al. study cell metabolism by culturing within a microfluidic that had been integrated with chambers for solid phase extraction (SPE) for sample desalting and purification (Abonnenc, Dayon, Perruche, Lion, & Girault, 2008). Similarly, Wei et al. developed a chip to co-culture different neuronal tissues and probe for growth factor signaling (Wei, Li, Mao, & Lin, 2011). Still a majority of these Chip-MS culturing cells on 2D and there have yet to be a Chip-MS utilizing 3D culture (van Duinen, Trietsch, Joore, Vulto, &

Hankemeier, 2015). We envision that future work will trend towards more biomimetic systems utilizing 3D culture.

5.3.3 Approaching Personalized Medicine

Much of cancer research is still devoted to utilizing cancer cell lines due to their ease and feasibility for drug screening (Garnett et al., 2012). However, cell lines do not represent the heterogeneic nature of tumors found in patients that affect drug response. Personalize medicine is a new and evolving field that attempts to tailor drugs based on the patient's genomic and phenotypic profile (Cheng et al., 2012). Although personalized genomic profiling can provide biomarkers, such as mutations or overexpressed proteins, that could be used to predict drug response, this method is still not reliable (Costello et al., 2014).

To overcome some of these issues, testing of the patient's own cells using technologies such as microfluidics could prove to be a powerful method for predicting drug response. Work done in Chapter 3 and 4 of this dissertation demonstrated to feasibility of using patient-derived cells in microfluidics. A limitation for many studies using convention *in vitro* techniques is that patient-derived cells may be difficult to grow in large-scale. However, one advantage that is specifically leveraged when using microfluidics is the small-scale nature of this technology enabling low sample input. Coupling this fact with the ability for microfluidics to assemble the tumor microenvironment through precise control of cell culture conditions demonstrates the capability of microfluidics technologies for personalized medicine.

Several works have already begun to utilize microfluidics to study personalized medicine using patient sample. Ruppen *et al.* developed a platform containing eight replicates of patient-derived cancer spheroids consisting of primary lung cancer cells and pericytes (Ruppen et al., 2015). Their work demonstrated that inclusion of patient-derived pericytes reduced drug efficacy of cisplatin. Furthermore, as we described in the previous section, the studies on the influence of ECM on cancer behavior within microfluidics has not been as well developed. In that regard, some works have utilized patient-derived ECM that could potentially be combined with microfluidics to build a more biomimetic model of cancer (Choi et al., 2014). Cukeirman *et al*. developed a method for producing 3D *in-vivo*-like matrices with patient-derived fibroblasts, called cell-derived ECM (CDM), to better mimic native ECM for mechanistic studies of different diseases (Franco-Barraza, Beacham, Amatangelo, & Cukierman, 2016). This method was adopted to characterize a series of patient-derived fibroblasts demonstrating that fibroblasts grown in their own CDM mimicked their *in vivo* characteristics in terms of expression of α-SMA and activated FAK (Quiros et al., 2008). As such, adopting these methods for patient-derived ECM with microfluidic technology could provide a potential avenue towards personalized medicine and building a better and more predictive model of tumor behavior.

Abonnenc, M., Dayon, L., Perruche, B., Lion, N., & Girault, H. H. (2008). Electrospray micromixer chip for on-line derivatization and kinetic studies. *Anal Chem, 80*(9), 3372-3378. doi:10.1021/ac800058h

Acerbi, I., Cassereau, L., Dean, I., Shi, Q., Au, A., Park, C., . . . Weaver, V. M. (2015). Human breast cancer invasion and aggression correlates with ECM stiffening and immune cell infiltration. *Integr Biol (Camb), 7*(10), 1120-1134. doi:10.1039/c5ib00040h

Akagi, K., Ikeda, Y., Miyazaki, M., Abe, T., Kinoshita, J., Maehara, Y., & Sugimachi, K. (2000). Vascular endothelial growth factor-C (VEGF-C) expression in human colorectal cancer tissues. *Br J Cancer, 83*(7), 887-891. doi:10.1054/bjoc.2000.1396

Alexeyenko, A., Alkasalias, T., Pavlova, T., Szekely, L., Kashuba, V., Rundqvist, H., . . . Klein, G. (2015). Confrontation of fibroblasts with cancer cells in vitro: gene network analysis of transcriptome changes and differential capacity to inhibit tumor growth. *J Exp Clin Cancer Res, 34*, 62. doi:10.1186/s13046-015-0178-x

Alkasalias, T., Alexeyenko, A., Hennig, K., Danielsson, F., Lebbink, R. J., Fielden, M., . . . Pavlova, T. (2017). RhoA knockout fibroblasts lose tumor-inhibitory capacity in vitro and promote tumor growth in vivo. *Proc Natl Acad Sci U S A, 114*(8), E1413-E1421. doi:10.1073/pnas.1621161114

Alkasalias, T., Flaberg, E., Kashuba, V., Alexeyenko, A., Pavlova, T., Savchenko, A., . . . Guven, H. (2014). Inhibition of tumor cell proliferation and motility by fibroblasts is both contact and soluble factor dependent. *Proc Natl Acad Sci U S A, 111*(48), 17188-17193. doi:10.1073/pnas.1419554111

Allinen, M., Beroukhim, R., Cai, L., Brennan, C., Lahti-Domenici, J., Huang, H., . . . Polyak, K. (2004). Molecular characterization of the tumor microenvironment in breast cancer. *Cancer Cell, 6*(1), 17-32. doi:10.1016/j.ccr.2004.06.010

Audia, A., Conroy, S., Glass, R., & Bhat, K. P. L. (2017). The Impact of the Tumor Microenvironment on the Properties of Glioma Stem-Like Cells. *Front Oncol, 7*, 143. doi:10.3389/fonc.2017.00143

Ayuso, J. M., Virumbrales-Munoz, M., Lacueva, A., Lanuza, P. M., Checa-Chavarria, E., Botella, P., . . . Ochoa, I. (2016). Development and characterization of a microfluidic model of the tumour microenvironment. *Sci Rep, 6*, 36086. doi:10.1038/srep36086

Balkwill, F., & Mantovani, A. (2001). Inflammation and cancer: back to Virchow? *Lancet, 357*(9255), 539-545. doi:10.1016/S0140-6736(00)04046-0

Bao, C., Kim, M. C., Chen, J., Song, J., Ko, H. W., & Lee, H. J. (2016). Sulforaphene Interferes with Human Breast Cancer Cell Migration and Invasion through Inhibition of Hedgehog Signaling. *J Agric Food Chem, 64*(27), 5515-5524. doi:10.1021/acs.jafc.6b02195

Bao, S., Wu, Q., McLendon, R. E., Hao, Y., Shi, Q., Hjelmeland, A. B., . . . Rich, J. N. (2006). Glioma stem cells promote radioresistance by preferential activation of the DNA damage response. *Nature, 444*(7120), 756-760. doi:10.1038/nature05236

Bardos, H., Molnar, P., Csecsei, G., & Adany, R. (1996). Fibrin deposition in primary and metastatic human brain tumours. *Blood Coagul Fibrinolysis, 7*(5), 536-548.

Bayne, L. J., Beatty, G. L., Jhala, N., Clark, C. E., Rhim, A. D., Stanger, B. Z., & Vonderheide, R. H. (2012). Tumor-derived granulocyte-macrophage colony-stimulating factor regulates myeloid inflammation and T cell immunity in pancreatic cancer. *Cancer Cell, 21*(6), 822-835. doi:10.1016/j.ccr.2012.04.025

Bersini, S., Jeon, J. S., Dubini, G., Arrigoni, C., Chung, S., Charest, J. L., . . . Kamm, R. D. (2014). A microfluidic 3D in vitro model for specificity of breast cancer metastasis to bone. *Biomaterials, 35*(8), 2454-2461. doi:10.1016/j.biomaterials.2013.11.050

Beyer, M., & Schultze, J. L. (2006). Regulatory T cells in cancer. *Blood, 108*(3), 804-811. doi:10.1182/blood-2006-02-002774

Bian, X. W., Yang, S. X., Chen, J. H., Ping, Y. F., Zhou, X. D., Wang, Q. L., . . . Wang, J. M. (2007). Preferential expression of chemokine receptor CXCR4 by highly malignant human gliomas and its association with poor patient survival. *Neurosurgery, 61*(3), 570-578; discussion 578-579. doi:10.1227/01.NEU.0000290905.53685.A2

Bissell, M. J., Radisky, D. C., Rizki, A., Weaver, V. M., & Petersen, O. W. (2002). The organizing principle: microenvironmental influences in the normal and malignant breast. *Differentiation, 70*(9-10), 537-546. doi:10.1046/j.1432-0436.2002.700907.x

Boghaert, E., Gleghorn, J. P., Lee, K., Gjorevski, N., Radisky, D. C., & Nelson, C. M. (2012). Host epithelial geometry regulates breast cancer cell invasiveness. *Proceedings of the National Academy of Sciences, 109*(48), 19632-19637. doi:10.1073/pnas.1118872109

Bremnes, R. M., Donnem, T., Al-Saad, S., Al-Shibli, K., Andersen, S., Sirera, R., . . . Busund, L. T. (2011). The role of tumor stroma in cancer progression and

prognosis: emphasis on carcinoma-associated fibroblasts and non-small cell lung cancer. *J Thorac Oncol, 6*(1), 209-217. doi:10.1097/JTO.0b013e3181f8a1bd

Breyer, R., Hussein, S., Radu, D. L., Putz, K. M., Gunia, S., Hecker, H., . . . Stan, A. C. (2000). Disruption of intracerebral progression of C6 rat glioblastoma by in vivo treatment with anti-CD44 monoclonal antibody. *J Neurosurg, 92*(1), 140-149. doi:10.3171/jns.2000.92.1.0140

Brockmann, M. A., Ulbricht, U., Gruner, K., Fillbrandt, R., Westphal, M., & Lamszus, K. (2003). Glioblastoma and cerebral microvascular endothelial cell migration in response to tumor-associated growth factors. *Neurosurgery, 52*(6), 1391-1399; discussion 1399.

Brown, C. K., Khodarev, N. N., Yu, J., Moo-Young, T., Labay, E., Darga, T. E., . . . Mauceri, H. J. (2004). Glioblastoma cells block radiation-induced programmed cell death of endothelial cells. *FEBS Lett, 565*(1-3), 167-170. doi:10.1016/j.febslet.2004.03.099

Bruna, A., Darken, R. S., Rojo, F., Ocana, A., Penuelas, S., Arias, A., . . . Seoane, J. (2007). High TGFbeta-Smad activity confers poor prognosis in glioma patients and promotes cell proliferation depending on the methylation of the PDGF-B gene. *Cancer Cell, 11*(2), 147-160. doi:10.1016/j.ccr.2006.11.023

Cabioglu, N., Yazici, M. S., Arun, B., Broglio, K. R., Hortobagyi, G. N., Price, J. E., & Sahin, A. (2005). CCR7 and CXCR4 as novel biomarkers predicting axillary lymph node metastasis in T1 breast cancer. *Clinical Cancer Research, 11*(16), 5686-5693.

Calabrese, C., Poppleton, H., Kocak, M., Hogg, T. L., Fuller, C., Hamner, B., . . . Gilbertson, R. J. (2007). A perivascular niche for brain tumor stem cells. *Cancer Cell, 11*(1), 69-82. doi:10.1016/j.ccr.2006.11.020

Camp, J. T., Elloumi, F., Roman-Perez, E., Rein, J., Stewart, D. A., Harrell, J. C., . . . Troester, M. A. (2011). Interactions with fibroblasts are distinct in Basal-like and luminal breast cancers. *Mol Cancer Res, 9*(1), 3-13. doi:10.1158/1541-7786.MCR-10-0372

Campbell, L. L., & Polyak, K. (2007). Breast tumor heterogeneity: cancer stem cells or clonal evolution? *Cell Cycle, 6*(19), 2332-2338.

Cancer Genome Atlas, N. (2012). Comprehensive molecular portraits of human breast tumours. *Nature, 490*(7418), 61-70. doi:10.1038/nature11412

Carey, S. P., Starchenko, A., McGregor, A. L., & Reinhart-King, C. A. (2013). Leading malignant cells initiate collective epithelial cell invasion in a three-dimensional

heterotypic tumor spheroid model. *Clinical & Experimental Metastasis, 30*(5), 615-630. doi:10.1007/s10585-013-9565-x

Carmeliet, P., & Jain, R. K. (2000). Angiogenesis in cancer and other diseases. *Nature, 407*(6801), 249-257. doi:10.1038/35025220

Carper, M. B., Boskovic, G., Denvir, J., Primerano, D., Hardman, W. E., & Claudio, P. P. (2013). Investigation of RGS16 mediated inhibition of pancreatic cancer metastasis. *The FASEB Journal, 27*(1 Supplement), 611.616-611.616.

Casey, T., Bond, J., Tighe, S., Hunter, T., Lintault, L., Patel, O., . . . Plaut, K. (2009). Molecular signatures suggest a major role for stromal cells in development of invasive breast cancer. *Breast Cancer Res Treat, 114*(1), 47-62. doi:10.1007/s10549-008-9982-8

Castells, M., Thibault, B., Delord, J. P., & Couderc, B. (2012). Implication of tumor microenvironment in chemoresistance: tumor-associated stromal cells protect tumor cells from cell death. *Int J Mol Sci, 13*(8), 9545-9571. doi:10.3390/ijms13089545

Cerami, E., Gao, J., Dogrusoz, U., Gross, B. E., Sumer, S. O., Aksoy, B. A., . . . Schultz, N. (2012). The cBio cancer genomics portal: an open platform for exploring multidimensional cancer genomics data. *Cancer Discov, 2*(5), 401-404. doi:10.1158/2159-8290.CD-12-0095

Chang, H. Y., Sneddon, J. B., Alizadeh, A. A., Sood, R., West, R. B., Montgomery, K., . . . Brown, P. O. (2004). Gene expression signature of fibroblast serum response predicts human cancer progression: similarities between tumors and wounds. *PLoS Biol, 2*(2), E7. doi:10.1371/journal.pbio.0020007

Charles, N., Ozawa, T., Squatrito, M., Bleau, A. M., Brennan, C. W., Hambardzumyan, D., & Holland, E. C. (2010). Perivascular nitric oxide activates notch signaling and promotes stem-like character in PDGF-induced glioma cells. *Cell Stem Cell, 6*(2), 141-152. doi:10.1016/j.stem.2010.01.001

Chen, H., & Nalbantoglu, J. (2014). Ring cell migration assay identifies distinct effects of extracellular matrix proteins on cancer cell migration. *BMC Res Notes, 7*, 183. doi:10.1186/1756-0500-7-183

Cheng, L., Alexander, R. E., Maclennan, G. T., Cummings, O. W., Montironi, R., Lopez-Beltran, A., . . . Zhang, S. (2012). Molecular pathology of lung cancer: key to personalized medicine. *Mod Pathol, 25*(3), 347-369. doi:10.1038/modpathol.2011.215

Choi, S. Y., Lin, D., Gout, P. W., Collins, C. C., Xu, Y., & Wang, Y. (2014). Lessons from patient-derived xenografts for better in vitro modeling of human cancer. *Adv Drug Deliv Rev, 79-80*, 222-237. doi:10.1016/j.addr.2014.09.009

Chonan, Y., Taki, S., Sampetrean, O., Saya, H., & Sudo, R. (2017). Endothelium-induced three-dimensional invasion of heterogeneous glioma initiating cells in a microfluidic coculture platform. *Integr Biol (Camb), 9*(9), 762-773. doi:10.1039/c7ib00091j

Christiansen, A., & Detmar, M. (2011). Lymphangiogenesis and cancer. *Genes Cancer, 2*(12), 1146-1158. doi:10.1177/1947601911423028

Chung, S., Sudo, R., Mack, P. J., Wan, C. R., Vickerman, V., & Kamm, R. D. (2009). Cell migration into scaffolds under co-culture conditions in a microfluidic platform. *Lab Chip, 9*(2), 269-275. doi:10.1039/b807585a

Conklin, M. W., & Keely, P. J. (2012). Why the stroma matters in breast cancer: insights into breast cancer patient outcomes through the examination of stromal biomarkers. *Cell Adh Migr, 6*(3), 249-260. doi:10.4161/cam.20567

Costello, J. C., Heiser, L. M., Georgii, E., Gonen, M., Menden, M. P., Wang, N. J., . . . Stolovitzky, G. (2014). A community effort to assess and improve drug sensitivity prediction algorithms. *Nat Biotechnol, 32*(12), 1202-1212. doi:10.1038/nbt.2877

Cox, M. C., Reese, L. M., Bickford, L. R., & Verbridge, S. S. (2015). Toward the Broad Adoption of 3D Tumor Models in the Cancer Drug Pipeline. *ACS Biomaterials Science & Engineering, 1*(10), 877-894. doi:10.1021/acsbiomaterials.5b00172

Cui, X., Morales, R. T., Qian, W., Wang, H., Gagner, J. P., Dolgalev, I., . . . Chen, W. (2018). Hacking macrophage-associated immunosuppression for regulating glioblastoma angiogenesis. *Biomaterials, 161*, 164-178. doi:10.1016/j.biomaterials.2018.01.053

Curiel, T. J. (2007). Tregs and rethinking cancer immunotherapy. *J Clin Invest, 117*(5), 1167-1174. doi:10.1172/JCI31202

Curiel, T. J., Coukos, G., Zou, L., Alvarez, X., Cheng, P., Mottram, P., . . . Zou, W. (2004). Specific recruitment of regulatory T cells in ovarian carcinoma fosters immune privilege and predicts reduced survival. *Nat Med, 10*(9), 942-949. doi:10.1038/nm1093

Curtis, C., Shah, S. P., Chin, S. F., Turashvili, G., Rueda, O. M., Dunning, M. J., . . . Aparicio, S. (2012). The genomic and transcriptomic architecture of 2,000 breast tumours reveals novel subgroups. *Nature, 486*(7403), 346-352. doi:10.1038/nature10983

Deisboeck, T. S., Berens, M. E., Kansal, A. R., Torquato, S., Stemmer-Rachamimov, A. O., & Chiocca, E. A. (2001). Pattern of self-organization in tumour systems: complex growth dynamics in a novel brain tumour spheroid model. *Cell Prolif, 34*(2), 115-134.

dit Faute, M. A., Laurent, L., Ploton, D., Poupon, M. F., Jardillier, J. C., & Bobichon, H. (2002). Distinctive alterations of invasiveness, drug resistance and cell-cell organization in 3D-cultures of MCF-7, a human breast cancer cell line, and its multidrug resistant variant. *Clin Exp Metastasis, 19*(2), 161-168.

Dobin, A., & Gingeras, T. R. (2015). Mapping RNA-seq Reads with STAR. *Curr Protoc Bioinformatics, 51*, 11 14 11-19. doi:10.1002/0471250953.bi1114s51

Dudu, V., Able, R. A., Jr., Rotari, V., Kong, Q., & Vazquez, M. (2012). Role of Epidermal Growth Factor-Triggered PI3K/Akt Signaling in the Migration of Medulloblastoma-Derived Cells. *Cell Mol Bioeng, 5*(4), 502-413.

Dvorak, H. F. (1986). Tumors: wounds that do not heal. *New England Journal of Medicine, 315*(26), 1650-1659.

Dvorak, H. F. (1986). Tumors: wounds that do not heal. Similarities between tumor stroma generation and wound healing. *N Engl J Med, 315*(26), 1650-1659. doi:10.1056/NEJM198612253152606

Dvorak, H. F. (2015). Tumors: wounds that do not heal-redux. *Cancer Immunol Res, 3*(1), 1-11. doi:10.1158/2326-6066.CIR-14-0209

Egeblad, M., Rasch, M. G., & Weaver, V. M. (2010). Dynamic interplay between the collagen scaffold and tumor evolution. *Curr Opin Cell Biol, 22*(5), 697-706. doi:10.1016/j.ceb.2010.08.015

Ehtesham, M., Mapara, K. Y., Stevenson, C. B., & Thompson, R. C. (2009). CXCR4 mediates the proliferation of glioblastoma progenitor cells. *Cancer Lett, 274*(2), 305-312. doi:10.1016/j.canlet.2008.09.034

Erez, N., Truitt, M., Olson, P., Arron, S. T., & Hanahan, D. (2010). Cancer-Associated Fibroblasts Are Activated in Incipient Neoplasia to Orchestrate Tumor-Promoting Inflammation in an NF-kappaB-Dependent Manner. *Cancer Cell, 17*(2), 135-147. doi:10.1016/j.ccr.2009.12.041

Evans, R. A., Tian, Y. C., Steadman, R., & Phillips, A. O. (2003). TGF-beta1-mediated fibroblast-myofibroblast terminal differentiation-the role of Smad proteins. *Exp Cell Res, 282*(2), 90-100.

Even-Ram, S., & Yamada, K. M. (2005). Cell migration in 3D matrix. *Curr Opin Cell Biol, 17*(5), 524-532. doi:10.1016/j.ceb.2005.08.015

Evers, P., Lee, P. P., DeMarco, J., Agazaryan, N., Sayre, J. W., Selch, M., & Pajonk, F. (2010). Irradiation of the potential cancer stem cell niches in the adult brain improves progression-free survival of patients with malignant glioma. *BMC Cancer, 10*, 384. doi:10.1186/1471-2407-10-384

Faber, A., Aderhold, C., Goessler, U. R., Hoermann, K., Schultz, J. D., Umbreit, C., . . . Stern-Straeter, J. (2014). Interaction of a CD44+ head and neck squamous cell carcinoma cell line with a stromal cell-derived factor-1-expressing supportive niche: An in vitro model. *Oncol Lett, 7*(1), 82-86. doi:10.3892/ol.2013.1673

Farahat, W. A., Wood, L. B., Zervantonakis, I. K., Schor, A., Ong, S., Neal, D., . . . Asada, H. H. (2012). Ensemble analysis of angiogenic growth in three-dimensional microfluidic cell cultures. *PLoS ONE, 7*(5), e37333. doi:10.1371/journal.pone.0037333

Feng, X., Liu, B. F., Li, J., & Liu, X. (2015). Advances in coupling microfluidic chips to mass spectrometry. *Mass Spectrom Rev, 34*(5), 535-557. doi:10.1002/mas.21417

Finak, G., Bertos, N., Pepin, F., Sadekova, S., Souleimanova, M., Zhao, H., . . . Park, M. (2008). Stromal gene expression predicts clinical outcome in breast cancer. *Nat Med, 14*(5), 518-527. doi:10.1038/nm1764

Fiorentini, C., Bodei, S., Bedussi, F., Fragni, M., Bonini, S. A., Simeone, C., . . . Sigala, S. (2014). GPNMB/OA protein increases the invasiveness of human metastatic prostate cancer cell lines DU145 and PC3 through MMP-2 and MMP-9 activity. *Exp Cell Res, 323*(1), 100-111. doi:10.1016/j.yexcr.2014.02.025

Florin, L., Maas-Szabowski, N., Werner, S., Szabowski, A., & Angel, P. (2005). Increased keratinocyte proliferation by JUN-dependent expression of PTN and SDF-1 in fibroblasts. *J Cell Sci, 118*(Pt 9), 1981-1989. doi:10.1242/jcs.02303

Fraley, S. I., Feng, Y., Krishnamurthy, R., Kim, D. H., Celedon, A., Longmore, G. D., & Wirtz, D. (2010). A distinctive role for focal adhesion proteins in three-dimensional cell motility. *Nat Cell Biol, 12*(6), 598-604. doi:10.1038/ncb2062

Franco-Barraza, J., Beacham, D. A., Amatangelo, M. D., & Cukierman, E. (2016). Preparation of Extracellular Matrices Produced by Cultured and Primary Fibroblasts. *Curr Protoc Cell Biol, 71*, 10 19 11-10 19 34. doi:10.1002/cpcb.2

Friedl, P., & Alexander, S. (2011). Cancer invasion and the microenvironment: plasticity and reciprocity. *Cell, 147*(5), 992-1009. doi:10.1016/j.cell.2011.11.016

Friedl, P., & Wolf, K. (2003). Tumour-cell invasion and migration: diversity and escape mechanisms. *Nat Rev Cancer, 3*(5), 362-374. doi:10.1038/nrc1075

Gaggioli, C., Hooper, S., Hidalgo-Carcedo, C., Grosse, R., Marshall, J. F., Harrington, K., & Sahai, E. (2007). Fibroblast-led collective invasion of carcinoma cells with differing roles for RhoGTPases in leading and following cells. *Nat Cell Biol, 9*(12), 1392-1400. doi:10.1038/ncb1658

Galan-Moya, E. M., Le Guelte, A., Lima Fernandes, E., Thirant, C., Dwyer, J., Bidere, N., . . . Gavard, J. (2011). Secreted factors from brain endothelial cells maintain glioblastoma stem-like cell expansion through the mTOR pathway. *Embo Reports, 12*(5), 470-476. doi:10.1038/embor.2011.39

Gao, J., Aksoy, B. A., Dogrusoz, U., Dresdner, G., Gross, B., Sumer, S. O., . . . Schultz, N. (2013). Integrative analysis of complex cancer genomics and clinical profiles using the cBioPortal. *Sci Signal, 6*(269), pl1. doi:10.1126/scisignal.2004088

Garnett, M. J., Edelman, E. J., Heidorn, S. J., Greenman, C. D., Dastur, A., Lau, K. W., . . . Benes, C. H. (2012). Systematic identification of genomic markers of drug sensitivity in cancer cells. *Nature, 483*(7391), 570-575. doi:10.1038/nature11005

Gerstner, E. R., & Batchelor, T. T. (2012). Antiangiogenic therapy for glioblastoma. *Cancer J, 18*(1), 45-50. doi:10.1097/PPO.0b013e3182431c6f

Giannoni, E., Bianchini, F., Masieri, L., Serni, S., Torre, E., Calorini, L., & Chiarugi, P. (2010). Reciprocal activation of prostate cancer cells and cancer-associated fibroblasts stimulates epithelial-mesenchymal transition and cancer stemness. *Cancer Res, 70*(17), 6945-6956. doi:10.1158/0008-5472.CAN-10-0785

Gioiella, F., Urciuolo, F., Imparato, G., Brancato, V., & Netti, P. A. (2016). An Engineered Breast Cancer Model on a Chip to Replicate ECM-Activation In Vitro during Tumor Progression. *Adv Healthc Mater, 5*(23), 3074-3084. doi:10.1002/adhm.201600772

Glentis, A., Oertle, P., Mariani, P., Chikina, A., El Marjou, F., Attieh, Y., . . . Vignjevic, D. M. (2017). Cancer-associated fibroblasts induce metalloprotease-independent cancer cell invasion of the basement membrane. *Nat Commun, 8*(1), 924. doi:10.1038/s41467-017-00985-8

Goswami, S., Sahai, E., Wyckoff, J. B., Cammer, M., Cox, D., Pixley, F. J., . . . Condeelis, J. S. (2005). Macrophages promote the invasion of breast carcinoma cells via a colony-stimulating factor-1/epidermal growth factor paracrine loop. *Cancer Res, 65*(12), 5278-5283. doi:10.1158/0008-5472.CAN-04-1853

Grasman, J. M., & Kaplan, D. L. (2017). Human endothelial cells secrete neurotropic factors to direct axonal growth of peripheral nerves. *Sci Rep, 7*(1), 4092. doi:10.1038/s41598-017-04460-8

Gritsenko, P., Leenders, W., & Friedl, P. (2017). Recapitulating in vivo-like plasticity of glioma cell invasion along blood vessels and in astrocyte-rich stroma. *Histochem Cell Biol, 148*(4), 395-406. doi:10.1007/s00418-017-1604-2

Grundy, T. J., De Leon, E., Griffin, K. R., Stringer, B. W., Day, B. W., Fabry, B., . . . O'Neill, G. M. (2016). Differential response of patient-derived primary glioblastoma cells to environmental stiffness. *Sci Rep, 6*, 23353. doi:10.1038/srep23353

Guo, Y., Liu, S., Wang, P., Zhao, S., Wang, F., Bing, L., . . . Hao, A. (2011). Expression profile of embryonic stem cell-associated genes Oct4, Sox2 and Nanog in human gliomas. *Histopathology, 59*(4), 763-775. doi:10.1111/j.1365-2559.2011.03993.x

Gupta, G. P., & Massague, J. (2006). Cancer metastasis: building a framework. *Cell, 127*(4), 679-695. doi:10.1016/j.cell.2006.11.001

Ha, S. Y., Yeo, S. Y., Xuan, Y. H., & Kim, S. H. (2014). The prognostic significance of cancer-associated fibroblasts in esophageal squamous cell carcinoma. *PLoS One, 9*(6), e99955. doi:10.1371/journal.pone.0099955

Haessler, U., Kalinin, Y., Swartz, M. A., & Wu, M. (2009). An agarose-based microfluidic platform with a gradient buffer for 3D chemotaxis studies. *Biomed Microdevices, 11*(4), 827-835. doi:10.1007/s10544-009-9299-3

Hagemann, T., Robinson, S. C., Schulz, M., Trumper, L., Balkwill, F. R., & Binder, C. (2004). Enhanced invasiveness of breast cancer cell lines upon co-cultivation with macrophages is due to TNF-alpha dependent up-regulation of matrix metalloproteases. *Carcinogenesis, 25*(8), 1543-1549. doi:10.1093/carcin/bgh146

Hambardzumyan, D., & Bergers, G. (2015). Glioblastoma: Defining Tumor Niches. *Trends Cancer, 1*(4), 252-265. doi:10.1016/j.trecan.2015.10.009

Hanahan, D., & Coussens, L. M. (2012). Accessories to the crime: functions of cells recruited to the tumor microenvironment. *Cancer Cell, 21*(3), 309-322. doi:10.1016/j.ccr.2012.02.022

Hanahan, D., & Weinberg, R. A. (2011). Hallmarks of cancer: the next generation. *Cell, 144*(5), 646-674. doi:10.1016/j.cell.2011.02.013

Heffernan, J. M., McNamara, J. B., Borwege, S., Vernon, B. L., Sanai, N., Mehta, S., & Sirianni, R. W. (2017). PNIPAAm-co-Jeffamine((R)) (PNJ) scaffolds as in vitro

models for niche enrichment of glioblastoma stem-like cells. *Biomaterials, 143*, 149-158. doi:10.1016/j.biomaterials.2017.05.007

Henriksson, M. L., Edin, S., Dahlin, A. M., Oldenborg, P. A., Oberg, A., Van Guelpen, B., . . . Palmqvist, R. (2011). Colorectal cancer cells activate adjacent fibroblasts resulting in FGF1/FGFR3 signaling and increased invasion. *Am J Pathol, 178*(3), 1387-1394. doi:10.1016/j.ajpath.2010.12.008

Hirakawa, S., Brown, L. F., Kodama, S., Paavonen, K., Alitalo, K., & Detmar, M. (2007). VEGF-C-induced lymphangiogenesis in sentinel lymph nodes promotes tumor metastasis to distant sites. *Blood, 109*(3), 1010-1017. doi:10.1182/blood-2006-05-021758

Hirakawa, S., Detmar, M., Kerjaschki, D., Nagamatsu, S., Matsuo, K., Tanemura, A., . . . Hashimoto, K. (2009). Nodal lymphangiogenesis and metastasis: Role of tumor-induced lymphatic vessel activation in extramammary Paget's disease. *Am J Pathol, 175*(5), 2235-2248. doi:10.2353/ajpath.2009.090420

Huang, C. P., Lu, J., Seon, H., Lee, A. P., Flanagan, L. A., Kim, H. Y., . . . Jeon, N. L. (2009). Engineering microscale cellular niches for three-dimensional multicellular co-cultures. *Lab Chip, 9*(12), 1740-1748. doi:10.1039/b818401a

Huang, Y. L., Segall, J. E., & Wu, M. (2017). Microfluidic modeling of the biophysical microenvironment in tumor cell invasion. *Lab Chip, 17*(19), 3221-3233. doi:10.1039/c7lc00623c

Hughes-Alford, S. K., & Lauffenburger, D. A. (2012). Quantitative analysis of gradient sensing: towards building predictive models of chemotaxis in cancer. *Curr Opin Cell Biol, 24*(2), 284-291. doi:10.1016/j.ceb.2012.01.001

Huh, D., Hamilton, G. A., & Ingber, D. E. (2011). From 3D cell culture to organs-on-chips. *Trends Cell Biol, 21*(12), 745-754. doi:10.1016/j.tcb.2011.09.005

Hutmacher, D. W., Loessner, D., Rizzi, S., Kaplan, D. L., Mooney, D. J., & Clements, J. A. (2010). Can tissue engineering concepts advance tumor biology research? *Trends Biotechnol, 28*(3), 125-133. doi:10.1016/j.tibtech.2009.12.001

Infanger, D. W., Cho, Y., Lopez, B. S., Mohanan, S., Liu, S. C., Gursel, D., . . . Fischbach, C. (2013). Glioblastoma stem cells are regulated by interleukin-8 signaling in a tumoral perivascular niche. *Cancer Res, 73*(23), 7079-7089. doi:10.1158/0008-5472.CAN-13-1355

Jain, R. K., Duda, D. G., Clark, J. W., & Loeffler, J. S. (2006). Lessons from phase III clinical trials on anti-VEGF therapy for cancer. *Nature Clinical Practice Oncology, 3*, 24-40. doi:10.1038/ncponc0403

Jain, R. K., Koenig, G. C., Dellian, M., Fukumura, D., Munn, L. L., & Melder, R. J. (1996). Leukocyte-endothelial adhesion and angiogenesis in tumors. *Cancer Metastasis Rev, 15*(2), 195-204.

Jensen, S. S., Meyer, M., Petterson, S. A., Halle, B., Rosager, A. M., Aaberg-Jessen, C., . . . Kristensen, B. W. (2016). Establishment and Characterization of a Tumor Stem Cell-Based Glioblastoma Invasion Model. *PLoS One, 11*(7), e0159746. doi:10.1371/journal.pone.0159746

Jeon, J. S., Bersini, S., Gilardi, M., Dubini, G., Charest, J. L., Moretti, M., & Kamm, R. D. (2015). Human 3D vascularized organotypic microfluidic assays to study breast cancer cell extravasation. *Proc Natl Acad Sci U S A, 112*(1), 214-219. doi:10.1073/pnas.1417115112

Jeon, J. S., Bersini, S., Whisler, J. A., Chen, M. B., Dubini, G., Charest, J. L., . . . Kamm, R. D. (2014). Generation of 3D functional microvascular networks with human mesenchymal stem cells in microfluidic systems. *Integrative Biology, 6*(5), 555-563. doi:10.1039/c3ib40267c

Jeong, S.-Y., Lee, J.-H., Shin, Y., Chung, S., & Kuh, H.-J. (2016). Co-Culture of Tumor Spheroids and Fibroblasts in a Collagen Matrix-Incorporated Microfluidic Chip Mimics Reciprocal Activation in Solid Tumor Microenvironment. *PLOS ONE, 11*(7), e0159013. doi:10.1371/journal.pone.0159013

Jia, C. C., Wang, T. T., Liu, W., Fu, B. S., Hua, X., Wang, G. Y., . . . Zhang, Q. (2013). Cancer-associated fibroblasts from hepatocellular carcinoma promote malignant cell proliferation by HGF secretion. *PLoS One, 8*(5), e63243. doi:10.1371/journal.pone.0063243

Jiang, Z., Zhou, W., Guan, S., Wang, J., & Liang, Y. (2013). Contribution of SDF-1alpha/CXCR4 signaling to brain development and glioma progression. *Neurosignals, 21*(3-4), 240-258. doi:10.1159/000339091

Jimenez Valencia, A. M., Wu, P.-H., Yogurtcu, O. N., Rao, P., DiGiacomo, J., Godet, I., . . . Wirtz, D. (2015). *Collective cancer cell invasion induced by coordinated contractile stresses*.

Joyce, J. A., & Pollard, J. W. (2009). Microenvironmental regulation of metastasis. *Nat Rev Cancer, 9*(4), 239-252. doi:10.1038/nrc2618

Kaemmerer, E., Melchels, F. P. W., Holzapfel, B. M., Meckel, T., Hutmacher, D. W., & Loessner, D. (2014). Gelatine methacrylamide-based hydrogels: An alternative three-dimensional cancer cell culture system. *Acta Biomaterialia, 10*(6), 2551-2562. doi:10.1016/j.actbio.2014.02.035

Kalluri, R. (2016). The biology and function of fibroblasts in cancer. *Nat Rev Cancer, 16*(9), 582-598. doi:10.1038/nrc.2016.73

Kalluri, R., & Zeisberg, M. (2006). Fibroblasts in cancer. *Nat Rev Cancer, 6*(5), 392-401. doi:10.1038/nrc1877

Karagiannis, G. S., Schaeffer, D. F., Cho, C. K., Musrap, N., Saraon, P., Batruch, I., . . . Diamandis, E. P. (2014). Collective migration of cancer-associated fibroblasts is enhanced by overexpression of tight junction-associated proteins claudin-11 and occludin. *Mol Oncol, 8*(2), 178-195. doi:10.1016/j.molonc.2013.10.008

Kerbel, R. S. (2008). Tumor angiogenesis. *N Engl J Med, 358*(19), 2039-2049. doi:10.1056/NEJMra0706596

Khamis, Z. I., Sahab, Z. J., & Sang, Q. X. (2012). Active roles of tumor stroma in breast cancer metastasis. *Int J Breast Cancer, 2012*, 574025. doi:10.1155/2012/574025

Kim, B. J., Hannanta-anan, P., Chau, M., Kim, Y. S., Swartz, M. A., & Wu, M. (2013). Cooperative roles of SDF-1alpha and EGF gradients on tumor cell migration revealed by a robust 3D microfluidic model. *PLoS ONE, 8*(7), e68422. doi:10.1371/journal.pone.0068422

Kim, C., Kasuya, J., Jeon, J., Chung, S., & Kamm, R. D. (2015). A quantitative microfluidic angiogenesis screen for studying anti-angiogenic therapeutic drugs. *Lab Chip, 15*(1), 301-310. doi:10.1039/c4lc00866a

Kim, J., Chung, M., Kim, S., Jo, D. H., Kim, J. H., & Jeon, N. L. (2015). Engineering of a Biomimetic Pericyte-Covered 3D Microvascular Network. *PLoS One, 10*(7), e0133880. doi:10.1371/journal.pone.0133880

Kim, M., Koh, Y. J., Kim, K. E., Koh, B. I., Nam, D. H., Alitalo, K., . . . Koh, G. Y. (2010). CXCR4 signaling regulates metastasis of chemoresistant melanoma cells by a lymphatic metastatic niche. *Cancer Res, 70*(24), 10411-10421. doi:10.1158/0008-5472.CAN-10-2591

Kim, S., Lee, H., Chung, M., & Jeon, N. L. (2013). Engineering of functional, perfusable 3D microvascular networks on a chip. *Lab Chip, 13*(8), 1489-1500. doi:10.1039/c3lc41320a

Kim, S. A., Lee, E. K., & Kuh, H. J. (2015). Co-culture of 3D tumor spheroids with fibroblasts as a model for epithelial-mesenchymal transition in vitro. *Exp Cell Res, 335*(2), 187-196. doi:10.1016/j.yexcr.2015.05.016

Kim, Y., Kim, E., Wu, Q., Guryanova, O., Hitomi, M., Lathia, J. D., . . . Rich, J. N. (2012). Platelet-derived growth factor receptors differentially inform intertumoral

and intratumoral heterogeneity. *Genes Dev, 26*(11), 1247-1262. doi:10.1101/gad.193565.112

Kioi, M., Vogel, H., Schultz, G., Hoffman, R. M., Harsh, G. R., & Brown, J. M. (2010). Inhibition of vasculogenesis, but not angiogenesis, prevents the recurrence of glioblastoma after irradiation in mice. *The Journal of clinical investigation, 120*(3), 694-705.

Knowlton, S., Onal, S., Yu, C. H., Zhao, J. J., & Tasoglu, S. (2015). Bioprinting for cancer research. *Trends Biotechnol, 33*(9), 504-513. doi:10.1016/j.tibtech.2015.06.007

Kolde, R. (2015). Pretty Heatmaps: CRAN.

Kopanska, K. S., Alcheikh, Y., Staneva, R., Vignjevic, D., & Betz, T. (2016). Tensile Forces Originating from Cancer Spheroids Facilitate Tumor Invasion. *PLOS ONE, 11*(6), e0156442. doi:10.1371/journal.pone.0156442

Kothapalli, C. R., & Honarmandi, P. (2014). Theoretical and experimental quantification of the role of diffusive chemogradients on neuritogenesis within three-dimensional collagen scaffolds. *Acta Biomater, 10*(8), 3664-3674. doi:10.1016/j.actbio.2014.05.009

Kramer, R. H., & Nicolson, G. L. (1979). Interactions of tumor cells with vascular endothelial cell monolayers: a model for metastatic invasion. *Proc Natl Acad Sci U S A, 76*(11), 5704-5708.

Kraning-Rush, C. M., Carey, S. P., Lampi, M. C., & Reinhart-King, C. A. (2013). Microfabricated collagen tracks facilitate single cell metastatic invasion in 3D. *Integr Biol (Camb), 5*(3), 606-616. doi:10.1039/c3ib20196a

Kurebayashi, J., Otsuki, T., Kunisue, H., Mikami, Y., Tanaka, K., Yamamoto, S., & Sonoo, H. (1999). Expression of vascular endothelial growth factor (VEGF) family members in breast cancer. *Jpn J Cancer Res, 90*(9), 977-981.

Lammermann, T., Bader, B. L., Monkley, S. J., Worbs, T., Wedlich-Soldner, R., Hirsch, K., . . . Sixt, M. (2008). Rapid leukocyte migration by integrin-independent flowing and squeezing. *Nature, 453*(7191), 51-55. doi:10.1038/nature06887

Lathia, J. D., Gallagher, J., Myers, J. T., Li, M., Vasanji, A., McLendon, R. E., . . . Rich, J. N. (2011). Direct in vivo evidence for tumor propagation by glioblastoma cancer stem cells. *PLoS One, 6*(9), e24807. doi:10.1371/journal.pone.0024807

Lathia, J. D., Mack, S. C., Mulkearns-Hubert, E. E., Valentim, C. L., & Rich, J. N. (2015). Cancer stem cells in glioblastoma. *Genes Dev, 29*(12), 1203-1217. doi:10.1101/gad.261982.115

Le Bras, G. F., Taylor, C., Koumangoye, R. B., Revetta, F., Loomans, H. A., & Andl, C. D. (2015). TGFbeta loss activates ADAMTS-1-mediated EGF-dependent invasion in a model of esophageal cell invasion. *Exp Cell Res, 330*(1), 29-42. doi:10.1016/j.yexcr.2014.07.021

Lee, H., Kim, S., Chung, M., Kim, J. H., & Jeon, N. L. (2014). A bioengineered array of 3D microvessels for vascular permeability assay. *Microvasc Res, 91*, 90-98. doi:10.1016/j.mvr.2013.12.001

Lee, H., Park, W., Ryu, H., & Jeon, N. L. (2014). A microfluidic platform for quantitative analysis of cancer angiogenesis and intravasation. *Biomicrofluidics, 8*(5), 054102. doi:10.1063/1.4894595

Lee, J. M., Mhawech-Fauceglia, P., Lee, N., Parsanian, L. C., Lin, Y. G., Gayther, S. A., & Lawrenson, K. (2013). A three-dimensional microenvironment alters protein expression and chemosensitivity of epithelial ovarian cancer cells in vitro. *Laboratory Investigation; a Journal of Technical Methods and Pathology, 93*, 528-542. doi:10.1038/labinvest.2013.41

Lee, K., Zhang, H., Qian, D. Z., Rey, S., Liu, J. O., & Semenza, G. L. (2009). Acriflavine inhibits HIF-1 dimerization, tumor growth, and vascularization. *Proc Natl Acad Sci U S A, 106*(42), 17910-17915. doi:10.1073/pnas.0909353106

Li, Z., Bao, S., Wu, Q., Wang, H., Eyler, C., Sathornsumetee, S., . . . Rich, J. N. (2009). Hypoxia-inducible factors regulate tumorigenic capacity of glioma stem cells. *Cancer Cell, 15*(6), 501-513. doi:10.1016/j.ccr.2009.03.018

Ligon, K. L., Huillard, E., Mehta, S., Kesari, S., Liu, H., Alberta, J. A., . . . Rowitch, D. H. (2007). Olig2-regulated lineage-restricted pathway controls replication competence in neural stem cells and malignant glioma. *Neuron, 53*(4), 503-517. doi:10.1016/j.neuron.2007.01.009

Liu, C., Pham, K., Luo, D., Reynolds, B. A., Hothi, P., Foltz, G., & Harrison, J. K. (2013). Expression and functional heterogeneity of chemokine receptors CXCR4 and CXCR7 in primary patient-derived glioblastoma cells. *PLoS One, 8*(3), e59750. doi:10.1371/journal.pone.0059750

Liu, J. M., Zhao, K., Du, L. X., Zhou, Y., Long, X. H., Chen, X. Y., & Liu, Z. L. (2017). AMD3100 inhibits the migration and differentiation of neural stem cells after spinal cord injury. *Sci Rep, 7*(1), 64. doi:10.1038/s41598-017-00141-8

Loessner, D., Stok, K. S., Lutolf, M. P., Hutmacher, D. W., Clements, J. A., & Rizzi, S. C. (2010). Bioengineered 3D platform to explore cell-ECM interactions and drug resistance of epithelial ovarian cancer cells. *Biomaterials, 31*(32), 8494-8506. doi:10.1016/j.biomaterials.2010.07.064

Lois, C., Garcia-Verdugo, J. M., & Alvarez-Buylla, A. (1996). Chain migration of neuronal precursors. *Science, 271*(5251), 978-981.

Lu, P., Weaver, V. M., & Werb, Z. (2012). The extracellular matrix: a dynamic niche in cancer progression. *J Cell Biol, 196*(4), 395-406. doi:10.1083/jcb.201102147

Luo, H., Tu, G., Liu, Z., & Liu, M. (2015). Cancer-associated fibroblasts: a multifaceted driver of breast cancer progression. *Cancer Lett, 361*(2), 155-163. doi:10.1016/j.canlet.2015.02.018

Ma, H., Liu, T., Qin, J., & Lin, B. (2010). Characterization of the interaction between fibroblasts and tumor cells on a microfluidic co-culture device. *Electrophoresis, 31*(10), 1599-1605. doi:10.1002/elps.200900776

Ma, L., Teruya-Feldstein, J., & Weinberg, R. A. (2007). Tumour invasion and metastasis initiated by microRNA-10b in breast cancer. *Nature, 449*(7163), 682-688. doi:10.1038/nature06174

Ma, X. J., Dahiya, S., Richardson, E., Erlander, M., & Sgroi, D. C. (2009). Gene expression profiling of the tumor microenvironment during breast cancer progression. *Breast Cancer Res, 11*(1), R7. doi:10.1186/bcr2222

Mak, I. W., Evaniew, N., & Ghert, M. (2014). Lost in translation: animal models and clinical trials in cancer treatment. *Am J Transl Res, 6*(2), 114-118.

Mao, Y., Keller, E. T., Garfield, D. H., Shen, K., & Wang, J. (2013). Stromal cells in tumor microenvironment and breast cancer. *Cancer Metastasis Rev, 32*(1-2), 303-315. doi:10.1007/s10555-012-9415-3

Maric, G., Annis, M. G., Dong, Z., Rose, A. A., Ng, S., Perkins, D., . . . Siegel, P. M. (2015). GPNMB cooperates with neuropilin-1 to promote mammary tumor growth and engages integrin alpha5beta1 for efficient breast cancer metastasis. *Oncogene, 34*(43), 5494-5504. doi:10.1038/onc.2015.8

McMillin, D. W., Negri, J. M., & Mitsiades, C. S. (2013). The role of tumour-stromal interactions in modifying drug response: challenges and opportunities. *Nat Rev Drug Discov, 12*(3), 217-228. doi:10.1038/nrd3870

Mehta, S. (2018). the role of Microenvironment in the Homing, Maintenance, and release of Glioma Stem-like Cells. *Frontiers in oncology, 8*, 7.

Mehta, S., Huillard, E., Kesari, S., Maire, C. L., Golebiowski, D., Harrington, E. P., . . . Stiles, C. D. (2011). The central nervous system-restricted transcription factor Olig2 opposes p53 responses to genotoxic damage in neural progenitors and malignant glioma. *Cancer Cell, 19*(3), 359-371. doi:10.1016/j.ccr.2011.01.035

Meng, Q., Xia, C., Fang, J., Rojanasakul, Y., & Jiang, B. H. (2006). Role of PI3K and AKT specific isoforms in ovarian cancer cell migration, invasion and proliferation through the p70S6K1 pathway. *Cell Signal, 18*(12), 2262-2271. doi:10.1016/j.cellsig.2006.05.019

Mosadegh, B., Saadi, W., Wang, S. J., & Jeon, N. L. (2008). Epidermal growth factor promotes breast cancer cell chemotaxis in CXCL12 gradients. *Biotechnol Bioeng, 100*(6), 1205-1213. doi:10.1002/bit.21851

Mouneimne, G., Hansen, S. D., Selfors, L. M., Petrak, L., Hickey, M. M., Gallegos, L. L., . . . Brugge, J. S. (2012). Differential remodeling of actin cytoskeleton architecture by profilin isoforms leads to distinct effects on cell migration and invasion. *Cancer Cell, 22*(5), 615-630. doi:10.1016/j.ccr.2012.09.027

Mueller, M. M., & Fusenig, N. E. (2004). Friends or foes - bipolar effects of the tumour stroma in cancer. *Nat Rev Cancer, 4*(11), 839-849. doi:10.1038/nrc1477

Muller, A., Homey, B., Soto, H., Ge, N., Catron, D., Buchanan, M. E., . . . Zlotnik, A. (2001). Involvement of chemokine receptors in breast cancer metastasis. *Nature, 410*(6824), 50-56. doi:10.1038/35065016

Mutch, L. J., Howden, J. D., Jenner, E. P., Poulter, N. S., & Rappoport, J. Z. (2014). Polarised clathrin-mediated endocytosis of EGFR during chemotactic invasion. *Traffic, 15*(6), 648-664.

Nagaraju, S., Truong, D., Mouneimne, G., & Nikkhah, M. (2018). Microfluidic Tumor-Vascular Model to Study Breast Cancer Cell Invasion and Intravasation. *Adv Healthc Mater*. doi:10.1002/adhm.201701257

Nakagawa, H., Liyanarachchi, S., Davuluri, R. V., Auer, H., Martin, E. W., de la Chapelle, A., & Frankel, W. L. (2004). Role of cancer-associated stromal fibroblasts in metastatic colon cancer to the liver and their expression profiles. *Oncogene, 23*(44), 7366-7377.

Navaei, A., Saini, H., Christenson, W., Sullivan, R. T., Ros, R., & Nikkhah, M. (2016). Gold nanorod-incorporated gelatin-based conductive hydrogels for engineering cardiac tissue constructs. *Acta Biomaterialia, 41*, 133-146. doi:http://dx.doi.org/10.1016/j.actbio.2016.05.027

Nelson, C. M., & Bissell, M. J. (2005). Modeling dynamic reciprocity: engineering three-dimensional culture models of breast architecture, function, and neoplastic transformation. *Semin Cancer Biol, 15*(5), 342-352. doi:10.1016/j.semcancer.2005.05.001

Nelson, C. M., Inman, J. L., & Bissell, M. J. (2008). Three-dimensional lithographically defined organotypic tissue arrays for quantitative analysis of morphogenesis and neoplastic progression. *Nature Protocols, 3*(4), 674-678. doi:10.1038/nprot.2008.35

Nelson, C. M., VanDuijn, M. M., Inman, J. L., Fletcher, D. A., & Bissell, M. J. (2006). Tissue Geometry Determines Sites of Mammary Branching Morphogenesis in Organotypic Cultures. *Science, 314*(5797), 298-300. doi:10.1126/science.1131000

Ngo, M. T., & Harley, B. A. (2017). The Influence of Hyaluronic Acid and Glioblastoma Cell Coculture on the Formation of Endothelial Cell Networks in Gelatin Hydrogels. *Adv Healthc Mater, 6*(22). doi:10.1002/adhm.201700687

Nichol, J. W., Koshy, S., Bae, H., Hwang, C. M., Yamanlar, S., & Khademhosseini, A. (2010). Cell-laden microengineered gelatin methacrylate hydrogels. *Biomaterials, 31*(21), 5536-5544. doi:10.1016/j.biomaterials.2010.03.064

Nikkhah, M., Eshak, N., Zorlutuna, P., Annabi, N., Castello, M., Kim, K., . . . Khademhosseini, A. (2012). Directed endothelial cell morphogenesis in micropatterned gelatin methacrylate hydrogels. *Biomaterials, 33*(35), 9009-9018. doi:10.1016/j.biomaterials.2012.08.068

Nikkhah, M., Strobl, J. S., De Vita, R., & Agah, M. (2010). The cytoskeletal organization of breast carcinoma and fibroblast cells inside three dimensional (3-D) isotropic silicon microstructures. *Biomaterials, 31*(16), 4552-4561. doi:10.1016/j.biomaterials.2010.02.034

Nikkhah, M., Strobl, J. S., Peddi, B., & Agah, M. (2009). Cytoskeletal role in differential adhesion patterns of normal fibroblasts and breast cancer cells inside silicon microenvironments. *Biomed Microdevices, 11*(3), 585-595. doi:10.1007/s10544-008-9268-2

Nikkhah, M., Strobl, J. S., Schmelz, E. M., Roberts, P. C., Zhou, H., & Agah, M. (2011). MCF10A and MDA-MB-231 human breast basal epithelial cell co-culture in silicon micro-arrays. *Biomaterials, 32*(30), 7625-7632. doi:10.1016/j.biomaterials.2011.06.041

Ohlund, D., Elyada, E., & Tuveson, D. (2014). Fibroblast heterogeneity in the cancer wound. *J Exp Med, 211*(8), 1503-1523. doi:10.1084/jem.20140692

Olsen, C. J., Moreira, J., Lukanidin, E. M., & Ambartsumian, N. S. (2010). Human mammary fibroblasts stimulate invasion of breast cancer cells in a three-dimensional culture and increase stroma development in mouse xenografts. *BMC Cancer, 10*, 444. doi:10.1186/1471-2407-10-444

Olumi, A. F., Grossfeld, G. D., Hayward, S. W., Carroll, P. R., Tlsty, T. D., & Cunha, G. R. (1999). Carcinoma-associated fibroblasts direct tumor progression of initiated human prostatic epithelium. *Cancer Res, 59*(19), 5002-5011.

Omuro, A., & DeAngelis, L. M. (2013). Glioblastoma and other malignant gliomas: a clinical review. *JAMA, 310*(17), 1842-1850. doi:10.1001/jama.2013.280319

Orimo, A., Gupta, P. B., Sgroi, D. C., Arenzana-Seisdedos, F., Delaunay, T., Naeem, R., . . . Weinberg, R. A. (2005). Stromal fibroblasts present in invasive human breast carcinomas promote tumor growth and angiogenesis through elevated SDF-1/CXCL12 secretion. *Cell, 121*(3), 335-348. doi:10.1016/j.cell.2005.02.034

Osswald, M., Jung, E., Sahm, F., Solecki, G., Venkataramani, V., Blaes, J., . . . Winkler, F. (2015). Brain tumour cells interconnect to a functional and resistant network. *Nature, 528*(7580), 93-98. doi:10.1038/nature16071

Oyewumi, M. O., Manickavasagam, D., Novak, K., Wehrung, D., Paulic, N., Moussa, F. M., . . . Safadi, F. F. (2016). Osteoactivin (GPNMB) ectodomain protein promotes growth and invasive behavior of human lung cancer cells. *Oncotarget, 7*(12), 13932-13944. doi:10.18632/oncotarget.7323

Paguirigan, A. L., Puccinelli, J. P., Su, X., & Beebe, D. J. (2010). Expanding the available assays: adapting and validating In-Cell Westerns in microfluidic devices for cell-based assays. *Assay Drug Dev Technol, 8*(5), 591-601. doi:10.1089/adt.2010.0274

Paraiso, K. H. T., & Smalley, K. S. M. (2013). Fibroblast-mediated drug resistance in cancer. *Biochemical Pharmacology, 85*(8), 1033-1041. doi:10.1016/j.bcp.2013.01.018

Paszek, M. J., Zahir, N., Johnson, K. R., Lakins, J. N., Rozenberg, G. I., Gefen, A., . . . Weaver, V. M. (2005). Tensional homeostasis and the malignant phenotype. *Cancer Cell, 8*(3), 241-254. doi:10.1016/j.ccr.2005.08.010

Patsialou, A., Wyckoff, J., Wang, Y., Goswami, S., Stanley, E. R., & Condeelis, J. S. (2009). Invasion of human breast cancer cells in vivo requires both paracrine and autocrine loops involving the colony-stimulating factor-1 receptor. *Cancer Res, 69*(24), 9498-9506. doi:10.1158/0008-5472.CAN-09-1868

Peela, N., Barrientos, E. S., Truong, D., Mouneimne, G., & Nikkhah, M. (2017). Effect of suberoylanilide hydroxamic acid (SAHA) on breast cancer cells within a tumor-stroma microfluidic model. *Integr Biol (Camb), 9*(12), 988-999. doi:10.1039/c7ib00180k

Peela, N., Sam, F. S., Christenson, W., Truong, D., Watson, A. W., Mouneimne, G., . . . Nikkhah, M. (2016). A three dimensional micropatterned tumor model for breast cancer cell migration studies. *Biomaterials, 81*, 72-83. doi:10.1016/j.biomaterials.2015.11.039

Peela, N., Truong, D., Barrientos, E., Mouneimne, G., & Nikkhah, M. (2016). *Evaluation of anti-cancer drug Suberoylanilide Hydroxamic Acid (SAHA) on cancer cell phenotype in a three-dimensional (3D) breast tumor-stroma platform.* Paper presented at the 20th International Conference on Miniaturized Systems for Chemistry and Life Sciences, MicroTAS 2016.

Peela, N., Truong, D., Saini, H., Chu, H., Mashaghi, S., Ham, S. L., . . . Nikkhah, M. (2017). Advanced biomaterials and microengineering technologies to recapitulate the stepwise process of cancer metastasis. *Biomaterials, 133*, 176-207. doi:10.1016/j.biomaterials.2017.04.017

Pereira, B., Chin, S. F., Rueda, O. M., Vollan, H. K., Provenzano, E., Bardwell, H. A., . . . Caldas, C. (2016). The somatic mutation profiles of 2,433 breast cancers refines their genomic and transcriptomic landscapes. *Nat Commun, 7*, 11479. doi:10.1038/ncomms11479

Piccinini, F., Kiss, A., & Horvath, P. (2015). CellTracker (not only) for dummies. *Bioinformatics, 32*(6), 955-957.

Pinner, S., & Sahai, E. (2008). Imaging amoeboid cancer cell motility in vivo. *Journal of Microscopy-Oxford, 231*(3), 441-445. doi:DOI 10.1111/j.1365-2818.2008.02056.x

Price, J. T., Tiganis, T., Agarwal, A., Djakiew, D., & Thompson, E. W. (1999). Epidermal growth factor promotes MDA-MB-231 breast cancer cell migration through a phosphatidylinositol 3 '-kinase and phospholipase C-dependent mechanism. *Cancer research, 59*(21), 5475-5478.

Provenzano, P. P., Eliceiri, K. W., Campbell, J. M., Inman, D. R., White, J. G., & Keely, P. J. (2006). Collagen reorganization at the tumor-stromal interface facilitates local invasion. *BMC Med, 4*(1), 38. doi:10.1186/1741-7015-4-38

Provenzano, P. P., Inman, D. R., Eliceiri, K. W., Knittel, J. G., Yan, L., Rueden, C. T., . . . Keely, P. J. (2008). Collagen density promotes mammary tumor initiation and progression. *BMC Med, 6*, 11. doi:10.1186/1741-7015-6-11

Quatromoni, J. G., & Eruslanov, E. (2012). Tumor-associated macrophages: function, phenotype, and link to prognosis in human lung cancer. *Am J Transl Res, 4*(4), 376-389.

Quiros, R. M., Valianou, M., Kwon, Y., Brown, K. M., Godwin, A. K., & Cukierman, E. (2008). Ovarian normal and tumor-associated fibroblasts retain in vivo stromal characteristics in a 3-D matrix-dependent manner. *Gynecol Oncol, 110*(1), 99-109. doi:10.1016/j.ygyno.2008.03.006

R Development Core Team. (2010). R: A language and environment for statistical computing.

Raftopoulou, M., & Hall, A. (2004). Cell migration: Rho GTPases lead the way. *Dev Biol, 265*(1), 23-32.

Rao, S., Sengupta, R., Choe, E. J., Woerner, B. M., Jackson, E., Sun, T., . . . Rubin, J. B. (2012). CXCL12 mediates trophic interactions between endothelial and tumor cells in glioblastoma. *PLoS One, 7*(3), e33005.

Rape, A., Ananthanarayanan, B., & Kumar, S. (2014). Engineering strategies to mimic the glioblastoma microenvironment. *Adv Drug Deliv Rev, 79-80*, 172-183. doi:10.1016/j.addr.2014.08.012

Redjal, N., Chan, J. A., Segal, R. A., & Kung, A. L. (2006). CXCR4 inhibition synergizes with cytotoxic chemotherapy in gliomas. *Clinical Cancer Research, 12*(22), 6765-6771. doi:10.1158/1078-0432.CCR-06-1372

Rhodes, D. R., Yu, J., Shanker, K., Deshpande, N., Varambally, R., Ghosh, D., . . . Chinnaiyan, A. M. (2004). ONCOMINE: a cancer microarray database and integrated data-mining platform. *Neoplasia, 6*(1), 1-6.

Richardson, A. L., Wang, Z. C., De Nicolo, A., Lu, X., Brown, M., Miron, A., . . . Ganesan, S. (2006). X chromosomal abnormalities in basal-like human breast cancer. *Cancer Cell, 9*(2), 121-132. doi:10.1016/j.ccr.2006.01.013

Ridky, T. W., Chow, J. M., Wong, D. J., & Khavari, P. A. (2010). Invasive three-dimensional organotypic neoplasia from multiple normal human epithelia. *Nat Med, 16*(12), 1450-1455. doi:10.1038/nm.2265

Robinson, M. D., McCarthy, D. J., & Smyth, G. K. (2010). edgeR: a Bioconductor package for differential expression analysis of digital gene expression data. *Bioinformatics, 26*(1), 139-140. doi:10.1093/bioinformatics/btp616

Rose, A. A., Grosset, A.-A., Dong, Z., Russo, C., MacDonald, P. A., Bertos, N. R., . . . Park, M. (2010). Glycoprotein nonmetastatic B is an independent prognostic indicator of recurrence and a novel therapeutic target in breast cancer. *Clinical Cancer Research, 16*(7), 2147-2156.

Rose, A. A., Pepin, F., Russo, C., Abou Khalil, J. E., Hallett, M., & Siegel, P. M. (2007). Osteoactivin promotes breast cancer metastasis to bone. *Mol Cancer Res, 5*(10), 1001-1014. doi:10.1158/1541-7786.MCR-07-0119

Rubenstein, J. L., Kim, J., Ozawa, T., Zhang, M., Westphal, M., Deen, D. F., & Shuman, M. A. (2000). Anti-VEGF antibody treatment of glioblastoma prolongs survival but results in increased vascular cooption. *Neoplasia, 2*(4), 306-314.

Ruppen, J., Wildhaber, F. D., Strub, C., Hall, S. R., Schmid, R. A., Geiser, T., & Guenat, O. T. (2015). Towards personalized medicine: chemosensitivity assays of patient lung cancer cell spheroids in a perfused microfluidic platform. *Lab Chip, 15*(14), 3076-3085. doi:10.1039/c5lc00454c

Ryu, H., Oh, S., Lee, H. J., Lee, J. Y., Lee, H. K., & Jeon, N. L. (2015). Engineering a Blood Vessel Network Module for Body-on-a-Chip Applications. *J Lab Autom, 20*(3), 296-301. doi:10.1177/2211068214562831

Saadi, W., Wang, S. J., Lin, F., & Jeon, N. L. (2006). A parallel-gradient microfluidic chamber for quantitative analysis of breast cancer cell chemotaxis. *Biomed Microdevices, 8*(2), 109-118. doi:10.1007/s10544-006-7706-6

Sabeh, F., Shimizu-Hirota, R., & Weiss, S. J. (2009). Protease-dependent versus -independent cancer cell invasion programs: three-dimensional amoeboid movement revisited. *J Cell Biol, 185*(1), 11-19. doi:10.1083/jcb.200807195

Sadlonova, A., Mukherjee, S., Bowe, D. B., Gault, S. R., Dumas, N. A., Van Tine, B. A., . . . Frost, A. R. (2007). Human breast fibroblasts inhibit growth of the MCF10AT xenograft model of proliferative breast disease. *Am J Pathol, 170*(3), 1064-1076. doi:10.2353/ajpath.2007.060031

Saini, H., Navaei, A., Van Putten, A., & Nikkhah, M. (2015). 3D Cardiac Microtissues Encapsulated with the Co-Culture of Cardiomyocytes and Cardiac Fibroblasts. *Advanced Healthcare Materials, 4*(13), 1961-1971. doi:10.1002/adhm.201500331

Salmaggi, A., Gelati, M., Pollo, B., Frigerio, S., Eoli, M., Silvani, A., . . . De Rossi, M. (2004). CXCL12 in malignant glial tumors: a possible role in angiogenesis and cross-talk between endothelial and tumoral cells. *J Neurooncol, 67*(3), 305-317.

Sander, L. M., & Deisboeck, T. S. (2002). Growth patterns of microscopic brain tumors. *Phys Rev E Stat Nonlin Soft Matter Phys, 66*(5 Pt 1), 051901. doi:10.1103/PhysRevE.66.051901

Santos, A. M., Jung, J., Aziz, N., Kissil, J. L., & Pure, E. (2009). Targeting fibroblast activation protein inhibits tumor stromagenesis and growth in mice. *J Clin Invest, 119*(12), 3613-3625. doi:10.1172/JCI38988

Schaupp, A., Sabet, O., Dudanova, I., Ponserre, M., Bastiaens, P., & Klein, R. (2014). The composition of EphB2 clusters determines the strength in the cellular repulsion response. *J Cell Biol, 204*(3), 409-422. doi:10.1083/jcb.201305037

Schlenska-Lange, A., Knupfer, H., Lange, T. J., Kiess, W., & Knupfer, M. (2008). Cell proliferation and migration in glioblastoma multiforme cell lines are influenced by insulin-like growth factor I in vitro. *Anticancer Res, 28*(2A), 1055-1060.

Schulte, A., Gunther, H. S., Martens, T., Zapf, S., Riethdorf, S., Wulfing, C., . . . Lamszus, K. (2012). Glioblastoma Stem-like Cell Lines with Either Maintenance or Loss of High-Level EGFR Amplification, Generated via Modulation of Ligand Concentration. *Clinical Cancer Research, 18*(7), 1901-1913. doi:10.1158/1078-0432.Ccr-11-3084

Scotton, C. J., Wilson, J. L., Scott, K., Stamp, G., Wilbanks, G. D., Fricker, S., . . . Balkwill, F. R. (2002). Multiple actions of the chemokine CXCL12 on epithelial tumor cells in human ovarian cancer. *Cancer Res, 62*(20), 5930-5938.

Sharma, A., & Shiras, A. (2016). Cancer stem cell-vascular endothelial cell interactions in glioblastoma. *Biochem Biophys Res Commun, 473*(3), 688-692. doi:10.1016/j.bbrc.2015.12.022

Shields, J. D., Emmett, M. S., Dunn, D. B., Joory, K. D., Sage, L. M., Rigby, H., . . . Bates, D. O. (2007). Chemokine-mediated migration of melanoma cells towards lymphatics--a mechanism contributing to metastasis. *Oncogene, 26*(21), 2997-3005. doi:10.1038/sj.onc.1210114

Shields, J. D., Fleury, M. E., Yong, C., Tomei, A. A., Randolph, G. J., & Swartz, M. A. (2007). Autologous chemotaxis as a mechanism of tumor cell homing to lymphatics via interstitial flow and autocrine CCR7 signaling. *Cancer Cell, 11*(6), 526-538. doi:10.1016/j.ccr.2007.04.020

Siegel, R., Ma, J., Zou, Z., & Jemal, A. (2014). Cancer statistics, 2014. *CA Cancer J Clin, 64*(1), 9-29. doi:10.3322/caac.21208

Siegel, R. L., Miller, K. D., & Jemal, A. (2018). Cancer statistics, 2018. *CA Cancer J Clin, 68*(1), 7-30. doi:10.3322/caac.21442

Singh, S. K., Fiorelli, R., Kupp, R., Rajan, S., Szeto, E., Lo Cascio, C., . . . Mehta, S. (2016). Post-translational Modifications of OLIG2 Regulate Glioma Invasion through the TGF-beta Pathway. *Cell Rep, 16*(4), 950-966. doi:10.1016/j.celrep.2016.06.045

Siqueira, A. S., Pinto, M. P., Cruz, M. C., Smuczek, B., Cruz, K. S., Barbuto, J. A., . . . Jaeger, R. G. (2016). Laminin-111 peptide C16 regulates invadopodia activity of malignant cells through beta1 integrin, Src and ERK 1/2. *Oncotarget, 7*(30), 47904-47917. doi:10.18632/oncotarget.10062

Smalley, K. S., Lioni, M., & Herlyn, M. (2006). Life isn't flat: taking cancer biology to the next dimension. *In Vitro Cell Dev Biol Anim, 42*(8-9), 242-247. doi:10.1290/0604027.1

Smuczek, B., Santos, E. S., Siqueira, A. S., Pinheiro, J. J. V., Freitas, V. M., & Jaeger, R. G. (2017). The laminin-derived peptide C16 regulates GPNMB expression and function in breast cancer. *Exp Cell Res, 358*(2), 323-334. doi:10.1016/j.yexcr.2017.07.005

Soon, P. S., Kim, E., Pon, C. K., Gill, A. J., Moore, K., Spillane, A. J., . . . Baxter, R. C. (2013). Breast cancer-associated fibroblasts induce epithelial-to-mesenchymal transition in breast cancer cells. *Endocr Relat Cancer, 20*(1), 1-12. doi:10.1530/ERC-12-0227

Strobl, J. S., Nikkhah, M., & Agah, M. (2010). Actions of the anti-cancer drug suberoylanilide hydroxamic acid (SAHA) on human breast cancer cytoarchitecture in silicon microstructures. *Biomaterials, 31*(27), 7043-7050. doi:10.1016/j.biomaterials.2010.05.023

Stuelten, C. H., DaCosta Byfield, S., Arany, P. R., Karpova, T. S., Stetler-Stevenson, W. G., & Roberts, A. B. (2005). Breast cancer cells induce stromal fibroblasts to express MMP-9 via secretion of TNF-alpha and TGF-beta. *J Cell Sci, 118*(Pt 10), 2143-2153. doi:10.1242/jcs.02334

Stylianopoulos, T., Diop-Frimpong, B., Munn, L. L., & Jain, R. K. (2010). Diffusion anisotropy in collagen gels and tumors: the effect of fiber network orientation. *Biophys J, 99*(10), 3119-3128. doi:10.1016/j.bpj.2010.08.065

Sugimoto, H., Mundel, T. M., Kieran, M. W., & Kalluri, R. (2006). Identification of fibroblast heterogeneity in the tumor microenvironment. *Cancer Biol Ther, 5*(12), 1640-1646.

Sundar, S. J., Hsieh, J. K., Manjila, S., Lathia, J. D., & Sloan, A. (2014). The role of cancer stem cells in glioblastoma. *Neurosurg Focus, 37*(6), E6. doi:10.3171/2014.9.FOCUS14494

Sung, K. E., & Beebe, D. J. (2014). Microfluidic 3D models of cancer. *Adv Drug Deliv Rev, 79-80*, 68-78. doi:10.1016/j.addr.2014.07.002

Sung, K. E., Su, X., Berthier, E., Pehlke, C., Friedl, A., & Beebe, D. J. (2013). Understanding the impact of 2D and 3D fibroblast cultures on in vitro breast cancer models. *PLoS ONE, 8*(10), e76373. doi:10.1371/journal.pone.0076373

Sung, K. E., Yang, N., Pehlke, C., Keely, P. J., Eliceiri, K. W., Friedl, A., & Beebe, D. J. (2011). Transition to invasion in breast cancer: a microfluidic in vitro model enables examination of spatial and temporal effects. *Integr Biol (Camb), 3*(4), 439-450. doi:10.1039/c0ib00063a

Taichman, R. S., Cooper, C., Keller, E. T., Pienta, K. J., Taichman, N. S., & McCauley, L. K. (2002). Use of the stromal cell-derived factor-1/CXCR4 pathway in prostate cancer metastasis to bone. *Cancer Res, 62*(6), 1832-1837.

Tchou, J., & Conejo-Garcia, J. (2012). Targeting the tumor stroma as a novel treatment strategy for breast cancer: shifting from the neoplastic cell-centric to a stroma-centric paradigm *Advances in pharmacology* (Vol. 65, pp. 45-61): Elsevier.

Teng, F., Tian, W. Y., Wang, Y. M., Zhang, Y. F., Guo, F., Zhao, J., . . . Xue, F. X. (2016). Cancer-associated fibroblasts promote the progression of endometrial cancer via the SDF-1/CXCR4 axis. *J Hematol Oncol, 9*, 8. doi:10.1186/s13045-015-0231-4

Thoma, C. R., Zimmermann, M., Agarkova, I., Kelm, J. M., & Krek, W. (2014). 3D cell culture systems modeling tumor growth determinants in cancer target discovery. *Adv Drug Deliv Rev, 69-70*, 29-41. doi:10.1016/j.addr.2014.03.001

Tian, F., Liu, C., Wu, Q., Qu, K., Wang, R., Wei, J., . . . Chang, H. (2013). Upregulation of glycoprotein nonmetastatic B by colony-stimulating factor-1 and epithelial cell adhesion molecule in hepatocellular carcinoma cells. *Oncol Res, 20*(8), 341-350. doi:10.3727/096504013X13657689382851

Truong, D., Fiorelli, R., Barrientos, E. S., Melendez, E. L., Sanai, N., Mehta, S., & Nikkhah, M. (2018). A three-dimensional (3D) organotypic microfluidic model for glioma stem cells–Vascular interactions. *Biomaterials*.

Truong, D., Puleo, J., Llave, A., Mouneimne, G., Kamm, R. D., & Nikkhah, M. (2016). Breast Cancer Cell Invasion into a Three Dimensional Tumor-Stroma Microenvironment. *Sci Rep, 6*. doi:10.1038/srep34094

Tyan, S.-W., Kuo, W.-H., Huang, C.-K., Pan, C.-C., Shew, J.-Y., Chang, K.-J., . . . Lee, W.-H. (2011). Breast Cancer Cells Induce Cancer-Associated Fibroblasts to Secrete Hepatocyte Growth Factor to Enhance Breast Tumorigenesis. *PLoS One, 6*, e15313. doi:10.1371/journal.pone.0015313

Vaahtomeri, K., Brown, M., Hauschild, R., De Vries, I., Leithner, A. F., Mehling, M., . . . Sixt, M. (2017). Locally Triggered Release of the Chemokine CCL21 Promotes Dendritic Cell Transmigration across Lymphatic Endothelia. *Cell Rep, 19*(5), 902-909. doi:10.1016/j.celrep.2017.04.027

van Duinen, V., Trietsch, S. J., Joore, J., Vulto, P., & Hankemeier, T. (2015). Microfluidic 3D cell culture: from tools to tissue models. *Curr Opin Biotechnol, 35*, 118-126. doi:10.1016/j.copbio.2015.05.002

Venere, M., Fine, H. A., Dirks, P. B., & Rich, J. N. (2011). Cancer stem cells in gliomas: identifying and understanding the apex cell in cancer's hierarchy. *Glia, 59*(8), 1148-1154. doi:10.1002/glia.21185

Wakimoto, H., Mohapatra, G., Kanai, R., Curry, W. T., Jr., Yip, S., Nitta, M., . . . Rabkin, S. D. (2012). Maintenance of primary tumor phenotype and genotype in glioblastoma stem cells. *Neuro Oncol, 14*(2), 132-144. doi:10.1093/neuonc/nor195

Wang, C., Lu, H., & Schwartz, M. A. (2012). A novel in vitro flow system for changing flow direction on endothelial cells. *J Biomech, 45*(7), 1212-1218. doi:10.1016/j.jbiomech.2012.01.045

Wang, L., Wang, Z., Yang, B., Yang, Q., Wang, L., & Sun, Y. (2009). CXCR4 nuclear localization follows binding of its ligand SDF-1 and occurs in metastatic but not primary renal cell carcinoma. *Oncol Rep, 22*(6), 1333-1339.

Wang, Q., Villeneuve, G., & Wang, Z. X. (2005). Control of epidermal growth factor receptor endocytosis by receptor dimerization, rather than receptor kinase activation. *Embo Reports, 6*(10), 942-948. doi:10.1038/sj.embor.7400491

Wang, S. J., Saadi, W., Lin, F., Minh-Canh Nguyen, C., & Li Jeon, N. (2004). Differential effects of EGF gradient profiles on MDA-MB-231 breast cancer cell chemotaxis. *Exp Cell Res, 300*(1), 180-189. doi:10.1016/j.yexcr.2004.06.030

Wang, Z., Ma, Q., Liu, Q., Yu, H., Zhao, L., Shen, S., & Yao, J. (2008). Blockade of SDF-1/CXCR4 signalling inhibits pancreatic cancer progression in vitro via inactivation of canonical Wnt pathway. *Br J Cancer, 99*(10), 1695-1703. doi:10.1038/sj.bjc.6604745

Warrington, N. M., Woerner, B. M., Daginakatte, G. C., Dasgupta, B., Perry, A., Gutmann, D. H., & Rubin, J. B. (2007). Spatiotemporal differences in CXCL12 expression and cyclic AMP underlie the unique pattern of optic glioma growth in neurofibromatosis type 1. *Cancer Res, 67*(18), 8588-8595. doi:10.1158/0008-5472.CAN-06-2220

Watkins, S., Robel, S., Kimbrough, I. F., Robert, S. M., Ellis-Davies, G., & Sontheimer, H. (2014). Disruption of astrocyte-vascular coupling and the blood-brain barrier by invading glioma cells. *Nat Commun, 5*, 4196. doi:10.1038/ncomms5196

Wei, H., Li, H., Mao, S., & Lin, J. M. (2011). Cell signaling analysis by mass spectrometry under coculture conditions on an integrated microfluidic device. *Anal Chem, 83*(24), 9306-9313. doi:10.1021/ac201709f

Weigelt, B. (2014). The need for complex 3D culture models to unravel novel pathways and identify. *0*, 42-51. doi:10.1016/j.addr.2014.01.001

Weigelt, B., Ghajar, C. M., & Bissell, M. J. (2014). The need for complex 3D culture models to unravel novel pathways and identify accurate biomarkers in breast cancer. *Adv Drug Deliv Rev, 69-70*, 42-51. doi:10.1016/j.addr.2014.01.001

Wick, W., Gorlia, T., Bendszus, M., Taphoorn, M., Sahm, F., Harting, I., . . . van den Bent, M. J. (2017). Lomustine and Bevacizumab in Progressive Glioblastoma. *N Engl J Med, 377*(20), 1954-1963. doi:10.1056/NEJMoa1707358

Wurth, R., Bajetto, A., Harrison, J. K., Barbieri, F., & Florio, T. (2014). CXCL12 modulation of CXCR4 and CXCR7 activity in human glioblastoma stem-like cells and regulation of the tumor microenvironment. *Front Cell Neurosci, 8*, 144. doi:10.3389/fncel.2014.00144

Wyckoff, J., Wang, W., Lin, E. Y., Wang, Y., Pixley, F., Stanley, E. R., . . . Condeelis, J. (2004). A paracrine loop between tumor cells and macrophages is required for tumor cell migration in mammary tumors. *Cancer Res, 64*(19), 7022-7029. doi:10.1158/0008-5472.CAN-04-1449

Wyckoff, J. B., Wang, Y., Lin, E. Y., Li, J. F., Goswami, S., Stanley, E. R., . . . Condeelis, J. (2007). Direct visualization of macrophage-assisted tumor cell intravasation in mammary tumors. *Cancer Res, 67*(6), 2649-2656. doi:10.1158/0008-5472.CAN-06-1823

Xiao, W., Sohrabi, A., & Seidlits, S. K. (2017). Integrating the glioblastoma microenvironment into engineered experimental models. *Future science OA, 3*(3), FSO189.

Yamada, K. M., & Cukierman, E. (2007). Modeling tissue morphogenesis and cancer in 3D. *Cell, 130*(4), 601-610. doi:10.1016/j.cell.2007.08.006

Yan, G. N., Yang, L., Lv, Y. F., Shi, Y., Shen, L. L., Yao, X. H., . . . Guo, D. Y. (2014). Endothelial cells promote stem-like phenotype of glioma cells through activating the Hedgehog pathway. *J Pathol, 234*(1), 11-22. doi:10.1002/path.4349

Yang, K., Park, H. J., Han, S., Lee, J., Ko, E., Kim, J., . . . Cho, S. W. (2015). Recapitulation of in vivo-like paracrine signals of human mesenchymal stem cells for functional neuronal differentiation of human neural stem cells in a 3D microfluidic system. *Biomaterials, 63*, 177-188. doi:10.1016/j.biomaterials.2015.06.011

Yu, H., Lim, K. P., Xiong, S., Tan, L. P., & Shim, W. (2013). Functional morphometric analysis in cellular behaviors: shape and size matter. *Adv Healthc Mater, 2*(9), 1188-1197. doi:10.1002/adhm.201300053

Zeelenberg, I. S., Ruuls-Van Stalle, L., & Roos, E. (2003). The chemokine receptor CXCR4 is required for outgrowth of colon carcinoma micrometastases. *Cancer research, 63*(13), 3833-3839.

Zervantonakis, I., Chung, S., Sudo, R., Zhang, M., Charest, J., & Kamm, R. (2010). Concentration gradients in microfluidic 3D matrix cell culture systems. *International Journal of Micro-Nano Scale Transport, 1*(1), 27-36. doi:10.1260/1759-3093.1.1.27

Zervantonakis, I. K., Hughes-Alford, S. K., Charest, J. L., Condeelis, J. S., Gertler, F. B., & Kamm, R. D. (2012). Three-dimensional microfluidic model for tumor cell intravasation and endothelial barrier function. *Proc Natl Acad Sci U S A, 109*(34), 13515-13520. doi:10.1073/pnas.1210182109

Zhang, Y., Tang, H., Cai, J., Zhang, T., Guo, J., Feng, D., & Wang, Z. (2011). Ovarian cancer-associated fibroblasts contribute to epithelial ovarian carcinoma metastasis by promoting angiogenesis, lymphangiogenesis and tumor cell invasion. *Cancer Lett, 303*(1), 47-55. doi:10.1016/j.canlet.2011.01.011

Zhou, L., Liu, F., Li, Y., Peng, Y., Liu, Y., & Li, J. (2012). Gpnmb/osteoactivin, an attractive target in cancer immunotherapy. *Neoplasma, 59*(1), 1-5.

Zhu, T. S., Costello, M. A., Talsma, C. E., Flack, C. G., Crowley, J. G., Hamm, L. L., . . . Fan, X. (2011). Endothelial cells create a stem cell niche in glioblastoma by providing NOTCH ligands that nurture self-renewal of cancer stem-like cells. *Cancer Res, 71*(18), 6061-6072. doi:10.1158/0008-5472.CAN-10-4269

APPENDIX A

SUPPLEMENTARY FIGURES FOR CHAPTER 2

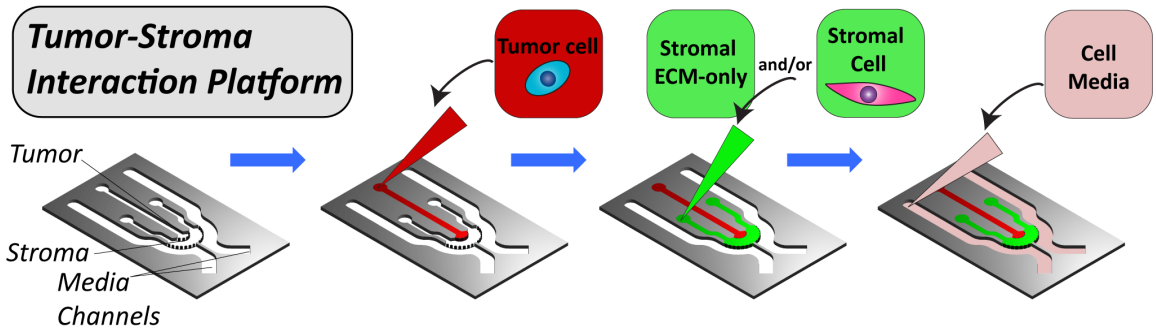

Figure A.1. Detailed schematic of tumor-stroma loading. Cancer cells (red) are injected into the tumor region. The stroma (green), with or without stromal cells, are injected into the stromal region. Media is added into the media channels.

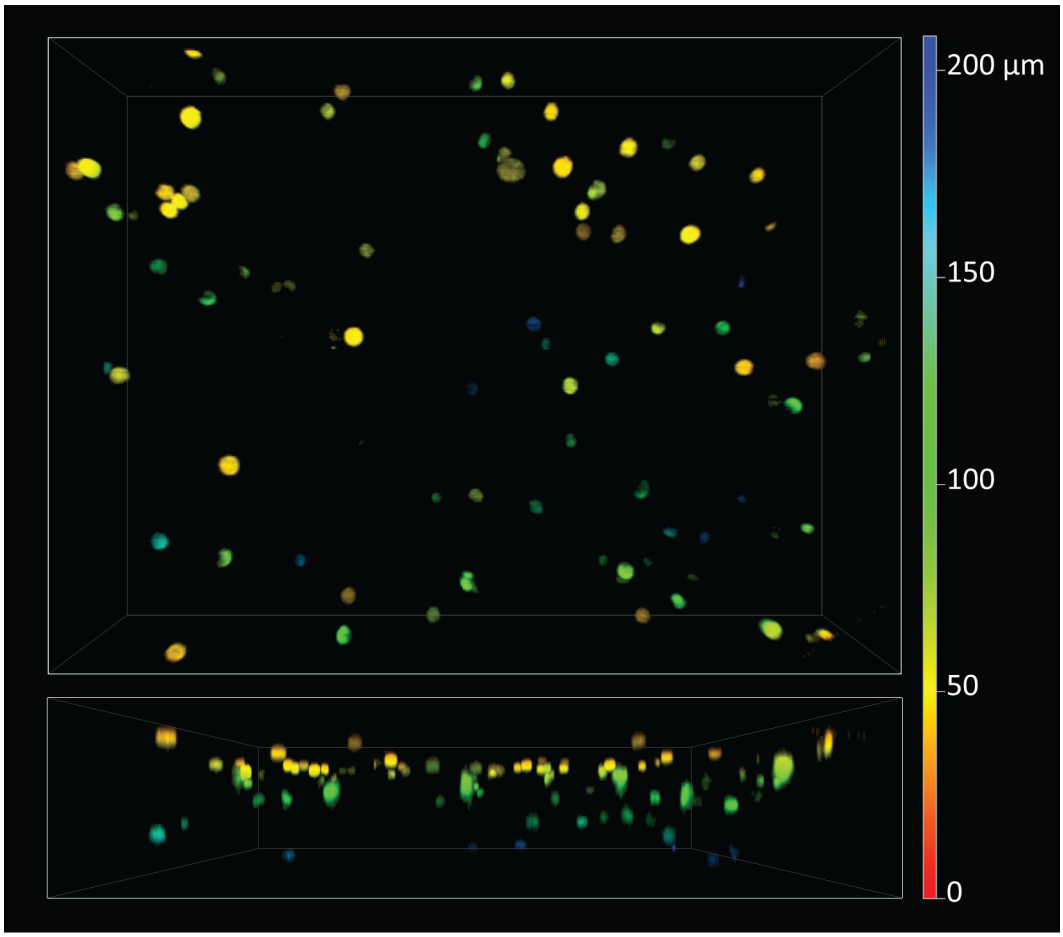

Figure A.2. Depth coding of cells encapsulated within the matrix. The color represents where the cells are located within the 3D space.

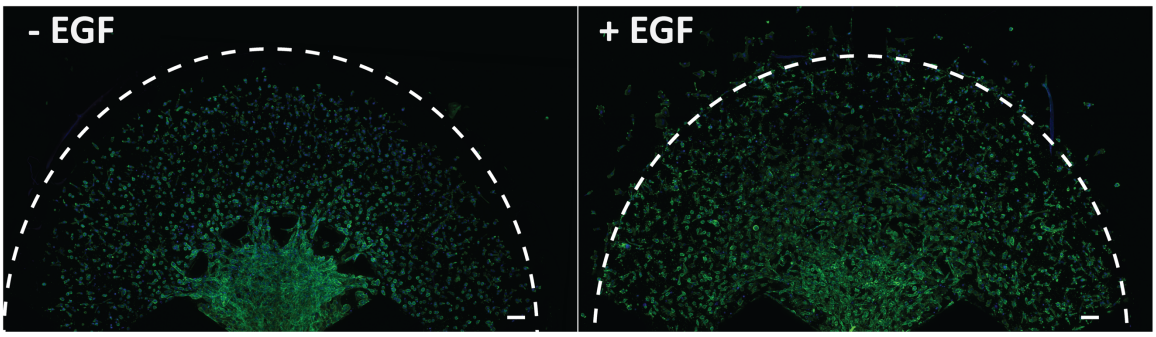

Figure A.3. Whole-device images taken of actin-stained (green) cells in both conditions on day 4. It was apparent that by day 4, more cells within the (+) EGF group reached the area past the stroma (scale bar: 100 μm).

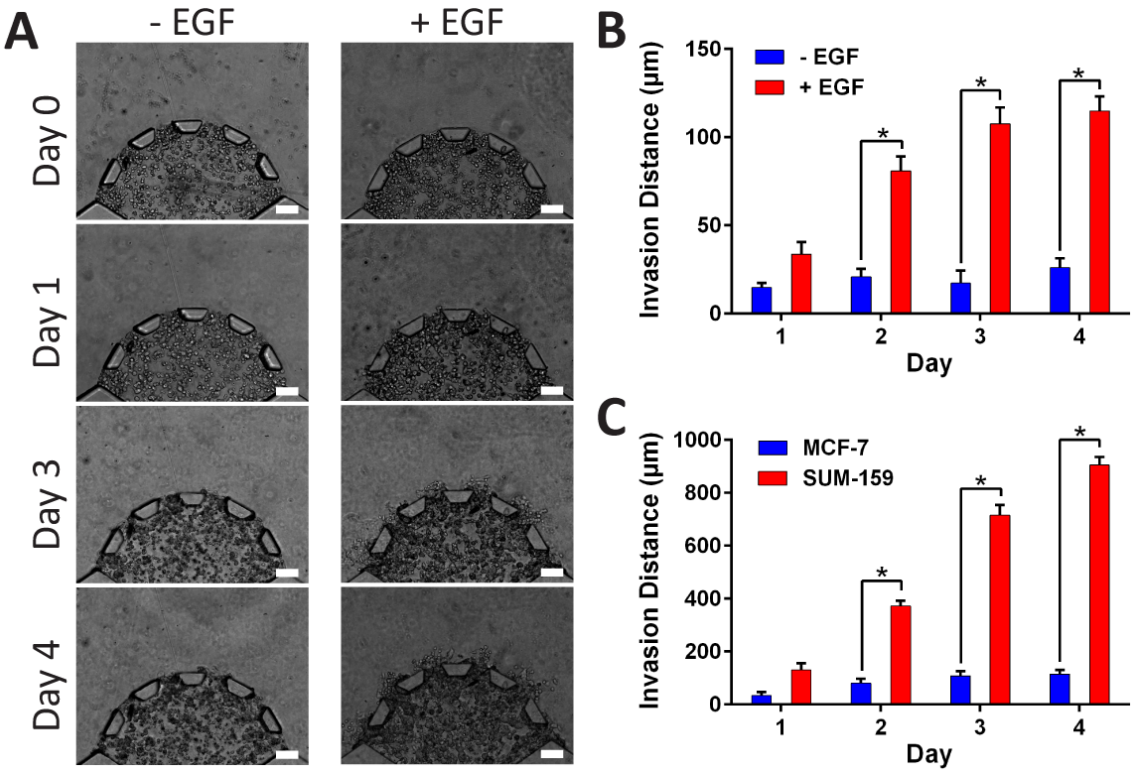

Figure A.4. MCF-7 3D invasion assay. (A) Devices were split into two groups where one group (+ EGF) was introduced to EGF (50 ng/mL) and the other was not exposed to EGF (- EGF). (+) EGF MCF-7 cells migrated out from the tumor region by day 2 with minor invasion by day 4. (-) EGF group showed little migration (scale bar: 100 μm). (B) Invasion distance of the tumor front was calculated from the radial distances of the furthest cells from the tumor region. (+) EGF exhibited significantly higher invasion by day 2 ($P < 0.05$ calculated from student's T test with more than three devices for each condition). (D) Comparing (+) EGF groups between SUM-159 and MCF-7 cells showed that SUM-159 had almost 10-fold higher invasion ($P < 0.05$ calculated from student's T test with more than three devices for each condition).

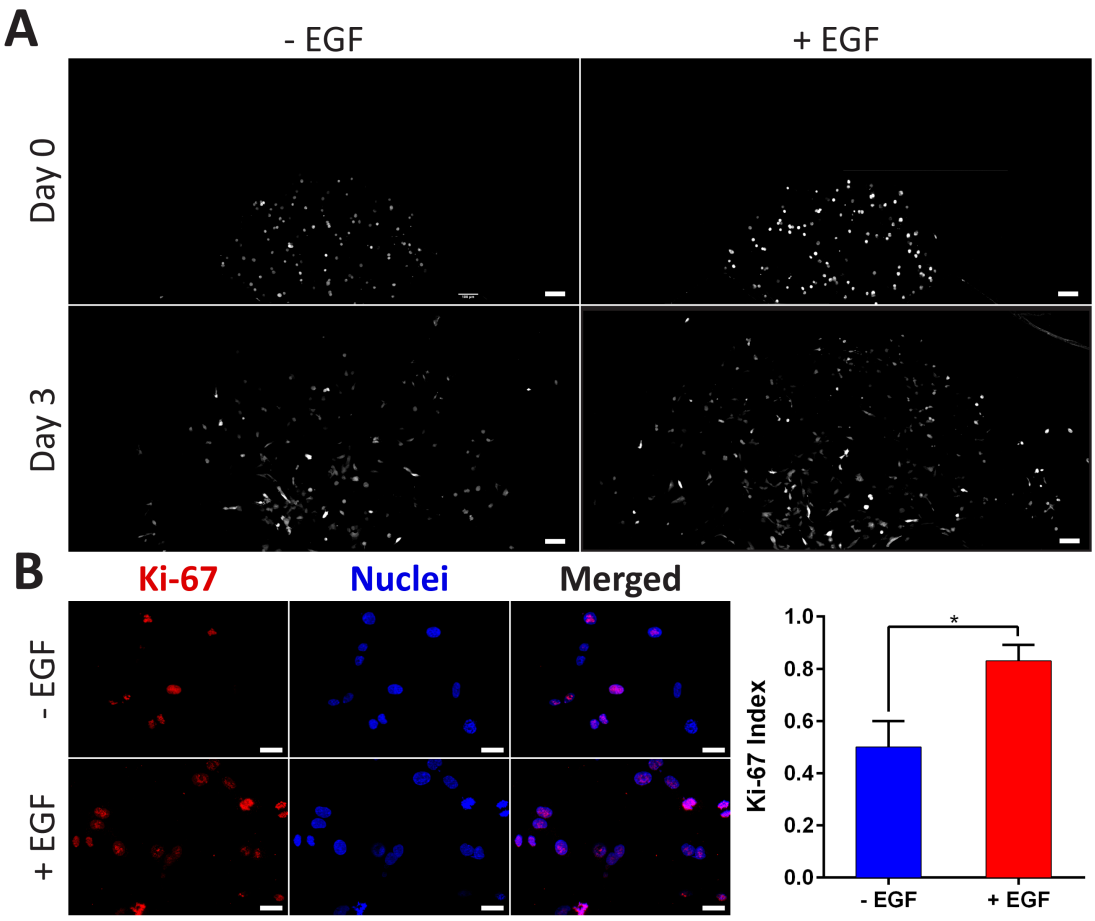

Figure A.5. (A) Cell count was quantified as the increase in fluorescently labeled cells over time (scale bar: 100 µm). (B) Ki-67 index was imaged and quantified by comparing expression of Ki-67 (red) and nuclei (blue) (scale bar: 20 µm). (+) EGF group showed significantly higher expression of Ki-67 compared to (-) EGF ($P < 0.05$ calculated from student's T test with more than three devices for each condition).

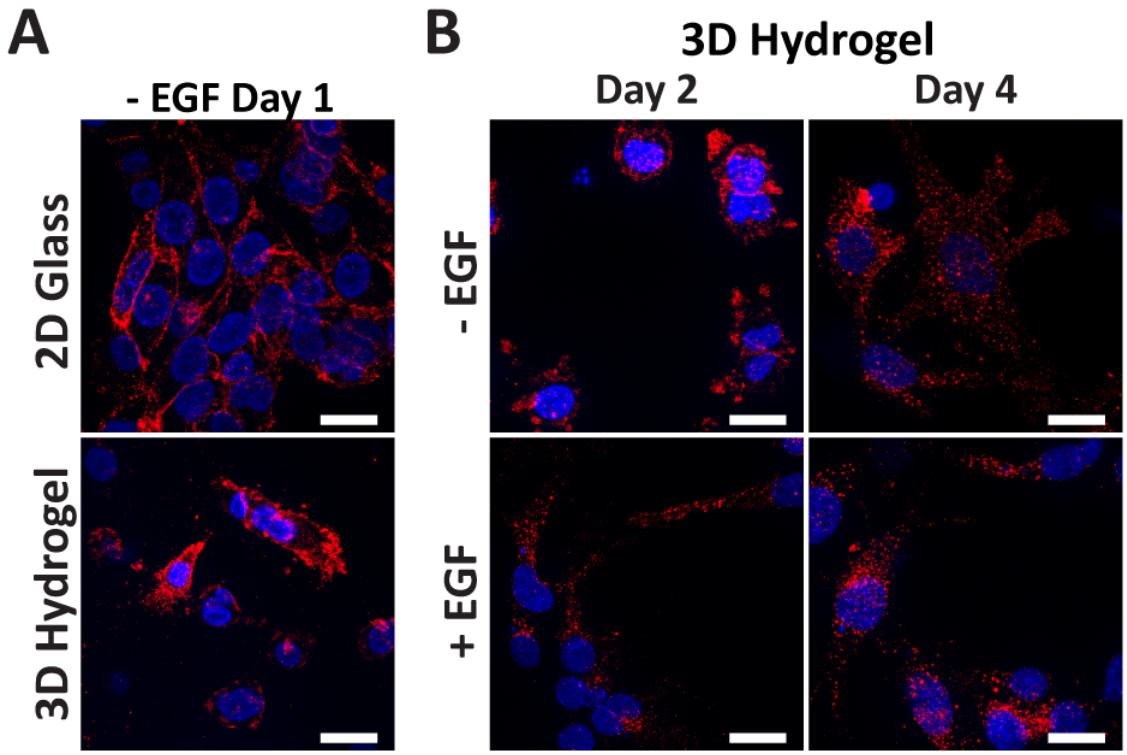

Figure A.6. Investigation of EGFRs over time. (A) Cells were stained for EGFR (red) and nuclei (blue) (scale bar: 20 μm) within the first 24 h of culture on 2D glass and in the microfluidic device. Z-projection of cells showed EGFR near the membrane. (B) Cells were treated with EGF for 24 h (Day 2) and 72 h (Day 4). By day 2, (+) EGF demonstrated punctate EGFRs in the cytoplasm while (-) EGF showed localization to the cell membrane still. Day 4 showed that both conditions had punctate EGFRs but (+) EGF displayed clustering toward the nuclei.

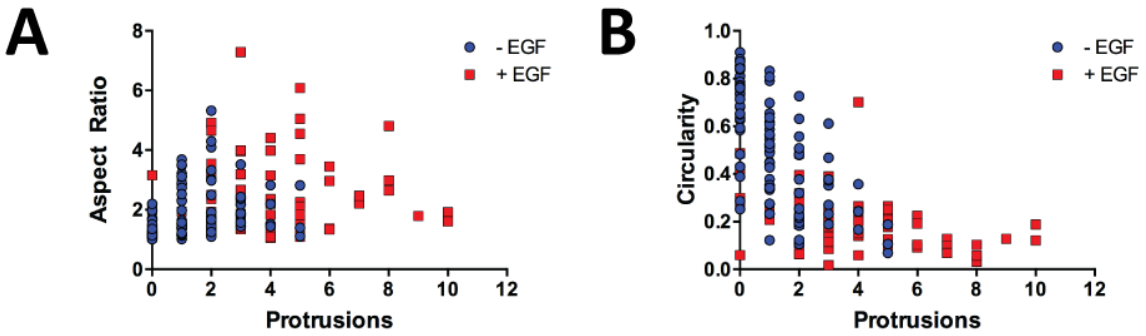

Figure A.7. (A) AR was correlated to protrusions under the two conditions and R-squared for both conditions were determined to be 0.11 ($p < 0.001$) and 0.00 ($p = 0.61$) for (-) EGF and (+) EGF respectively. These results suggested that AR and cell protrusions slightly correlated prior to EGF stimulation, but upon introduction of EGF the correlation was reduced to none or could not be determined. (B) When correlated to circularity, it could be seen under (-) EGF condition that the circularity sharply decreased when cell protrusions increased (R-squared = 0.45, $p < 0.0001$). For (+) EGF, circularity moderately declined with increasing cell extensions where the correlation was weaker than without EGF (R-squared = 0.16, $p < 0.001$).

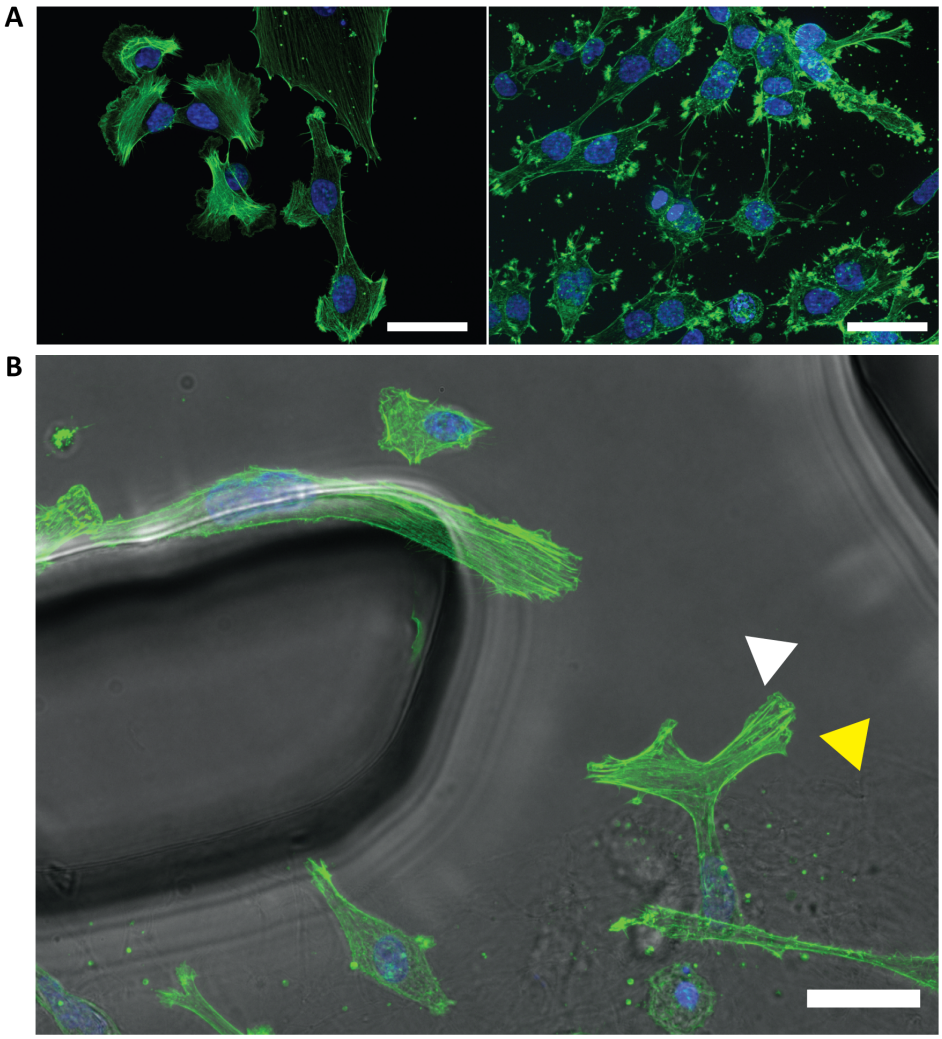

Figure A.8. (A) Z-projection of actin-stained images of cells on 2D substrate (left) and within the 3D matrix (right, scale bar: 25 μm). (B) Z-projection of F-actin staining of cells leaving the collagen matrix (yellow arrow) and protruding toward the glass (white arrow, scale bar: 50 μm).

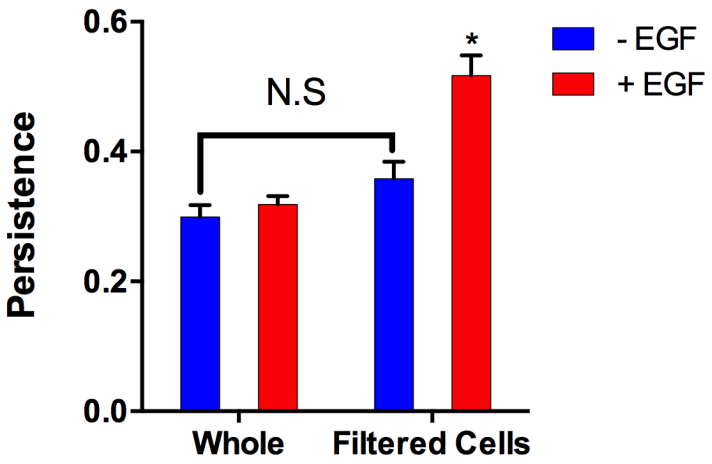

Figure A.9. Analysis of persistence between the whole-population of cells to the filtered cells using a two-way ANOVA and multiple comparison's test. * indicates a significantly different group when $P < 0.05$.

APPENDIX B

SUPPLEMENTARY FIGURES FOR CHAPTER 3

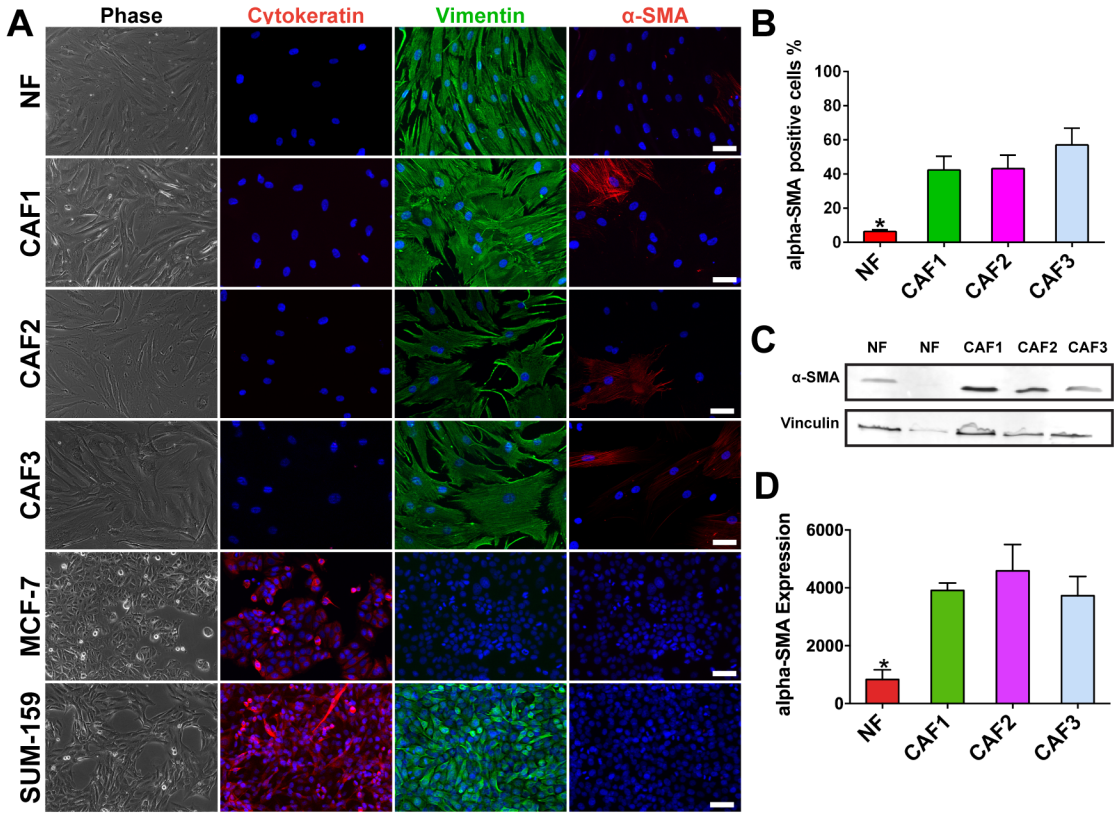

Figure B.1. Characterization of fibroblast markers. (A) Fibroblasts expressed vimentin and αSMA but did not express cytokeratin. MCF-7 expressed cytokeratin but did not express vimentin or αSMA. SUM-159 expressed cytokeratin and vimentin but not αSMA. Scale bar: 50 μm. (B) Percent of αSMA positive fibroblasts were significantly lower in NFs. * denotes a significantly different group for p <0.05. (C) Western blot of αSMA corroborated the imaging data. Vinculin was used as the loading control. (D) Quantification of western blot showed significantly lower αSMA expression in NFs. * denotes a significantly different group for p <0.05.

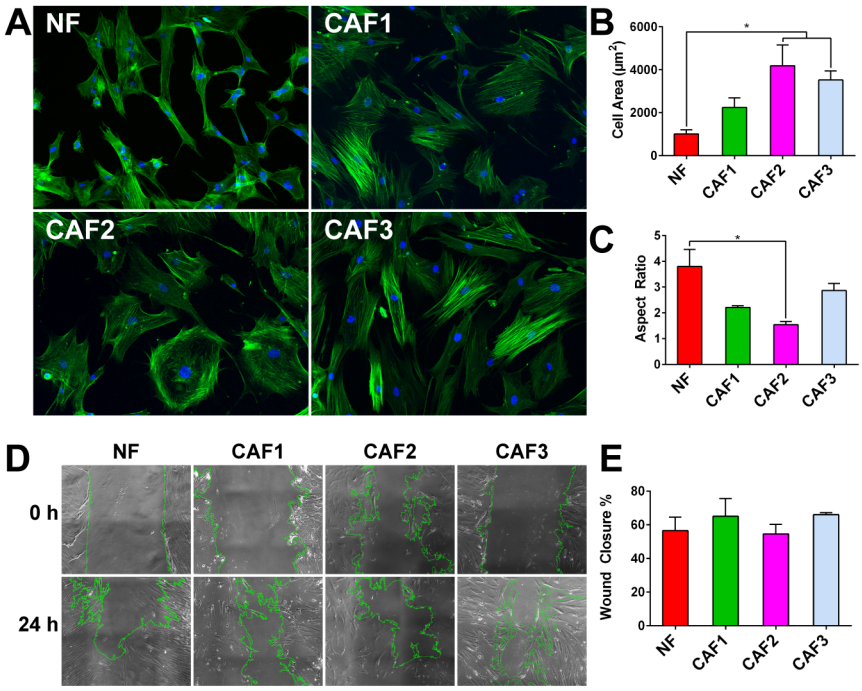

Figure B.2. Characterization of fibroblast behavior. (A) F-actin staining was used to delineate cell shape and area. (B) CAF2 and CAF3 had significantly enhanced cell area. (C) NFs had significantly increased aspect ratio compared to CAF2. * denotes a significantly difference for $p < 0.05$. (D, E) Wound healing assay depicts 2D migration of fibroblasts with no significant difference between them.

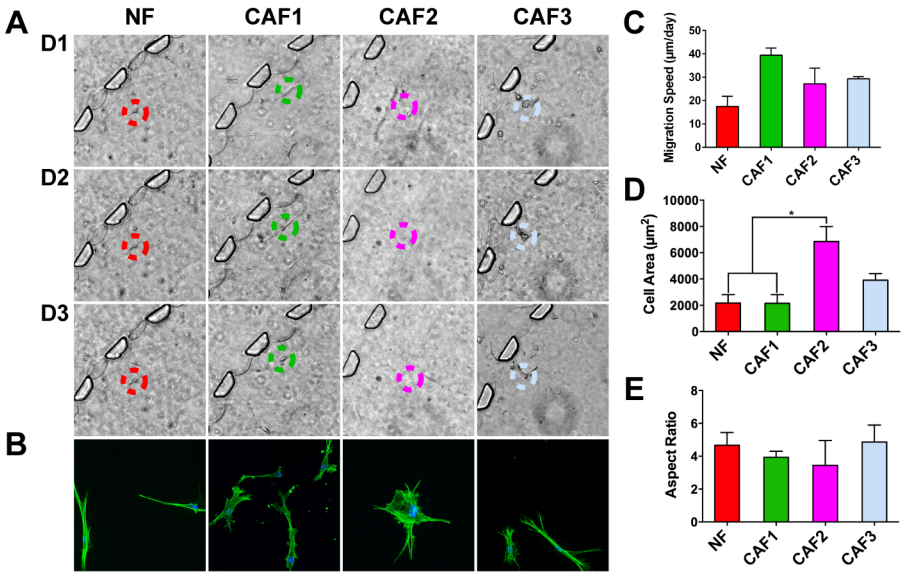

Figure B.3. Patient-derived fibroblast behavior in the stroma region of the microfluidic device. (A) Representative images of fibroblast location over 3 days. (B) Representative actin cytoskeleton image of fibroblasts in 3D. (C) Migration per day of fibroblasts. (D) Spreading cell area within 3D stroma region. * denotes a significantly different group for $p < 0.05$. (E) Aspect ratio of fibroblasts.

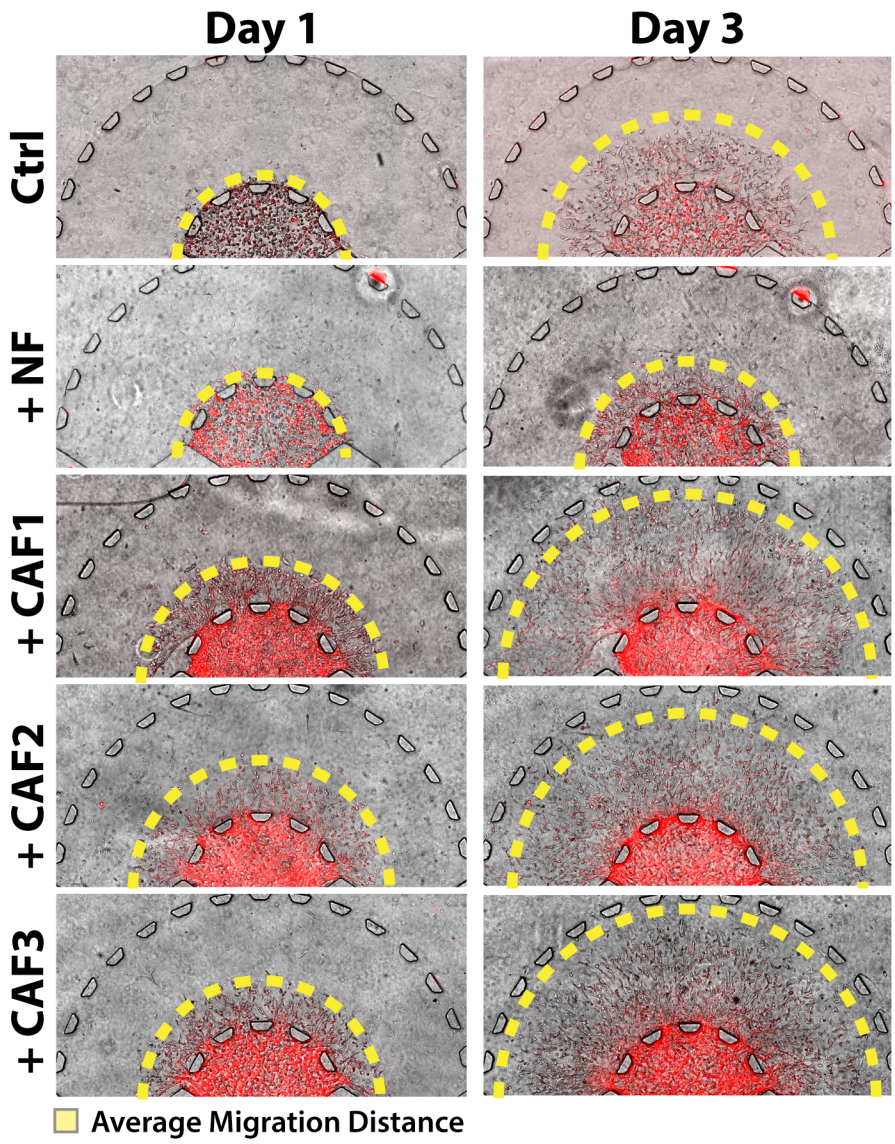

Figure B.4. SUM-159 migration in microfluidic over time. SUM-159 cells migrated in presence or absence of fibroblasts. Dashed lines represent average invading tumor front.

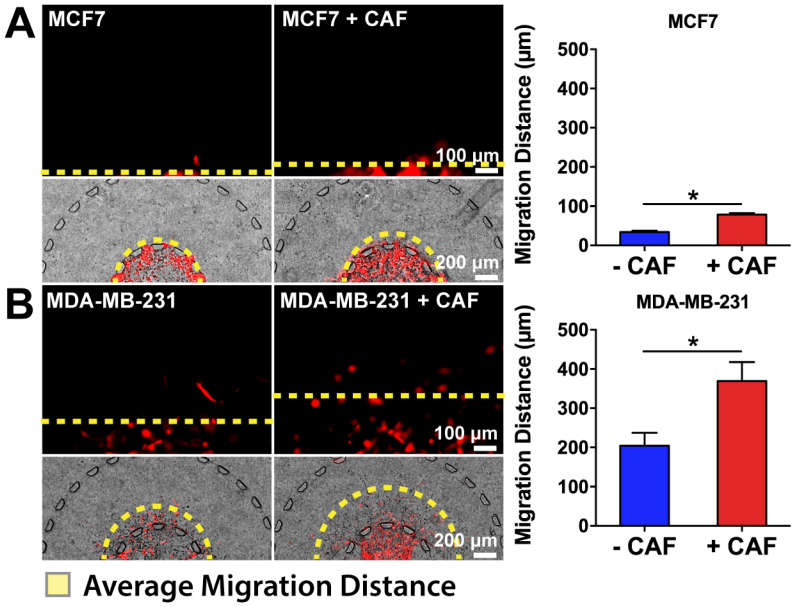

Figure B.5. Breast cancer cell line behavior in response to CAF co-culture. (A) MCF7 cells migrated into stroma in presence or absence of CAFs. * denotes a significant difference for $p < 0.05$; paired t-test. (B) MDA-MB-231 cells migrated into stroma in presence or absence of CAFs. * denotes a significant difference for $p < 0.05$.

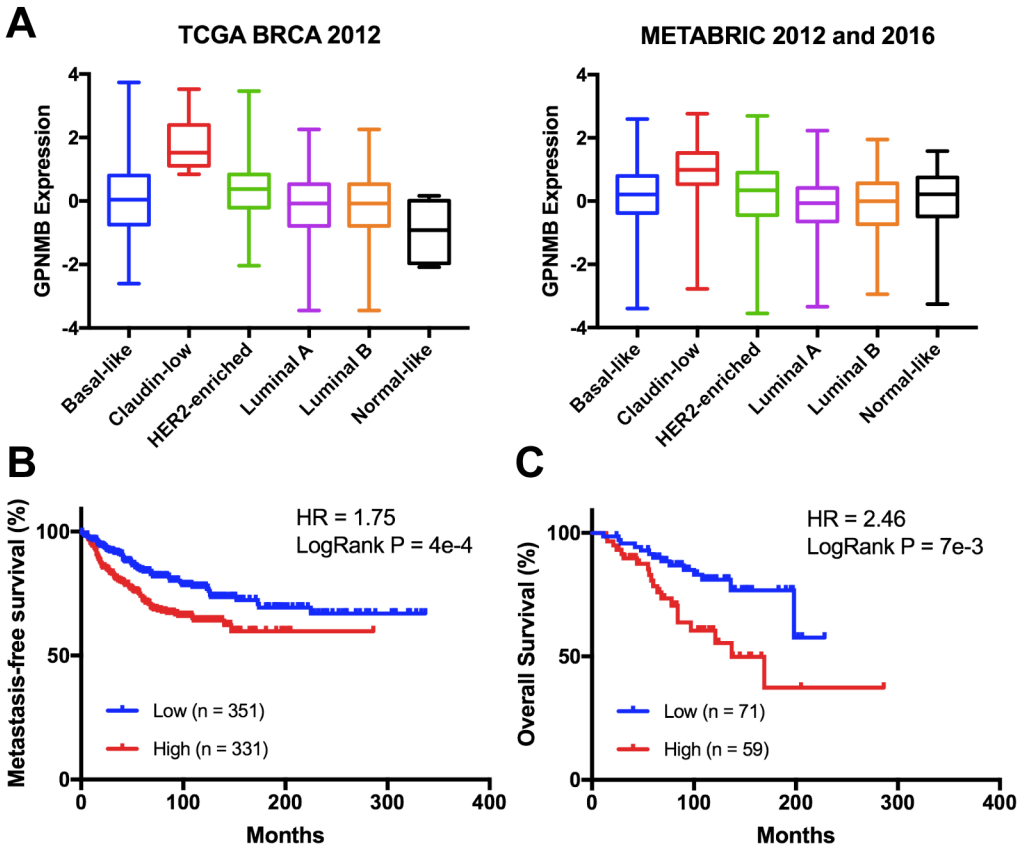

Figure B.6. Additional clinical data determining the relevance of *GPNMB* in breast cancer. (A) *GPNMB* expression in different breast cancer subtype extracted from data sets queried in CBioPortal. (B) Kaplan–Meier analysis of distant metastasis free survival based on high or low *GPNMB* expression from Geneanalytics tool (http://geneanalytics.duhs.duke.edu). Patients were divided into two groups with different survival curves using *GPNMB* gene expression (quartile cutoff was set at 25% high and 75% low *GPNMB* expressions). HR, 1.75; *P* = 4e-4. (C) Kaplan–Meier analysis of overall survival based on high or low *GPNMB* expression from GeneAnalytics tool. HR, 2.46; *P* = 7e-4

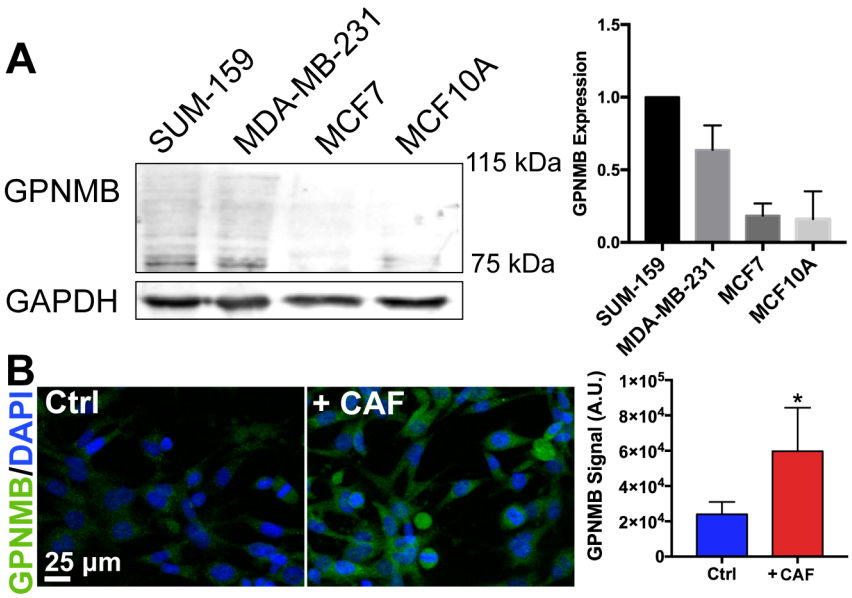

Figure B.7. GPNMB expression in breast cancer cell line. (A) Western blot showed high expression in SUM-159 and MDA-MB-231 cells and low in MCF7 and MCF10A cells. Expression was relative to SUM-159. (B) Maximum intensity z-projection demonstrated that expression of GPNMB was increased in SUM-159 breast cancer cells in co-culture. * denotes significant difference for $p < 0.05$; unpaired t-test.

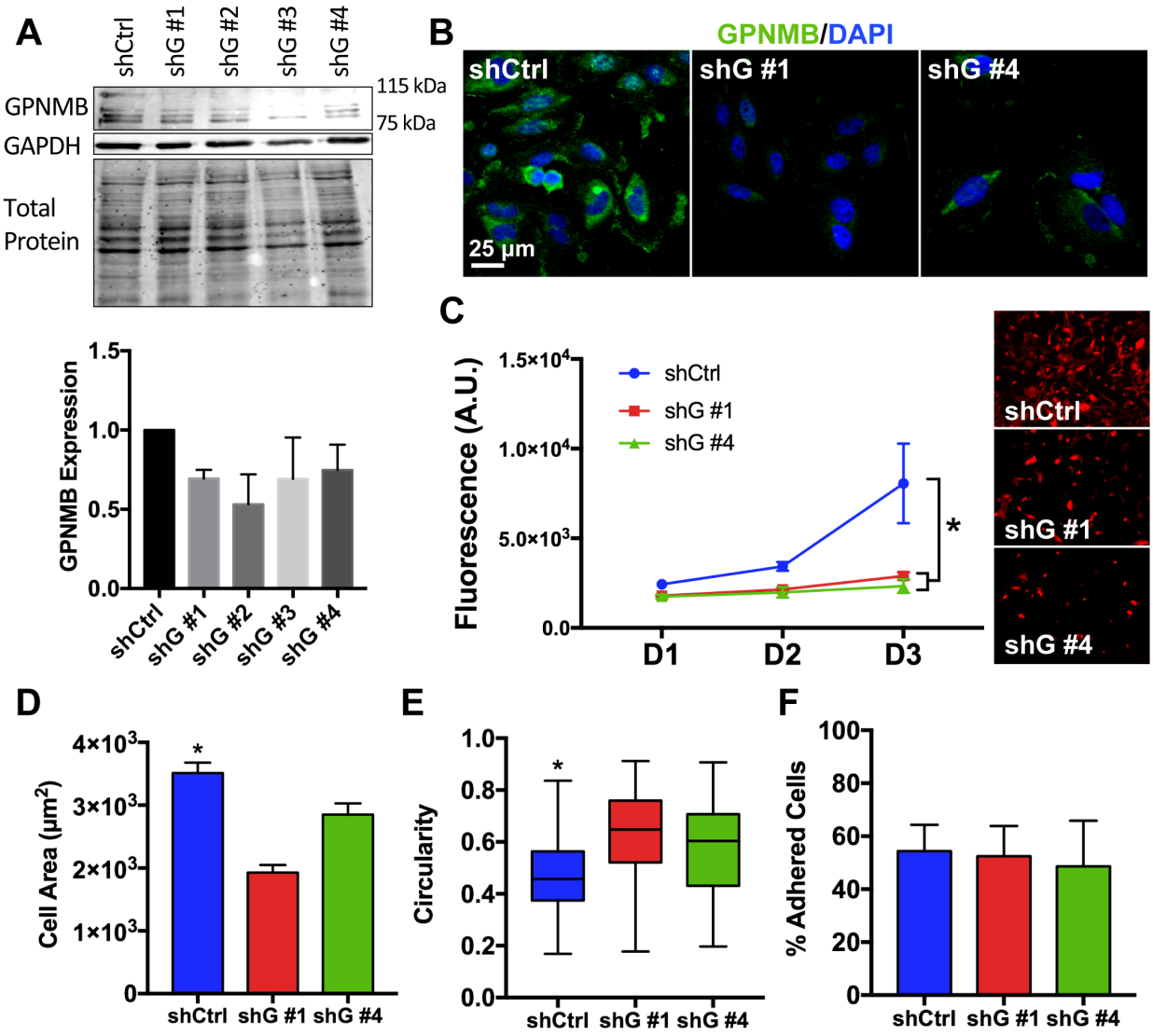

Figure B.8. Characterization of GPNMB knockdown lines. (A) Western blot showed knockdown of GPNMB in SUM-159 breast cancer cells. Expression was normalized to total protein. shG #1 and shG #4 were chosen for subsequent experiments. shG #2 had little growth in culture. (B) Maximum intensity z-projection demonstrated that GPNMB expression in knockdown lines on 2D glass substrate. (C) 2D Proliferation assay using AlamarBlue® for knockdown lines. shCtrl showed higher cell count after 3 days. * denotes a significant difference for $p < 0.05$. (D, E) 2D Morphometric analysis showed

lower cell area and higher circularity for GPNMB knockdown lines suggesting lesser invasive capacity. * denotes a significant difference for $p < 0.05$. (F) 2D collagen adhesion assay showed no statistical difference in adhesion for shCtrl and shG lines.

APPENDIX C

SUPPLEMENTARY FIGURES FOR CHAPTER 4

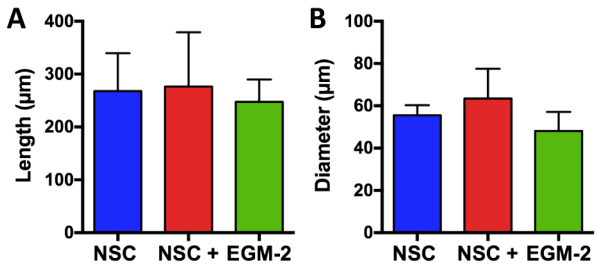

Figure C.1. Vessel morphology during GSC invasion. (A) Comparison of length of vessels between junctions and (B) diameter of vessels under different media conditions. (1-way ANOVA with Tukey's post-hoc test; n = 3 for each data set).

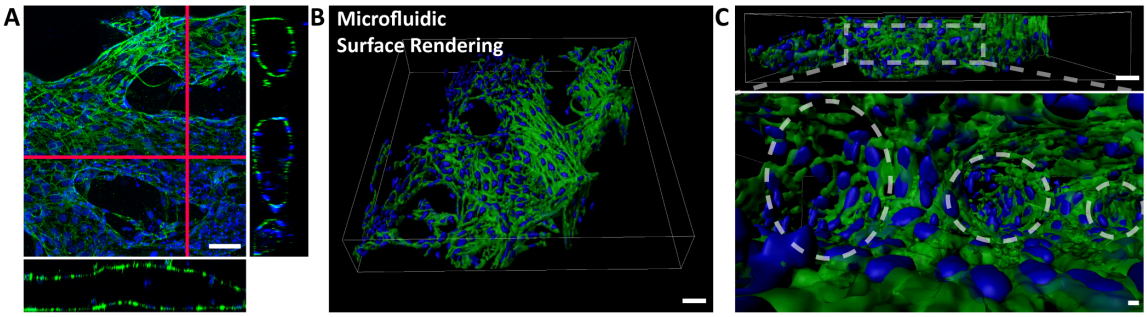

Figure C.2. Microvascular network morphology in co-culture with GSCs. (A) Immunofluorescence staining of established vasculature (CD-31, green) in microfluidic model in co-culture with GSCs. Cross-sectional view (red lines) depicting the hollow lumen of microvascular network; Scale bar: 50 µm. (B) Surface rendering with (C) front view (Scale bar: 50 µm) and inner membrane of the network. The white dashed circles show the different vascular branches; Scale bar: 10 µm.

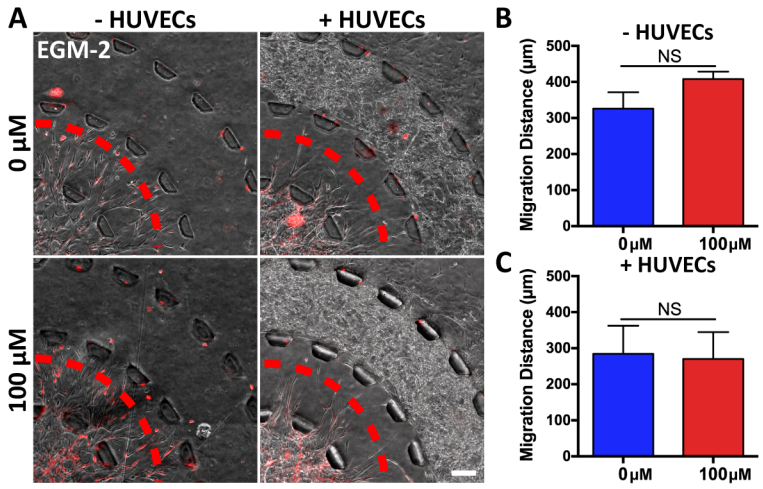

Figure C.3. CXCL12/CXCR4 signaling in EGM-2 condition. (A) Phase-contrast image of GSC (red) invading in presence of HUVECs in different concentrations of AMD3100 in EGM-2 condition. Red dashed line delineates average migration boundary; Scale bar: 100 µm. (B and C) Quantification of migration distance in mono- and co-culture conditions. (* denotes $p < 0.05$; Student's T-test; $n > 3$ for each data set).

APPENDIX D

LIST OF SUPPLEMENTARY OF VIDEOS

Supplementary videos are readable using media players in Windows operating system.

Chapter 2:

Movie D.1. Time-lapse movie of cells migrating throughout the stroma. Movie duration: 18h, time interval: 45 min, scale bar: 200 μm.

Movie D.2. Z-projection movie of migrating cells within the stroma matrix.

Movie D.3. 3D movie of migrating cells within the stroma matrix (scale bar: 100 μm). The cells were analyzed using the NIS Elements AR Microscope Imaging Software by Nikon. The fluorescent movies were converted to binary and thresholded. The software automatically calculated 3D cell bodies based on the Z-stack images. Next, the cells were tracked using the tracking module, which revealed the differences in cell speed and persistence.

Movie D.4. Z-projection of actin (green) and tubulin (red) stained cells in (-) EGF condition.

Movie D.5. Z-projection of actin (green) and tubulin (red) stained cells in (+) EGF condition.

Movie D.6. Z-projection of actin (green) and tubulin (red) stained cells comparing the cells on 2D substrate and within the 3D stroma.

Movie D.7. Z-projection movie of migrating cells on 2D plane.

Chapter 3:

Movie D.8. Time-lapse imaging of SUM-159 breast cancer cells migrating through the 3D stroma in absence of CAFs.

Movie D.9. Time-lapse imaging of SUM-159 breast cancer cells migrating through the 3D stroma in presence of CAFs.

Movie D.10. Time-lapse imaging of CAFs migrating through the 3D stroma in absence of SUM-159 breast cancer cells.

Movie D.11. Time-lapse imaging of CAFs migrating through the 3D stroma in presence of SUM-159 breast cancer cells.

Movie D.12. Time-lapse imaging of shCtrl line migrating through the 3D stroma.

Movie D.13. Time-lapse imaging of shG #4 line migrating through the 3D stroma.

Chapter 4:

Movie D.14. GSC invasion in microfluidic. Surface rendering with fly through of migrating GSCs (red) near vasculature (green) within the microfluidic model.

Movie D.15. Microvascular network morphology in co-culture with GSCs. Fly through of surface rendering showing the open lumens and inner membrane of the network.

APPENDIX E

LIST OF SUPPLEMENTARY OF TABLES

Table E.1 Patient data for the patient-derived cancer-associated fibroblasts

	Patient #1	**Patient #2**	**Patient #3**
Age	71	50	82
Type	Infiltrating Lobular	Invasive ductal carcinoma with focal squamous differentiation	Invasive
Tumor Size	2.1 cm	2.3 cm	2.6 cm
Stage	1	2	3
Receptor Status	ER+, PR+, Her2-	ER+, PR+, Her2-	ER-, PR-, Her2-
Lymph Node	3/6	1/2	1/11

Table E.2. List of differentially expressed genes between CAF and NF co-cultures

Gene ID	Gene Symbol	Description	Log2(fold change) CAF/NF	p-value	FDR
10324	KLHL41	kelch like family member 41	1.15	4.8E-05	3.6E-02
6843	VAMP1	vesicle associated membrane protein 1	1.11	2.5E-05	3.1E-02
693197	MIR612	microRNA 612	1.00	3.4E-05	3.5E-02
64129	TINAGL1	tubulointerstitial nephritis antigen like 1	0.94	2.3E-05	3.1E-02
10457	GPNMB	glycoprotein nmb	0.91	1.3E-06	6.3E-03
633	BGN	biglycan	0.86	4.3E-05	3.6E-02
402778	IFITM10	interferon induced transmembrane protein 10	0.82	2.1E-05	3.1E-02
149954	BPIFB4	BPI fold containing family B member 4	0.78	7.4E-05	4.8E-02
114823	LENG8	leukocyte receptor cluster member 8	0.73	5.1E-05	3.6E-02
51286	CEND1	cell cycle exit and neuronal differentiation 1	0.72	4.6E-05	3.6E-02
3576	CXCL8	C-X-C motif chemokine ligand 8	-0.55	5.6E-05	3.8E-02
4604	MYBPC1	myosin binding protein C, slow type	-0.62	2.6E-05	3.1E-02
54935	DUSP23	dual specificity phosphatase 23	-0.71	3.0E-05	3.2E-02
9021	SOCS3	suppressor of cytokine signaling 3	-0.77	1.8E-05	3.1E-02
848879	MFSD2A	major facilitator superfamily domain containing 2A	-0.81	4.0E-05	3.6E-02
5142	PDE4B	phosphodiesterase 4B	-0.88	4.1E-05	3.6E-02
3569	IL6	interleukin 6	-0.98	9.4E-06	2.2E-02
6288	SAA1	serum amyloid A1	-1.44	2.4E-07	3.4E-03

7850	IL1R2	interleukin 1 receptor type 2	-1.49	3.6E-06	1.3E-02
6004	RGS16	regulator of G-protein signaling 16	-1.49	6.1E-07	4.3E-03
6289	SAA2	serum amyloid A2	-1.73	1.2E-05	2.4E-02
6279	S100A8	S100 calcium binding protein A8	-2.40	8.3E-06	2.2E-02

APPENDIX F

COPYRIGHT PERMISSIONS

ELSEVIER LICENSE
TERMS AND CONDITIONS

Oct 22, 2018

This Agreement between Mr. Danh Truong ("You") and Elsevier ("Elsevier") consists of your license details and the terms and conditions provided by Elsevier and Copyright Clearance Center.

License Number	4454320433530
License date	Oct 22, 2018
Licensed Content Publisher	Elsevier
Licensed Content Publication	Advanced Drug Delivery Reviews
Licensed Content Title	Microfluidic 3D models of cancer
Licensed Content Author	Kyung Eun Sung,David J. Beebe
Licensed Content Date	Dec 15, 2014
Licensed Content Volume	79
Licensed Content Issue	n/a
Licensed Content Pages	11
Start Page	68
End Page	78
Type of Use	reuse in a thesis/dissertation
Portion	figures/tables/illustrations
Number of figures/tables/illustrations	1
Format	both print and electronic
Are you the author of this Elsevier article?	No
Will you be translating?	No
Original figure numbers	Figure 1
Title of your thesis/dissertation	Microfluidic Models of Tumor-Stroma Interactions to Study the Interplay of Cancer Cells with their Surrounding Microenvironment
Expected completion date	Oct 2018
Estimated size (number of pages)	230
Requestor Location	Mr. Danh Truong 4505 S. Hardy Dr Apt 2126 TEMPE, AZ 85282 United States Attn: Mr. Danh Truong
Publisher Tax ID	98-0397604
Total	0.00 USD
Terms and Conditions	